GEOMECHANICAL ANALYSIS APPLIED TO GEOLOGICAL CARBON DIOXIDE SEQUESTRATION, INDUCED SEISMICITY IN DEEP MINES, AND DETECTION OF STRESS-INDUCED VELOCITY ANISOTROPY IN SUB-SALT ENVIRONMENTS

A DISSERTATION
SUBMITTED TO THE DEPARTMENT OF GEOPHYSICS
AND THE COMMITTEE ON GRADUATE STUDIES
OF STANFORD UNIVERSITY
IN PARTIAL FULFILLMENT OF THE REQUIREMENTS
FOR THE DEGREE OF
DOCTOR OF PHILOSOPHY

Amie Marie Lucier
November 2007

I certify that I have read this dissertation and that, in my opinion, it is fully adequate in scope and quality as a dissertation for the degree of Doctor of Philosophy.

Mark D. Zoback (Principal Adviser)

I certify that I have read this dissertation and that, in my opinion, it is fully adequate in scope and quality as a dissertation for the degree of Doctor of Philosophy.

Jerry M. Harris

I certify that I have read this dissertation and that, in my opinion, it is fully adequate in scope and quality as a dissertation for the degree of Doctor of Philosophy.

Gregory C. Beroza

I certify that I have read this dissertation and that, in my opinion, it is fully adequate in scope and quality as a dissertation for the degree of Doctor of Philosophy.

Norman H. Sleep

Approved for the University Committee on Graduate Studies.

ABSTRACT

This thesis presents contributions towards better understanding of the wide ranging applications of geomechanical modeling, with emphasis on carbon dioxide (CO_2) sequestration in deep saline aquifers, mining-induced stress perturbations and associated induced seismicity, and detection of stress-induced shear wave velocity anisotropy in a sub-salt environment.

The role of geomechanical analysis in characterizing the feasibility of CO_2 sequestration in deep saline aquifers is addressed in two investigations. The first investigation focuses on a site-specific geomechanics-based characterization of CO_2 sequestration potential, and the second investigation focuses on a geomechanics-based workflow for assessing the economic feasibility of regional deep saline aquifer CO_2 injection and sequestration.

The first investigation was completed as part of the Ohio River Valley CO_2 Storage Project. We completed a geomechanical analysis of the Rose Run Sandstone, a potential injection zone, and its adjacent formations at the American Electric Power's 1.3 GW Mountaineer Power Plant in New Haven, West Virginia. The results of this analysis were then used to evaluate the feasibility of anthropogenic CO_2 sequestration in the potential injection zone. First, we incorporated the results of the geomechanical analysis with a geostatistical aquifer model in CO_2 injection flow simulations to test the effects of introducing a hydraulic fracture to increase injectivity. We observed a nearly fourfold increase of injection rate due to the introduction of a hydraulic fracture in the injection zone. The flow simulations predict that a single vertical well with a hydraulic fracture could inject a maximum of 300-400 kt of CO_2/year. Then, we determined that horizontal injection wells at the Mountaineer site are feasible because the high rock strength ensures that such wells would be stable in the local stress state. Finally, we evaluated the potential for injection-induced seismicity. If pre-existing, but undetected, nearly vertical faults striking NNE or ENE are present, the increased pore pressure from CO_2 injection would raise their reactivation potential. Geomechanical analysis of potential CO_2 sequestration sites provides critical information required to evaluate its sequestration potential and associated risks.

The second investigation concerning CO_2 sequestration was motivated by the modeling and fluid flow simulation results from the first study. The first study showed that limited CO_2 injectivity may influence the feasibility of large scale sequestration at the Mountaineer site and other similar locations. For this reason, we determined that it was necessary to develop a workflow for assessing regional feasibility for CO_2 injection and storage that accounts for both economical and geomechanical constraints.

The geomechanics-based assessment workflow follows a bottom-up approach for evaluating regional deep saline aquifer CO_2 injection and storage feasibility. The CO_2 storage capacity of an aquifer is a function of its porous volume as well as its CO_2 injectivity. For a saline aquifer to be considered feasible in this assessment it must be able to store a specified amount of CO_2 at a reasonable cost per ton of CO_2. The proposed assessment workflow has seven steps that include (1) defining the CO_2 capture and storage (CCS) project and goals, (2) characterizing the geology and developing a geomechanical model of the aquifer, (3) constructing 3D aquifer models, (4) simulating CO_2 injection, (5, 6) evaluating CO_2 injection and storage feasibility (with and without injection well stimulation), and (7) determining whether it is economically feasible to proceed with the CCS project. The workflow was applied to a case study of the Rose Run sandstone in the eastern Ohio River Valley. We found that it is feasible in this region to inject and store 113 Mt CO_2/yr for 30 years at an associated well cost of less than 1.31 US$/t CO_2, but only if injectivity enhancement techniques such as hydraulic fracturing and injection induced micro-seismicity are implemented.

The second issue to which we apply geomechanical analysis in this thesis is mining-induced stress perturbations and induced seismicity in the TauTona gold mine, which is located in the Witwatersrand Basin of South Africa and is one of the deepest underground mines in the world. For over a century, numerous, often deadly, mining-induced earthquakes have been observed in this region. We completed this work as part of the Natural Earthquake Laboratory in South African Mines (NELSAM). Again we address this subject with two investigations. In the first investigation, we characterize the virgin stress state away from the mining-perturbed stresses. The second investigation incorporates the far-field stress state from the previous study to examine observed mining-induced seismicity.

In the first investigation, we developed and tested a new technique for determining the virgin stress state near the TauTona gold mine. This technique follows an iterative forward modeling approach that combines observations of drilling induced borehole failures in borehole images, boundary element modeling of the mining-induced stress perturbations, and forward modeling of borehole failures based on the results of the boundary element modeling. The final result was a well constrained range of principal stress orientations and magnitudes that are consistent with all the observed failures and other stress indicators. We found that the state of stress is a normal faulting regime with principal stress orientations that are slightly deviated from vertical and horizontal and therefore denoted with a (*). The maximum principal stress, S_{v*}, is deviated 0-20º from vertical towards the NNW with a magnitude gradient of 27 ± 0.3 MPa/km. The intermediate principal stress, S_{Hmax*}, is inclined 0-20º from horizontal with an azimuth of 145º to 168º and has a magnitude gradient of 21.5 to 26 MPa/km. The least principal stress, S_{hmin*}, is inclined 0-10º from horizontal with an azimuth of 235º to 258º and has a magnitude gradient of 13 to 15.5 MPa/km.

In the second investigation, we used this constrained stress state to examine the likelihood of faulting to occur both on pre-existing fault planes that are optimally oriented to the virgin stress state and on faults affected by the mining-perturbed stress field, the latter of which is calculated with boundary element modeling. A fault is critically stressed when the shear stress resolved on the fault plane is equal to or greater than the product of the coefficient of sliding friction and the effective normal stress. With respect to the far-field stress state, the critically stressed faults are normal faults generally striking SSE and NNW. The mining-induced stress perturbation affects faults relatively closer to the mining excavation. We analyzed active faults observed in borehole image log data and mapped in the TauTona access tunnels. We also investigated the likelihood of fault reactivation on the Pretorius Fault Zone (PFZ), an ancient (Pre-Cambrian) fault system which intersects the NELSAM study area. As a result of this modeling, we were able to further constrain the far-field stress state. More importantly, by using this far-field stress state in a detailed boundary element model we were able to make several observations that lead to a better understanding of the mining-induced seismicity that is occurring around the NELSAM study area in

TauTona. Finally, based on these results, we made several recommendations that could potentially increase safety in deep South African mines as development continues.

Finally, the third issue addressed in this thesis is the detection of stress-induced shear wave velocity anisotropy in a sub-salt environment. This investigation was motivated by the fact that the number of wells drilled through and near salt structures continues to increase and these wells are among the most expensive wells to drill in part because they are prone to numerous drilling problems. Better understanding of the geomechanical setting in proximity to salt results in more successful drilling and completion of these wells. One promising area of study for investigating the perturbation of the stress field in and around salt bodies is numerical modeling. However, in order to apply the results of the simulated stress field from a numerical model to a well drilled near a real salt body with confidence, it is necessary to compare the modeled results to data observations. Therefore, it is important to have independent observations of the stress state near the salt body. One technique for determining principal stress directions uses cross-dipole shear wave velocity anisotropy data. However, shear wave velocity anisotropy can be induced by mechanisms related to the rock structure such as bedding as well as stress-related mechanisms. In this study, we tested a technique proposed by Boness and Zoback (2006) to identify structure-induced velocity anisotropy and isolate possible stress-induced velocity anisotropy. The investigation used cross-dipole sonic data from three deep water sub-salt wells in the Gulf of Mexico. First, we determined the parameters necessary to ensure the quality of the fast azimuth data used in our analysis. We then characterized the quality controlled measured fast directions as either structure-induced or stress-induced based on the results of the Boness and Zoback (2006) technique. We found that this technique supplements the use of dispersion curve analysis for characterizing anisotropy mechanisms. We also find that this technique has the potential to provide information on the stresses that can be used to validate numerical models of salt-related stress perturbations.

ACKNOWLEDGEMENTS

This thesis would not have been possible without the contributions and support of a number of people.

I especially would like to acknowledge the help and support of my Ph.D. advisor, Prof. Mark Zoback. He has been a great source of knowledge, experience and support. He is a wonderful teacher, mentor, role model, and friend. He fosters the perfect work environment that is focused on trust, respect, hard work, and work-life balance. He embodies an exceptional standard to which I know I will hold all of my future bosses.

I would also like to thank all of my committee members, Prof. Norm Sleep, Prof. Gregory Beroza, and Prof. Jerry Harris, for their thoughtful comments and suggestions and for taking the time to be involved in my research. I would also like to thank the members of my original Qualifying Exam committee that provided important guidance early in my graduate student life, Prof. Lynn Orr and Prof. Stephan Graham, who also kindly chaired my defense committee.

I would also like to acknowledge my collaborators. I enjoyed working with Neeraj Gupta of Battelle Memorial Institute and T.S. Ramakrishnan of Schlumberger-Doll Research on my CO_2 sequestration work. A thanks to Vincent Heesakkers and Ze'ev Reches of the University of Oklahoma and Shaun Murphy of ISS International for their help on the NELSAM project. And thanks to Dan Moos of GeoMechanics International and Naomi Boness, formerly of the Stress group and currently at Chevron, for their help with my shear wave anisotropy research.

My time at Stanford would not have been the same if it had not been for the other members of the Stress and Crustal Mechanics Group. Thank you to Laura Chiaramonte, Ellen Mallman, Hannah Ross, Amy Day-Lewis, John Vermylen, Pijush Paul, Hiroki Sone, Paul Hagin (and JoJo), Naomi Boness, Lourdes Colmenares, Alvin Chan, John Townend, Charley Weiland, and Susan Philips-Moskowitz. I have had a great time working with you. But more important than work, I have also enjoyed our travels, group lunches, coffee breaks, ski trips, group dinners, and just chatting in the lab.

In addition to learning about geomechanics during my time at Stanford, I have also learned to ski, golf, and play field hockey better. I want to thank all of my skiing and golfing buddies and my field hockey team, the Feisties! I also took up cycling during

my time here and want to thank Ellen, Lindsey, Vanessa, and Jon, among others, for all the great rides.

There are so many people that made my years at Stanford so great. I want to acknowledge my roommates for all their support and friendship. Thanks Ellen, Kristina, Sara, Jess, Heidi, and Kyle! And thanks to the inhabitants of Maddux (Kyle, Jeff, Cam, Helen, Ashley, Chris, Ben, Jacob, and Warren) for hosting all the best parties and BBQs, particularly the Annual Carol Sing, my birthday, and my Ph.D. Extravaganza. I also want to thank Dave, Kyle, Ben, Lindsey, Ellen, Jeff, Elliot, Kevin, Laura, Bill, Hannah, Warren, Jacob, and Cam for being such great friends.

Most importantly, I want to acknowledge my family for all of their love and support. Thanks Mom for always being there to listen. Thanks Dad, since we both know I get my "brains" from your side of the family. Thanks Mike for being such a great big brother, always there to brag about me and look out for me. Thanks to Kimberly and Tyson, the newest members of the family. And I want to make a special acknowledgement for my grandmother, Betty Rooney, who was such a great example of a strong, intelligent, and independent woman with a drive for lifelong learning. She always supported my academic pursuits and amazed me with her ability to grasp complex scientific subject matters. I dedicate this thesis in her memory.

CONTENTS

LIST OF FIGURES

LIST OF TABLES

CHAPTER 1

INTRODUCTION

1.1 OVERVIEW

The work presented in this thesis illustrates the widely ranging applications of geomechanical modeling to relevant topics related to global climate change, seismology, mine safety, and petroleum exploration and production. The main goals of this thesis are (1) to build comprehensive geomechanical models in new regions with complex stress states, (2) to develop and test new techniques that are necessary to carry out geomechanical analyses in these regions, and (3) to use the results of the analyses to answer key questions relevant to the topic of investigation.

In this work, I present the results from three projects that are divided into five distinct investigations. These five investigations correspond to the remaining five chapters contained in this thesis. In the first project, I evaluated the geological CO_2 storage potential of deep saline aquifers in the Midwestern United States. This work was divided into two investigations. The first investigation was a site specific geomechanics-based characterization of the CO_2 storage potential at the Mountaineer power plant in New Haven, WV. In the second investigation, I developed a geomechanics-based workflow for assessing the economic feasibility of regional deep saline aquifer CO_2 injection and storage and apply the workflow to the region surrounding the Mountaineer power plant. The second project, which was also divided into two investigations, examines mining-induced seismicity near a deep underground gold mine in South Africa. In the first investigation, I characterized the virgin stress state away from the mining-perturbed stresses. The second investigation incorporated that far-field stress state into the modeling of the mining-perturbed stress field to examine observed mining-induced seismicity. Finally, in the third project, I tested a new technique for characterizing principal stress orientations in the complex stress fields adjacent to a salt structure in the deep water Gulf of Mexico using shear wave velocity anisotropy data from well logging.

While these three projects are distinctly different from each other, they are tied together by the principles that guide the geomechanical analysis. The main component of a comprehensive geomechanical model is the determination of the in situ stress state in the region of interest. This involves constraining the magnitude and orientations of the three principal stresses and the magnitude of the in situ fluid pressure. A second component of a complete geomechanical model is to characterize the pre-existing faults. This includes determining the orientation of the faults, their frictional strength, and their likelihood of slip in the existing stress field. The state of stress not only controls the likelihood of slip on pre-existing faults, but also controls the stability of boreholes, safe fluid injection rates, and the creation of hydraulic fractures for reservoir enhancement. Some or all of these topics are examined in each of the three projects contained in this thesis.

Another overarching theme that ties these three projects together is that the geomechanical analysis occurs in a complex and/or changing stress field. In the cases where the state of stress is changing due to either fluid injection or mine excavation, I not only characterized the initial stress state, but also evaluated the perturbations of the stress state. In the CO_2 sequestration project, I evaluated the perturbation of the in situ stress state through the injection of large volumes of CO_2. I investigated how the expected changes in the stress field affect (1) the injection rates of CO_2 in the region, (2) the ability to enhance injection through reservoir stimulation, and (3) the leakage risks associated with regional sequestration. In the South African gold mine project, I developed a new technique for constraining the virgin stress state that uses data both away from and within the complex stress environment that the mining excavation creates. I also modeled the stress perturbation associated with the mining excavation to better understand the mining-induced seismicity observed in the vicinity of the mine. Finally, in the Gulf of Mexico, I tested a new technique for characterizing the principal stress directions in the complex stress field that exists near a salt structure.

In the next section, I broadly introduce the motivations behind the three projects and describe the importance of applying a geomechanical analysis to them. Following the project motivations, I outline the remaining chapters of the thesis and include a brief introduction for each of the investigations.

1.2 PROJECT MOTIVATIONS

1.2.1 Geological CO_2 Sequestration

In recent years, global climate change has been brought to the forefront by scientists, public policy makers, and the media. Concern about global climate change resulting from anthropogenic emissions of greenhouse gases, such as CO_2, has prompted scientist to search for means of mitigating these emissions. One emerging technology for the mitigation of CO_2 emissions is geological CO_2 sequestration, which is also referred to as CO_2 capture and storage (CCS). In the process of geological CCS, CO_2 is captured and separated at point sources, such as coal burning power plants. It is then purified and compressed to a supercritical state and transported by pipeline to a storage location. At the storage location, the CO_2 is injected into a geological formation, such as a deep saline aquifer, unmineable coal seam, or depleted oil and gas field, for long term storage. In order for large scale geological CCS to be an effective mitigation strategy, the technologies require at each step of the CCS process must be improved and the costs must be decreased. In this thesis, I focus on the improvements that are necessary for identifying feasible storage locations in deep saline aquifers and improving the injection rates at these locations.

One problem faced in geological CO_2 sequestration is that many large point sources of CO_2 are far removed from ideal injection sites and the cost of transporting CO_2 over long distances is high. Because of the expense of transporting CO_2, it may be more economic to store CO_2 in "less than ideal" geological formations rather than transport it. All potential CO_2 storage sites must meet certain criteria. They are required to have (1) injection intervals that are deep enough that the CO_2 reaches a super-critical phase, (2) an impermeable caprocks to trap the CO_2 for long term storage, and (3) minimal leakage risks associated with existing faults and boreholes. Furthermore, potential injection sites should have sufficient porosity and thickness to provide storage volume and sufficient thickness and permeability to allow for reasonable rates of injection. A "less than ideal" storage site meets the required criteria, but may have low to moderate porosity, permeability, and/or thickness which limit the amount of CO_2 that can be injected and sequestered. In order to evaluate the CCS potential of a "less than ideal" injection site, it is necessary to have measures that define the feasibility such as

constraints on the maximum number of injection wells, minimum injection rates, or maximum costs associated with injection.

Geomechanical analysis plays an important role in the evaluation of a potential CO_2 injection and storage site. In order to evaluate CO_2 injection into a storage interval, such as a deep saline aquifer, I used 3D reservoir modeling and fluid flow simulation. A full geomechanical characterization is necessary for determining essential input into the fluid flow simulator, such as initial formation pore pressures (P_p) and safe injection pressures. A safe injection pressure is one that falls below the least compressive principal stress (S_3), also referred to as the fracture pressure. A full geomechanical analysis also provides information for calculating whether the in situ fracture network is hydraulically conductive and therefore able to enhance the overall bulk permeability of the injection zone. Furthermore, the geomechanical characterization is used for evaluating the feasibility of using horizontal injection wells and stimulation techniques that increase injectivity such as hydraulic fracturing and injection induced micro-seismicity for permeability enhancement.

1.2.2 Natural Earthquake Laboratory in South African Mines (NELSAM)

As mining around the world moves deeper underground, the dangers associated with mining-induced stress perturbations and associated seismicity become amplified. Induced seismicity near deep underground mines has serious implications for mine safety. While many seismic events induced by mining are small with moment magnitudes (M_w) of less than 2, they occasionally have M_w 4 and greater. However, even the smaller events at depth inside a mine are very dangerous and can result in damage to the excavation, injuries or fatalities. Seismicity is induced in mining regions by the stress perturbations associated with the mining excavation. Increased understanding of which faults are likely to slip as the stress state is perturbed can lead to more informed decision making during the planning and execution of mine development and thus increased safety in the mines.

The Natural Earthquake Laboratory in South African Mines (NELSAM) project is working to develop a very near-field laboratory to study earthquake physics and mechanics at seismogenic depths (Reches, 2006; Reches and Ito, 2007; Reches et al., 2005). The gold mines in the Witwatersrand Basin of South Africa are some of the

deepest mines in the world. In this region, deep underground mining and mining-induced seismicity has been occurring for over a century. Because of the high rates of seismicity induced by the mining activity and the accessibility of faults at depth, the deep gold mines of South Africa are unique locations for near-field studies of earthquake mechanics. However, the perturbation of the in situ stresses by mining activities creates a complex stress field that complicates the understanding of the physical mechanisms controlling the induced seismicity.

Much of the previous published work on characterizing the far-field in situ stress state near the deep mines in the Witwatersrand Basin relies on borehole strain relief measurements (Gay, 1972). In the TauTona gold mine, in which the NELSAM study is being carried out, the only direct measurements of the stresses are from overcoring measurements completed in the shaft pillar. While these measurements provide information about the mining perturbed stresses in the shaft pillar, they do not provide reliable information about the stresses near the NELSAM study area or in the far-field. In order to be able to effectively study the earthquakes occurring in the mines and to improve safety in deep mines, it is necessary to develop methods for accurately characterizing the far-field stresses and for modeling the mining-induced stress perturbations.

1.2.3 Complex Stress Field Adjacent to Salt Structures

As oil and gas exploration moves into more complex environments, such as deep water, sub-salt reservoirs in the Gulf of Mexico, drilling costs increase dramatically. With drilling costs reaching 10s to 100s of millions of dollars per well, the costs associated with drilling and wellbore stability problems are quite significant. Hazards related to drilling through and near salt diapers include, but are not limited to, tectonic instability, rubble zones from perturbed tectonic stresses, salt gouge at low effective stress (due to near lithostatic pore pressure conditions), and highly fractured sediments leading to mud loss (Fredrich et al., 2003). Better understanding of the geomechanical setting in proximity to salt results in more successful drilling and completion of these wells.

The complexity of the stress fields found around salt structures is a function of the constitutive behavior of salt. Salt is an isotropic material that cannot support anisotropic

stresses. However, the formations adjacent to salt bodies are typically subjected to anisotropic tectonic forces. The stresses in the formations directly adjacent to the salt are perturbed from the far-field stress state to allow for equilibrium in the salt body and continuity in the stress field at the interface between the salt and the formation. This perturbed stress state is complex and difficult to quantify.

One promising area of study for investigating the perturbation of the stress field in and around salt bodies is numerical modeling. However, in order to apply the results of the simulated stress field from a numerical model to a well drilled near a real salt body with confidence, it is necessary to compare the modeled results to data observations. Therefore, it is important to have independent observations of the stress state near the salt body. One method for determining in situ principal stress orientations in oil and gas fields is to use the presence of drilling induced wellbore failures, such as breakouts and tensile fractures (reviewed in (Zoback et al., 2003)). However, in the Gulf of Mexico oil and gas field setting this method is often ineffectual due to the presence of keyseats in deviated wells that mimic breakouts and typically small differential stresses, which are not sufficient for the formation of drilling induced tensile fractures.

Another technique employed to determine principal stress directions uses cross-dipole shear wave velocity anisotropy data. Shear wave velocity anisotropy can be induced by both structural- and stress-related mechanisms. One method for determining the mechanism that is controlling the observed shear wave velocity anisotropy is dispersion curve analysis, which requires advanced frequency-domain processing of the cross-dipole log data (Plona et al., 2002). The frequency-domain processing is not part of the traditional processing of DSI data, which occurs in the time-domain. However, Boness and Zoback (2006) developed a technique to identify the structural-induced components using the time-domain processed cross-dipole shear wave data. In theory, if the structural-induced shear wave velocity anisotropy is identified, then the stress-induced components can be isolated. Once the stress-induced shear wave anisotropy is characterized, it can be used to determine stress orientations, which are an important part of a geomechanical model.

1.3 THESIS OUTLINE

In Chapter 2, **Geomechanical aspects of CO_2 Sequestration in a deep saline aquifer in the Ohio River Valley region**, I present a complete geomechanical analysis of the Rose Run Sandstone, a potential injection zone, and its adjacent formations at the American Electric Power's 1.3 GW Mountaineer Power Plant in New Haven, West Virginia. This work was carried out as part of the Ohio River Valley CO_2 Storage Project. The results of this analysis were applied to three investigations used to evaluate the feasibility of anthropogenic CO_2 sequestration in the potential injection zone. First, I incorporated the results of the geomechanical analysis in CO_2 injection flow simulations to test the effects of introducing a hydraulic fracture to increase injectivity. I showed a nearly fourfold increase of injection rate due to the introduction of a hydraulic fracture in the injection zone. In the second investigation, I showed that horizontal injection wells at the Mountaineer site are feasible because deviated wells are stable in the local stress state. Finally, I used the geomechanical analysis results to evaluate the potential for injection-induced seismicity. I found that the increased pore pressure from CO_2 injection raises the reactivation potential of pre-existing, optimally oriented faults.

Based on the modeling and fluid flow simulation results in Chapter 2, it was apparent that limited CO_2 injectivity may influence the feasibility of large scale sequestration at the Mountaineer site and other similar locations. For this reason, I determined that it was necessary to develop a workflow for assessing regional feasibility for CO_2 injection and sequestration that accounts for both economical and geomechanical constraints.

In Chapter 3, **Assessing the economic feasibility of regional deep saline aquifer CO_2 injection and storage: A geomechanics-based workflow applied to the Rose Run Sandstone in Eastern Ohio, USA**, I present a workflow in terms of a case study based on the region surrounding the Mountaineer power plant. The assessment workflow proposed has seven steps that include (1) defining the CCS project and goals, (2) characterizing the geology and developing a geomechanical model of the aquifer, (3) constructing 3D aquifer models, (4) simulating CO_2 injection, (5,6) evaluating CO_2 injection and storage feasibility (with and with out injection well stimulation), and (7) determining whether it is economically feasible to proceed with the CCS project. For a saline aquifer to be considered feasible it must be able to storage a specified amount of

CO_2 at a reasonable cost per ton of CO_2. I applied the workflow to a case study of the Rose Run sandstone aquifer in the eastern Ohio River Valley. I showed that it is feasible to inject and store 113 Mt CO_2/yr for 30 years in this region at an associated well cost of less than 1.31 US$/t CO_2, but only if injectivity enhancement techniques such as hydraulic fracturing and injection induced micro-seismicity are implemented.

In Chapter 4, **Constraining the far-field in situ stress state near a deep South African gold mine**, I transition to the second project that focuses on work completed as part of the Natural Earthquake Laboratory in South African Mines (NELSAM) project. In this chapter, I develop and test a new technique for determining the far-field virgin state of stress near the TauTona gold mine. The technique I used to constrain the far-field stress state follows an iterative forward modeling approach that combines observations of drilling induced borehole failures in borehole images, boundary element modeling of the mining-induced stress perturbations, and forward modeling of borehole failures based on the results of the boundary element modeling. The final result was a well constrained range of principal stress orientations and magnitudes that are consistent with all the observed failures and other stress indicators. This stress state indicates that the crust is in a state of frictional faulting equilibrium, such that normal faulting is likely to occur on pre-existing fault planes that are optimally oriented to the stress field.

In Chapter 5, **Effects of mining-induced stress perturbations on pre-existing faults near a deep South African gold mine**, I investigate the likelihood of faulting to occur both on pre-existing fault planes that are optimally oriented to the virgin stress state and on faults affected by the mining-perturbed stress field, the latter of which is calculated with boundary element modeling. I showed that with respect to the far-field stress state, the critically stressed faults are generally normal faults that strike SSE or NNW. The mining-induced stress perturbation affects faults relatively closer to the mining excavation. I analyzed active faults observed in borehole image log data and mapped in the TauTona access tunnels. In the borehole image logs, I found evidence of recent slip on faults that have become critically stressed due to the mining-induced stress perturbation. In my investigation of the Pretorius Fault Zone (PFZ), an ancient (Pre-Cambrian) fault system, I found that stress perturbations due to recent mining

advances may be responsible for reactivating segments of the PFZ that were observed to slip during a M_w 2.2 event recorded in December 2004.

The final project on the complex stress field adjacent to salt structures is presented in Chapter 6, **Characterizing mechanisms of shear wave velocity anisotropy near a salt structure in deep water Gulf of Mexico**. In this study, I investigated a technique proposed by Boness and Zoback (2006) to identify structure-induced velocity anisotropy and to characterize possible stress-induced velocity anisotropy. The investigation used cross-dipole sonic data from three deep water sub-salt wells in the Gulf of Mexico. I examined (1) if stress-induced anisotropy is observed in the wells, (2) if this technique replaces or supplements dispersion curve analysis as a means for classifying the mechanisms of anisotropy, and (3) if this technique provides information that can be used to validate a potential numerical model of the salt-related stress perturbations. First, I determined the parameters necessary to ensure the quality of the fast azimuth data used in the analysis. I then characterized the quality controlled measured fast directions as either structure-induced or stress-induced based on the results of the Boness and Zoback (2006) technique. I found that this technique supplements the use of dispersion curve analysis for characterizing anisotropy mechanisms. I also found that this technique has the potential to provide information on the stresses that can be used to validate a potential numerical model of the salt-related stress perturbations.

CHAPTER 2

GEOMECHANICAL ASPECTS OF CO_2 SEQUESTRATION IN A DEEP SALINE RESERVOIR IN THE OHIO RIVER VALLEY REGION[1]

2.1 ABSTRACT

The Ohio River Valley CO_2 Storage Project is an ongoing characterization of deep saline formations being considered as potential sites for geological CO_2 sequestration. We completed a geomechanical analysis of the Rose Run Sandstone, a potential injection zone, and its adjacent formations at the American Electric Power's 1.3 GW Mountaineer Power Plant in New Haven, West Virginia. The results of this analysis were then applied to three investigations used to evaluate the feasibility of anthropogenic CO_2 sequestration in the potential injection zone. First, we incorporated the results of the geomechanical analysis with a geostatistical aquifer model in CO_2 injection flow simulations to test the effects of introducing a hydraulic fracture to increase injectivity. We observed a nearly fourfold increase of injection rate due to the introduction of a hydraulic fracture in the injection zone. The flow simulations predict that a single vertical well with a hydraulic fracture could inject a maximum of 300-400 kt of CO_2/year. In the second investigation, we determined that horizontal injection wells at the Mountaineer site are feasible because the high rock strength ensures that such wells would be stable in the local stress state. The third investigation used the geomechanical analysis results to evaluate the potential for injection-induced seismicity. If pre-existing, but undetected, nearly vertical faults striking NNE or ENE are present, the increased pore pressure from CO_2 injection would raise their reactivation potential. Geomechanical analysis of potential CO_2 sequestration sites provides critical information required to evaluate its sequestration potential and associated risks.

[1] *This paper was previously published as Lucier, A., M. Zoback, N. Gupta, and T.S. Ramakrishnan, 2006, Geomechanical aspects of CO_2 sequestration in a deep saline reservoir in the Ohio River Valley region: Environmental Geosciences, 13, 2, 85-103.*

2.2 INTRODUCTION

In regions like the Ohio River Valley that have many large point sources of CO_2 emissions and limited options for CO_2 sequestration in other geological media such as oil and gas reservoirs, the feasibility evaluation of CO_2 sequestration in deep saline aquifers is essential. Within the states of West Virginia, Ohio, Pennsylvania, Kentucky, Illinois and Indiana, annual CO_2 emissions from power plants reached nearly 700 Mt in 2000. This mass of CO_2 corresponds to a volume 1 x 10^6 m^3 if the CO_2 is compressed to a density of 700 kg/m^3. More than 98% of these emissions were from 185 coal burning power plants (Fig. 2-1a). According to the Environmental Protection Agency's (EPA) eGRID2002 database, 108 of the 185 coal plants emitted more than 1 Mt CO_2/yr, with 22 emitting over 10 Mt CO_2/yr (2002). Locating CO_2 sequestration sites in close proximity to large point sources such as these can significantly reduce the total cost of sequestration by minimizing the associated transportation costs. Failure to find sites with acceptable storage capacity in the vicinity of these CO_2 sources could make geological sequestration an impractical option for mitigating greenhouse gas emissions in a large portion of the conterminous United States.

While finding sequestration capacity in the region is of great importance, it is equally necessary to ascertain the safety of potential sequestration sites. If the potential for and risk of CO_2 leakage is significant, a site will not be considered any further, even if it possesses the needed capacity. One important aspect of assessing the risk associated with CO_2 sequestration is to understand the tectonic setting and state of stress at a potential sequestration site. Regionally, the Ohio River Valley is located in a relatively stable, intraplate tectonic setting. In general, the regional stress state is strike-slip to reverse faulting, with the maximum horizontal stress (S_{Hmax}) oriented northeast to east-northeast (Fig. 2-1b) (Zoback and Zoback, 1989). While earthquakes in this region are rare, they do occur. Figure 2-1b indicates the locations of seismic events that have occurred in the region over the last 40 years (black circles). The presence of seismic activity, both natural and induced, is of great importance when evaluating CO_2 sequestration potential. Extensive fault zones may provide leakage pathways along which CO_2 could migrate. The injection of large volumes of CO_2 into a deep aquifer will result in an increase in pore pressure by several MPa in and around the injection zone, especially during the injection period. This pressure change can lead to slip on

pre-existing faults when the state of stress is near frictional equilibrium, which is often the case in intraplate regions (Townend and Zoback, 2000). Quantifying the localized stress state and fault orientations at potential CO_2 sequestration sites provides the necessary information to assess safe injection pressures and to understand the possibility of CO_2 injection to induce seismicity for specific injection sites.

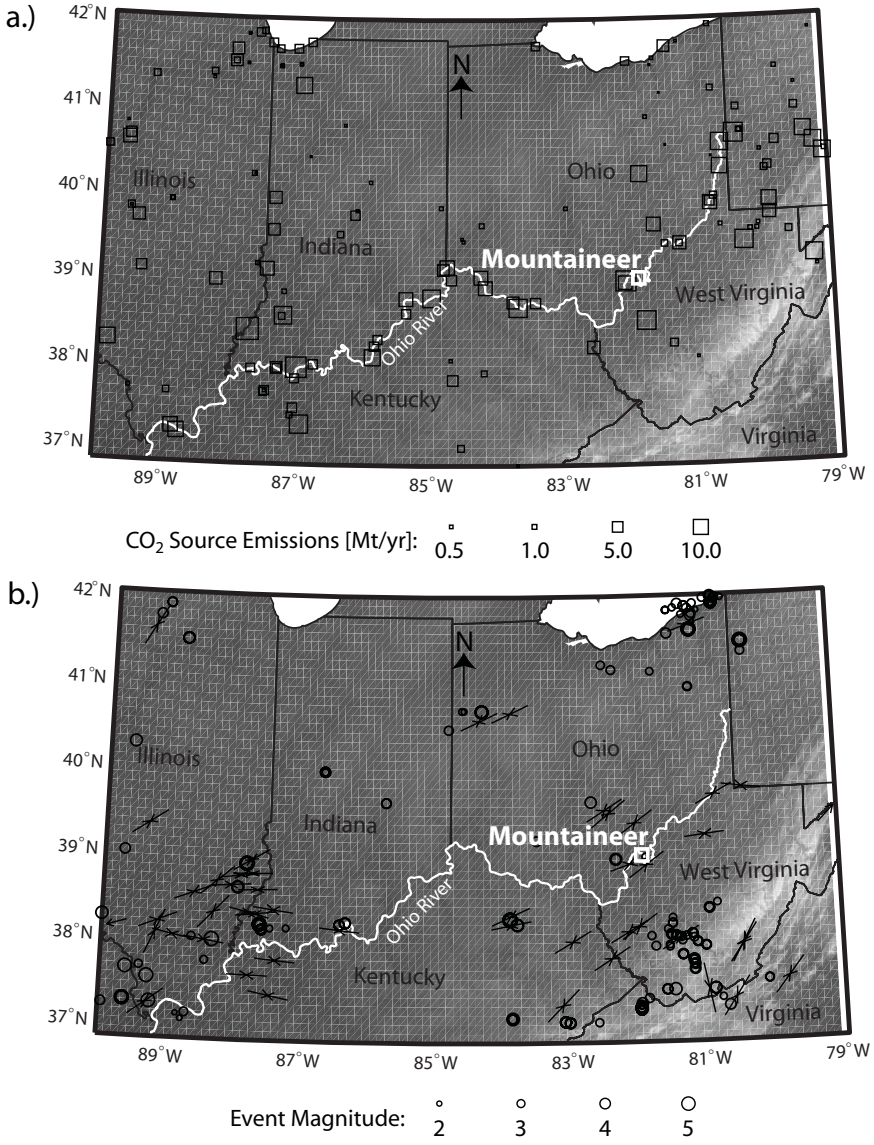

Figure 2-1: Regional map of the Ohio River Valley. The Ohio River is shown in white. (a) Power plants are shown by squares scaled by the total CO_2 emissions for each site in 2000. The Mountaineer site is indicated in white. (b) The tectonic setting is illustrated with S_{Hmax} stress orientations (inverted arrows) and seismic events since 1964 (circles). The regional S_{Hmax} orientation trends approximately Northeast-Southwest (Zoback and Zoback, 1989).

The Ohio River Valley CO_2 Storage Project seeks to evaluate the potential of deep saline aquifer sequestration at the site of one of the large point sources discussed above (Gupta et al., 2005). Specifically, this project focuses on a site-specific characterization of the subsurface beneath American Electric Power's 1.3 GW Mountaineer Power Plant in New Haven, West Virginia, which emitted 7.2 Mt of CO_2 in 2000 (Fig. 2-1). The evaluation of this site is based on data collected from a seismic reflection survey, geophysical logging and well testing of a 2800 m (below ground surface), vertical borehole (AEP#1 well), and regional field data. A schematic diagram of the Mountaineer site is depicted in Figure 2-2, showing the AEP#1 well at depth and in relation to the Mountaineer Power Plant.

During the site characterization, several potential injection zones were identified based on permeability and porosity logs (Fig. 2-3). Out of these, three zones were selected for further assessment (Gupta et al., 2005). Two zones are located in dolomites with secondary permeability and porosity. One of these is at a depth of about 2260 m in the Ordovician Beekmantown Dolomite, and the other is in the Cambrian Copper Ridge Dolomite at around 2490 m. The third zone is in the Ordovician Rose Run Sandstone from about 2355 m to 2388 m. The permeability, determined from a nuclear magnetic resonance (NMR) transverse relaxation log, is < 1 mD for much of the borehole but occasionally peaks to about 50-100 mD in selected sections. We also analyzed pre-existing fractures in the potential injection zones as a source of effective permeability. Using an electrical image log that measures formation microresistivity, we identified the natural fractures that intersect the borehole and determined the strike, dip, and aperture of the fractures. However, we found that natural fractures do not appear to significantly increase permeability. The effective porosity ranges from about 0% to 10%, with a mean porosity of 2.8%. The zones identified as possible injection sites have average effective porosities ranging from 4.1% to 6.9%.

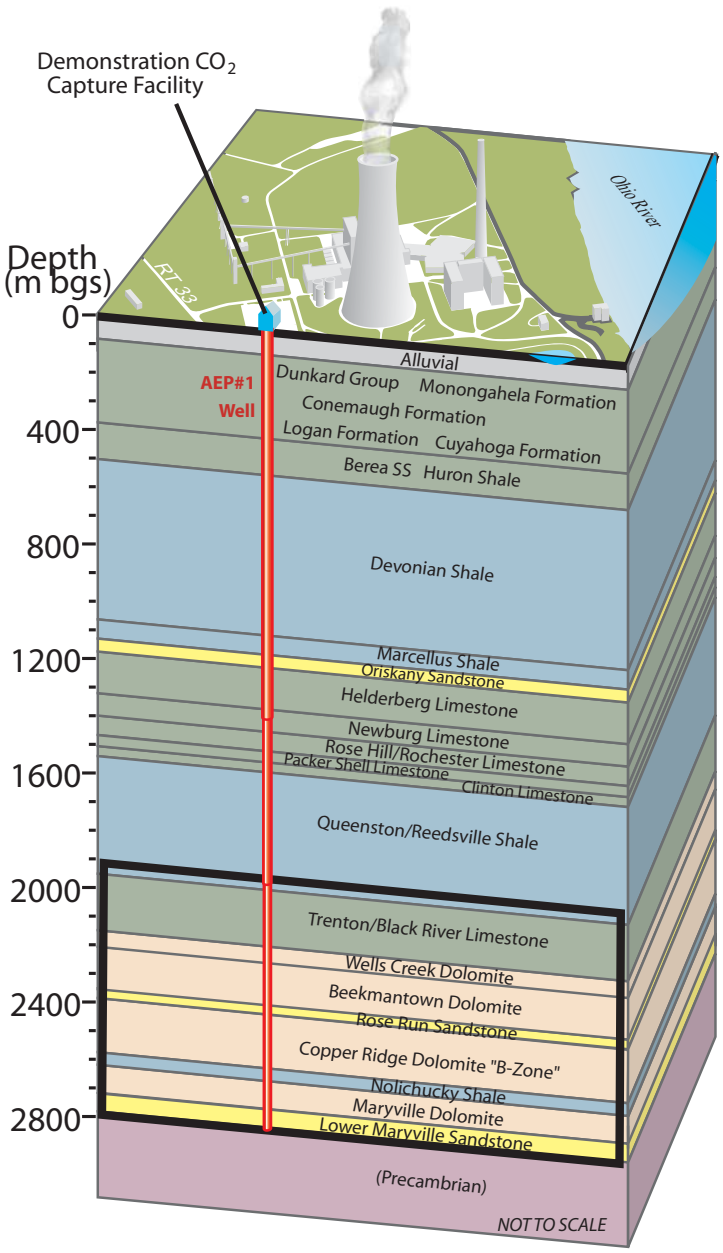

Figure 2-2: A 3-D schematic of the characterization site at the Mountaineer Power Plant. The diagram illustrates the well location relative to the power plant and the general stratigraphy intersected by the well. The black box outlines the depths focused on in this paper.

The fact that possible injection zones in deep sedimentary basins such as the Appalachian Basin appear to have low-to-moderate permeability and porosity reinforces the need to understand the geomechanical influences that will guide any reservoir stimulation techniques. This study focuses on the Rose Run Sandstone as a potential

injection zone. We completed a geomechanical analysis of the site and incorporated the results into CO_2 injection flow simulations. Carbon dioxide injection simulations in 3D Rose Run Sandstone reservoir models were used to investigate the effectiveness of hydraulic fracturing to increase injectivity. Another option being considered to increase injectivity is the drilling of deviated and horizontal wells, therefore we looked at the stability of various well orientations in the given stress field. Finally, we made a preliminary examination of the pressure conditions and fault orientations that, if present, would increase the potential of induced seismicity in the caprock.

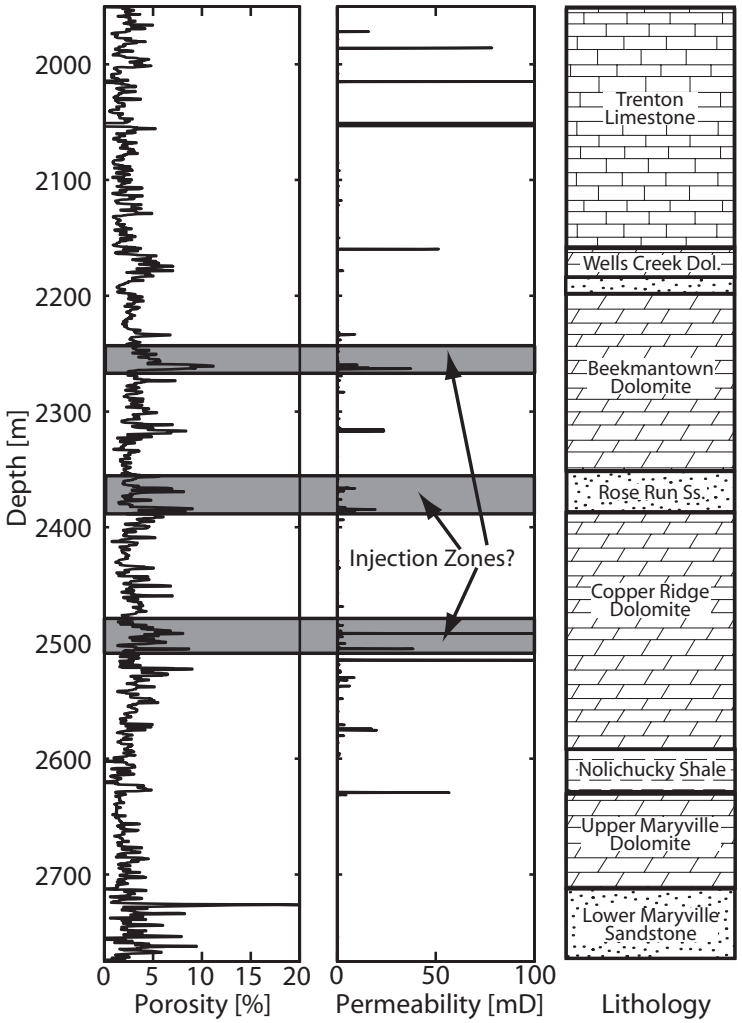

Figure 2-3: Density porosity log and NMR permeability log from the AEP#1 well (processed with a median filter of order N=9). The general lithology is shown to the right. Three possible injection zones are highlighted in gray.

2.3 BUILDING A GEOMECHANICAL MODEL

From a geomechanical standpoint, a suitable site for CO_2 sequestration must have sufficient injectivity while maintaining caprock integrity. The caprock must not be susceptible to hydraulic fracture propagation, and the formation itself should be resistant to fault slippage. A suitable sequestration site must also have a caprock capable of resisting the buoyancy driven flow of CO_2, so that the fluid can be stored over appreciable time scales (hundreds to thousands of years) without leaking. In the geographical region and geological setting of this study, we foresee that reservoir stimulation that preserves the efficacy of the caprock will be necessary for cost-effective sequestration. Since successful reservoir stimulation requires knowledge of the in situ stresses, we completed a geomechanical characterization of the Mountaineer site.

The goal of our analysis was to quantify the magnitude and orientation of the three principal stresses and determine whether the stress state affects the viability of the Rose Run Sandstone to act as an effective CO_2 storage unit. The three principal stresses are the vertical stress (S_v) and the minimum and maximum horizontal stresses (S_{hmin} and S_{Hmax}). Our methodology for determining the in situ stress state followed Zoback et al. (2003):

1. Calculate elastic moduli from velocity and density logs;
2. Calculate the vertical stress (S_v) by integrating the density log;
3. Identify the occurrence of drilling induced tensile fractures and wellbore breakouts using electrical image log and caliper data to determine stress orientation;
4. Utilize uniaxial compressive strength (C_o) from core samples to analyze compressive wellbore failures;
5. Interpret minifrac tests to determine allowable range of S_{hmin} magnitudes and pore pressure (P_p);
6. Interpret available data to constrain the possible values of S_{Hmax}.

Once the state of stress was determined, we used the information to obtain safe injection pressures, model a hydraulic fracture to enhance injectivity, analyze horizontal well stability, and investigate the possibilities of induced seismicity at the site.

2.3.1 Calculation of Elastic Moduli

We used the P- and S- wave velocity logs and the density log from the suite of geophysical logs available from the AEP#1 well to evaluate the Poisson's ratio and Young's modulus associated with different lithologies. Poisson's ratio (ν) is calculated from the following relationship between the P-wave velocity (V_P) and the S-wave velocity (V_S):

$$\nu = \frac{V_P^2 - 2V_S^2}{2(V_P^2 - V_S^2)} \tag{2-1}$$

Young's modulus (E) is then calculated from rock density (ρ), V_S, and ν:

$$E = 2\rho V_S^2 (1 + \nu) \tag{2-2}$$

The geophysical logs and the results of the elastic moduli calculations are shown along with the general lithology of the well in Figure 2-4. In the Rose Run Sandstone, V_P decreases significantly more than V_S relative to the adjacent dolomite formations accounting for the sandstone's lower ν value. Along with the decrease in ν in the Rose Run Sandstone, the lower values of V_S and ρ in the sandstone result in a lower E. Poisson's ratio and Young's modulus are material property inputs used in a later section to constrain the possible S_{Hmax} magnitudes allowable under the Mohr-Coulomb criterion for frictional strength.

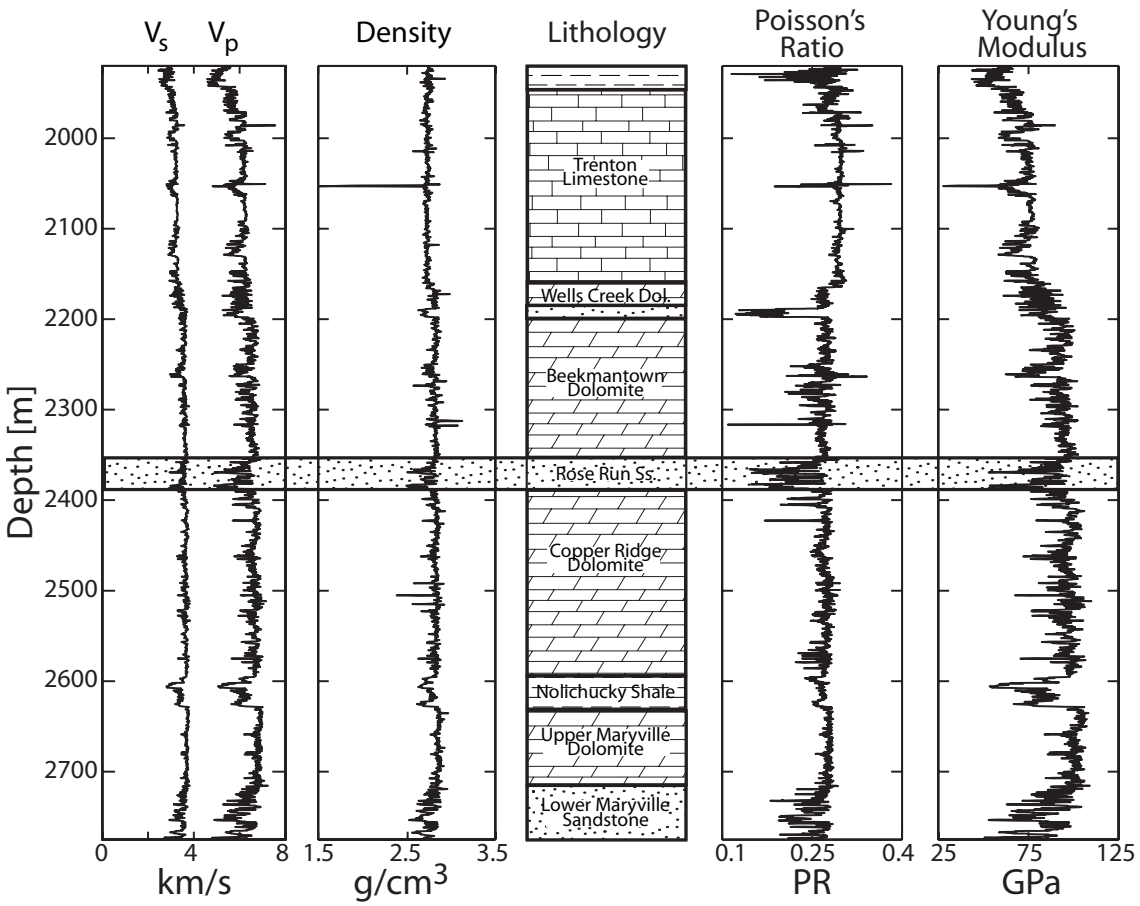

Figure 2-4: Velocity and density logs from AEP#1 and the calculated Poisson's ratio and Young's modulus. A generalized lithology is shown for reference.

2.3.2 Vertical Stress Determination

To characterize the in situ state of stress, we determined the orientation and magnitude of the three, mutually orthogonal, principal stresses. We assumed that one of the principal stresses has a nearly vertical orientation (within 5º), such that the magnitude of this vertical stress is determined by the weight of the overlying rock material. This assumption was validated by observations of drilling-induced tensile fractures as discussed below. We calculated the magnitude of S_v by integrating the density log over the depth of the well:

$$S_v = \int \rho(z) g dz \approx \sum \rho_{avg} g \Delta z \qquad (2\text{-}3)$$

where ρ is rock density, g is gravity acceleration , z is depth, and ρ_{avg} is the average density over the depth interval Δz. Figure 2-5 shows the density log over the entire depth range of the well and a plot of depth vs. S_v as determined from the density log.

The shallowest 75 m of the density log is extrapolated with a cubic equation to account for the presence of low density, Cenozoic, unconsolidated, alluvial sediments. The interpolation between 550 and 1191 m is linear. The gradient of S_v with depth determined from a linear fit to the density integration is 26.2 MPa/km. A typical overburden gradient for most clastic sedimentary rocks with an average porosity of 15% is around 23 MPa/km, but the relatively high density and low porosity of the overburden material at this site results in a higher gradient.

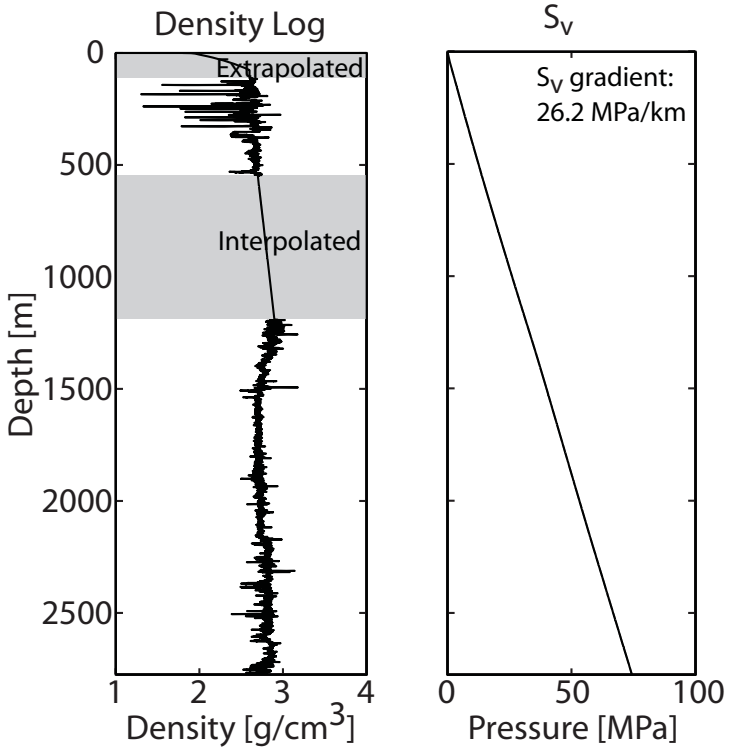

Figure 2-5: Density log and calculated vertical stress (S_v) magnitude with depth. At some depth intervals, the density was extrapolated or interpolated to compensate for data gaps. The S_v gradient is 26.2 MPa/km.

2.3.3 Determination of Stress Orientation

As a well is drilled, stress is concentrated at the wellbore wall. This stress concentration is described by the well-known Kirsch equations (Kirsch, 1898). In a vertical well, the effective stresses at the wellbore wall are described as the hoop stress ($\sigma_{\theta\theta}$), the radial stress (σ_{rr}), and the stress parallel to the wellbore wall (σ_{zz}) (Jaeger and Cook, 1979):

$$\sigma_{\theta\theta} = S_{hmin}+S_{Hmax}-2(S_{Hmax}-S_{hmin})\cos(2\theta)-2P_p-\Delta P-\sigma^{\Delta T} \quad (2\text{-}4)$$

$$\sigma_{rr} = \Delta P \quad (2\text{-}5)$$

$$\sigma_{zz} = S_v - 2\nu(S_{Hmax}-S_{hmin})\cos(2\theta) - P_p - \sigma^{\Delta T} \qquad (2\text{-}6)$$

where θ is the angle around the hole measured from the azimuth of S_{Hmax}, P_p is the pore pressure, ΔP is the difference between wellbore pressure (resulting from the weight of the drilling mud column) and P_p, $\sigma^{\Delta T}$ is the thermal stress induced by cooling of the wellbore by ΔT degrees, and ν is the static Poisson's ratio. In certain in situ stress states, the stress concentration may lead to tensile failure along the wellbore wall, creating drilling induced fractures and/or compressional failure, resulting in breakouts. Drilling-induced tensile (hydraulic) fractures occur where the effective stress components, usually the hoop stress, becomes negative and equal in magnitude to the tensile strength T_o of the rock; breakouts occur where the one of the stress components reaches a maximum and exceeds the compressive strength C_o (Fig. 2-6a) (Zoback et al., 2003).

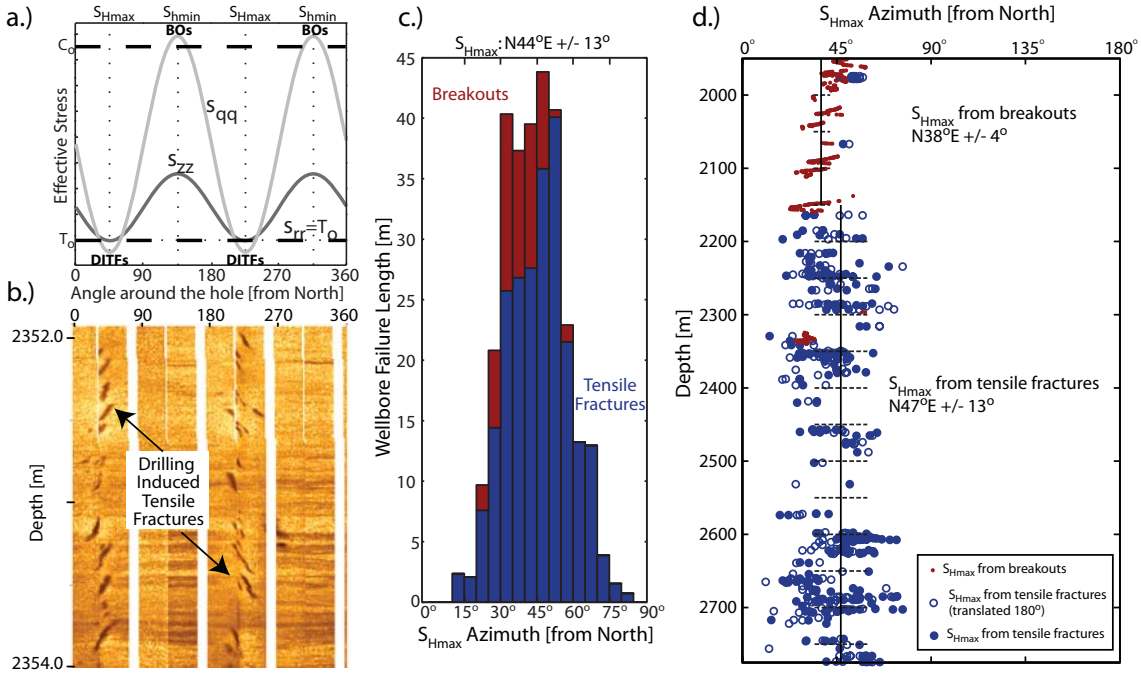

Figure 2-6: Determining horizontal stress orientation from drilling induced wellbore failure. (a) Schematic of stress concentrations at the wellbore wall leading to wellbore failure. Where $\sigma_{\theta\theta}$ falls below the tensile strength, T_o, tensile fractures form. Where $\sigma_{\theta\theta}$ is greater than the compressive rock strength, C_o, breakouts form. The orientation of tensile fractures coincides with the far field S_{Hmax} orientation, while breakouts form in the direction of S_{hmin}. (b) Example of drilling induced tensile fractures in the AEP#1 electrical image log. (c) Histogram of S_{Hmax} azimuth where frequency corresponds to length of the wellbore in failure. (d) S_{Hmax} azimuth inferred from tensile fracture and breakout occurrences.

Moos and Zoback (1990) demonstrated that, in the absence of excessive mud weights or of wellbore cooling during drilling, drilling-induced tensile fractures are

most likely to form in vertical wells when the state of stress is in a strike-slip regime, such that S_v is the intermediate principal stress and there is high horizontal stress anisotropy ($S_{hmin} < S_v < S_{Hmax}$). They may also form when the stress state is nearly strike slip, such that the magnitude of Sv is almost equal to that of one of the horizontal stresses. In a vertical well, the tensile fractures form 180° apart in the direction of S_{Hmax} (Fig. 2-6a). We used the electrical image log to pick drilling-induced tensile fractures along the wellbore from 1900 m to 2800 m, their presence indicating that indeed the stress regime is strike-slip to nearly strike slip. An example of drilling-induced tensile fractures from the electrical image log is shown in Figure 2-6b. The presence of en echelon tensile fractures in the near-vertical wellbore indicates that a small stress perturbation caused the vertical stress to rotate from a principal stress direction (Peska and Zoback, 1995). Based on modeling results, the en echelon fracture pattern observed in the electrical image implies only a small (5 to 10º) rotation of the vertical stress. As shown below, the state of stress is normal to strike-slip in the Rose Run and strike-slip in the adjacent formations. This is consistent with the observations of the drilling-induced tensile fractures.

The best data for observing the presence of breakouts is an ultrasonic borehole televiewer (Zoback et al., 1985), but this log was not available for the AEP#1 well. In some instances, breakouts can also be detected in the electrical image as out-of-focus zones, where the pads are not making contact with the wellbore walls. However, the data quality was such that we could not detect breakouts from the electrical image log with certainty. Instead, we used the four-arm caliper data from the electrical image tool to determine the presence of breakouts (Plumb and Hickman, 1985). We analyzed the caliper data for evidence of wellbore elongation. When the difference between the wellbore diameters measured by the two perpendicular caliper arms was greater than 1.02 cm and the caliper arms did not rotate more than 15˚ over a 5 m depth interval, then a breakout was recorded. The hole was considered “washed out” if the minimum caliper diameter measured more than 1.27 cm larger than the drill bit size of 15.5 cm. The orientation of the caliper pair with the greatest measured diameter determined the azimuth of the breakout and therefore the azimuth of S_{hmin}. Because “keyseating” of the borehole wall can occur from mechanical erosion of the wellbore during the drilling

process in wells even slightly deviated from vertical, we checked their occurrence against the direction of the hole to discount this effect.

Taking the breakout and drilling-induced tensile fracture occurrences together, the results of the wellbore failure analysis indicate an average S_{Hmax} orientation of N44˚E ± 13˚ (Fig. 2-6c). The orientations are corrected for any deviations from vertical in the wellbore trajectory. The breakouts, which occur primarily between 1950 and 2150 m, suggest an S_{Hmax} azimuth of N38˚E ± 4˚ (Fig. 2-6d). The drilling-induced tensile fractures occur primarily between 2150 and 2775 m, a zone that includes the Rose Run Sandstone, and they indicate an S_{Hmax} azimuth of N47˚E ± 13˚ (Fig. 2-6d). There may be a slight shift in the orientation of S_{Hmax} with depth, or the difference may be an artifact of the less reliable breakout determinations. Since we have focused on a depth interval in which drilling induced tensile fractures were observed, we used an S_{Hmax} azimuth of N47˚E ± 13˚ for the geomechanical model of the Rose Run Sandstone and adjacent formations. This S_{Hmax} azimuth is consistent with the regional stress orientations shown with inverted arrows in Figure 2-1b (Zoback and Zoback, 1989). The presence of borehole failures not only gives the orientation of horizontal stresses, it is also used in conjunction with the other data and observations to constrain the magnitude of S_{Hmax}.

2.3.4 Uniaxial Compressive Strength Measurements

The uniaxial compressive strength, C_o, for four rock samples located in the Rose Run and adjacent dolomite formations was measured in laboratory triaxial tests. Core samples from three different lithologic units indicate very high C_o, particularly in the dolomite layers. The Wells Creek and Beekmantown Dolomites have compressive strengths of about 350 MPa. Two samples from the Rose Run Sandstone have C_o values of 238 and 256 MPa. There are no tests for the Queenstone/Reedsville Shale or Trenton Limestone, which are the units with breakouts present. Since breakouts are limited to these units, the rock strength is likely to be significantly less than those determined for the dolomites and sandstone. We estimated a rock strength of 130 ± 25 MPa for these rocks based on observations discussed in the later section on constraining S_{Hmax} magnitudes. Typical C_o values observed for these rock types with similar values for

elastic moduli based on the geophysical logs are consistent with this estimation (Chang et al., 2006).

2.3.5 Minifrac Test Analysis

The next step in developing a geomechanical model of this site was to measure the magnitude of the least principal stress, S_3, which in this case is S_{hmin}. As drilling induced tensile fractures already exist along the wellbore wall, when the wellbore fluid pressure exceeds the magnitude of S_{hmin}, a hydraulic fracture should propagate away from the wall in the plane normal to the S_{hmin} direction. The fracture closes when the pressure falls below S_{hmin}. During a minifrac test, a small hydraulic fracture is created and the pressures at which the fracture forms, propagates and closes is directly measured. Therefore, minifrac tests are used to determine the magnitude of the least principal stress (Fig. 2-7a). The instantaneous shut-in pressure (ISIP) is a good indicator of the magnitude of S_{hmin}. Once the injection stops, this pressure is reached almost immediately as the fracture closes (Haimson and Fairhurst, 1970). Fracture closure pressure (FCP) is another common estimate of the least principal stress, however it is nearly the same as ISIP when low viscosity fluids and low pumping rates are used during the minifrac. The leak-off pressure (LOP) and the fracture propagation pressure (FPP) also provide less accurate but reasonable estimates for the least principal stress magnitude when injection rates and fluid viscosities are low.

In AEP#1, five open-hole minifrac tests were completed in and around the Rose Run Sandstone: two tests were completed above it; one test was completed in the sandstone; and two more were completed below it. The tests were conducted using a straddle packer to isolate the test intervals within the uncased borehole section. All the pressure readings for the tests were taken with the same gauge located between the packers. The Rose Run minifrac test was carried out near the top of the unit at 2358.55 m (Fig. 2-7b). We interpreted the S_{hmin} value measured from this test to be 31 – 32.5 MPa. The results from all the tests and their quality are summarized in Table 1. The tests have varying degrees of quality, the highest being A, which are ranked and explained in the table.

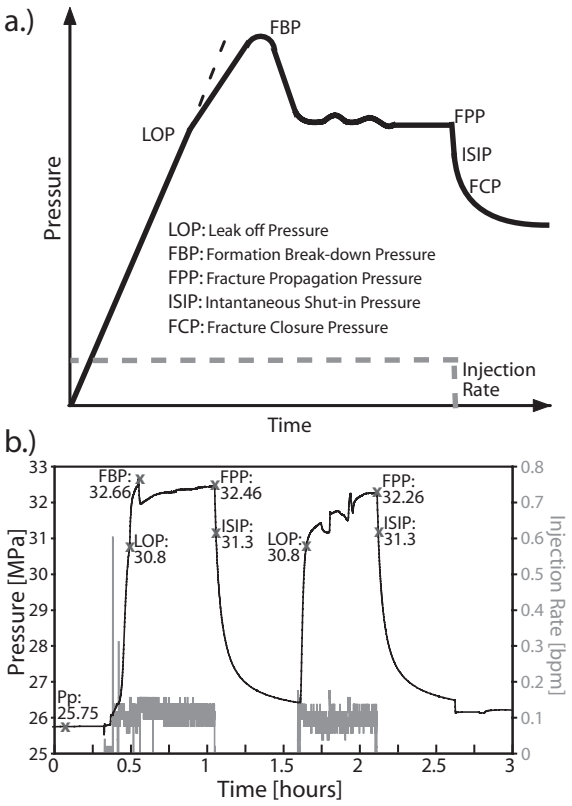

Figure 2-7: Minifrac tests to measure S_3 magnitude. (a) Example of an ideal minifrac (Gaarenstroom et al., 1993). Injection rate remains constant until shut-in. Pressure builds linearly until leak off (LOP) is reached. Pressure declines after the fracture breakdown pressure (FBP). Pressure remains nearly constant at the fracture propagation pressure (FPP) as injection continues. Once injection ends, pressure bleeds off, first reaching the instantaneous shut-in pressure (ISIP) and then the fracture closure pressure (FCP). (b) Minifrac test in the Rose Run Sandstone.

Table 2-1: Results of minifrac test analysis. The S_{hmin} magnitude range represents the instantaneous shut-in pressure (ISIP) to the fracture propagation pressure (FPP). In some tests, it is unclear if the pressure increased above the fracture break-down pressure (FBP) or FPP. These tests are given a lower quality rating. Tests with poor injection rate data quality are ranked the lowest. The S_{hmin} magnitude has a local minimum in the Rose Run Sandstone.

Depth [m]	**Lithologic Unit**	**S_{hmin} range [MPa]**	**Test quality**	Reason for quality rating
2077	Trenton Ls.	42 →	B	Unclear if FBP or FPP reached
2343	Beekmantown Dol.	35-37	A	Good test
2359	Rose Run Ss.	31-32.5	A	Good test
2413	Copper Ridge Dol.	34 →	C	Unclear if FBP or FPP reached Injection rate not constant
2418	Copper Ridge Dol	44-48	C	Injection rate unavailable ISIP difficult to pick

The most notable observation from these results is that the magnitudes of S_{hmin} from the tests in the Rose Run Sandstone and in the rock units directly adjacent to it are significantly lower than the magnitude of S_{hmin} above and below this zone. This difference may be related to the fact that this is a layered system with varying rock stiffness, as illustrated by the variation of log-derived Young's modulus with depth (Fig. 2-4). In a layered system such as this, application of a far-field compressive stress would tend to concentrate stress in the stiffer layers. Correspondingly, stress in the more compliant layers (like the Rose Run Sandstone) would have lower magnitudes than the adjacent layers with greater stiffness. While such a heuristic model is intuitively appealing, it is not possible to accurately match the contrast in stress magnitudes observed with either log-based gravity loading models that predict stress variations with depth based on variations of Poisson's ratio (Anderson et al., 1973; Hareland and Harikrishnan, 1996) or modifications of that model that allow for application of tectonic strain and incorporate variations of Young's modulus with depth (Blanton and Olson, 1999).

The pressure in each test interval was allowed to equilibrate for about one day prior to the minifrac tests. The pre-injection pressure measurements from the minifrac tests indicate the formation pore pressure (P_p) at depth. We used a linear fit to these data points and obtained a P_p gradient of 11 MPa/km, which is slightly higher than freshwater hydrostatic. This higher gradient is due to the higher density of the high salinity brine compared to freshwater (Gupta et al., 2005). Given this pressure gradient, the density of CO_2 at the in-situ conditions of the Rose Run Sandstone at 2365 m, with a Pp of 26 MPa and a temperature of 63.1°C, is ≈ 782 kg/m^3 (Span and Wagner, 1996).

2.3.6 Constraining S_{Hmax}

In order to determine the magnitude of S_{Hmax}, we integrated the data and analyses discussed above (rock properties, failure occurrences, stress magnitudes, and pore pressure) along with drilling conditions and the Mohr-Coulomb failure criterion to build "constrain stress" diagrams as described by Moos and Zoback (1990). The first step was creating a "stress polygon" that constrains the possible stress relationships between S_{Hmax} and S_{hmin} allowable under the Mohr-Coulomb failure criterion for a given depth. The sides of this polygon are functions of S_v, P_p, and the coefficient of sliding friction

(μ) for the specified depth. Laboratory experiments have shown that at depth μ tends to fall within the range of 0.6-1.0 (Byerlee, 1978). In this case, we used the S_v gradient of 26.2 MPa/km, the P_p gradient of 11 MPa/km, and μ=0.8 to define the dimensions of the polygon (Fig. 2-8). Once the polygon was created, we further constrained the possible state of stress by incorporating the presence or absence of drilling-induced tensile fractures and/or breakouts, along with breakout width if present. Several other inputs are needed to constrain the stress state consistent with the occurrence of wellbore failures at a given depth. These include material properties, drilling conditions and an estimate of S_{hmin} magnitude. The necessary material properties are Poisson's ratio, ν, Young's modulus, E, the coefficient of thermal expansion, α, and tensile and compressive strengths, T_o and C_o, respectively. Drilling conditions that can influence the formation of drilling-induced wellbore failures are ΔT, the difference between the formation temperature and the mud temperature, and ΔP, the pressure difference between the well pressure (from drilling mud weight) and formation pressure (P_p). In this case, the mud weight is equal to P_p, so ΔP=0. The final constraint in determining the S_{Hmax} magnitude is the S_{hmin} magnitude obtained (or extrapolated) from the minifrac test results. The values used to build the "constrain stress" plots are provided in Table 2.

Table 2-2: Input data and S_{hmin} constraints for the S_{Hmax} "constrain stress" determinations. Wellbore failure types are drilling-induced tensile fractures (DITF) and breakouts (BO). Compressive rock strength, Co, for the four shallowest depths are from the results of the "constrain stress" diagram at 1975 m (Fig. 2-8). The other Co values are from the triaxial test results. The value of ΔT is the temperature difference of the drilling fluids and the formation temperature.

Depth [m]	S_v [MPa]	P_p [MPa]	Failure type	B0 width [°]	Poisson's Ratio	Young's Modulus [GPa]	C_o [MPa]	Δ T [°C]	S_{hmin} [MPa]
1925	50.44	21.18	BO	50	0.29	60	105-155	-7	40-44
1975	51.75	21.73	BO, DITF	50	0.31	74	105-155	-7.8	40-44
2050	53.71	22.55	BO	50	0.31	76	105-155	-9	41-45
2125	55.67	23.38	BO	50	0.3	68	105-155	-10.3	42-46
2265	59.34	24.92	DITF	0	0.29	94	350	-12.5	44-48
2365	61.96	26.02	DITF	0	0.25	85	240	-14.1	34-36
2465	64.58	27.12	DITF	0	0.28	95	350	-15.7	46-50
2502	65.55	27.52	DITF	0	0.28	100	350	-16.3	47-51
2625	68.77	28.88	DITF	0	0.27	72	350	-17.8	49-53

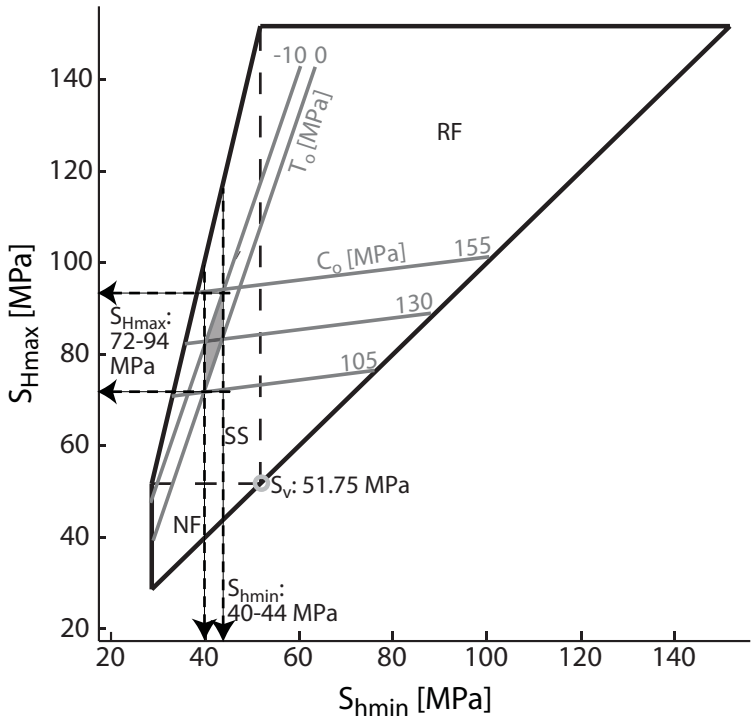

Figure 2-8: S_{Hmax} magnitude estimation from "constrain stress" method in Trenton Limestone at 1975 m depth. Since breakouts and tensile fractures are observed at this depth, the C_o contours (105, 130, and 155 MPa) and the T_o contours (-10 and 0 MPa) are used to constrain the possible stress magnitudes. Given the S_{hmin} constraint of 40-44 MPa, the gray shaded region represents the S_{hmin}/S_{Hmax} magnitudes consistent with all the data and observations at this depth.

Due to the close spacing of most of the minifrac tests, we picked nine depths with wellbore failure observations at which to constrain S_{Hmax} magnitudes (Table 2). First we examined the stress state in the caprock. We show in Figure 2-8 one example of utilizing the "constrain stress" diagram to estimate the magnitude of S_{Hmax} at a depth of 1975 m. The black polygon outlines the possible stress magnitudes constrained by frictional rock strength and Mohr-Coulomb failure criteria. The presence of both drilling-induced tensile fractures and breakouts at this depth provides further constraints on the stresses. The -10 MPa and 0 MPa contours reflect the range in tensile strength, T_o, assumed for the rock. Since tensile fractures are observed, the stresses must fall between the contours. If no tensile fractures were observed, then the stresses would fall to the right of the contours. The 105, 130, 155 MPa contours represent different C_o values. Since breakouts are observed, the stresses are constrained to lie between the C_o contours corresponding to the estimated C_o magnitude range of the rock. If breakouts

were not observed, then the stresses would lie below the C_o contour for the estimated rock strength. However, since no rock strength measurements were made in this formation this constraint is not used in this particular case. Instead, the S_{hmin} magnitudes determined from the minifrac tests act as the final constraint for isolating allowable S_{hmin}/S_{Hmax} relationships. We used S_{hmin} magnitudes ranging between a lower bound of 40 MPa and an upper bound of 44 MPa to constrain S_{Hmax}. We used this range because the closest minifrac test was taken at 2076.9 m and has uncertainty associated with it (Table 1). Based on the S_{hmin}, tensile fracture and breakout constraints, we can estimate that the rock strength in the Trenton Limestone is 130 ± 25 MPa. This rock strength estimate is likely to be applicable to other formations where breakouts are present. Therefore we used C_o equal to 130 ± 25 MPa as an additional constraint in stress determinations where breakouts were present, but drilling induced tensile fractures were not. From this information, we estimate an S_{Hmax} magnitude of 83 ± 11 MPa (Table 3). The possible range in S_{hmin} and S_{Hmax} values in the Trenton Limestone at 1975 m is highlighted by the shaded region in Figure 2-8. At this depth, S_v is the intermediate principal stress, such that the stress state in the Trenton Limestone falls within the strike-slip stress regime.

Table 2-3: Results of the maximum horizontal stress magnitude analysis using the "constrain stress" method along with the other principal stress magnitudes and pore pressures. Included in bold for reference at each depth are estimates of stress magnitudes and pore pressure at the top and bottom of the Rose Run sandstone; the (*) indicates that the value is from a minifrac test.

Lithologic Unit	Depth [m]	P_p [MPa]	S_{hmin} [MPa]	S_v [MPa]	S_{Hmax} [MPa]
Queenstone Sh	1925	21.2	40-44	50.4	71-88
Trenton Ls	1975	21.7	40-44	51.7	72-94
Trenton Ls	2050	22.5	41-45	53.7	73-90
Trenton Ls	2125	23.4	42-46	55.7	74-91
Trenton Ls	2265	24.9	44-48	59.3	75-95
Top Rose Run Ss	**2355**	**25.9**	**31-32***	**61.7**	**42-63**
Rose Run Ss	2365	26.0	34-36	62.0	42-63
Bottom Rose Run Ss	**2388**	**26.3**	**35-37**	**62.6**	**42-63**
Copper Ridge Dol	2465	27.1	46-50	64.6	73-95
Copper Ridge Dol	2502	27.5	47-51	65.5	73-95
Nolichucky Sh	2625	28.9	49-53	68.8	81-100

In the Rose Run Sandstone, we constrained the stress at 2365 m. This is slightly deeper than the minifrac test depth (2358 m). We used a range for S_{hmin} of 34-36 MPa because of the low values of S_{hmin} suggested by the minifrac tests at 2343 m, 2358 m and 2413 m (Table 1). The S_{hmin} lower bound of 34 MPa at this depth is constrained by the Mohr-Coulomb failure criterion for normal faulting. Based on the S_{hmin} constraint and the presence of drilling-induced tensile fractures, we interpreted the S_{Hmax} magnitude to be 52.5 ± 10.5 MPa, falling in the normal faulting to strike-slip stress regime (S_v is the greatest principal stress). The S_{Hmax} determinations for all the depths are shown in Figure 2-9 and outlined in Table 3 along with P_p, S_v, minifrac interpretation results and approximate S_{hmin} used to constrain the S_{Hmax} magnitudes.

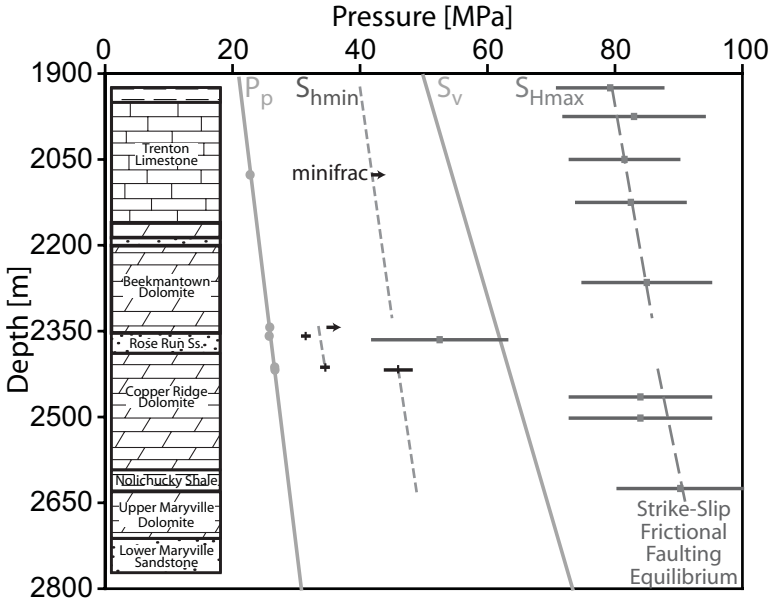

Figure 2-9: Pressure versus depth plot of the stress magnitude results. The P_p gradient determined from minifrac test data is 11 MPa/km. The S_v gradient is 26.2 MPa/km. The minifrac test analysis (black) indicates that the S_{hmin} magnitude has two trends, illustrated by the gray dashed lines (short dashes). The S_{hmin} magnitude in and around the Rose Run Sandstone is significantly less than that above and below this zone. The S_{Hmax} estimates from the "constrain stress" method are shown with solid gray bars. The dashed gray line (long dashes) is the S_{Hmax} value predicted by frictional faulting theory for a strike-slip stress regime based on the measured values of S_{hmin} and P_p and a coefficient of sliding friction of 0.6.

2.3.7 Results and Implications of the Geomechanical Analysis

To briefly summarize, by utilizing several types of data and observations, we were able to constrain the in situ state of stress at the Mountaineer site. We calculated S_v to

have a gradient of 26.2 MPa/km. The electrical image log and caliper data allowed us to establish the horizontal stress orientations in the Rose Run Sandstone and adjacent dolomites, with S_{Hmax} oriented N47°E (±12.6°) and S_{hmin} oriented N43°W (±12.6°). The minifrac test analysis provides the magnitude for the least principal stress, which at this site is S_{hmin}, for specific depths. The minifrac data show a significant difference in S_{hmin} magnitude between the Rose Run Sandstone and adjacent formations, which may be a function of the variability of the rock stiffness. The P_p in the formations, as measured during the minifrac testing, is nearly hydrostatic with a gradient of 11 MPa/km. Through the integration of stress and P_p data with calculated rock properties and information about the drilling operations, we constrained the magnitude of S_{Hmax} with depth (Fig. 2-9, Table 3).

The state of stress in the caprock is in a strike-slip stress regime, where $S_{hmin} \leq S_v \leq S_{Hmax}$. The Rose Run Sandstone appears to be in a normal faulting regime where S_{Hmax} is the intermediate principal stress. This stress variation with depth is beneficial in terms of the CO_2 sequestration potential of the Rose Run Sandstone. Due to the much lower value of the least principal stress in and around the Rose Run Sandstone relative to that of the surrounding formations, this layer will allow for hydraulic fracture propagation at much lower pressures than the formations above and below. Therefore, it would be possible to fracture this zone during injection without compromising the integrity of the caprock. The benefits of hydraulic fracturing for increasing injectivity are investigated in the next section using geostatistical aquifer modeling and fluid flow simulations. Also, the wellbore wall stability of deviated wells is examined for both the caprock and Rose Run Sandstone stress states.

Furthermore, the stress state of the caprock appears to be in strike-slip faulting frictional equilibrium (Fig. 2-9). That is, the stress magnitudes are limited by the frictional strength of widely distributed, pre-existing planar discontinuities in the crust as reviewed by Townend and Zoback (2000) and discussed by many others. Therefore, perturbations in the state of stress, such as pore pressure changes due to fluid injection, may induce shear slip if optimally oriented faults are present and the pressure perturbations are large enough. To investigate the possibility of inducing seismicity, we need to determine which faults are optimally oriented in the in situ stress state and what increase in pore pressure would result in slip on those faults.

It should be noted that a coupling between stress magnitudes and pore pressure exists such that the increases in pore pressure associated with CO_2 injection are expected to lead to increases in the horizontal stress magnitudes. The extent of this effect can be predicted using poroelastic theory. As discussed by Brown et al. (1994), assuming no lateral strain the change in total horizontal stress (ΔS_{hor}) for a given change in pore fluid pressures (ΔP_p) can be determined by

$$\Delta S_{hor} = \alpha \Delta P_p \left(\frac{1-2\nu}{1-\nu}\right) \tag{2-7}$$

where ν is Poisson's ratio and α is Biot's coefficient ($\alpha = 1 - K_b/K_g$, where K_b is the bulk modulus of the dry rock and K_g is the bulk modulus of the rock forming mineral). At the Mountaineer site the mean ν is 0.28 and α ranges from 0.03-0.2, with a mean of 0.1. For the mean case, the ΔS_{hor} would be about $0.06\Delta P_p$. Because the effect of the pressure change on stress magnitude is so small, it is not considered in the following work.

2.4 MODELING AND SIMULATION OF CO_2 INJECTION

Several tools and techniques commonly applied in the petroleum industry are valuable for assessing the CO_2 sequestration potential in deep saline reservoirs. Modeling 3D reservoir geometry and stochastic simulation of petrophysical properties are important techniques for capturing the geological characteristics and heterogeneities of potential CO_2 injection sites while accounting for different levels of uncertainty. These models are then used as inputs into fluid flow simulations. Numerical flow simulations using robust 3D reservoir models provide estimates of fluid flow behavior, fluid interactions, and sequestration capacity in deep saline formations, even when there are limited data available. Furthermore, as we have mentioned, reservoir stimulation techniques, such as hydraulic fracturing, may be needed to improve injectivity in the less porous and less permeable deep aquifers. The benefits of reservoir stimulation can be evaluated with the aid of appropriate reservoir models and flow simulation analysis. Fluid flow simulation studies are an integral step in understanding and quantifying CO_2 sequestration potential not only in deep aquifers but also in other geological settings.

2.4.1 Modeling Reservoir Architecture

Given the information collected during the Mountaineer site characterization, we built two 3D reservoir models to represent the Rose Run Sandstone. It should be noted that more detailed compositional reservoir modeling to develop injection and monitoring system designs is being conducted separately (White et al., 2005) and that the current simulations are specifically focused on the geomechanical aspects. Two models were used in this study to represent the Rose Run Sandstone: (1) in its native state and (2) with a stimulated hydraulic fracture. The geometry of the models is the same and was based on a regional data set for the Rose Run Sandstone, which indicates a N10ºE strike, a gentle 2-3º dip to the SE and a thickness varying on average between 15 and 50 m. At the Mountaineer site, the top of the Rose Run is at 2355 m depth and the unit is 33 m thick (from AEP#1 well data). We built a 6 km by 6 km grid centered around the AEP#1 well. To introduce a hydraulic fracture, we oriented the grid blocks in a direction consistent with that of S_{Hmax}, N45ºE (Figs. 2-6c and d). The width of the grid blocks along the center diagonal is about 1 m in the NW-SE direction, to approximate the presence of a hydraulic fracture. We determined that a 150 x 172 x 5 grid allowed for efficient simulation runs while maintaining a significant amount of information on the aquifer properties. We used the same grid for both models, but populated the petrophysical properties differently.

We used the sequential Gaussian simulation (SGS) method (Isaaks, 1990) to produce equally probable realizations of porosity and permeability that reflect the data variability and spatial statistics while incorporating both "hard" (i.e., well data) and "soft" (i.e., property correlations) data (Deutsch, 2002). The only hard data available on permeability and porosity for the location came from the NMR permeability and density porosity logs of the AEP#1 well (Fig. 2-3). Based on these porosity and permeability data, we chose consistent, yet subjective, distributions to use in the property simulations of the larger scaled grid (Fig. 2-10). We investigated a lower and upper bound of permeability with the distributions differing by an order of magnitude to reflect the uncertainty in the upscaled permeability values. By plotting the density porosity log data against the NMR permeability data (log scale), we found a correlation coefficient of 0.65, which we used as "soft" data in the property simulations. The spatial variability of the properties was incorporated into the SGS algorithm using a semivariogram. Due

to the lack of data, our choice of semivariogram was highly subjective. Because the Rose Run Sandstone is in a sedimentary basin, we expect a significant amount of lateral correlation in the properties. We chose a normalized, spherical semivariogram model with a 0.2 nugget effect and an isotropic range of 500 m in the geological coordinate system. We created 20 realizations: five realizations for each of the permeability distributions for both of the models (without and with a hydraulic fracture). To incorporate the hydraulic fracture in the second model, we assigned a porosity of ≈30% and permeability of 1000 mD to the thin grid blocks extending 300 m from the center grid block (AEP#1 well location) along the N45ºE axis. We believe that these property values approximate those associated with the fracture and surrounding formation after fracturing.

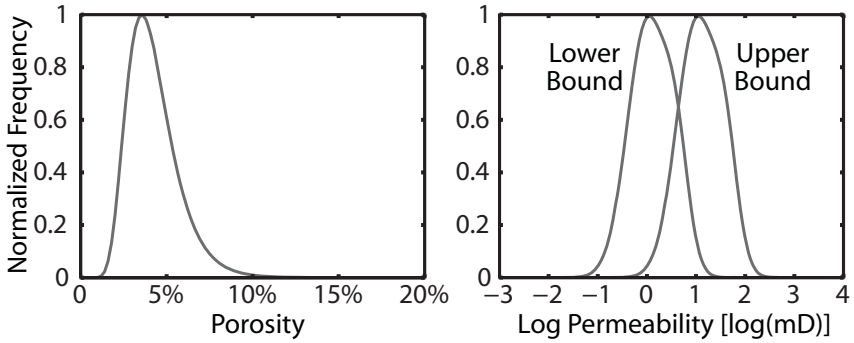

Figure 2-10: Porosity and log permeability histograms used in the Sequential Gaussian Simulation algorithm to populate the aquifer models with petrophysical properties. Porosity is modeled with a lognormal distribution; log permeability is modeled with a multigaussian distribution. The lower and upper bound permeabilities differ by an order of magnitude.

2.4.2 CO_2 Injection Simulations

We used a commercial black-oil simulator for these preliminary flow simulations. While the simulator has limitations when simulating CO_2 injection, it has sufficient capabilities for the purpose of this study. Namely, we were looking for the approximate magnitude of CO_2 injection over 30 years, the effect that a hydraulic fracture with a 300 m half-length would have on injection rate, and the changes in reservoir pore pressure with injection. The simulator input is based on the characterization and geomechanical analysis of the Mountaineer site. The temperature of the Rose Run sandstone is 63º C. The pore pressure gradient is 11 MPa/km. The injection rate of the AEP#1 well is controlled by a bottom hole pressure (BHP) constraint. In the case with no hydraulic

fracture, the BHP constraint is set at 32 MPa, which is close to the fracture pressure of the Rose Run sandstone as determined in the geomechanical analysis. The BHP constraint in the hydraulically fractured case is 42 MPa, which is just below the fracture pressure of the caprock. We included producer wells along the boundary of the grid to enforce a constant pressure boundary condition that is consistent with the open system of the reservoir. These wells produce when their BHP exceeds the ambient 11 MPa/km gradient. In the simulator, water was modeled as "oil" and CO_2 as gas, allowing the CO_2 to dissolve in the water. The fluid properties of the water and CO_2 are functions of pressure and temperature, and salinity in the case of water. On average, the values are: water formation factor (Bw) of 1.04 reservoir m^3/standard m^3, CO_2 formation factor of 1.8×10^{-3} reservoir m^3/standard m^3, water viscosity of 7.3×10^{-4} Pa·s (0.73 cP), and CO_2 viscosity of 1.01×10^{-4} Pa·s (0.101 cP). The CO_2 solubility is dependent on temperature, pressure and salinity, the effects of which are modeled by a Sechnow coefficient and fitted to literature data (Ennis-King, personal communication). The CO_2 solubility (Rsw) calculated at reservoir temperature and salinity ranged from 29.7 to 33.9 standard m^3/standard m^3 over pressures of 25 to 42 MPa. We used relative permeability curves adapted from the van Genuchten (1980) function with an irreducible gas saturation of 0.05, an irreducible liquid saturation of 0.2, and an exponent (λ) of 0.457, resulting in crossover at 0.75 gas saturation. Variations of the van Genuchten relative permeability function were implemented in several test problems in the Pruess et al. (2002) numerical simulation code comparison study. By using a small residual gas saturation, we can account for the presence of isolated gas. This could occur due to snap-off mechanisms that act when the pore body to pore throat ratio is large, or when dissolved CO_2 comes out of solution in isolated low pressure areas.

We simulated CO_2 injection for 30 years on all 20 realizations. The CO_2 saturation and formation pressure are shown in Figure 2-11 for one realization of each model for both permeability distributions. In all cases, as expected, the pressure front moves out ahead of the CO_2 front, with the highest reservoir pressures closest to the well (Fig. 2-11). This is consistent with the values of the fluids' compressibilities. The hydraulic fracture increases injection rate and cumulative injection by nearly a factor of four over the non-fractured cases (Fig. 2-12). In the lower bound permeability realizations, the

injection rate remains nearly constant after 5 years, at about 8 kt CO_2/yr (without fracture) and 31 kt CO_2/yr (with fracture). A small amount of variability is apparent between realizations. In the upper bound permeability cases, the effects of relative permeability can be observed. As the CO_2 saturation increases near the injection well the CO_2 flows more easily, resulting in an increased injection rate with time. In these simulations, the injection rate increases with time, from about 70 kt CO_2/yr to 140 kt CO_2/yr (without fracture) and from about 320 kt CO_2/yr to 470 kt CO_2/yr (with fracture). In the upper bound permeability realizations, the cumulative injection after 30 years is 12-15 times higher than that of the associated lower bound permeability realizations. Further increase in the injection rates at the site may be possible with use of the horizontal or multilateral wells and multiple injection zones. In the fractured model – upper bound permeability cases, the CO_2 reaches the extent of the 6 km x 6 km area (Fig. 2-11). We also observed that the injection rate in these cases is affected by the grid boundaries after injecting about 10 Mt CO_2 (Fig. 2-12). These results suggest that every 10-12 Mt of CO_2 injected requires about a 6 km x 6 km area given the thickness and porosity of the Rose Run Sandstone.

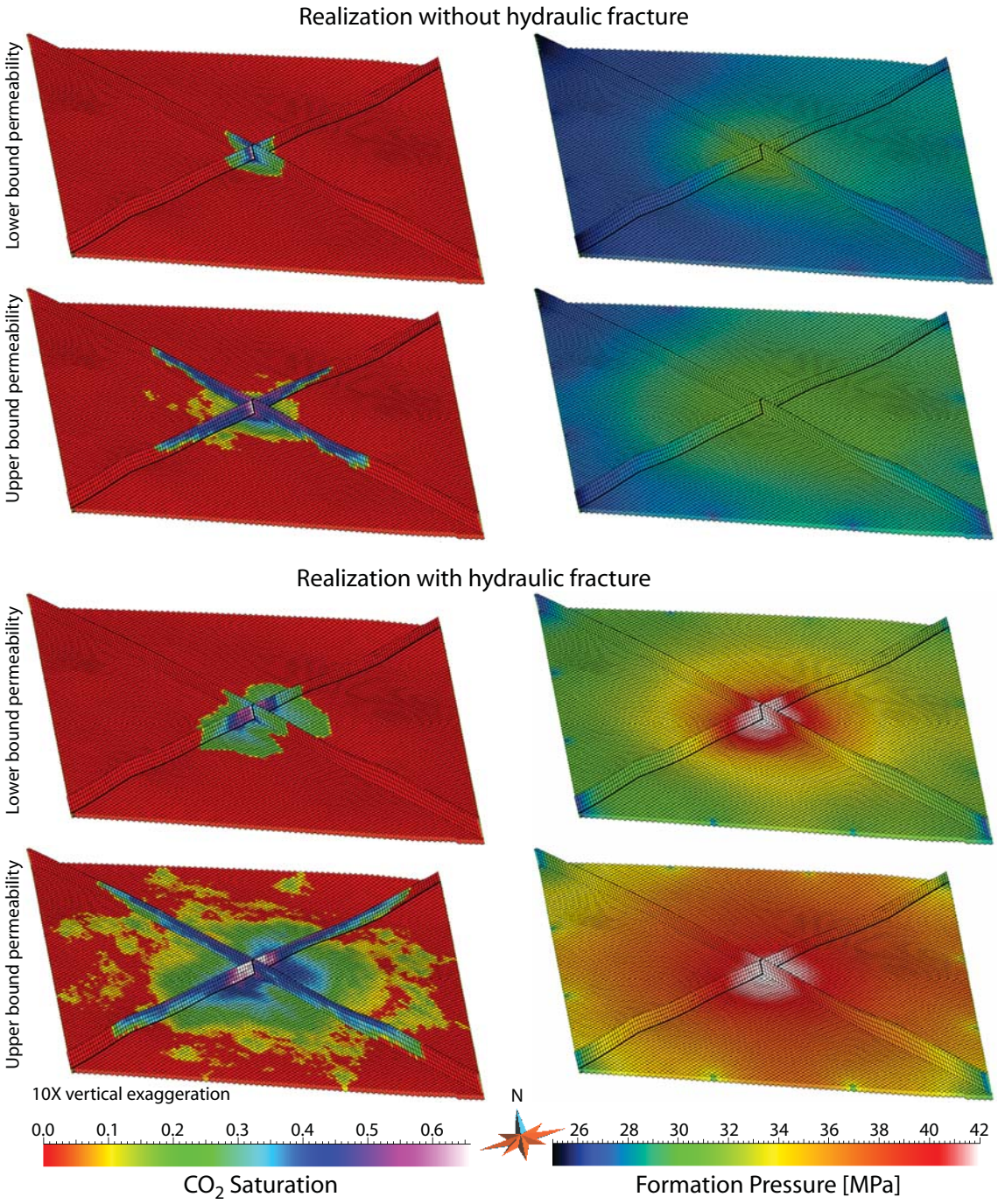

Figure 2-11: CO_2 injection simulation results after 30 years for the lower and upper bound permeability fields for one realization of each of the two models. The lateral extent of the grid is 6 km x 6 km. The presence of the hydraulic fracture significantly increases total amount of CO_2 injected. To prevent a fracture from forming in the realization without a hydraulic fracture, the bottom hole pressure (BHP) constraint must be below the fracture pressure of the injection zone. In the fractured case, the injection rate is controlled by a higher BHP constraint which is just below the caprock fracture pressure. Therefore, the total aquifer pressure is much higher in the fractured simulations.

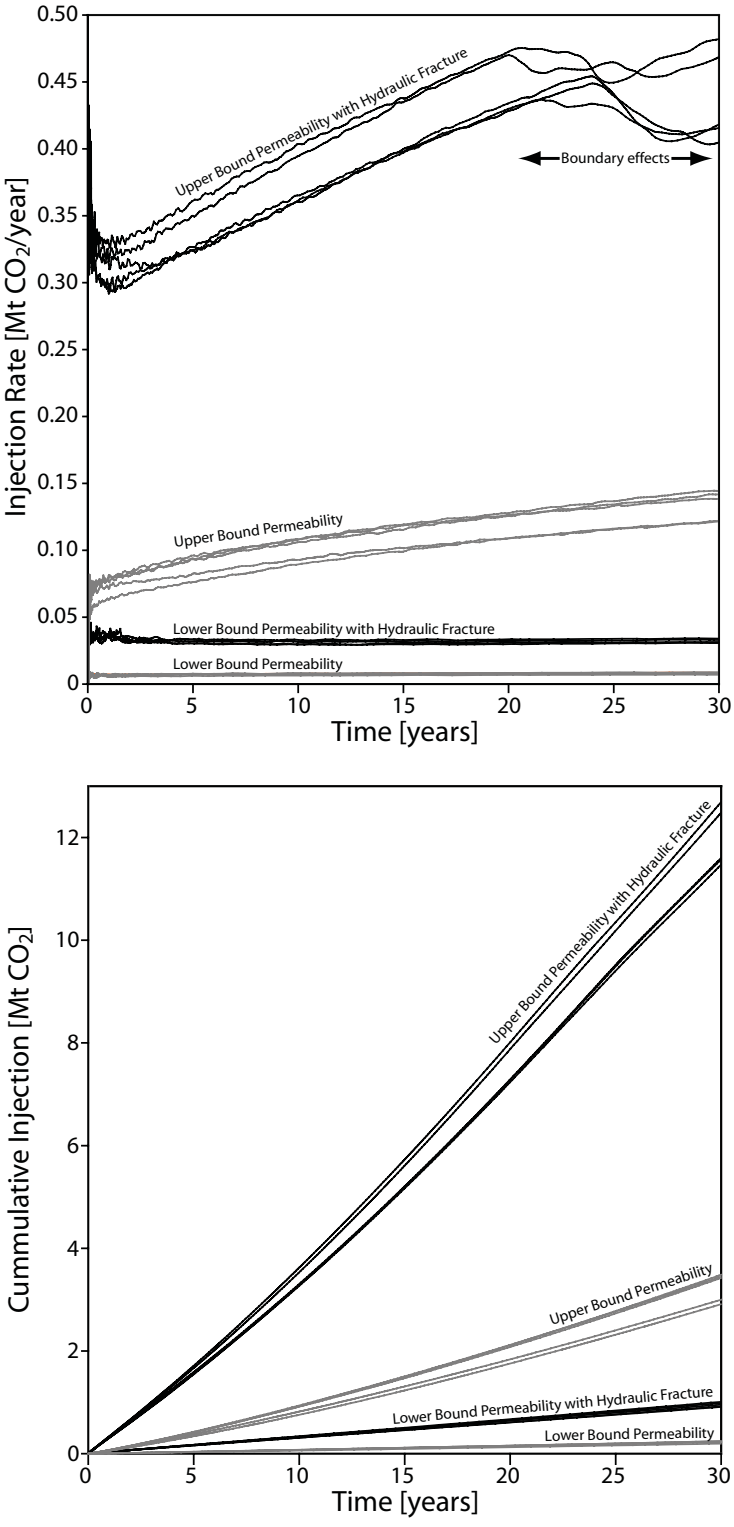

Figure 2-12: CO_2 injection rate and cumulative CO_2 injection over 30 years for 20 realizations.

2.5 HORIZONTAL WELL STABILITY

Another option for increasing CO_2 injection is drilling horizontal wells that extend several hundred meters in the injection zone. These wells would remain uncased to maximize the surface area through which the CO_2 could enter the formation. Because the horizontal wells remain open and deviated drilling tends to be more difficult than vertical drilling, we examined which orientations would be favorable for deviated wells to remain stable in the local stress field. In order to evaluate well stability, we determined the necessary rock strength, C_o, needed to completely prevent breakouts from occurring for various well orientations given the stress state determined in the geomechanical analysis. For simplicity, the analysis assumes balanced drilling, in which the mud weight equals the formation pore pressure. This is an extremely conservative analysis because in many cases a well will remain stable even with breakouts present and breakout widths up to 70-90º (39-50% of wellbore wall).

We investigated the stability of wells drilled with varying degrees of deviation from vertical. One case we examine is drilling a horizontal well in the direction of S_{Hmax}, the same direction that a hydraulic fracture would form. In this case, it would be possible to implement both a longitudinal hydraulic fracture along with the horizontal well to increase injectivity if deemed safe and economical. We examined well stability in both the strike-slip stress state of the caprock and the normal faulting stress state of the injection zone. In this way, we know if the well deviation can begin in the caprock and continue into the injection unit despite the difference in stress state.

The results of this analysis are presented in Figure 2-13. In the caprock, we find that, as the well deviation in the S_{Hmax} direction increases from vertical to horizontal, the well stabilizes. In fact, a vertical well, like AEP#1, has the least stable well trajectory for the strike-slip state of stress. However, we observed very few breakouts in the caprock below 2180 m in this well. In the caprock stress state, breakouts would form in a NE-SW oriented horizontal well only in rocks with a C_o less than 85 MPa. The measured C_o in the Beekmantown Dolomite is more than 300 MPa; therefore, a deviated well will remain stable in this unit. In the Rose Run Sandstone state of stress, a horizontal well would require a higher C_o to prevent breakouts than a vertical well, so it would be less stable. A horizontal well in the direction of S_{Hmax} has the least stable well trajectory in the injection zone stress state. However, breakouts will only occur in a NE-

SW oriented horizontal well in rocks with C_o less than 100 MPa. The C_o measured in the Rose Run Sandstone is more than 200 MPa. Based on this analysis, it is clear that directional drilling can be effectively implemented at the Mountaineer site. Furthermore, the injection process, which is analogous to overbalanced drilling, will continue to support the horizontal well stability.

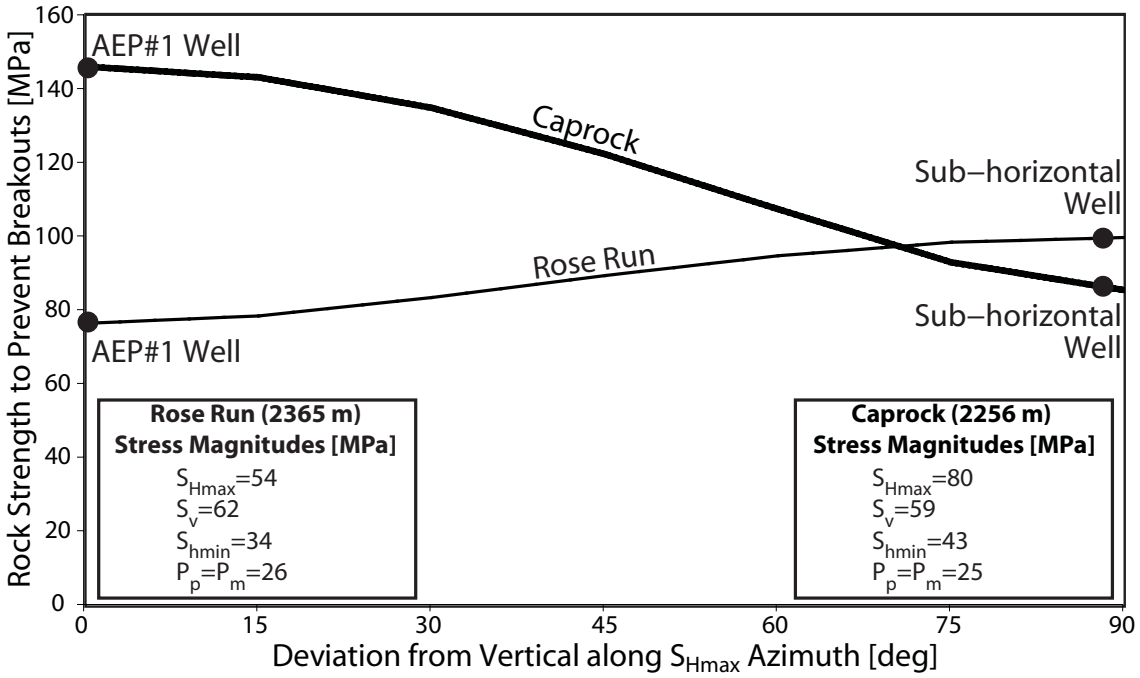

Figure 2-13: Plot of the change in minimum required rock strength to prevent breakouts as the well trajectory deviates from vertical in the S_{Hmax} direction. In the caprock, a well becomes more stable as the borehole deviation increases towards horizontal. In the Rose Run Sandstone, the borehole stability slightly decreases with increased deviation, but the required rock strength to prevent breakouts is still less than that needed for most deviation angles in the caprock.

2.6 INVESTIGATING INDUCED SEISMICITY

Injection induced seismicity occurs when the increase in pore pressure caused by fluid injection decreases the effective normal stress resolved on optimally oriented, pre-existing faults such that it induces fault slip. The occurrence of injection-induced seismicity is well documented at a number of sites in tectonically stable intraplate areas (Pine et al., 1983; Raleigh et al., 1976; Zoback and Harjes, 1997). As previously stated, in a stress state in frictional equilibrium, even small pressure perturbations can induce slip if faults with optimal orientation are present. It is thought that much of the

intraplate continental crust is likely in frictional equilibrium (Townend and Zoback, 2000). For this reason, the investigation of induced seismicity potential as it relates to CO_2 sequestration is important for understanding the risks associated with such an endeavor (Sminchak and Gupta, 2003). Although injection-induced seismicity has not been an issue in the past for the Appalachian Basin, previous injection has not been at the same scale as CO_2 sequestration, making this an important issue to consider in future site studies. The S_{Hmax} values determined at the Mountaineer site are consistent with the S_{Hmax} magnitudes predicted by Coulomb frictional-failure theory assuming that the coefficient of friction on pre-existing faults is 0.6 (Fig. 2-9). The frictional equilibrium stress state is also supported by the drilling-induced tensile fractures observed along much of the borehole from 2150 to 2775 m.

Figure 2-14a illustrates the fault orientations and associated changes in the pore pressure, P_p, that could lead to induced seismicity near the Mountaineer site. Hot colors indicate that small increases in P_p could result in slip. The black dots are fracture pole orientations of fractures observed in the Beekmantown Dolomite on the electrical image log. The white dots are the fracture poles of hypothetical optimally oriented faults. They represent the orientations of the faults that are most likely to slip given the in situ stress state in the caprock. Assuming that the coefficient of sliding friction along the optimal fault planes is 0.6, reactivation could occur with very small increases in P_p. The optimally oriented faults for the caprock stress state are nearly vertical strike-slip faults that strike north-northeast or east-northeast (Fig. 2-14b). If the coefficient of sliding friction along the faults is higher (e.g., 0.8), a larger P_p perturbation is necessary to induce slip. Likewise, faults with less optimal orientations require greater P_p changes for slip to occur. The results suggest that further work on the topic is necessary to understand the risks of sequestering CO_2 in the Appalachian Basin. Given that small P_p perturbations have the potential to induce seismicity in the given stress state, and the lack of laterally extensive data for identifying faults in the area, monitoring of microseismic events will be an important technique for any sequestration project in the region.

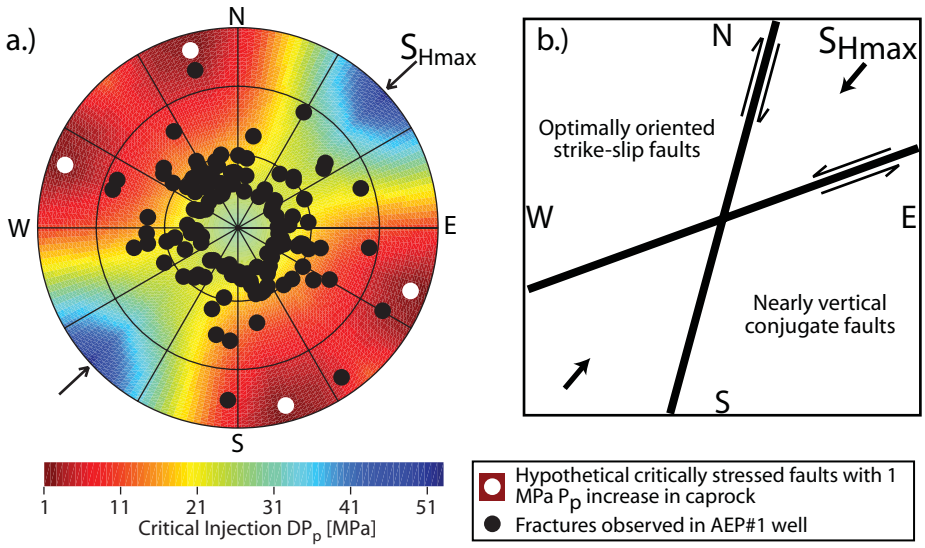

Figure 2-14: Induced seismicity and critically stressed faults in the caprock. (a) Lower hemisphere stereonet plot of critical pore pressure change due to injection as a function of fracture pole-to-plane orientation. Each location within the circle represents a pole perpendicular to a fracture plane projected onto a 2D representation of the lower half of a sphere. The colorbar indicates the amount that the P_p would need to increase above the initial state to induce slip on existing faults with a certain fracture pole orientation. Areas with hot colors represent fracture pole orientations that are likely to slip with small P_p perturbations. The black circles are fracture poles of fractures observed in the AEP#1 electrical image log of the Beekmantown Dolomite from 2200-2350 m. The white circles are the hypothetical fracture poles that would be most likely to slip given a small P_p increase in the current state of stress. (b) Map view schematic of faults corresponding to the hypothetical fracture pole orientations shown in white on the stereonet plot.

2.7 CONCLUSIONS

The limited thickness and low-to-moderate porosity and permeability of the Rose Run Sandstone are formidable challenges to the injection and sequestration of the CO_2 emitted from the Mountaineer power plant. Similar challenges may hamper sequestration in other deep aquifer settings in the region. At the Mountaineer site, the dominant stress state is strike-slip faulting near frictional equilibrium. However, the stress state in the Rose Run Sandstone is normal faulting. The lower magnitude of S_{hmin} in the Rose Run Sandstone (compared to adjacent units) makes it attractive to utilize hydraulic fracturing to stimulate injectivity. A 300 m half-length hydraulic fracture increases injectivity by nearly a factor of four. If the average formation permeability is more similar to an assumed upper-bound distribution (2-63 mD), the preliminary simulations indicate a maximum injection of about 6% of the Mountaineer emissions (7 Mt/yr) for a single vertical well with an induced hydraulic fracture in the Rose Run

Sandstone injection zone. Assuming a 30 m average thickness and a porosity ranging between 2% and 10%, up to a 600 km^2 area may be needed to accommodate the volume of CO_2 from the Mountaineer plant to be injected over 30 years (about 210 Mt). This likely requires sequestration in multiple horizons and the utilization of hydraulic fractures and/or extended horizontal injection wells. Induced seismicity in the caprock could occur with small increases in P_p if optimally oriented faults are present. As the pressure front associated with injection moves ahead of the CO_2 front, if induced seismicity occurred, injection could be terminated prior to the CO_2 front reaching the fault(s) associated with the induced seismicity, thus limiting the risk of leakage. These conclusions suggest that microseismic networks should be part of CO_2 sequestration monitoring programs in the region.

2.8 ACKNOWLEDGEMENTS

We would like to thank Phil Jagucki, Frank Spane, Joel Sminchak, and Danielle Meggyesy of Battelle Memorial Institute, and Austin Boyd and Nadja Muller of Schlumberger for their contributions in the collection and analysis of field data, and Kristian Jessen and Taku Ide of the Petroleum Engineering Department at Stanford University for their help with the flow simulations. We would like to thank GeoMechanics International for the use of their software. Funding for this study was provided through Stanford University's Global Climate and Energy Project (GCEP). Funding for the Ohio River Valley CO_2 Storage Project was provided by DOE's Office of Fossil Energy through National Energy Technology Laboratory (NETL). Other sponsors include: American Electric Power (AEP), BP, Ohio Coal Development Office of the Ohio Air Quality Development Office, Battelle, Pacific Northwest National Laboratory, and Schlumberger.

CHAPTER 3

ASSESSING THE ECONOMIC FEASIBILITY OF REGIONAL DEEP SALINE AQUIFER CO_2 INJECTION AND STORAGE: A GEOMECHANICS-BASED WORKFLOW APPLIED TO THE ROSE RUN SANDSTONE IN EASTERN OHIO, USA[1]

3.1 ABSTRACT

Typical top-down regional assessments of CO_2 storage feasibility are sufficient for determining the maximum volumetric capacity of deep saline aquifers. However, they do not reflect the regional economic feasibility of storage. This is controlled, in part, by the number and type of injection wells that are necessary to achieve regional CO_2 storage goals. In contrast, the geomechanics-based assessment workflow that we present in this paper follows a bottom-up approach for evaluating regional deep saline aquifer CO_2 storage feasibility. The CO_2 storage capacity of an aquifer is a function of its porous volume as well as its CO_2 injectivity. For a saline aquifer to be considered feasible in this assessment it must be able to store a specified amount of CO_2 at a reasonable cost per ton of CO_2. The proposed assessment workflow has seven steps that include (1) defining the storage project and goals, (2) characterizing the geology and developing a geomechanical model of the aquifer, (3) constructing 3D aquifer models, (4) simulating CO_2 injection, (5, 6) evaluating CO_2 injection and storage feasibility (with and without injection well stimulation), and (7) determining whether it is economically feasible to proceed with the storage project. The workflow was applied to a case study of the Rose Run sandstone aquifer in the eastern Ohio River Valley, USA. We found that it is feasible in this region to inject 113 Mt CO_2/yr for 30 years at an associated well cost of less than 1.31 US$/t CO_2, but only if injectivity enhancement techniques such as hydraulic fracturing and injection induced micro-seismicity are implemented.

[1] The work presented in this chapter was accepted by A.M. Lucier and M.D. Zoback for publication in the International Journal of Greenhouse Gas Controls under the same title in September, 2007.

3.2 INTRODUCTION

The atmospheric concentration of CO_2 continues to increase at record-setting rates due to increases in anthropogenic emissions, contributing to global climate change (IPCC, 2007). The anthropogenic CO_2 emissions are primarily from the combustion of fossil fuels for energy. As humans continue to rely on fossil fuels for energy, it is necessary to develop mitigation strategies for the associated CO_2 emissions. An emerging technology for mitigating CO_2 emissions from point sources is CO_2 Capture and Storage (CCS). In CCS, CO_2 is captured and separated at point sources, such as coal burning power plants, and then injected into deep geological formations for long term storage. Because of their close proximity to many CO_2 point sources, deep saline aquifers are promising sites for storage.

Many regional assessments of CCS in deep saline aquifers have followed a top-down approach that focuses on the volume constraints for CO_2 storage within the aquifer (e.g., Carr et al., 2005; MRCSP, 2005; Shafeen et al., 2004). This step in a feasibility analysis provides a theoretical maximum capacity but does not reflect the economically and technically viable CO_2 storage potential of an aquifer. Many sedimentary basins where CCS is being considered, such as the Midwestern United States, have laterally extensive aquifers such that even with low to moderate porosity the potential storage volume is immense. While the volume constraints of these aquifers are minimal, the costs of filling these large volumes with CO_2 could be prohibitive due to the number of wells that would be required to inject the CO_2 at safe injection rates.

One example of a top-down approach to analyzing regional CCS feasibility is outlined in the Midwest Regional Carbon Storage Partnership (MRCSP) Phase I Report (MRCSP, 2005). The Geographic Information System (GIS) based analysis presented in this report suggests that the deep saline aquifers (Rose Run, Mt. Simon, and St. Peter sandstones) within the states of Maryland, West Virginia, Pennsylvania, Ohio, Kentucky, Indiana, and Michigan have the potential to store 450-500 Gt of CO_2. According to the Environmental Protection Agency (EPA), the annual point source CO_2 emissions in the Midwestern United States was on the order of 700 Mt in 2004 (EPA, 2006). Based on the MRCSP assessment, the deep aquifers in the region could easily store more than 100 years of CO_2 emissions from the Midwest. However, the large volume capacity estimates from the top-down analysis do not reflect the effective CO_2

storage capacity, which is limited by both technical and economical constraints. Characterizing CO_2 storage capacity in relation to realistic injection rates is the next step in evaluating the feasibility of CCS as a tool for mitigating regional greenhouse gas emissions.

A major factor controlling the implementation of deep aquifer CO_2 storage is the cost. A number of factors contribute to the ultimate costs associated with CCS. These include costs associated with capture, separation, compression, transportation, injection, and monitoring. The goal set by the Department of Energy's Carbon Sequestration Program, which is implemented through the National Energy Technology Laboratory (NETL), is "To develop by 2012 fossil fuel conversion systems that offer 90% CO_2 capture with 99% storage permanence at less than a 10% increase in the cost of energy services" (NETL, 2007). Currently, the largest CCS costs are associated with capture and separation of CO_2 at the point source. Transportation costs vary widely depending on the distance the CO_2 must be transported from source to sink. The cost of injection wells is often considered to be a fraction of the other costs. To create an economic framework for this study, we needed to set an economic feasibility threshold for the costs associated with the injection wells. This threshold is subjective and based on the assumption that while the costs associated with the drilling, logging, completing, characterizing, and maintaining the injection wells required for CCS in deep aquifers is significant, the costs associated with capture, separation, compression, transportation, and monitoring will require a much larger portion of the CCS budget. For the purpose of this study, we limited the well costs to a maximum of 10% of the total CCS budget.

One motivation for this work is to minimize the cost of CO_2 transportation by limiting the distance between the CO_2 sources and injection sites. However, this may require storage in less than optimal reservoirs, which may increase drilling costs and the number of wells needed. Therefore, we need to assess the regional storage potential of deep aquifers near large CO_2 point sources. Each region will have storage sites of variable quality. By developing a systematic method for assessing the economic feasibility of injecting and storing CO_2 in a region, we can determine whether it is more cost effective to store the CO_2 locally or to assume the costs of transporting it to more ideal storage locations.

We propose a bottom-up, geomechanics-based "workflow" for assessing regional CO_2 injection and storage feasibility and screening potential injection sites. This workflow focuses on defining the CO_2 injection capacity in individual injection intervals that model the regional aquifer heterogeneity. First, we propose the methodology in a general sense. We then apply the assessment to a case study of the Rose Run sandstone of the Ohio River Valley region. This case study incorporates the geological and geomechanical site characterization of the Mountaineer power plant in New Haven, WV, completed as part of the Ohio River Valley CO_2 Storage Project (Lucier et al., 2006). Thus, the results of the case study can be loosely applied to other deep saline aquifers with similar geological properties and in situ stress state.

3.3 GENERALIZED ASSESSMENT METHODOLOGY

While the overall success of a CCS project depends on many factors (e.g., CO_2 capture, transport, and long term storage potential), capacity is a primary control. In this study, capacity has two meanings. The apparent volume capacity is the amount of available storage space in the aquifer (i.e., accessible pore volume). The injection capacity is the amount of CO_2 that can be realistically injected into the aquifer and is controlled by the number of wells and their sustainable injection rates, which are limited by the fracture pressure in the aquifer and the caprock. Injection capacity, which provides a more conservative estimate, is the focus of this assessment.

The main steps of the feasibility assessment methodology are outlined in Figure 3-1. The first step is to define the CCS project and goals to outline the measures that limit the injection and storage feasibility of the project. Once the project has been defined, a potential injection aquifer is identified, and the geology is characterized so that the heterogeneity and uncertainty of the properties of the target aquifer can be represented in aquifer models. A geomechanical model is also developed to establish limits on injection pressures and evaluate aquifer stimulation techniques. In the third step, 3D aquifer models that represent the heterogeneity and uncertainty of the aquifer attributes are constructed using geostatistics. After the models are constructed, fluid flow simulations of CO_2 injection are run on them using the geomechanical constraints to control injection pressures. In step five, the results of the simulations are used to assess injection feasibility based on injectivity, well costs, and economic constraints. After this

initial assessment, the modeling, simulation and assessment steps are repeated to evaluate the potential of injectivity enhancement techniques (e.g., hydraulic fracturing, horizontal drilling, and induced micro-seismicity, which is a novel stimulation technique that uses injection-induced micro-earthquakes to enhance the bulk permeability of the aquifer) for increasing CO_2 injection feasibility. The final step is to determine regional storage feasibility and determine whether to proceed with the CCS assessment or abandon plans for that particular CCS project. The methodology allows for the assessment to be updated if new information is collected as CO_2 injection and storage proceeds. Each of these steps is described in more detail below and is applied to the case study.

While the proposed methodology is more difficult than a typical top-down feasibility assessment, it has a number of benefits. It provides realistic first-order estimates of CO_2 storage potential within the study area by considering both technical and economical controls. It is also adaptable to the scale, goals, and limitations of a variety of different CCS feasibility studies. Furthermore, the results of the analysis can be used not only to assess regional feasibility questions, but also to provide preliminary assessments of the CO_2 storage potential of other sites with hydrogeologic attribute values in the range of those investigated in the study. This last point is particularly important when planning new projects.

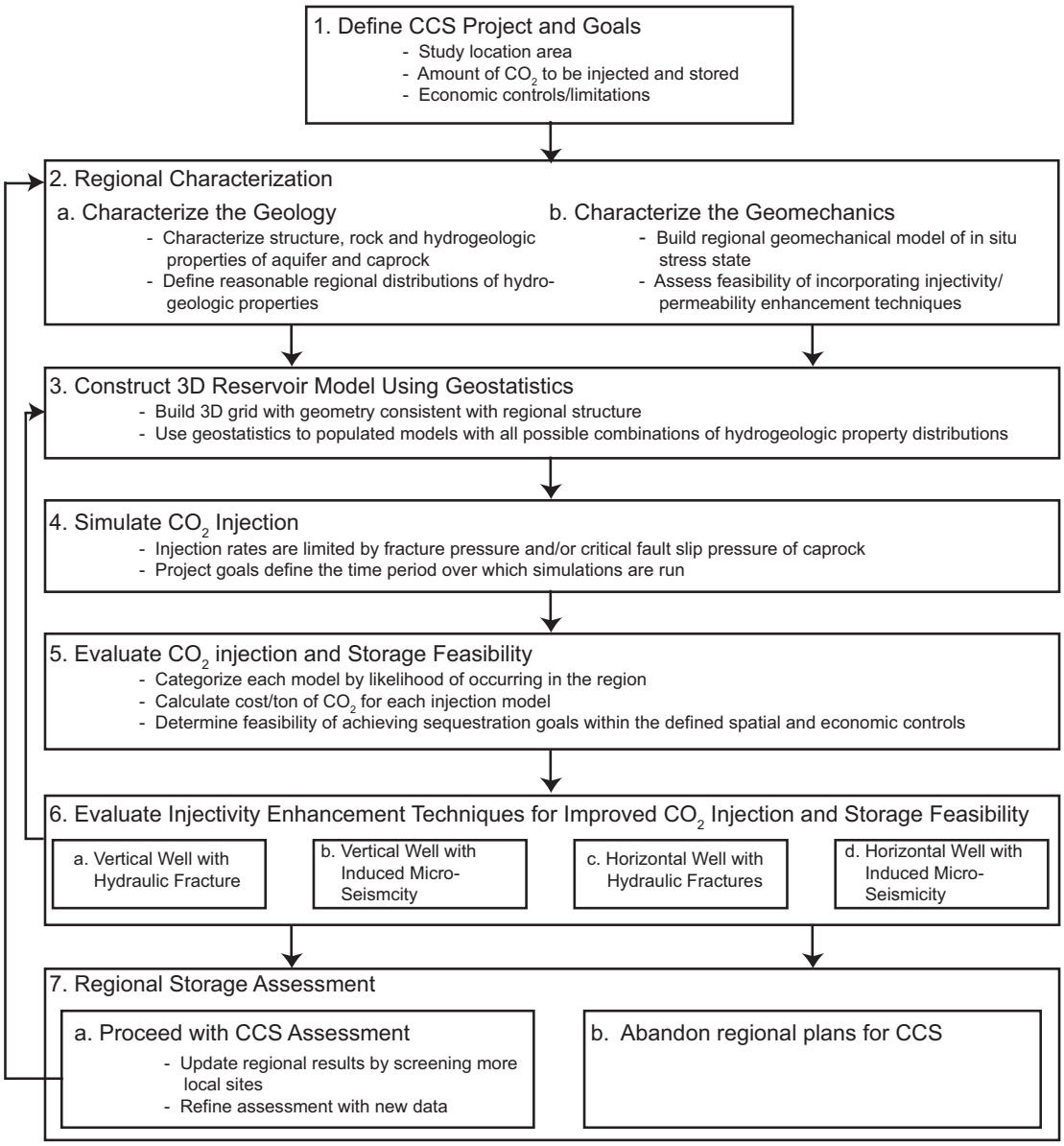

Figure 3-1: Proposed feasibility assessment workflow

3.4 CASE STUDY: ROSE RUN SANDSTONE IN THE EASTERN OHIO RIVER VALLEY

To illustrate the application of this assessment workflow, we present a case study developed from the geological and geomechanical characterization of the Rose Run sandstone aquifer at the Mountaineer power plant in New Haven, WV (Gupta et al., 2001; Lucier et al., 2006; White et al., 2005). In this case study, a CCS project that is relevant for the Rose Run sandstone is proposed, and then the feasibility of achieving

the CO_2 storage goals is evaluated using the methodology. In this way, we not only answer questions about CO_2 injection and storage potential in the Ohio River Valley, but also demonstrate the decision making process associated with the workflow.

3.4.1 Define the CCS Project and Goals

The first step of the feasibility assessment is to define the CCS project. This includes defining the geographic location of the study and the aquifer units of interest. In some cases, a single geographic location may have several possible injection intervals at different depths to be investigated. In this step, it is critical to stipulate the percentage of the supply volume of CO_2 that will be captured and stored during the CCS project. Because increasing the number of injection wells increases the CO_2 injection capacity, it is also necessary to state the maximum number of wells and/or the maximum cost per ton of CO_2 for the injection wells that define the feasibility threshold for evaluating the CCS project. This is controlled primarily by economics, but may also be controlled by the availability of drill rigs, timing constraints, and limited land access, each of which are unique to the project being considered. The degree to which the injection and storage goals of the CCS project can be met will be the measure by which feasibility is assessed in steps five through seven.

3.4.1.1 Rose Run Case Study

For the purpose of illustrating the proposed methodology and workflow, we developed and tested the injection and storage feasibility of a hypothetical regional CCS project for the Rose Run sandstone aquifer in the eastern Ohio River Valley region. In the Appalachian Basin, the Rose Run sandstone is approximately 2350±100 m deep near the eastern border of Ohio and the westerly portion of West Virginia (Fig. 3-2). This area is about 36 km wide in the dip direction (~N110ºE) and 360 km along strike. This study area was selected because it corresponds to the depth of the Rose Run sandstone at the Mountaineer power plant where a complete geological and geomechanical characterization was completed (Gupta et al., 2001; Lucier et al., 2006; White et al., 2005). In the vicinity of the study area (within 50 km), there are 23 large point sources, which emit approximately 126 Mt CO_2/yr based on data from 2004 (EPA,

2006). These are shown with white squares in Figure 3-2 along with the Mountaineer power plant which has a bold outline.

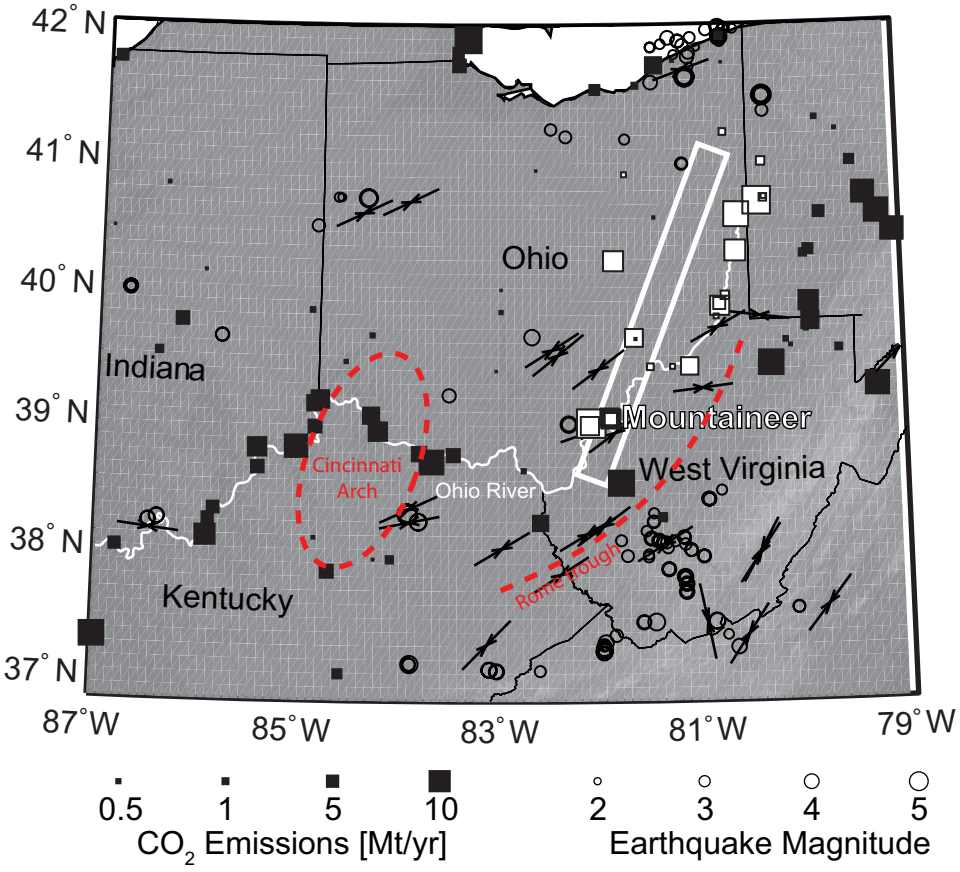

Figure 3-2: Ohio River Valley region map showing the approximate project area with the white box, S_{Hmax} orientations from the World Stress Map with black inverted arrows (Reinecker et al., 2005; Zoback and Zoback, 1989), regional earthquakes with black open circles and CO_2 point sources with the squares (EPA, 2006). The earthquakes are scaled by magnitude and the CO_2 point sources are scaled by annual CO_2 emission rates. The Mountaineer power plant site is labeled and shown by the white square with a bold black outline. The white squares with thin black outlines are other large point sources within 50 km of the study area. The red dashed curves show the approximate location of the Rome trough and Cincinnati Arch for reference.

The case study area is located within the region being characterized as part of the Midwest Regional Carbon Storage Partnership (MRCSP, 2005). The Midwestern United States could potentially play a large role in achieving national CO_2 storage goals. As mentioned above, the MRCSP report estimates a maximum CO_2 storage volume capacity of 450-500 Gt of CO_2 (MRCSP, 2005). The MRCSP region also contains 203 large point sources of CO_2, each emitting between 100 kt and 20 Mt of CO_2/yr (EPA, 2006) (Fig. 3-2). Their combined emission of about 695 Mt of CO_2/yr is more than 99%

of the annual regional CO_2 emissions from power plants. They also generate $6.84x10^8$ MWh of power each year. Using a cost of energy based on a report by the Energy Information Administration (EIA) that ranges between 0.08 and 0.12 US$/kWh (EIA, 2007), the future annual cost of energy in the region could range between 54.72 and 82.08 billion US$. To meet the goal of sequestering 90% of the CO_2 emissions (625.5 Mt of CO_2) at less than a 10% increase in the cost of energy, the CCS budget in this region would range between 8.75 and 13.12 US$/t CO_2 (EPA, 2006). For the purpose of this case study, we defined the feasibility threshold of the costs related to the injection wells to be 10% of the total CCS budget, such that the associated well costs should be less than 0.875 to 1.31 US$/t CO_2 depending on the cost of energy. This value is subjective and was chosen to reflect that while the injection well costs are significant, they should only account for a fraction of the total CCS budget.

Following the NETL guidelines (2007), the goal of this CCS project was to inject 90% of the emissions from the 23 power plants near the case study area for 30 years at the current emissions rate of 126 Mt CO_2/yr (i.e., 113 Mt CO_2/yr or 3.39 Gt CO_2 over 30 years) into the Rose Run sandstone between 2250 and 2450 m depth and store it with 99% storage permanence. The case study area has a map area of approximately 360 km by 36 km which constrains the number of wells that can be drilled. If well spacing were 4 km or 6 km, then the maximum number of wells that could be drilled is ~670 wells or ~260 wells respectively. The economic feasibility threshold for this assessment limited the costs associated with drilling, logging, completing, characterizing, and maintaining the injection wells in the region to ideally less than 0.875 US$/t CO_2 but up to 1.31 US$/t CO_2.

The associated well costs were estimated by the type of well, stimulation techniques, and maintenance costs for the lifetime of the well. In this study, we evaluated six types of injection wells: (1) vertical wells, (2) vertical wells with a single hydraulic fracture, (3) vertical wells with induced micro-seismicity treatments, (4) horizontal wells, (5) horizontal wells with four staggered hydraulic fractures, and (6) horizontal wells with induced micro-seismicity treatments. Table 3-1 summarizes the initial, annual maintenance, and total costs for each well type assuming a 30 year lifespan for injection at each well. Table 1 also outlines the maximum number of each well type that can be

used to inject 113 Mt of CO_2/yr for 30 years while keeping the associated well costs under 1.31 US$/t CO_2.

Table 3-1: Associated well costs and maximum number of wells for different well types

Well Type	Initial Cost (M US$)	Lifespan (years)	Annual Maintenance Cost (M US$)	Total Well Cost (M US$)	Maximum # of Wells
Vertical well	4.0	30	0.15	8.5	522
Vertical well with hydraulic fracture	4.5	30	0.15	9.0	493
Vertical well with induced micro-seismicity	5.5	30	0.15	10.0	444
Horizontal well	6.0	30	0.15	10.5	423
Horizontal well with 4 hydraulic fractures	7.5	30	0.15	12.0	370
Horizontal well with induced micro-seismicity	8.5	30	0.15	13.0	342

3.4.2a Characterize the Geology

To characterize the geology for a regional assessment, it is important to collect data at both a regional and site specific scales. The characterization includes the hydrogeological properties of all of the aquifers being examined as well as the existing natural fault and fracture systems. The presence of a sealing caprock for each aquifer unit is confirmed and the risk of leakage through the caprock characterized. These risks are important to note, but may not necessarily be included in this assessment, which focuses on the CO_2 injection and capacity rather than long term storage.

Another part of the geological characterization is to determine the property values that will be used to populate the 3D models. In a regional study, it is important to test a range of values for each property to get a complete understanding of how the injection capacity is influenced by the variability of the aquifer. The primary aquifer properties considered are thickness, porosity, and permeability. The values of these properties can range widely even within a single stratigraphic unit, particularly for aquifers extending for hundreds of kilometers. Since the 3D property modeling simulations use geostatistical methods, estimates of both the distribution of the property values and the

geospatial property continuity are required. Because the methodology is highly adaptable, other attributes that may influence storage capacity such as salinity, geothermal gradient and aquifer flow direction can also be characterized and later incorporated into the evaluation.

3.4.2a.1 Rose Run Case Study Regional Geological Characterization

This study compiled data on both a regional and a site specific scale. Regionally, data from the Rose Run sandstone has been collected for oil and gas exploration in the Appalachian Basin. Production in the Rose Run sandstone began in 1965, but the majority of the productions wells were drilled after 1986 (Riley et al., 1993). Fewer than a dozen wells have been drilled into the Rose Run sandstone in the depth interval of the case study area. Most of the wells were drilled to the northwest of the study area where the depth of the Rose Run sandstone ranges from 1500 to 2000 m. The Midwest Regional Carbon Storage Partnership (MRCSP) completed a regional characterization of the aquifers in the Midwestern United States (Wickstrom et al., 2005). The MRCSP report compiled and summarized the data collected in oil and gas exploration wells, providing information on the regional heterogeneity of the rock properties in the Rose Run sandstone. We used this data in conjunction with wellbore data collected as part of the Ohio River Valley CO_2 Storage Project at the Mountaineer power plant site. The data collected at the Mountaineer site included 2D seismic lines, geophysical wellbore logs, and well tests.

The geological characterization of the case study area included both the Rose Run sandstone and adjacent caprock formations. The Rose Run sandstone strikes approximately N10ºE at the Mountaineer site and slightly more easterly towards the northern part of the case study area. The formation dips shallowly towards the ESE, generally thickening down dip, averaging about 30 m in thickness but increasing to more than 60 m thick in places (Riley et al., 2003; Wickstrom et al., 2005). At the Mountaineer site, the Rose Run sandstone is 33 m thick. Also, according to Wickstrom et al. (2005), the Rose Run sandstone has very good seal coverage over nearly all of its extent. The very low permeability Beekmantown dolomite and Wells Creek Formation, which were observed at the Mountaineer site, overlie the Rose Run sandstone throughout the study area (Figs. 2-2 and 2-3). Shallower formations also provide sealing

potential, such as the Queenstone and Devonian shales. Furthermore, oil and gas accumulations in some areas are indicators of structural sealing capacity.

In this step, we characterized the heterogeneity and uncertainty of aquifer properties (i.e., thickness, porosity, and permeability) in the Rose Run sandstone. As previously mentioned, the mean thickness of the Rose Run sandstone is about 30 m, but in some areas it can be more than 60 m thick. Regional characterizations estimate the average porosity to be 8-9% (Riley et al., 2003; Wickstrom et al., 2005). However, in some areas, particularly where oil and gas has been discovered, the porosity can be ≥ 12%. At the Mountaineer site, the average porosity is closer to 4% (Fig. 2-3). Therefore, in order to investigate the role of porosity heterogeneity on injectivity, we defined three lognormal porosity distributions to evaluate with mean porosity values of 4%, 8%, and 12%. The permeability is the most heterogeneous and uncertain geological attribute to characterize. The regional permeability range from 0.01-198 mD, averaging 4-5 mD (Baranoski et al., 1996). Again, we modeled three permeability distributions. The lower bound permeability was a multigaussian distribution of log permeability with values ranging from 1.6-25 mD and a mean of about 4 mD. The lowest of the values of the permeability range were not included because these distributions represent the bulk permeability in grid blocks with volumes of approximately 8000 m^3, which have higher values than the smallest values measured in core samples. The intermediate distribution was five times the lower bound permeability distribution, ranging from 8-125 mD with a mean of about 20 mD. The upper bound permeability distribution was 10 times the lower bound distribution, ranging from 16-250 with a mean of about 40 mD. The permeability values in this distribution that are above the regional permeability range accounted for uncertainty in the observed permeability values, contributing to <<1% of the cumulative distribution function.

Other properties of the Rose Run sandstone that were measured at the Mountaineer site include downhole temperature and brine salinity. The temperature is about 62ºC. The brine has a high salinity with a total dissolved solid content of about 325,000 mg/L, dominated by chloride, sodium, and calcium (Gupta et al., 2005).

3.4.2b Characterize the Geomechanics

The second part of the regional characterization step is a geomechanical characterization. After consolidating regional and local geomechanical data, it is important to characterize the background seismicity. This provides insight into the existing stress state and can be used to evaluate the risks associated with leakage along active faults. Then, a full geomechanical characterization is necessary for determining essential input into the fluid flow simulator, such as initial formation pore pressures (P_p) and safe injection pressures. A safe injection pressure is one that falls below the least compressive principal stress (S_3) of the aquifer, also referred to as the fracture pressure. When hydraulic fracturing or injection induced micro-seismicity treatments are used, S_3 in the caprock limits the safe injection pressure A full geomechanical analysis also provides information for calculating whether the in situ fracture network is hydraulically conductive and therefore able to enhance the overall bulk permeability of the injection zone. Furthermore, the geomechanical characterization is used for evaluating the feasibility of using horizontal injection wells and stimulation techniques that increase injectivity such as hydraulic fracturing and injection induced micro-seismicity for permeability enhancement.

In areas where stress indicator data have been collected, it is possible to complete a comprehensive stress analysis. The stress analysis provides detailed information on P_p and the principal stress orientations and magnitudes. A comprehensive stress analysis follows the methodology outlined by Zoback et al. (2003). The required data include full-wave velocity and density logs for rock properties and elastic moduli, core samples for rock strength tests, borehole image logs for observing drilling induced failures, and minifrac tests that measure the S_3 magnitudes in the aquifer and the caprock. With these data it is possible to constrain the state of stress at the site. The World Stress Map database can be used to determine if the state of stress at the local site is consistent throughout the region of interest (Reinecker et al., 2005).

With a complete geomechanical model, it is possible to characterize the fracture-enhanced permeability, fault reactivation and leakage potential of the aquifer and adjacent layers, and maximum safe CO_2 column height. All of these characterizations rely on identifying faults and fractures that are either critically stressed in the current stress state or could become critically stressed with changes in aquifer pressure due to

fluid injection. A fault is critically stressed when the shear stress (τ) resolved on the fault plane is equal to or greater than the product of the effective normal stress (S_n-P_p) resolved on the fault plane and the coefficient of sliding friction (μ) along the fault plane.

$$\tau \geq \mu(S_n - P_p) \quad (3\text{-}1)$$

Faults that are critically stressed in the existing stress state tend to be hydraulically conductive pathways for fluid flow (Barton et al., 1995; Wiprut and Zoback, 2002). Therefore, critically stressed aquifer scale faults and fractures enhance the bulk permeability of the aquifer. However, large scale critically stressed faults that extend through the aquifer into the caprock should be considered leakage pathways.

Fractures that are not critically stressed in the existing stress state may become critically stressed as the P_p increases, decreasing the effective normal stress. The P_p at which a fracture of a given orientation begins to slip is referred to as the critical pore pressure (P_p^{crit}) and can be solved for using Equation 3-1.

$$P_p^{crit} = S_n - \tau/\mu \quad (3\text{-}2)$$

The P_p^{crit} can be used in three main ways. First, if the goal is to enhance the aquifer permeability using induced micro-seismicity then the P_p^{crit} is used along with the S_3 of the caprock to determine which fracture populations can be induced to slip without hydraulically fracturing the caprock. If the goal is to prevent induced seismicity and P_p^{crit} is less than S_3 of the aquifer, the minimum P_p^{crit} that could induce seismicity on a pre-existing fault in the aquifer should be used to limit the bottom-hole injection pressure. Finally, in structurally controlled aquifers with large elevation changes between the crest and the spill point, the P_p^{crit} can be used to determine the maximum safe CO_2 column height. In these cases, the buoyancy pressure exerted on the caprock at the crest of the structure by the CO_2 column should be less than P_p^{crit} to prevent induced seismicity at the crest.

A comprehensive geomechanical analysis that determines the existing state of stress and characterizes the faults and fractures is required to make decisions about the feasibility for increasing injectivity using permeability enhancing stimulation techniques like hydraulic fracturing or induced micro-seismicity and/or incorporating horizontal wells. Hydraulic fracturing is considered feasible if the aquifer can be hydraulically fractured without compromising the caprock. Injection induced micro-

seismicity for enhanced permeability requires a critically stressed crust with many fractures in orientations that are nearly optimally oriented for slip in the in situ stress state. As discussed above, small increases in the fluid pressures that reach the P_p^{crit} of a fault will cause the pre-existing fractures to shear and create high permeability conduits for fluid flow. An extended horizontal injection well is considered feasible if it can remain stable in the in situ stress conditions. For this methodology, we define a stable well trajectory as one in which breakouts along the wellbore walls form with breakout widths <60º. The width of the breakouts depends on the in situ stresses, rock strength, and borehole orientation. If these techniques are deemed feasible, they can be incorporated into the modeling and flow simulations for further evaluation as to their effectiveness and desirability in the overall storage feasibility analysis in step six.

3.4.2b.1 Rose Run Case Study Geomechanical Characterization

We carried out a localized geomechanical analysis using geophysical log data, image log data, core samples, and minifrac tests from the Mountaineer site. However, before undertaking the Mountaineer geomechanical characterization, we compiled regional stress data from the World Stress Map database (Reinecker et al., 2005; Zoback and Zoback, 1989). The orientation of the maximum compressive horizontal stress, S_{Hmax}, is consistently NE-SW as indicated by the black inverted arrows on Figure 3-2. According to the database, the dominant stress regime near the project area is strike-slip, where the vertical stress, S_v, is the intermediate principal stress. This is common for stable intercontinental crust in the conterminous United States (Zoback and Zoback, 1989).

The details of the Mountaineer site geomechanical analysis are presented in Lucier et al. (2006). For the purpose of this chapter, we only present the aspects of the stress characterization that are used in this feasibility assessment. Using the density log, we determined that the S_v gradient is 26.2 MPa/km (Fig. 2-5). Based on observations of drilling induced tensile fractures and breakouts along the wellbore walls from electrical image log data and 4-arm caliper data, we determined that the orientation of S_{Hmax} is N47ºE ± 13° (Fig. 2-6). Minifrac tests in the formations adjacent to the Rose Run sandstone suggest an S_{hmin} gradient of 19 MPa/km. In the Rose Run sandstone, two minifrac tests suggest an S_{hmin} gradient of 13.8 MPa/km (Fig. 2-9). Therefore, the Rose

Run sandstone has a lower fracture pressure than the adjacent caprock. This was also observed in Portage County, Ohio (near the Northwestern corner of the study area), where the Rose Run sandstone fracture pressure was measured as 14.8 MPa/km and that of the bounding units as 20.8 MPa/km (Fairchild Jr. and Williamson, 1998). The P_p gradient is 11 MPa/km, which is 10% higher than the hydrostatic freshwater gradient because of the high salinity of the brine. After constraining the magnitude of S_{Hmax}, we determined that the state of stress in the caprock is strike-slip ($S_{hmin} < S_v < S_{Hmax}$) and the state of stress in the Rose Run sandstone is normal to strike-slip ($S_{hmin} < S_{Hmax} \leq S_v$).

We used the resulting geomechanical model to investigate techniques for improving injectivity at the Mountaineer site and other similar locations. Extended horizontal injection wells can increase injection rates over traditional vertical wells by increasing the surface area through which injection occurs. Utilization of the geomechanical analysis indicated that horizontal wells will be stable in the existing Rose Run stress state at the Mountaineer site. This is illustrated in Figure 3-3. This lower hemisphere stereonet plot is color coded by the required rock strength necessary to prevent breakouts with breakout widths greater than 30° along the wellbore walls for different well trajectories for balanced drilling conditions (mud weight, P_m, equals P_p). A vertical well requires a rock strength of about 71 MPa to prevent breakouts with breakout widths greater than 30°, while a horizontal well deviated in the direction of S_{hmin} requires 78 MPa. As measured in triaxial tests on core samples, the rock strength in the Rose Run sandstone is more than 200 MPa (Lucier et al., 2006). Therefore horizontal well stability is not a problem for the region. Furthermore, injection pressures in the well that are greater than the fluid pressures in the rock will also support the wellbore wall stability in the same way that drilling with over pressured mud weights does.

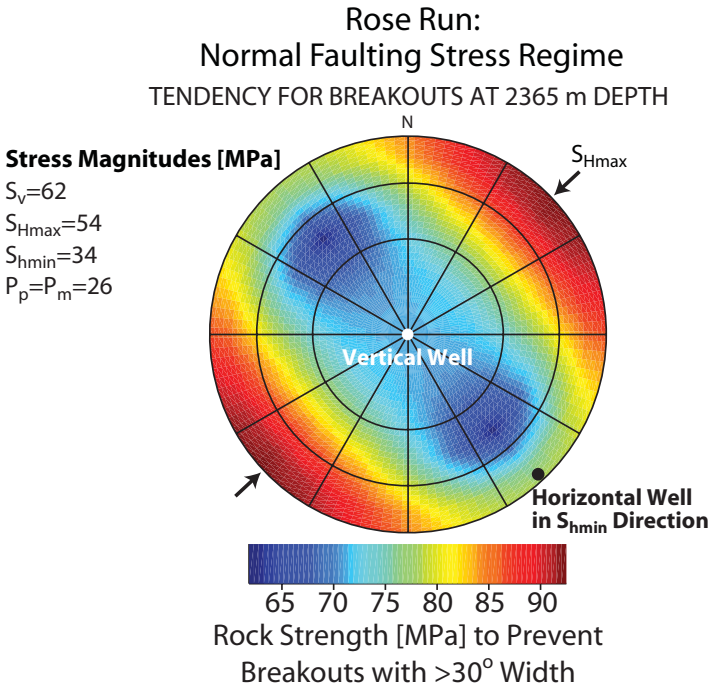

Figure 3-3: Lower hemisphere stereonet plot color coded by rock strength required to prevent breakouts with breakout widths greater than 30° for well trajectories. Well trajectories with hot colors require higher rock strengths to prevent breakouts and are therefore less stable. This assumes the wells are drilled with a balanced mud weight (P_m) that is equal to the P_p. The Rose Run rock strength was measured to be more than 200 MPa at the Mountaineer site, so all well trajectories are stable the Rose Run stress state.

Hydraulic fracturing is a technique used in the petroleum industry to enhance production by increasing the bulk permeability of the aquifer around the well. It can also be used to enhance injectivity. We determined that the use of hydraulic fracture treatments is technically feasible because the magnitude of S_{hmin} is lower in the Rose Run sandstone than in the overlying Beekmantown dolomite and Trenton limestone. A hydraulic fracture in the Rose Run sandstone at the Mountaineer site would propagate away from the wellbore towards the NE and SW (in the direction of S_{Hmax}). It could be formed at bottom-hole pressures greater than S_{hmin} in the Rose Run sandstone, but less than S_{hmin} in the surrounding formations, and thus be prevented from extending through the caprock. While the thermal effects due to the injection of fluids that are cooler than the in situ temperature do influence the stress concentration around the wellbore such that hydraulic fractures are induced at slightly lower pressures, the thermal effects on S_3 in the reservoir are second order (reviewed in (Zoback, 2007)). The thermal effects in

the caprock should be insignificant. As long as the injection pressures are 5-10% below S_3, a small change in S_3 should not affect the integrity of the caprock.

Finally, we investigated the potential of using induced micro-seismicity to enhance the bulk permeability of the injection zone. The state of stress in the Rose Run sandstone is in frictional faulting equilibrium, such that increases in P_p from controlled fluid injection could result in slip on optimally oriented pre-existing faults. The electrical image log of the wellbore wall from the Mountaineer well was used to determine the orientations of the fractures that intersect the well in the Rose Run sandstone. Figure 3-4a shows a plot of those fractures on a lower hemisphere stereonet. The background color coding demonstrates the likelihood of a fracture plane to slip in the in situ stress state. The orientation of the fracture plane is indicated by the pole to the fracture plane. For example, a nearly vertical fracture that strikes to the North (dips to the East) would have a pole to the fracture plane that plots near the outside of the stereonet in the westerly direction. Fractures that plot in the hot colors require no or little P_p increase to become critically stressed, while those in the cool colors require large pressure increases. Figure 3-4b plots the same information on a 3D Mohr diagram that illustrates the relationship between the normal and shear stresses resolved on the fracture planes. Laboratory experiments have shown that at depth μ tends to range between 0.6 and 1.0 (Byerlee, 1978). For this analysis, μ=0.6 was used to evaluate the likelihood of the fractures to slip.

In this normal to strike-slip stress regime with S_{Hmax} oriented N47ºE, fractures that are striking NE or SW and dipping more than 45º are most likely to slip. Three of the observed fractures are characterized as critically stressed at the in situ P_p gradient of 11 MPa/km. By injecting fluids up to the fracture pressure of the caprock, twelve more shallowly dipping fractures become critically stressed. This P_p is the absolute maximum pressure that could be used for an induced micro-seismicity treatment. In practice, the P_p should remain 5-10% lower than the caprock fracture pressure to account for the uncertainty in the minifrac tests and ensure the integrity of the caprock. This P_p increase would also create a hydraulic fracture since the injection pressures would exceed S_{hmin} in the Rose Run sandstone.

The potential permeability enhancement resulting from controlled induced micro-seismicity is difficult to predict. Therefore to include it in the feasibility assessment, we

estimated that an induced micro-seismicity treatment will enhance the injectivity by 5 times over the injection scenario with no stimulation. This estimate was based on previous induced seismicity experiments, primarily done in tight gas and geothermal reservoirs, that see up to and greater than an 8 fold increase in bulk permeability, which approximates injectivity increases (Palmer et al., 2007; Rahman et al., 2002; Tezuka, 2006). The permeability enhancements should be sustainable over the life of the project because the high injection pressures serve to decrease the effective normal stress acting on the reactivated fractures so that they remain critically stressed and continue to act as conduits for fluid flow.

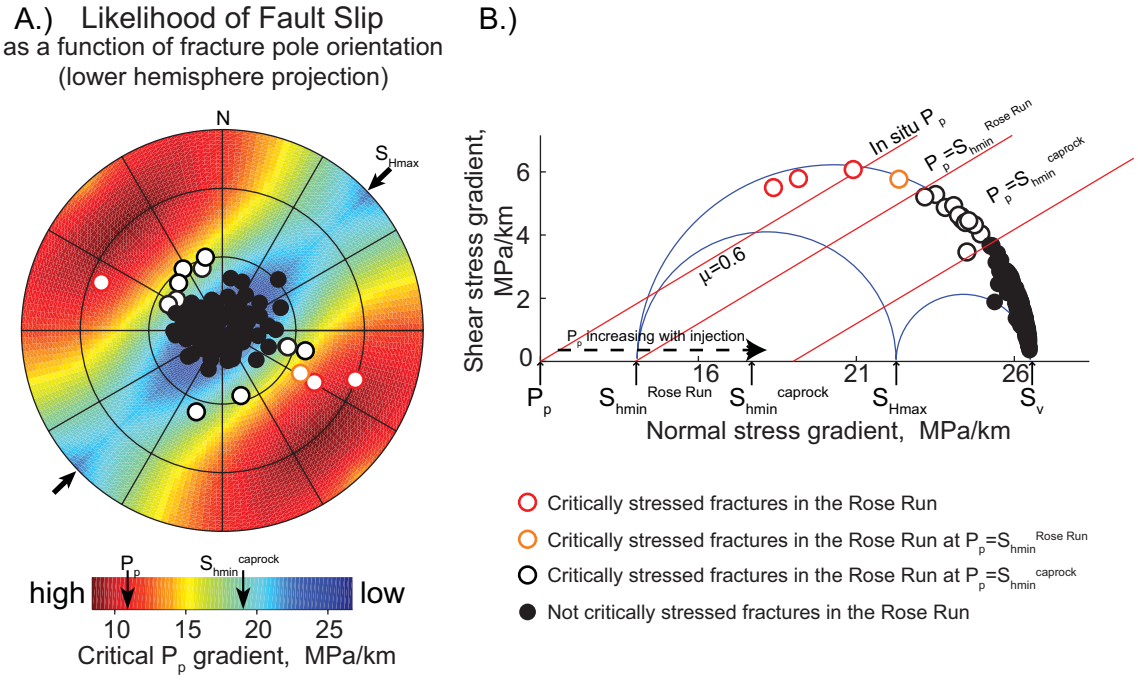

Figure 3-4: Critically stressed fractures in the Rose Run sandstone from electrical image log data. A.) A lower hemisphere stereonet plot indicating likelihood of fault slip as a function of pole to the fracture plane. Hot colors indicate high likelihood of slip and cool colors indicate low likelihood of slip. The fracture poles shown by white circles outlined in red are critically stressed in the current in situ stress conditions, assuming μ=0.6. The white circle with an orange outline is a critically stressed fracture at a P_p equal to S_{hmin} of the Rose Run sandstone. The white circles with black outlines become critically stressed as P_p increases to the S_{hmin} magnitude in the caprock. The black circles are fractures that are not critically stressed. The in situ P_p gradient is 11 MPa/km and the maximum safe increase in P_p due to fluid injection is 19 MPa/km. B.) Fractures plotted on a Mohr diagram, indicating their proximity to the failure lines (red). The slope of the failure lines is controlled by the μ value and the x-intercept is controlled by the P_p.

3.4.3 3D Geostatistical Modeling of the Rose Run Aquifer

One of the main purposes for the geological and geomechanical characterizations is to provide the necessary input for building 3D models that are representative of the aquifer's property variability. Because this methodology focuses on capturing and evaluating the heterogeneity and uncertainty of the aquifer properties, the use of geostatistical modeling is important. A geostatistical approach allows for the representation of structural variability and different aquifer property distributions on two scales. First, geostatistics is used to build several model geometries that incorporate different structural variability (e.g., thickness, dip angle, depth) and aquifer stimulation techniques such as hydraulic fracture treatments. Then, for each structurally variable model, geostatistics is used to populate rock properties such as permeability and porosity in a way that is geologically consistent and representative of the uncertainty and aquifer heterogeneity. The desired result of the 3D aquifer modeling is a set of injection interval types representative of the aquifer variability found in the region.

3.4.3.1 Rose Run Case Study 3D Geostatistical Modeling

Six geometry variations were modeled, based on the geological and geomechanical characterization of the case study area. The general structure of these models is the same. They are all 6 km x 6 km in the N-S and E-W directions, gently dipping (about 2-3º) towards the ESE, with slight topography and thickness variations. At the centre of the models, the depth of the top of the aquifer is 2350 m. The 2-3º slope, which is slightly more steep than the <0.5º regional trend, makes the up dip depth ~2250 m and the down dip depth ~2450 m. Therefore the models are representative of the depths of the study area.

Two aquifer thicknesses, one averaging 30 m (varying from 15 to 50 m) and the other averaging 60 m (varying from 45 to 80 m) we modeled. Each aquifer thickness was modeled three times: (1) without a hydraulic fracture,(2) with a single hydraulic fracture, (3) a third time with four, smaller, staggered hydraulic fractures that represent hydraulic fracturing along a horizontal well. Because the hydraulic fractures will propagate in the direction of S_{Hmax}, which is oriented NE-SW, the grid cells were oriented in that direction. Most of the models had 150 (NE to SW) x 172 (NW to SE) x 5 (down) grid cells. The grid cells are approximately 40 m x 40 m x 6 m in the 30 m

thick models and 40 m x 40 m x 12 m in the 60 m thick models, except the grid blocks on the NE to SW centre diagonal which are about 1 m wide in the NW to SE direction. In some models these grid cells were used to model a hydraulic fracture by altering the rock properties, but they were included in all the models for consistency. The models with the four staggered hydraulic fractures were the same as those described above with the addition of four 1 m thick cells separated by 200 m in the NW to SE direction, which increased the number of grid cells to 150 x 178 x 5. The hydraulic fractures were represented by altering the rock properties in some of these grid blocks as discussed below.

The models were populated with porosity and permeability values using the same technique described in Lucier et al. (2006). Using the sequential Gaussian simulation method, each of the six structurally variable models were populated with the nine possible combinations of the three porosity distributions (mean porosity = 4%, 8%, and 12%) and three horizontal permeability distributions (mean permeability = 4 mD, 20 mD, and 40 mD) defined above. In sedimentary basins, it is common for the permeability in the vertical direction to be less than the permeability in horizontal direction. For this reason, the vertical permeability was assumed to be half of the horizontal permeability for all the models. For the property simulations, a correlation coefficient between porosity and log permeability of 0.65 was used based on well log data from the Mountaineer site. The choice of the semivariogram, which defines the spatial continuity of properties, was highly subjective. However, since the Rose Run sandstone is in a sedimentary basin where significant lateral correlation in both porosity and permeability are expected, a semivariogram that models large scale spatial continuity with a small percentage of noise added in to account for heterogeneity was chosen (i.e., spherical variogram with a 0.2 nugget effect and an isotropic range of 500 m in the geological coordinate system). To model a single hydraulic fracture, the thin grid blocks extending 300 m from the centre grid block (location of injection well) toward the NE and SW were assigned a porosity of 30% and permeability of 1000 mD to approximate a 300 m half-length fracture and associated damage zone. For the models with four hydraulic fractures, NE-SW trending 100 m half-length fractures were created by assigning a porosity of 30% and permeability of 1000 mD to some of the 1 m thick grid blocks described above. This approach for modeling the hydraulic fractures

was subjective. However, we believe that populating 1 m wide grid cells with these property values effectively approximates those values associated with the hydraulic fracture and surrounding formation after fracturing.

3.4.4 Simulate CO_2 Injection

This feasibility analysis workflow hinges on the results of the CO_2 injection fluid flow simulations. Fluid flow simulations provide information on realistic injection rates for different aquifer properties and injection well configurations. The results are used to assess whether it is possible to achieve the storage goals of a project within defined economic controls. The goals of the project control how the simulations are set up. It is necessary to determine the time period for running the simulations. This includes deciding how long to inject the CO_2 and how long to monitor the plume after the injection stops. In most cases, the supply of CO_2 can be considered unlimited such that the factor limiting the injection rate is the maximum safe bottom-hole pressure.

3.4.4.1 Rose Run Case Study CO_2 Injection Flow Simulations

The CO_2 injection simulations in the Rose Run injection intervals were run using ECLIPSE 100™, a commercial simulator developed by Schlumberger. This simulator uses a three-component blackoil model and does not consider the effect of fluid phase composition on the fluid flow. This simulator has sufficient capabilities to determine the first-order injection rates that can be expected in injection intervals with the modeled properties. More complex fluid flow simulators, such as compositional simulators and those that include reactive transport modeling of the reactions between CO_2 and the mineral phases in the aquifer (e.g., Xu et al., 2006) may be more suitable for other types of investigations.

The fluid properties of the brine and CO_2 are functions of the in situ pressure, temperature and salinity. The average values used were: water formation factor of 1.04 reservoir m^3/standard m^3, CO_2 formation factor of 1.8×10^{-3} reservoir m^3/standard m^3, water viscosity of 7.3×10^{-4} Pa·s (0.73 cP), and CO_2 viscosity of 1.01×10^{-4} Pa·s (0.101 cP). The CO_2 solubility (Rsw) at aquifer temperature and salinity was modeled by a Sechnow coefficient and fitted to literature data (Ennis-King, personal communication). Over the aquifer pressure range of 25 to 42 MPa, Rsw ranged from 29.7 to 33.9

reservoir m^3/ reservoir m^3. We used relative permeability curves adapted from the van Genuchten (1980) function with an irreducible gas saturation of 0.05, an irreducible liquid saturation of 0.2, and an exponent of 0.457, resulting in a crossover at 0.75 gas saturation.

In this case study, CO_2 injection over a period of 30 years was modeled for 108 different injection scenarios, which are summarized in Figure 3-5. Six injection well scenarios were investigated: vertical injection well with two different injection pressure constraints, horizontal injection well with two different injection pressure constraints, vertical injection well with a single hydraulic fracture, and horizontal injection well with four staggered hydraulic fractures. The limiting factor controlling the injection rate was the maximum safe bottom-hole pressure (BHP). The vertical injection wells were located in the centre of the grids and the horizontal injection wells extended 1000 m along the centre of the NW-SE axis in the centre of the 4^{th} grid block from the top. Injection in these wells was simulated with two BHP limits. First, a BHP of 32 MPa at the top of the vertical well injection zone (2350 m) was used (i.e., 13.6 MPa/km). This is slightly less than the 13.8 MPa/km S_{hmin} gradient observed in the Rose Run sandstone at the Mountaineer site. The second BHP limit for the models without hydraulic fractures assumed a fracture pressure of 40 MPa, which is closer the S_{hmin} observed in the caprock. This was done because it is unclear whether the low S_{hmin} measured in the Rose Run as compared to the adjacent formations at the Mountaineer site is present throughout the region. For the hydraulically fractured models, the maximum BHP was set at 42 MPa at 2350 m, which is 5.9% less than the 44.65 MPa predicted at that depth using the caprock S_{hmin} gradient. The aquifers were modeled as open systems with a constant boundary pressure.

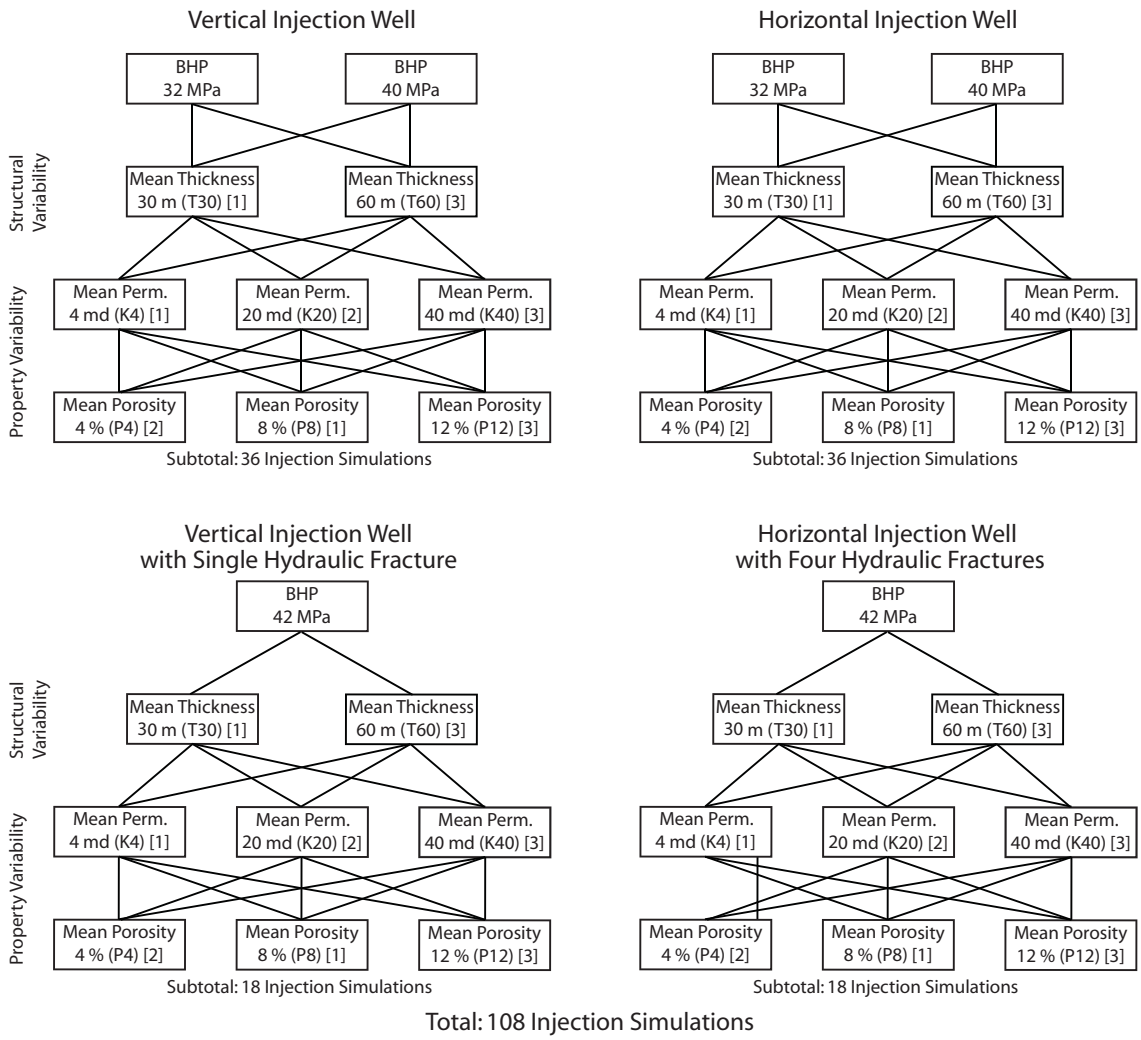

Figure 3-5: Outline of fluid flow simulations, organized by injection scenario. Two BHP constraints were modeled for the vertical and horizontal wells. The abbreviations in the parentheses refer to the naming convention for the models. The number in the brackets was used to categorize the likelihood of a given property to be found in the region, [1] is most likely and [3] is least likely.

Each of the six injection scenarios was simulated for the 18 models that represent the variability and uncertainty of the thickness and rock properties of the Rose Run sandstone. We developed a naming convention for the models to organize the simulation results. The abbreviations for the different properties are shown in parenthesis in Figure 3-5. Model names refer first to the mean thickness of the model, either 30 m or 60 m, with the abbreviations T30 or T60 respectively. Then the names refer to the mean horizontal permeability, either 4 mD, 20 mD, or 40 mD, with the

abbreviations K4, K20, or K40. The final part of the name refers to the mean model porosity, either 4%, 8%, or 12%, with the abbreviation P4, P8, or P12.

The results for the six injection scenarios of model T60_K20_P8 are summarized in Figure 3-6. The final extent and saturation of the CO_2 plume after 30 years of injection for each of the injection scenarios are shown in Figure 3-6a. The CO_2 plumes in the horizontal well injection scenarios are elongated in the direction of the wells, NE-SW. In the hydraulically fractured vertical well injection, the plume is elongated in the hydraulic fracture orientation, NE-SW. The cumulative CO_2 injected for each scenario is shown in Figure 3-6b. The horizontal wells (blues) have more cumulative injection than the vertical wells (grayscale) with the same injection conditions. The hydraulically fractured wells have the most cumulative injection.

The results of all the simulations are summarized in Figure 3-7 in terms of CO_2 injection rate averaged over the 30 years of injection. In Figure 3-7, the models are sorted first by thickness, then permeability and finally porosity. In the top figure, the vertical and horizontal well simulation results for injection scenarios with a 32 MPa BHP constraint are shown with the hydraulically fractured scenarios with a 42 MPa BHP constraint. The bottom figure shows the vertical and horizontal well simulation results with a 40 MPa BHP constraint and the same results as the previous figure for the hydraulically fracture scenarios. The BHP constraint had a large effect on the injection rate, such that the 25% increase in BHP from 32 to 40 MPa resulted in approximately 2.5 times higher injection rate. Increases in the thickness and permeability of the models also resulted in higher injection rates. Doubling the thickness nearly doubled the injection rate, while doubling the permeability more than doubled the injection rate. Increases in porosity had a small, negative effect on injection rate which is likely related to the extent of the CO_2 plume and its ability to encounter higher-permeability zones in the aquifer model. Injection scenarios utilizing horizontal wells rather than vertical wells resulted in 20% to 50% increases in injection rate due to the greater surface area for injection in the horizontal wells. Injection scenarios that include hydraulic fractures also saw an increase in injection rate. Hydraulic fractures increased injection rates by up to 4 times as compared to the non-fractured scenarios constrained with the 32 MPa BHP, largely due to the different injection pressures. Hydraulic

fractures increased injection rates by about 45% in the vertical wells and 21% in the horizontal wells with BHP constraints of 40 MPa.

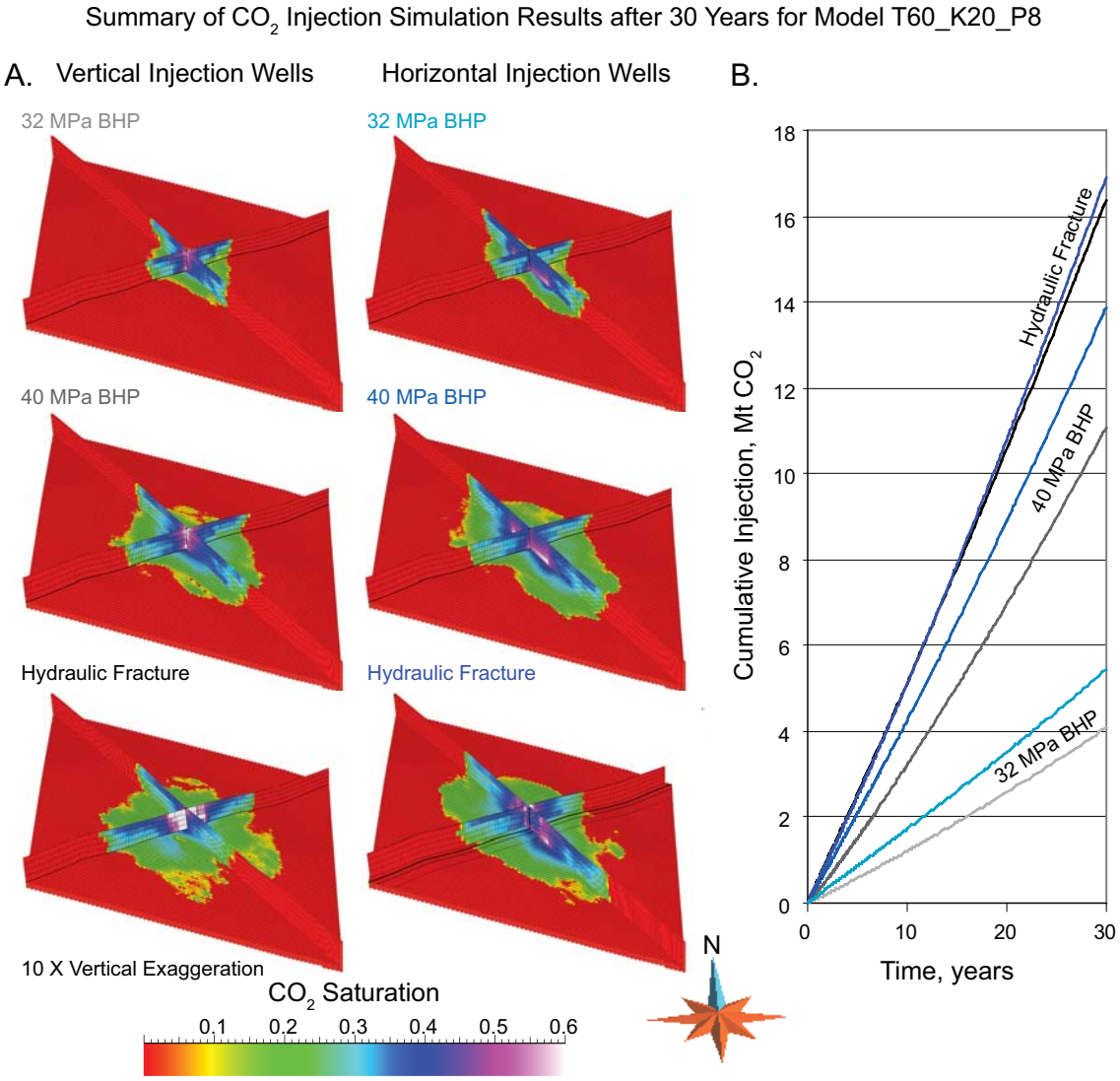

Figure 3-6: Summary of CO_2 injection simulation results after 30 years for model T60_K20_P8. A.) CO_2 saturation after 30 year of injection for the six injection scenarios that are simulated. The grids are approximately 6 km x 6 km x 60 m. The grid blocks shown are the central NE-SW and NW-SE horizontal axes and the bottom grid layer in the down direction. For the scenario with the hydraulically fractured horizontal injection well, the NE-SW horizontal axis shown is along one of the staggered hydraulic fractures and therefore slightly NW of the center. B.) Cumulative CO_2 injection over 30 years for the six scenarios. The grayscale lines are vertical wells and the blue-scale lines are horizontal wells.

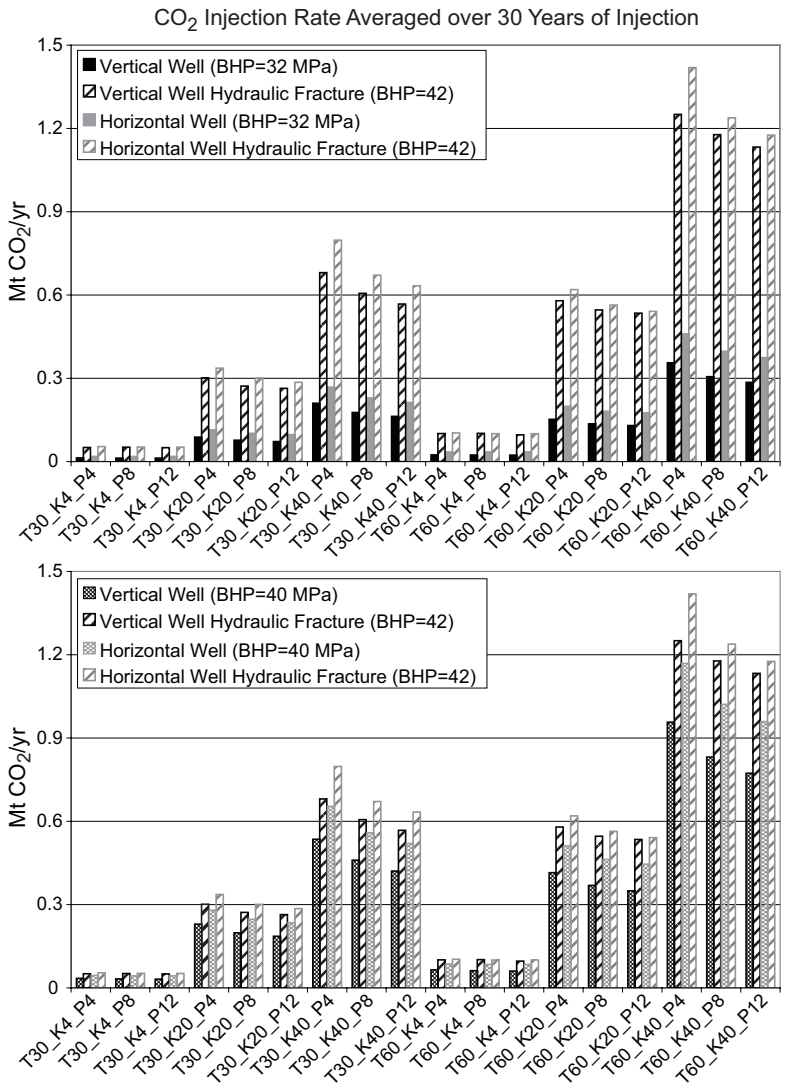

Figure 3-7: CO_2 injection rate averaged over 30 years of injection. Simulations are sorted in order by thickness (T30, T60), permeability (K4, K20, K40), and porosity (P4, P8, P12). The top plot shows the results for the vertical and horizontal wells injecting with a 32 MPa BHP, the bottom plot shows them with a 40 MPa BHP constraint. The hydraulic fracture results are the same for both plots.

In Figure 3-8, the results are summarized by a normalized histogram and cumulative distribution plot of the 30 year averaged injection rates. Nearly one third of the simulations have injection rates less than 0.15 Mt CO2/yr and about one half of the simulations have injection rates less than 0.25 Mt CO2/yr.

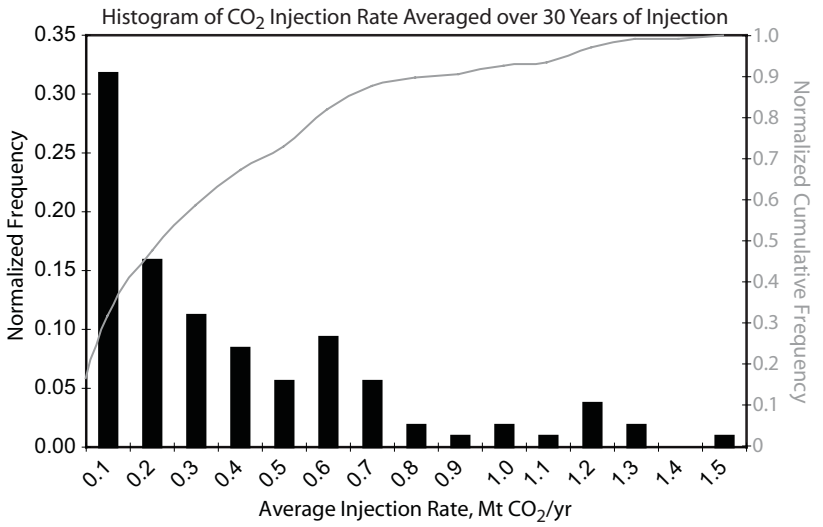

Figure 3-8: Summary of fluid flow simulation results from Figure 3-7 plotted as a histogram of the 30 year averaged injection rate in black and a cumulative distribution function in gray.

3.4.5 Evaluation of CO_2 Injection and Storage Feasibility

Once the CO_2 injection simulations have been run, it is possible to evaluate the feasibility of injecting and storing the amount of CO_2 defined in the CCS project goals. First, injection intervals are categorized by their likelihood of occurring in the region. Any ranking system that describes the likelihood of occurrence can be used to categorize the injection intervals. Then, to determine the spatial feasibility of the storage project the number of wells for each injection interval type and the minimum well spacing necessary to reach the cumulative CO_2 storage goal are calculated. Finally, the associated well cost per ton of CO_2 injected is determined for each injection interval. To do this, the cost of the well is divided by the cumulative CO_2 that can be injected by that well over its lifetime. The feasibility of the CO_2 storage project is assessed based on the spatial limitations of the region, the outlined economical constraints, and the likelihood of occurrence for the feasible models.

3.4.5.1 Evaluation of CO_2 Injection and Storage Feasibility in the Rose Run

For the evaluation in step five, injection and storage feasibility for vertical well injection with no aquifer stimulation was examined. First, each injection interval model was categorized by its likelihood of occurring in the region. The simple ranking system developed for this case study was based on assigning each property (i.e., thickness,

permeability, porosity) a value of 1 (most likely), 2, or 3 (least likely). For each combination of the 3 properties in a model, the assigned values were summed to get a value from 3 to 9. Models with lower values are representative of more of the region's aquifer area than those with larger values; therefore a randomly drilled well will more likely access an aquifer that is similar to a model with a low value (3-6) than one with a high value (7-9). In Figure 3-9, the models are arranged by increasing ranking values, which are appended to the beginning of the model names.

Once the injection interval models were categorized, we examined whether the storage goals of the project could be reached while honoring the region's spatial constraints. For each simulation, the surface area of the top of the CO_2 plume after 30 years of injection was calculated; and the number of wells necessary to inject 113 Mt CO_2/yr was determined for each injection scenario based on its average injection rate (Fig. 3-9b). By multiplying the surface area extent of the plume by the number of wells needed to achieve the injection goals, the percentage of the regional area (12960 km^2) required to reach the storage goals of the project was determined (Fig. 3-9a). All of the potential injection scenarios met the spatial feasibility constraint (i.e., required less than 100% of regional area).

To determine if the economic constraints could also be honored, either the number of wells (Fig. 3-9b) or the associated well costs (Fig. 3-9c) required to meet the injection goal could be examined. To meet the economic constraints described above, the injection goal must be met with fewer than 522 vertical wells which results in an associated well cost of less than \$1.31/t CO_2 to sequester 113 Mt CO_2/yr for 30 years (Table 3-1). When the injection rate was controlled by a BHP of 32 MPa, only three models met the economic constraint. These models had ranking values of 7 to 9 and represent only a very limited part of the study area. When the injection rate was controlled by a BHP of 40 MPa, ten of the models met the economic constraint. Four of these models had a ranking value of 5 or 6 (moderately likely) and the other six have values of 7-9 (least likely). The economically feasible models would require between 15-40% of the regional area to accommodate the storage needs. However, it is unlikely that the study area contains enough sites similar to these models to meet the injection and storage goals for the CCS project using only vertical injection wells.

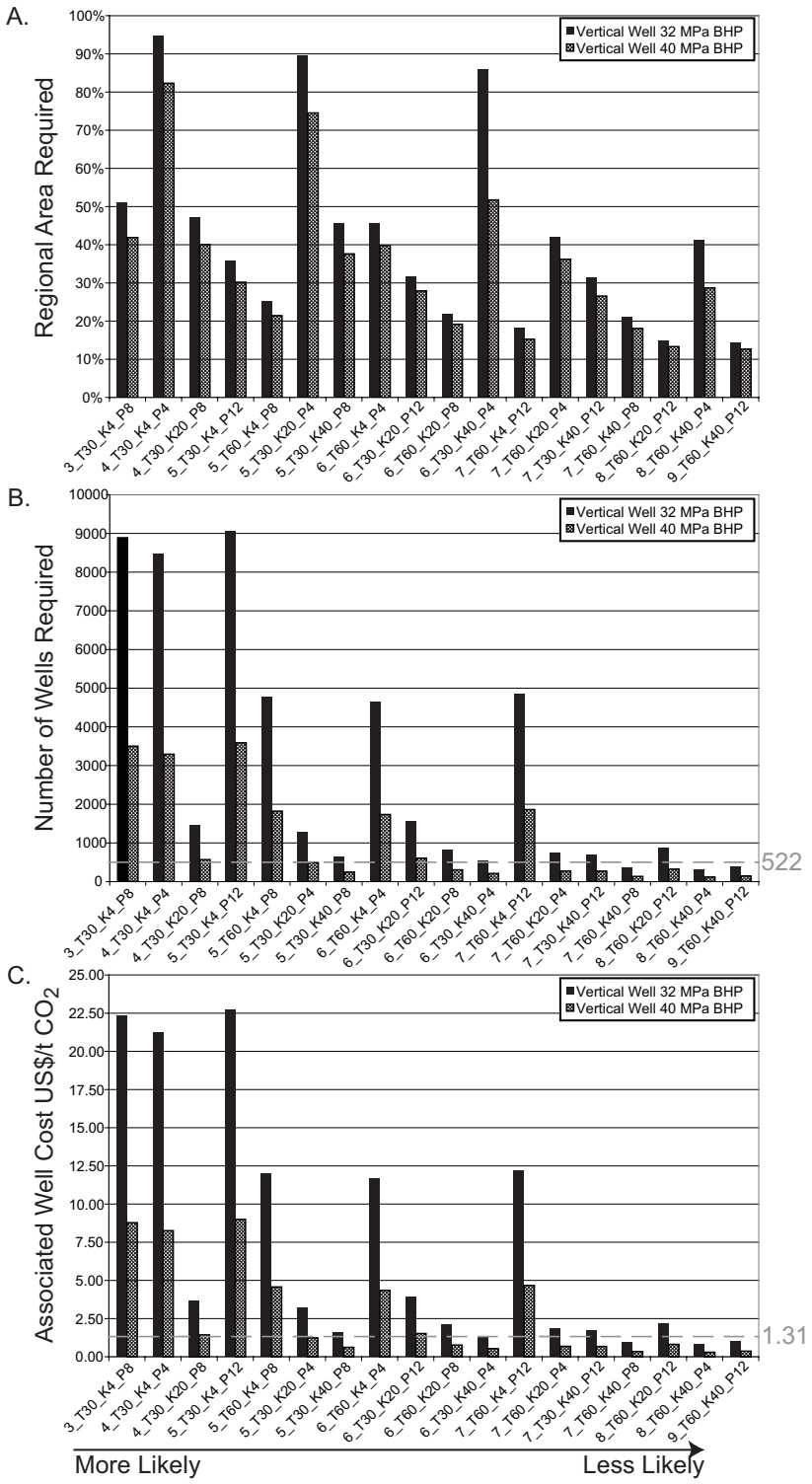

Figure 3-9: Evaluating the feasibility of vertical well injection scenarios with both 32 MPa and 40 MPa BHP constraints in the Rose Run region. Models are ranked and ordered by likelihood of occurring in the region (3 being most likely and 9 least likely). A.) Percentage of regional area required for storage. B.) Number of wells required to meet project goals (522 is economic threshold). C.) Associated well costs for each scenario ($1.31 is economic threshold).

3.4.6 Evaluate Potential for Injectivity Enhancement Techniques to Improve CO_2 Injection and Storage Feasibility

The associated well costs per ton of CO_2 are controlled by the costs associated with drilling, completing, logging, characterizing and maintaining the wells, the injection rate of the wells, and the lifetime of the wells. The rate of injection can be increased using stimulation techniques such as hydraulic fracturing and induced micro-seismicity and by drilling horizontal injection wells. The technical feasibility of these techniques is determined from the geomechanical characterization in step two. If these techniques can be safely implemented, it is necessary to evaluate whether the resulting increase in injection rate offsets the higher costs associated with the wells.

3.4.6.1 Rose Run Evaluation of Potential for Injectivity Enhancement Techniques to Improve CO_2 Injection and Storage Feasibility

The fluid flow simulations suggested that vertical injection wells did not provide adequate injection rates in enough of the more likely to occur models (i.e., ranking values of 3-6) to achieve the regional injection and storage goals. In the geomechanical characterization, we showed that other injection scenarios such as using horizontal wells, hydraulically fracturing vertical or horizontal wells, and induced micro-seismicity within the aquifer were all technically feasible ways to increase injection rates of wells in the study area. However, these potential increases in injection rates come with higher associated well costs (Table 3-1).

This evaluation step followed the same methodology used to evaluate the vertical injection wells. Like the vertical injection well scenarios, all of the enhanced injectivity scenarios simulated honor the regional spatial constraints (Fig. 3-10a). Again the models are ordered by the same ranking values as in the vertical well evaluation. The horizontal injection well scenario with the 32 MPa BHP required the most regional area for all the models to meet the storage goals. The induced micro-seismicity injection scenarios were not simulated; therefore there was no information on the extent of the CO_2 plume in the aquifer that could be expected. For this reason, the regional area required for injection wells with induced micro-seismicity treatments was not estimated for these scenarios.

The number of wells required to inject 113 Mt CO_2/yr was estimated for the six potential injectivity enhancement techniques (Fig. 3-10b). To do this, the injectivity enhancement from an induced micro-seismicity treatment had to be estimated based on the simulation results. While we showed that the Rose Run sandstone is a good candidate for induced micro-seismicity, we had no information on bulk aquifer permeability changes that could be expected from the implementation of this technique. Based on the results of other studies (Palmer et al., 2007; Rahman et al., 2002; Tezuka, 2006), we assumed that the injection rate would be five times that of the vertical or horizontal injection well scenarios simulated with a 40 MPa BHP. Because hydraulically fracturing the aquifer does not need to be avoided, injection could occur at just below the caprock fracture pressure. All of the scenarios required fewer wells than the vertical well scenario with the 32 MPa BHP. The horizontal well scenario with the 32 MPa BHP required more wells than the vertical well scenario with the 40 MPa BHP. The two hydraulic fracture scenarios (vertical injection well with a 300 m half length hydraulic fracture and horizontal injection well with four staggered 100 m half length hydraulic fractures) required similar numbers of wells for each model. The induced micro-seismicity scenarios were estimated to require the smallest number of wells, with the horizontal injection well requiring the fewest.

When the number of wells was translated into associated well costs per ton of CO_2, 15 of the 18 models had at least one injection scenario that was within the feasibility threshold cost of 1.31 US$/t of CO_2 (Fig. 3-10c). The three models that did not have any injection scenarios that met the economic constraints were all 30 m thick with a mean horizontal permeability of 4 mD. Unfortunately, these are some of the most likely aquifer types to be found in the region. Despite this, it appears that induced micro-seismicity has the potential to significantly decrease the associated well costs in these models to an economically feasible level if injection rates can be increased by 6 or 7 times (rather than the assumed 5 times). Such increases have been observed in other areas (Palmer et al., 2007; Rahman et al., 2002; Tezuka, 2006).

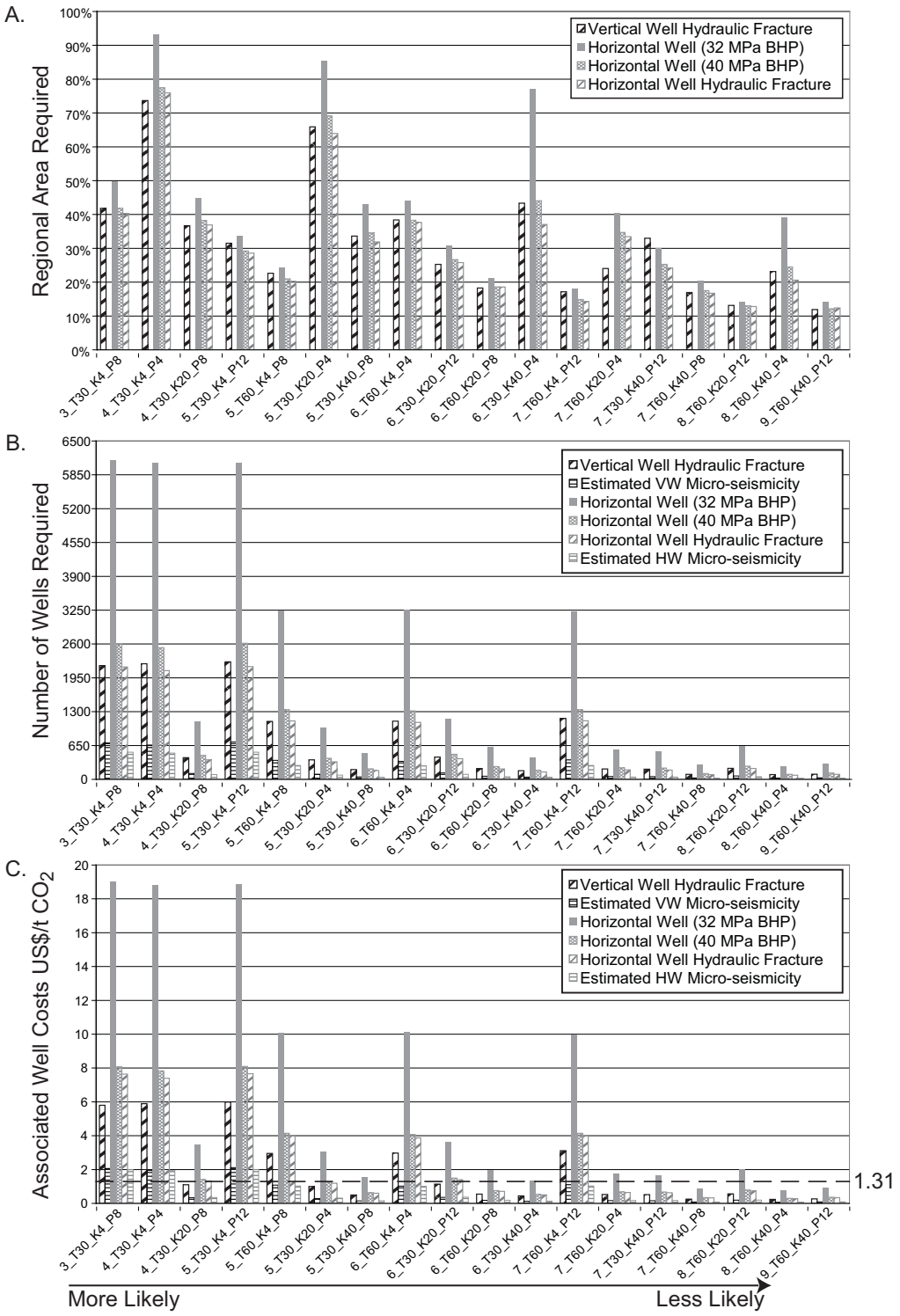

Figure 3-10: Evaluating the feasibility of injectivity enhancement injection scenarios in the Rose Run region. Models are ranked and ordered by decreasing likelihood of occurring in the region. A.) Percentage of regional area required for storage. B.) Number of well required to meet project goals. C.) Associated well costs for each scenario ($1.31 economic threshold).

Horizontal wells alone did not reduce the associated well costs enough to be economically feasible. Unlike the vertical injection well scenarios where only four out of eleven models with ranking values ≤ 6 (likely to moderately likely) had injection scenarios that were economically feasible, the enhanced injectivity scenarios had eight models with ranking values ≤ 6 that were economically feasible. Including injection wells with hydraulic fracturing and/or induced micro-seismicity in the CO_2 injection and storage feasibility assessment greatly increases the likelihood that the Rose Run study area CCS goals can be reached.

3.4.7 Regional Storage Assessment

The final step in the assessment workflow is to determine whether or not to continue with the regional CO_2 storage assessment. If the costs associated with the wells and injectivity potential in the region are not feasible for a large-scale CCS project, then it may be necessary to abandon injection and storage plans for that area and focus on locating more distant, but higher quality aquifers for storing the region's CO_2 emissions. If it is decided that well costs associated with storage in the region are reasonable and the injectivity potential is moderately feasible, it may be decided that the storage assessment should proceed by screening more local sites, updating the input into the assessment workflow, and reassessing the regional well costs. If the region is determined to be highly feasible based on the associated well costs and injectivity potential, then the assessment should continue by evaluating the other factors that control the overall feasibility of regional CCS (e.g., capture and separation, transportation, permitting, monitoring) that are outside the scope of this work.

3.4.7.1 Rose Run Case Study Regional Assessment

We summarize the regional assessment in Figure 3-11, which illustrates the economic feasibility for different injection scenarios based on the average permeability thickness, kH. We used the kH parameter in this analysis because we found that the permeability, k, and the thickness, H, are the primary properties controlling the injection rate in the models. The injection scenarios are ordered by increasing injection rate. The models were more likely to be economically feasible if they had large kH values and were stimulated with hydraulic fractures or induced micro-seismicity (Fig.

3-11a). The transition to being economically feasible depends on the economic threshold defined for the project. If larger than a 10% increase in the cost of energy was considered acceptable or if technologies improve for CO_2 capture and separation such that the percentage of the CCS budget that is allotted to well costs increases, more injection intervals would become economically viable. At a higher cost per ton of CO_2, models with smaller kH values and less aquifer stimulation become economically feasible (Fig. 3-11b). However, even if the economic threshold were tripled, many of the models would remain unfeasible without significant aquifer stimulation to enhance the injection rate.

With simple vertical or even horizontal injection wells, the region is unlikely to have enough effective injection capacity to make CO_2 storage feasible. Nevertheless, a large number of the models are economically feasible with the implementation of aquifer stimulation. The Rose Run case study region also meets the spatial requirements for storing 113 Mt CO_2/yr for 30 years. For these reasons, we have determined that this region of the Rose Run is likely a feasible location for CO_2 storage and that the injection and storage assessment should proceed with the screening of more local sites.

There are several areas of investigation that will lead to a more complete regional assessment. First, the stress state needs to be characterized at more locations to determine if the low S_{hmin} magnitude observed at the Mountaineer site is a local phenomena or representative of the entire region. This is important because the BHP constraint is a primary control over injectivity and economic feasibility. Also, further investigation should be done to find trends in aquifer thickness and permeability, so that new injection sites can be located in settings with high kH values. Finally, injection induced micro-seismicity experiments to determine the potential for increasing injectivity in the region are essential. Despite associated well costs of up to 13 M US$ per well, injection wells with induced micro-seismicity treatments have the most potential for making large scale CO_2 storage feasible in the Rose Run case study region.

There are other ways to increase the economic feasibility of CO_2 storage in this region besides increasing the feasibility cost threshold and/or the injectivity of the Rose Run sandstone. One area for consideration is identifying other injection units in the stratigraphic column that have storage potential. Studies are currently examining zones in the Copper Ridge dolomite for CO_2 storage potential in the case study region

(Jagucki et al., 2005). The more injection intervals that can be reached by a single well, the greater the injectivity of that well will be. With all of these possibilities, we believe that the region looks promising for large-scale CCS.

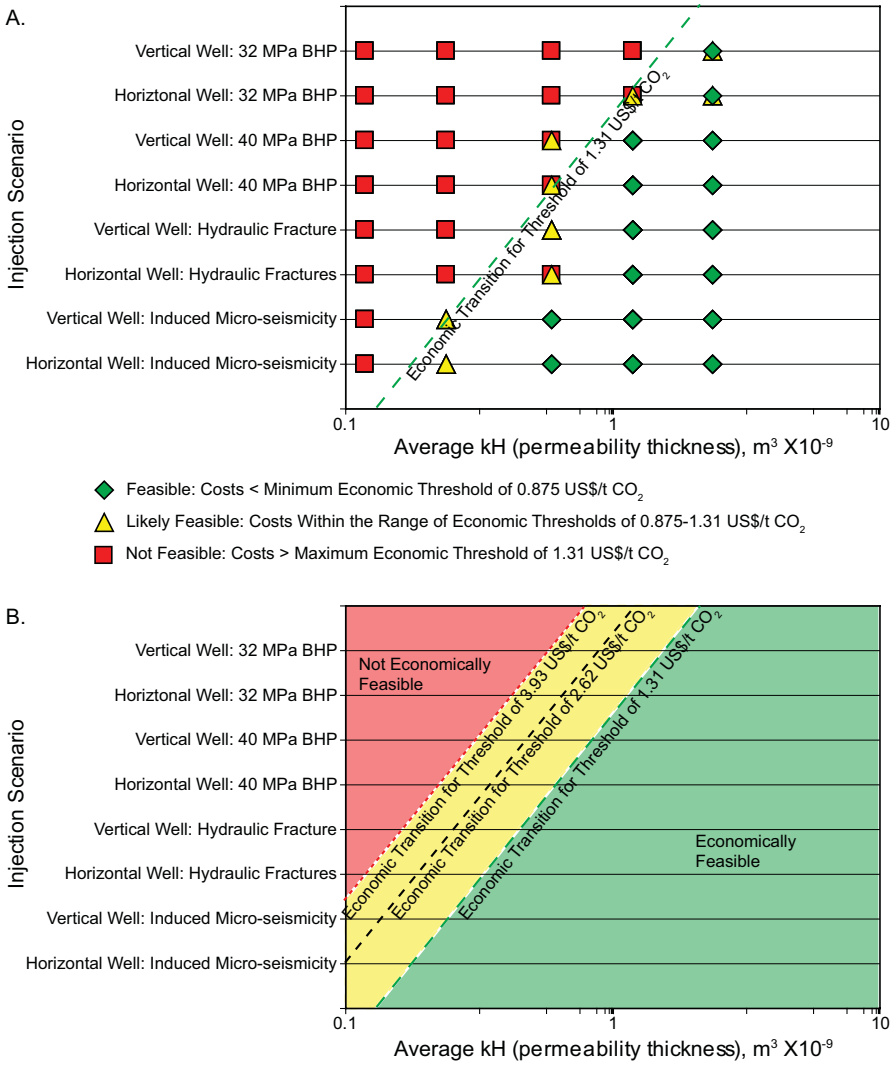

Figure 3-11: Summary of regional storage assessment. Average model log-scale permeability thickness (kH) is plotted against the different injection scenarios. The injection scenarios are ordered with increasing injection rate. A.) The color coding illustrates the economic feasibility for a given injection scenario in an aquifer model with the specified average permeability thickness. Red squares are not economically feasible, yellow triangles are likely economically feasible and green diamonds are economically feasible. The green dashed line estimates the transition between models that are feasible and those that are not. B.) Illustrating the effect of adjusting the economic threshold for the well costs associated with injection. The black dashed line is the economic transition if the threshold cost per ton of CO_2 is doubled and the red line is the economic transition if the threshold cost per ton of CO_2 is tripled. The green region of the plot is feasible and the red region in not feasible for all three economic thresholds. The feasibility in the yellow region depends on the economic threshold.

3.5 DISCUSSION AND CONCLUSIONS

The assessment methodology presented here is a tool for estimating regional effective CO_2 injection and storage capacity by considering available aquifer storage volumes, realistic well injection rates, and the costs associated with drilling and maintaining injection wells. This approach examines a region at the scale of individual injection intervals that represent the heterogeneity and uncertainty of regional aquifer properties. By including geomechanical characterization, aquifer modeling, and CO_2 injection simulation in the assessment methodology, it is possible to get a first order estimate of the injection capacity of the region, evaluate injectivity enhancement techniques, and estimate the effective storage capacity. As illustrated by the Rose Run case study, using this workflow will reduce the overall estimation of CO_2 injection and storage capacity for regions that have been characterized by a top-down approach. In regions with low-to-moderate permeability and aquifer thickness, the injectivity of an aquifer may severely limit its effective storage potential, particularly when injectivity enhancement techniques are not included in the assessment.

The case study illustrates the potential increases in injectivity and overall cost reduction that result from aquifer stimulation techniques despite their higher initial expenses. These methods for addressing limited aquifer injectivity require a complete geomechanical characterization. Understanding the state of stress at an injection site is necessary for controlling injection pressures, formulating stable deviated well trajectories, developing hydraulic fracture treatments, characterizing existing hydraulically conductive fractures, and planning induced micro-seismicity treatments. For CCS to be practical in a large portion of the Midwestern United States, and elsewhere in the country, stimulation techniques will need to be employed. Continued research as to their effectiveness and safety in CCS projects will be vital for securing the necessary public acceptance and legal permitting for them to be used in practical rather than just theoretical and pilot CCS projects.

3.6 ACKNOWLEDGEMENTS

Funding for this study was provided through Stanford University's Global Climate and Energy Project (GCEP). We want to thank Neeraj Gupta and Philip Jagucki of Batelle Memorial Institute and T.S. Ramakrishnan of Schlumberger Doll-Research for

their help with the Ohio River Valley CO_2 Storage Project work on the Mountaineer site characterization that was used as a base for the case study in this chapter. We also want to thank Kristian Jessen of the University of Southern California and Taku Ide of Stanford University with their help on the fluid flow simulations.

CHAPTER 4

CONSTRAINING THE FAR-FIELD IN SITU STRESS STATE NEAR A DEEP SOUTH AFRICAN GOLD MINE[1]

4.1 ABSTRACT

The gold mines in the Witwatersrand Basin of South Africa are some of the deepest underground mines in the world. For over a century, numerous, often deadly, mining-induced earthquakes have been observed. In this chapter, we develop and test a new technique for determining the virgin stress state near the TauTona gold mine. The results of this work will be used as part of the Natural Earthquake Laboratory in South African Mines (NELSAM) project to study the physics and mechanics of mining-induced earthquakes. This technique follows an iterative forward modeling approach that combines observations of drilling induced borehole failures in borehole images, boundary element modeling of the mining-induced stress perturbations, and forward modeling of borehole failures based on the results of the boundary element modeling. The final result was a well constrained range of principal stress orientations and magnitudes that are consistent with all the observed failures and other stress indicators. We found that the state of stress is a normal faulting regime with principal stress orientations that are slightly deviated from vertical and horizontal and therefore denoted with a (*). The maximum principal stress, S_{v*}, is deviated 0-20º from vertical towards the NNW with a magnitude gradient of 27 ± 0.3 MPa/km. The intermediate principal stress, S_{Hmax*}, is inclined 0-20º from horizontal with an azimuth of 145º to 168º and has a magnitude gradient of 21.5 to 26 MPa/km. The least principal stress, S_{hmin*}, is inclined 0-10º from horizontal with an azimuth of 235º to 258º and has a magnitude gradient of 13 to 15.5 MPa/km. This stress state indicates that the crust is in frictional faulting equilibrium, such that normal faulting is likely to occur on optimally oriented pre-existing faults. In the next chapter, we show that the mining-induced stress concentrations greatly alter the range of fault orientations with slip potential.

[1] This work is in preparation for submission to the International Journal of Rock Mechanics and Mining Sciences.

4.2 INTRODUCTION

As mining around the world moves deeper underground, understanding the stresses at depth and how mining activity perturbs them becomes increasingly important for mine safety. The seismicity associated with deep underground mining is typically separated into two types: (1) faulting on pre-existing planes of weakness and (2) formation of fractures at the stope faces (Gibowicz and Kijko, 1994). In cases when these seismic events are violent failures that cause damage to the excavation, they are referred to as rockbursts. Rockbursts are a small subset of the induced seismicity events, but because they cause damage to accessible areas they are the most likely to result in injuries and fatalities. A more complete characterization of the far-field stress will lead to better modeling of the mining-induced stress perturbations around the excavation. In turn, this can guide mining activities in the future and improve overall safety in the mines.

Constraining the far-field stress state is an important part of the Natural Earthquake Laboratory in South African Mines (NELSAM) project, which is working to develop a very near-field laboratory to study earthquakes at seismogenic depths (Reches, 2006; Reches and Ito, 2007; Reches et al., 2005). The deep gold mines of South Africa are unique locations for near-field studies of earthquake mechanics because of the high rates of seismicity induced by the mining activity and the accessibility of faults at depth. However, the perturbation of the in situ stresses by mining activities creates a complex stress field that complicates the understanding of the physical mechanisms controlling the induced seismicity. As part of the NELSAM project, we investigated the far-field in situ stress state surrounding the TauTona gold mine in the Western Deep Levels of the Witwatersrand Basin of South Africa (Fig. 4-1).

The gold mines in the Witwatersrand Basin of South Africa are some of the deepest mines in the world. Near these mines, seismicity was first reported in 1908, about 20 years after the onset of gold mining in the region. Gane et al. (1946) first directly associated the seismicity with the mining. Later, Gane et al. (1952) established the close proximity of the event locations to the active mining faces. Since that time, many studies have examined the effects of mining on induced seismicity as well as used the events recorded in the vicinity of the mines to examine the physics and mechanics of earthquakes. McGarr et al. (1975) showed that most of the seismicity occurs in regions

near the mining face with very large mining-induced stress perturbations. McGarr and Wiebols (1977) investigated the effects of mine geometry on seismicity, determining that volume of closure has a significant effect on the seismicity. A number of studies have also examined the deformation, source parameters, and ground motion parameters associated with seismicity observed in the region (e.g., Durrheim et al., 1998; McGarr, 1971; McGarr et al., 1989; McGarr et al., 1981; Spottiswoode and McGarr, 1975). The NELSAM project will extend this work with very near-field observations from borehole image logs, a dense seismic array, accelerometers, and strain meters in TauTona and other mines in the region.

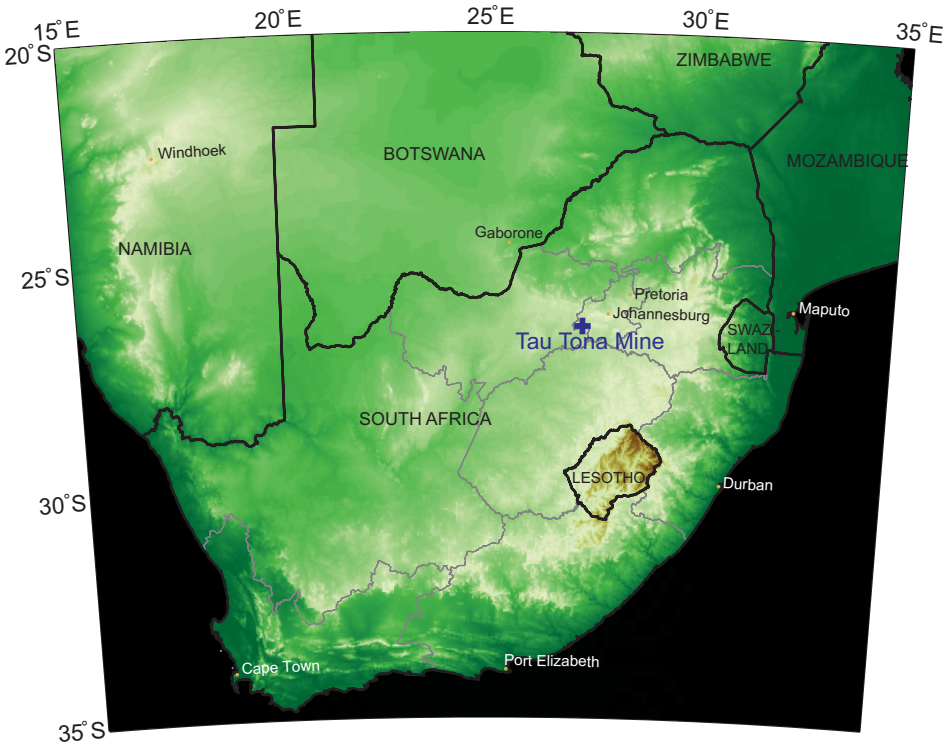

Figure 4-1: Map of South Africa, with the location of the TauTona gold mine

Much of the previous published work on characterizing the far-field in situ stress state near the deep mines in the Witwatersrand Basin relies on borehole strain relief measurements (Gay, 1972, 1975, 1977). In their review of global stress measurements, McGarr and Gay (1978) show that in South Africa the stress state is typically in a normal faulting stress regime, in which the vertical stress exceeds the horizontal stresses, at depths below 2 km. These measurements also show that the minimum horizontal stress, S_{hmin}, magnitude is typically much lower than the vertical stress

magnitude, S_v. In this study, we tested a new technique that incorporates both near- and far-field observations of stress indicators and boundary element modeling to constrain the far-field stress state and model the near-field perturbation of that stress state. The stress indicators we observe are drilling-induced failures (i.e., breakouts and drilling induced tensile fractures in the borehole walls) in image logs from boreholes drilled at a variety of orientations. Peska and Zoback (1995) discuss the mechanics controlling the formation of compressive and tensile failures in boreholes drilled at arbitrary orientations to principal stresses. These features have previously been used to constrain the stress states around oil and gas fields and other deep boreholes (e.g., Zoback et al., 2003). Because of the complexity of the stress perturbation around the mining excavation, the addition of boundary element modeling was necessary to analyze the drilling induced failure observed in the near-field of the excavation. This technique follows an iterative forward modeling approach to constrain a far-field stress state that best fits the stress indicator observations in the near- and far-field to the mining excavation.

4.3 DATA

4.3.1 Mine Layout and Rock Properties

Because the excavations in the mine perturb the in situ stress state, we needed a clear understanding of the geometry of the mine layout and the material properties of the in situ rock and backfill. The geometry of the mine is illustrated in Figure 4-2. The mining occurs along 0.5-1.5 m thick beds of gold-bearing conglomerates, referred to as "reefs". In the TauTona mine, the Carbon Leader Reef is mined; in the shallower Mponeng mine, which overlaps TauTona towards the southwest, the Ventersdorp Contact Reef is mined. The bedding dips about 20° towards the SSE. In Figure 4-2 (a-c), the white space is the intact host rock and the colored regions are where the reef has been mined. The mined out region of the reef is referred to as the stope. White spaces surrounded by the colored regions are support pillars. The largest one, located in the northwestern section of the mine, is the main shaft pillar. The red area is Mponeng mine, which is about 800 m shallower than TauTona. The blue area is the oldest part of

TauTona which was mined before backfill was used to replace the excavated material. The green and yellow regions are backfilled excavations in TauTona.

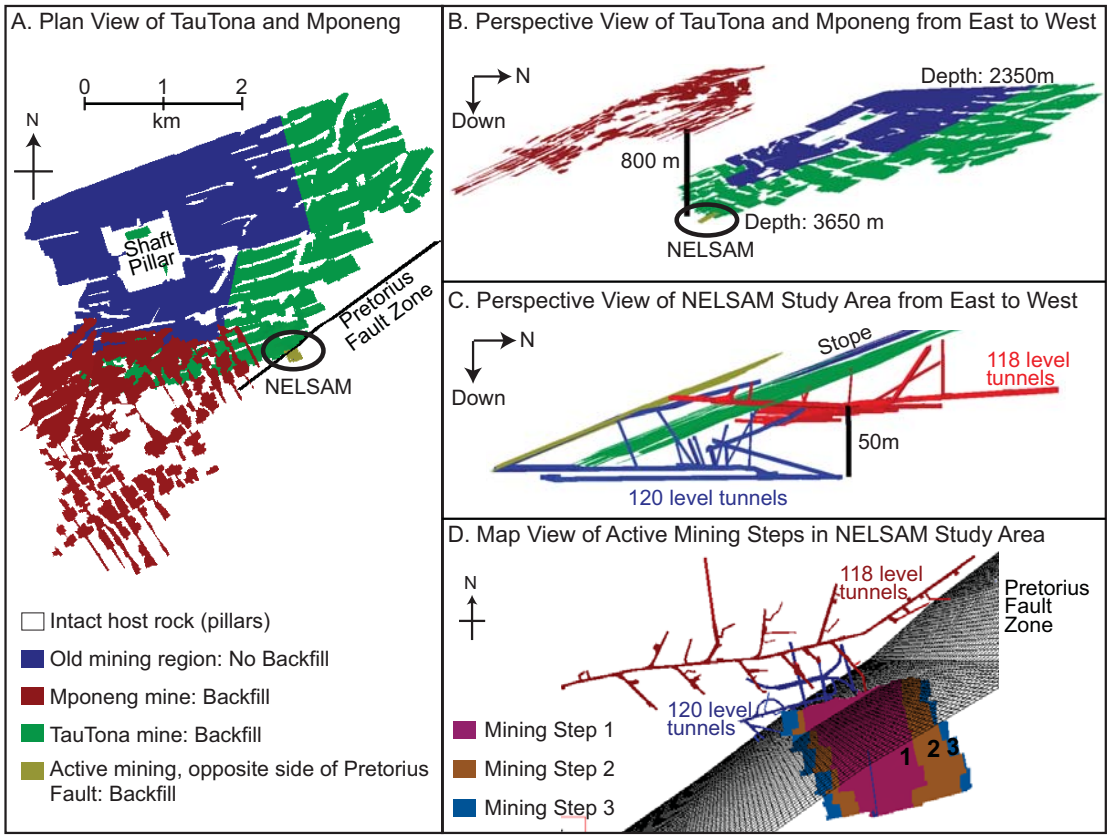

Figure 4-2: Layout of the mine. A.) Plan view of the stope of Mponeng mine (red) and TauTona mine (blue, green, yellow) and the PFZ (black). The white area is the intact host rock. The NELSAM study area is in the southeastern part of TauTona. B.) Perspective view of the stope from the east without the PFZ. The NELSAM study area is in the deepest part of the mine. Mponeng is about 800 m shallower than TauTona. C.) Zoomed in perspective view of the NELSAM study area from the east. The active mining (yellow) is offset from the older mining (green). The 118 and 120 level tunnels are also shown; they are separated by 50-60 m. D.) Map view of the NELSAM study area tunnels, the PFZ, and the active mining section, which is broken into 3 mining steps. The green region of the stope is not shown so that the tunnels are visible.

The intact host rock is primarily quartzite. The average material properties for the host rock that were used in the modeling include a uniaxial compressive strength of 200 MPa, Poisson's Ratio of 0.20 and a Young's modulus of 70 GPa, as based on laboratory measurements (Heesakkers and Reches, personal communication; Cartwright and Walker, 2000) and have been used in previous studies in TauTona (Hofmann and Murphy, 2007). The material properties of the backfill in TauTona and Mponeng vary

slightly. The properties we used were provided by the mine engineers (Shaun Murphy, personal communication). Both backfill materials have no cohesion or tensile strength and a friction angle of 10°. The Mponeng backfill has a shear modulus of 10 MPa and a normal modulus of 16 MPa and TauTona backfill has a shear modulus of 14.4 MPa and a normal modulus of 14.4 MPa. The shear and normal moduli relate the elastic shear and normal displacements (i.e., ride and closure) and the shear and normal stresses acting on the material.

The NELSAM study area is located in the vicinity of the yellow region in Figure 4-2 a-c and is shown in Figure 4-2d. This is an area of active mining and is near the deepest part of the mine. The reef in the yellow region is offset from the reef in the green region by the Pretorius Fault Zone (PFZ), an ancient normal to strike-slip fault zone that dips steeply and strikes approximately NE-SW. In Figure 4-2d, the region shown in yellow for Figures 4-2a-c is categorized into three mining steps shown in pink, orange and blue. These are representative of the extent of the mining in the yellow region at the times during which borehole drilling and image logging occurred. The mining shown in red, blue and green (Fig. 4-2) is included for all three mining steps. The three steps (1, 2, and 3) represent the extent of mining at June 2005, January 2006, and June 2006 respectively (Fig. 4-2d).

In the NELSAM study area, the locations of the access tunnels are also important for understanding the mining-induced stress perturbations. These have a more localized effect on the stress state than the stope and therefore, for the purpose of this work, they are only modeled in the areas where borehole logging was carried out. The tunnels in the 118 and 120 levels of the mine near the NELSAM study area are shown in Figure 4-2 (c-d).

4.3.2 Borehole Camera Image Logs

Borehole image logs provide oriented images of the walls of the boreholes. These data allow for the observation of drilling induced borehole failures such as drilling induced tensile fractures and borehole breakouts as well as observations of natural fractures that intersect the boreholes. Image logs were recorded in three types of boreholes: vertical boreholes within the mining-perturbed region, deviated boreholes within the mining-perturbed region, and a sub-horizontal borehole that extends from the

mining-perturbed region into the far-field virgin stress state. Data was collected in six 6.5-11.5 m vertical boreholes, two from the 118 level tunnels (sites 2 and 3) and four from the deepest 120 level (sites 7V, 9, 10, and 13) (Fig. 4-3). Data was collected in five 10-40 m long boreholes deviated 45-80° from vertical, three extending from the same area of the 118 level (site DAF) and two deviated towards each other on the same plane in the 120 level (site 7 N and S) (Fig. 4-3). Image log data was also collected in LIC118 in the 118 level. This borehole is deviated 70-85° from vertical towards the east. This borehole was drilled for exploration purposes and extends for more than 800 m away from the excavation. Of this length, 418 m was logged with the camera tool. Table 4-1 lists the boreholes and the date on which they were logged. Each borehole was assigned to one of the three mining steps based on the date of logging.

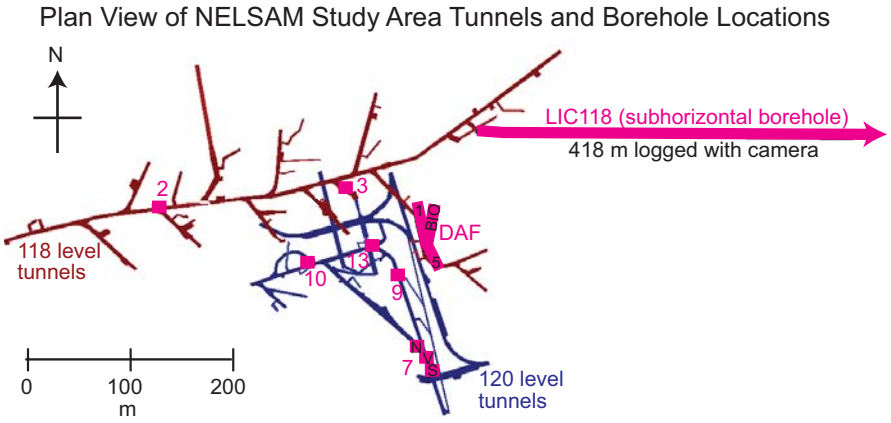

Figure 4-3: Locations of boreholes logged in the 118 and 120 level tunnel systems. Sites 2, 3, 7V, 9, 10, and 13 are vertical boreholes. The three boreholes at the DAF site (1, 5, and BIO) and two boreholes at site 7 (N, S) are deviated. The LIC118 borehole is sub-horizontal and extends away from the mining into the far-field.

Table 4-1: Borehole logging dates and associated mining steps

Borehole	Date (dd/mm/yyyy)	Mining Step
Site 10	18/05/2005	1
Site 13	30/06/2005	1
LIC118	14/7/2005	1
Site 9	09/01/2006	2
DAF 1	12/01/2006	2
Site 2	19/05/2006	3
Site 3	07/06/2006	3
DAF 5 & BIO	08/06/2006	3
Site 7 (3	12/09/2006	3

4.3.3 Overcoring Measurements

In February 2000, two in situ stress measurements were completed within the shaft pillar using the overcoring technique and reported in an internal report (Cartwright and Walker, 2000). These tests were carried out in the roof of a tunnel in the shaft pillar area at the 83 level which is at a depth of 2361 m from the surface. The measurements were taken between 10-11 m into the access boreholes. Although this test site is located several hundred meters from the stope, its location within the shaft pillar, the presence of access tunnels, and boundary element modeling all indicate that the stresses measured were influenced by the mining stress perturbation. However, we could use these measurements as a starting point for constraining far-field stress magnitudes as part of the workflow used to determine the far-field state of stress.

The results of these measurements are summarized in Figure 4-4. The maximum principal stress (S_1) is deviated about 20° from vertical towards the NNW. The magnitude gradient of S_1 is about 36 MPa/km which is significantly higher than the predicted vertical stress gradient of 27 MPa/km based on an average overburden density of 2700 kg/m^3. This is likely due to the stress concentration in the shaft pillar which is supporting the excess vertical load resulting from the excavation of the stope. A nearly vertical S_1 in the mining-perturbed stress state suggests that the far-field stress state is likely in a normal faulting stress regime where the maximum principal stress is vertical. The intermediate principal stress (S_2) is deviated about 20° from horizontal towards the SSE and has a magnitude gradient of about 19 MPa/km. The minimum principal stress (S_3) is nearly horizontal in the WSW direction with a gradient of about 10 MPa/km. Therefore, the minimum and maximum principal stress components in the shaft pillar region are significantly anisotropic. This observation is consistent with the stresses reported by McGarr and Gay (1978), which also indicate a normal faulting stress regime in South Africa.

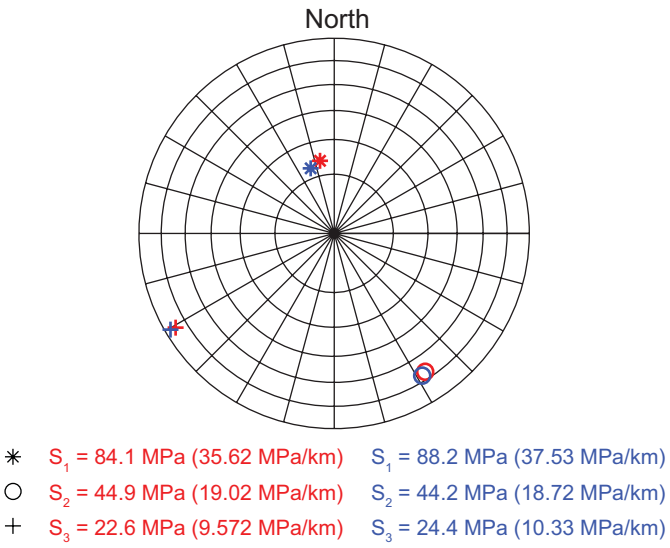

Figure 4-4: Orientations (lower hemisphere stereonet plot) and magnitudes of the principal stresses from two overcoring measurements in the 83 level shaft pillar (Cartwright and Walker, 2000).

4.4 METHODOLOGY FOR CONSTRAINING THE FAR-FIELD STRESSES

We followed an iterative forward modeling approach to characterize the far-field in situ stress state near TauTona mine. This workflow is outlined in Figure 4-5. First, we analyzed the borehole image log data for drilling induced borehole failures. Then we built a boundary element model (BEM) based on the geometry of the mine. In order to solve for the stress perturbation around the mine, we needed to input an initial far-field stress model which we constrained using the image log data. The stress magnitudes obtained by the overcoring data provided a starting point in our analysis and frictional faulting equilibrium theory was used to establish constraints on differential stress magnitudes (Moos and Zoback, 1990). We then used the stresses calculated by the BEM at the borehole locations to model the expected borehole failures and compare the borehole failures observed in the image logs to the modeled borehole failures. If the models were not consistent, we updated the estimates of the far-field stress model, reran the BEM, modeled the expected borehole failures based on the new stress calculations and then compared the new results with the borehole failure observations. If the modeled results were consistent with the observations, we varied the orientations and/or magnitudes of the far-field stress model to test the assumptions we used to constrain the model. The final result was to constrain the principal stress orientations and magnitudes that were consistent with all the observed failures and other data such that we could

determine the range of stress magnitudes and orientations that characterize a "best fit" model for the far-field stress state.

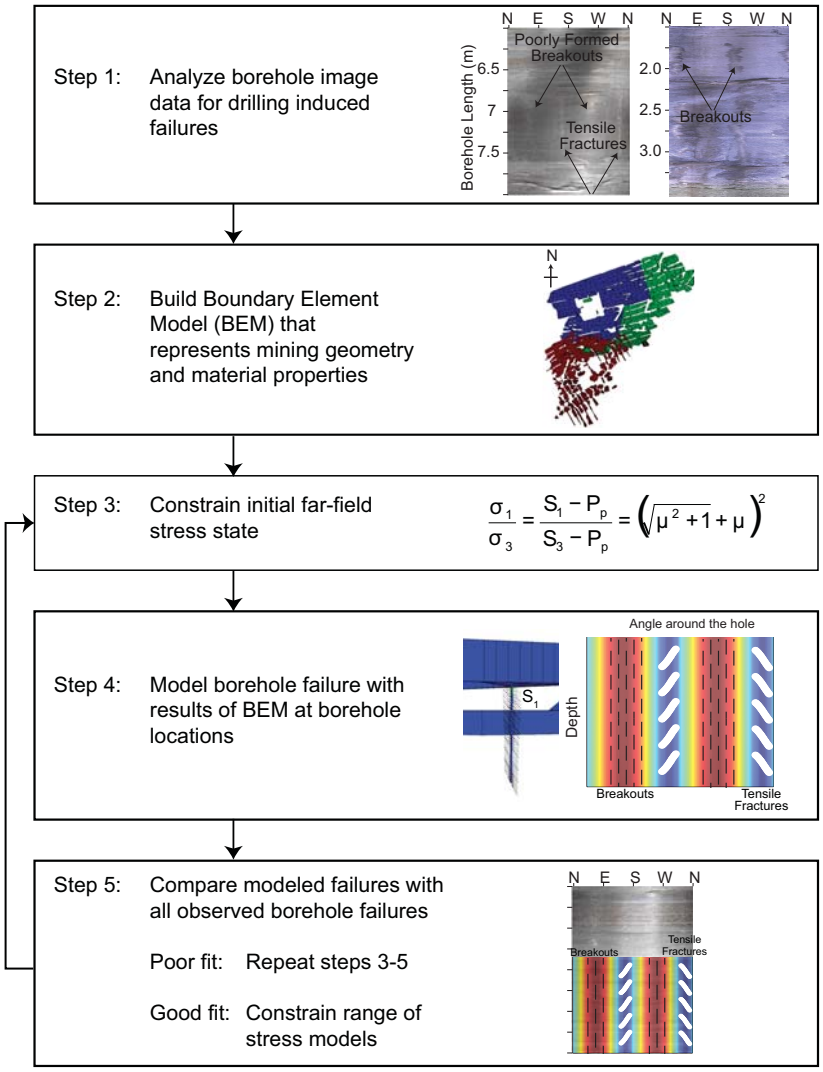

Figure 4-5: Iterative forward modeling workflow for constraining in situ far-field stresses

4.4.1 Borehole Data Analysis

The first step in constraining the far-field stresses was to analyze and document the drilling induced failures observed in the borehole image logs. The results of this analysis are summarized in Table 4-2. Site 10 was the only borehole where both drilling induced tensile fractures and breakouts are observed, although the breakouts were poorly formed. Site 13 and LIC118 both had breakouts present. Two of the boreholes at

the DAF site (5 and BIO) and the vertical borehole at site 7 (V) has drilling induced tensile fractures. In some of the boreholes, no drilling induced failures were observed (sites 2, 3, 9, and the deviated boreholes at site 7 (N and S)). The data collected in borehole 1 at the DAF site was of poor quality and could not be analyzed.

Table 4-2: Borehole observations of breakouts and drilling induced tensile fractures (DITF). For borehole trajectory, Dev is deviation from vertical and Azi is borehole azimuth.

Borehole	Tunnel Level	Borehole Trajectory	Length (m)	Drilling Induced Failure Observations	Image Quality
Site 2	118	Vertical	7.1	No failures observed	Good
Site 3	118	Vertical	8.5	No failures observed	Good
Site 7N	120	Dev: 47° Azi: 142°	10.5	No failures observed	Fair
Site 7V	120	Vertical	9.4	DITF: 6 m: Position 222°, Inclination 10° 8 m: Position 198°, Inclination 1° 9 m: Position 170°, Inclination 179°	Good
Site 7S	120	Dev: 43° Azi: 322°	9.6	Low quality data, no clear evidence for failures	Poor
Site 9	120	Vertical	11.4	No failures observed	Good
Site 10	120	Vertical	11.5	DITF: 6 m: Position 161°, Inclination 12° 9 m: Position 152°, Inclination 160° Breakouts: Poorly formed, position 62°,width 20°	Good
Site 13	120	Vertical	6.6	Breakouts: Well formed, some localized rotation	Good
DAF 2	118	Dev: 110° (20° up from horizontal) Azi: ~346°	39	Low quality data	Poor
DAF 5	118	Dev: 70° Azi: ~156°	19	DITF: 5 m: Position 90°, Inclination 15° 15 m: Position 105°, Inclination 176°	Good
DAF BIO	118	Dev: 110° (20° up from horizontal) Azi: ~353°	37.9	Low Quality Data DITF Evidence from 5-10 m: Position: 145-170°, Inclination 30°	Poor-Fair
LIC118	118	Dev: 75-85° Azi: ~90°	418 (logged)	Breakouts along extent of borehole, see Figure 4-6	Fair-Good

The LIC118 borehole was of particular importance because it was drilled into the far-field stress state away from the mining excavation. Breakouts were observed starting at a measured depth of about 35 meters and were observed throughout the

length of the borehole. The image quality of the log decreased towards the end of the hole making it difficult to observe the breakouts. The breakout observations for this borehole are shown in terms of position from the bottom of the hole, looking down the borehole in Figure 4-6. In LIC118, a large scale rotation in the breakout position was observed with increasing measured depth to about 150 m. From 150 m to the end of the borehole, the breakout positions and widths were relatively consistent. However, localized rotations in the breakout position as well as zones with no breakouts were observed in both the near- and far-field.

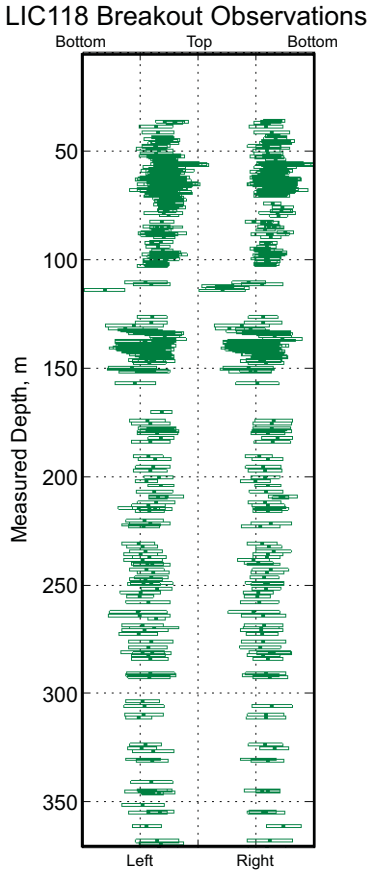

Figure 4-6: Breakout observations in the LIC118 borehole. These are shown as an "unwrapped" borehole wall, with angle around the hole plotted with measured depth. Breakout positions are plotted in a borehole reference frame that is relative to the bottom of the borehole looking down the borehole. The widths of the breakouts are also indicated.

4.4.2 Building Boundary Element Model

We used the boundary element modeling program Map3D, which was developed for mining applications, to numerically model the response of the rock to the mining

activity (Wiles, 2005a). Map3D is based on an Indirect Boundary Element Method. The program has been used to examine the stress perturbation from mining and the associated failure in several mine settings (e.g., Wiles, 2005b, 2006; Wiles et al., 2000). The modeling takes into account the geometry of the stope and access tunnels, the structural support provided by backfill materials, and the stress loading conditions applied by the far-field in situ stress state. The model simulates the rock mass response to these inputs while honoring the physical constraints of equilibrium, continuity, and elasticity. The model space begins as a homogeneous, elastic medium that approximates the in situ host rock; therefore far-field boundary conditions are accommodated. The mining excavation and access tunnel are then incorporated as elements and the response to these elements is calculated on specified grids.

The mine geometry shown in Figure 4-2 was modeled with two types of elements: fictitious forces and displacement discontinuities. The access tunnels, which are only modeled in the NELSAM study area, were modeled as fictitious force elements that have zero surface stresses. These act as void spaces. The mined out stope was modeled with displacement discontinuity elements. These elements were assigned material property values that reflect their backfill properties. As discussed above, the blue elements do not contain backfill and were therefore filled with a "null" material such that the stope could completely close under the normal stress acting on it. The red elements, representing Mponeng mine, had the properties of the Mponeng backfill. The green and yellow elements of TauTona had the properties of the TauTona backfill. The backfill elements were modeled with an elasto-plastic constitutive law.

In order to model the expected borehole failures for a particular far-field stress input, the stress state at each borehole needs to be analyzed based on the extent of the mining at the time of logging. Therefore the model of the mining stope was defined for three mining steps: June 2005, January 2006, and June 2006 (Fig. 4-2d). The BEM simulated the stress perturbations for each of the three mining steps and calculated the results on specified grids within the model. We specified grids at the borehole locations, on planes of interest near the boreholes, and along mapped fault planes.

4.4.3 Constraining initial far-field stress model

In order to solve for the mining-induced stress perturbations, we needed to input a far-field stress model as an initial condition. However, since the far-field stress state was what we were ultimately solving for we used an initial guess which was then updated based on the modeling results in an iterative manner. We used several types of information to constrain the initial far-field stress model. The iterative nature of our approach allowed us to update the stress model based on the comparison of the forward modeling of borehole failures from the BEM stress calculations and the observed borehole failures.

For an initial far-field stress model, we first assumed that the principal stresses were oriented vertically (S_v) and horizontally (S_{Hmax} and S_{hmin}). This is the simplest assumption and is often the observed case in stable cratonic crust (Zoback et al., 1989). In order to initially constrain the orientations of the horizontal stresses, we incorporated the overcoring stress measurements and the drilling induced failures observed in the vertical boreholes. The overcoring measurements indicated an S_{Hmax} of 153° (Cartwright and Walker, 2000). Assuming that the stress orientations observed in the vertical boreholes were indicative of a far-field stress state with vertical and horizontal principal stresses, the drilling induced tensile fractures observed at the end of the site 10 borehole suggest an S_{Hmax} azimuth of 158° and the breakouts observed at the bottom of the site 13 borehole suggest an S_{Hmax} direction of 155°. Based on these three consistent observations, we chose an initial S_{Hmax} orientation of 155° and an orthogonal S_{hmin} azimuth of 245°.

As we assumed that one of the principal stress directions is vertical, it was straightforward to constrain the magnitude of the vertical stress, S_v. The vertical stress is a result of the weight of the overburden material. The average density of the overburden at TauTona is estimated to be 2700 kg/m^3. Therefore we integrated that density over the depth and estimated that the average S_v gradient was 27 MPa/km.

Although the mines are dewatered, such that within the mine the pore pressure, P_p, is considered to be negligible, we assumed that in the far-field the P_p is hydrostatic at 10 MPa/km. Hydrostatic P_p has been observed in deep boreholes in low porosity (< 2%) and very-low permeability rocks (Coyle and Zoback, 1988; Huenges et al., 1997; Townend and Zoback, 2000). Given the low permeability of the rocks in TauTona (~10^{-}

^{20} m^2), the diffusion length was estimated to be on the order of 30 m over 10 years or 70 m over 50 years (Townend and Zoback, 2000). Therefore as observed in crystalline basement rocks in other intraplate regions, we assumed that the far-field virgin stress state has hydrostatic P_p despite the dewatering and general dryness observed in the mine (Townend and Zoback, 2000). The uncertainty in the P_p estimation results from an unknown water table depth and unknown salinity of the brine. High salinities increase the fluid density and lead to higher fluid pressure gradients.

Based on the breakout observations in the far-field of the LIC118 borehole, we used frictional faulting theory to constrain the initial magnitude of minimum principal stress, S_3 (Zoback et al., 2003). Previous studies have shown that local rotations in breakout positions and gaps in the breakouts are associated with slip on active faults (Barton and Zoback, 1994; Shamir and Zoback, 1992). Slip on faults in intraplate regions is indicative of a critically stressed crust that is in frictional faulting equilibrium. Therefore, the breakout rotations and gaps observed near the end of the LIC118 borehole suggest that the virgin stress state near the mine is critically stressed. Based on the critically stressed crust assumption, the ratio of the maximum effective stress (σ_1) to the minimum effective stress (σ_3) is controlled by the coefficient of friction (μ) of critically-oriented faults in the crust. This ratio is defined by frictional faulting theory:

$$\frac{S_1 - P_p}{S_3 - P_p} = \frac{\sigma_1}{\sigma_3} = \left(\sqrt{\mu^2 + 1} + \mu\right)^2 \qquad (4\text{-}1)$$

This equation solves for the upper limit for the σ_1/σ_3 ratio. For a μ=1, which is considered an upper limit for the general range of the coefficient of friction (0.6-1.0) observed in the brittle upper crust (Byerlee, 1978), this ratio equals about 5.8. Since the overcoring data and the breakout positions observed in the LIC118 borehole both indicated that the maximum compressive stress is vertical, we assumed that the state of stress is likely to be in a normal faulting regime, where $S_v \geq S_{Hmax} \geq S_{hmin}$. Therefore, solving for S_3 in Equation 4-1 predicts the lower bound for S_3. For example, with an S_v gradient of 27 MPa/km and a hydrostatic P_p gradient (10 MPa/km), the lower bound S_{hmin} (S_3) gradient is approximately 13 MPa/km.

To constrain the magnitude of the intermediate stress, S_{Hmax}, we again used the observations from the overcoring measurements and the drilling induced tensile fractures observed in the Site 10 borehole. In the overcoring measurements the

horizontal stress magnitudes differed by nearly a factor of two. Likewise, the presence of drilling induced tensile fractures suggests significant horizontal stress anisotropy. For those reasons, we assumed an initial S_{Hmax} gradient of 26 MPa/km, which is twice than that of S_{hmin} but less than S_v.

In summary, the initial model of the far-field stress state was a normal faulting regime with S_v, S_{Hmax}, S_{hmin}, and P_p gradients of 27, 26, 13, and 10 MPa/km respectively. The S_{Hmax} azimuth was 155° and the S_{hmin} azimuth was 245°. While these stress magnitudes and orientations provided a reasonable starting point for the far-field stress model, each of them was subject to updating once the results of the BEM were modeled and compared with the borehole observations.

4.4.4 Modeling Borehole Failure with BEM results

Drilling induced borehole failures result from the concentration of the effective stresses around the borehole walls during and after drilling. The position of the drilling induced failures depends on the relative orientations of the borehole and the principal stresses. Breakouts form when the stress concentration at the borehole wall exceeds the rock strength. In a vertical borehole with principal stresses oriented in the vertical and horizontal directions, breakouts form orthogonally to S_{Hmax} orientation in the direction of S_{hmin} (Zoback et al., 1985). Drilling induced tensile fractures form when the stress concentration at the wellbore wall is less than the tensile strength of the rock. In a vertical borehole with principal stresses oriented vertically and horizontally, drilling induced tensile fractures form in the direction of S_{Hmax}, opening in the S_{hmin} direction (Brudy and Zoback, 1999). However, when the borehole and/or the principal stress orientations are deviated from vertical, there is no simple relationship between the stress orientations and the position around the borehole at which the drilling induced failures will occur. In this study, we used a forward modeling tensor transformation technique to model failures when either or both the borehole and stress field are deviated from vertical (Peska and Zoback, 1995).

Once the BEM simulation was completed, we could determine the principal stress magnitudes and orientations along the boreholes. We used those stresses, the borehole orientations, and the rock properties to model the predicted borehole failures for the

mining geometry and far-field stress state. The results of the BEM and breakout modeling for the LIC118 borehole are shown in Figure 4-7 for the initial stress model.

4.4.5 Comparing Borehole Failure Observations with Modeling Results

The final step in this methodology was to compare the borehole failures modeled in the previous step with the observed borehole failures. The borehole observations are summarized in Table 4-2. The modeling results of the far-field breakouts in the LIC118 borehole are the most significant, because these were less dependent on the details of the boundary element model. If the model was not consistent with these observations, it was not considered within the range of acceptable models. In Figure 4-7b, we are comparing observed borehole failures in the LIC118 borehole with the borehole failures modeled based on the BEM results using the initial far-field stress model. Overall, the modeled breakouts were consistent with the observed breakouts. The modeling, which examines long wavelength stress variations, did not predict the absence of breakouts at the beginning of the borehole and could not resolve the localized rotations and gaps along the borehole. The localized rotations and gaps in the breakouts is a second order effect that we examine in the next chapter. At the end of the borehole the agreement between the modeled and observed breakouts is good.

In the other boreholes, the modeled results were mostly consistent with the observations. In sites 2, 7N, and 9, where no failures were observed, the model predicted no failures. However, at sites 3 and 7S, where no failures were observed, the model predicted the formation of drilling induced tensile fractures at the beginning of the boreholes and no failure at the ends. Breakouts and drilling induced tensile fractures modeled at site 10 matched the observations. But the breakouts modeled at both sites 10 and 13 had with larger widths than were observed. At site 7V, the modeled drilling induced tensile fractures were consistent with the observations. However, breakouts were modeled although not observed in the borehole. In both the DAF-BIO and DAF-5 boreholes, drilling induced tensile fractures are modeled and observed.

While the assumed initial stress state modeled the observed borehole failures with some accuracy, there was room for improvement. To improve the stress model and determine the range of stress models that are consistent with the observations, we repeated steps 3-5 of the methodology while testing the assumptions used to constrain

the initial model. Because of the nature of the borehole data, the limitations of the boundary element modeling, and the forward modeling approach, the solution to the far-field stress will be non-unique. The goal of this work was to constrain the range of stress models over which the modeled borehole failures are consistent with the observations. Because our initial model was consistent with a number of the observations, it provides a good starting point for the analysis.

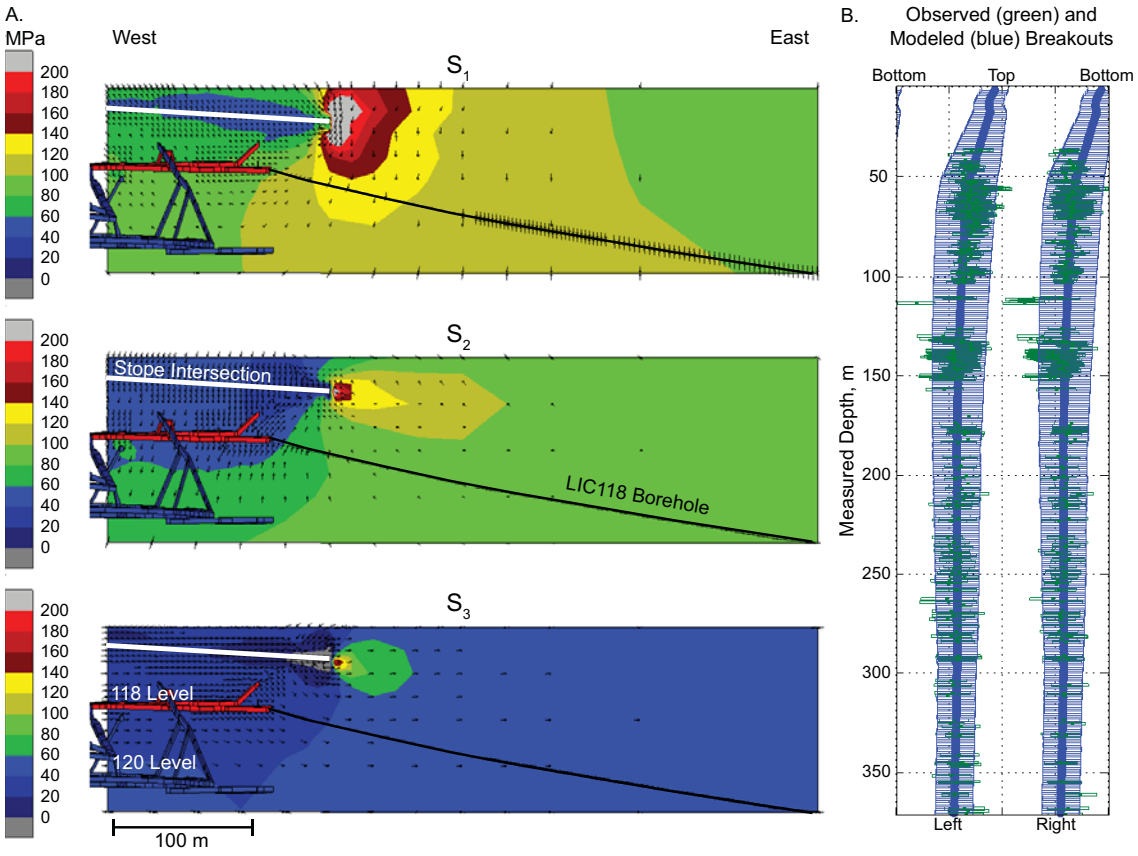

Figure 4-7: Boundary element modeling results based on the initial far-field stress model. A.) Principal stress orientations (arrows) and magnitudes (color scale) along a vertical plane extending from the LIC118 borehole trajectory. The intersection of the plane and the stope is shown by a white line. The 118 (red) and 120 (blue) tunnels are shown for reference. B.) Observed (green) and modeled (blue) breakouts along the LIC118 borehole. The data is plotted in a borehole reference frame looking down hole.

4.5 RESULTS

We tested the validity of four main assumptions that were used to constraint the initial far-field stress model. The results of these tests provided us with a well constrained stress model for the region around the TauTona gold mine. In Figure 4-8a,

we illustrate that for a specified S_{v*}, P_p, μ we can define the frictional failure limits for both S_{Hmax*} and S_{hmin*}. In this case, the (*) denotes that the stress orientations are nearly vertical (S_{v*}) or nearly horizontal (S_{Hmax*} and S_{hmin*}) (Moos and Zoback, 1990). The "constrain stress" polygon, which is defined by frictional faulting theory, increases in size with increasing values of μ (Fig. 4-8a). We used the "stress space" constrained by the polygons to limit the range in stress magnitudes that we tested for validity.

In Figure 4-8b, we zoom into the stress polygon region that represents the possible relationships between the principal stresses in a normal faulting (NF) regime. The stress magnitudes in the models that were tested in this analysis are labeled numerically 1 though 8. In Figure 4-8c, the stress orientations used in some of the models are labeled alphabetically A through D. We refer to the model parameters in terms of these labels. For example, the initial stress model which has the magnitudes summarized by the blue circle labeled (1) in Figure 4-8b and the orientations of the blue symbols labeled A in Figure 4-8c is called model 1A. First, we tested the assumption that the principal stresses are aligned vertically and horizontally, such that S_v, S_{Hmax}, and S_{hmin} are the principal stresses. Then we tested the assumption that S_{Hmax} is oriented 155° from north. The third assumption we tested was that the S_3 magnitude is limited by a coefficient of sliding friction in the crust of μ=1.0. Finally, we tested whether the state of stress is normal faulting and $S_2 >> S_3$.

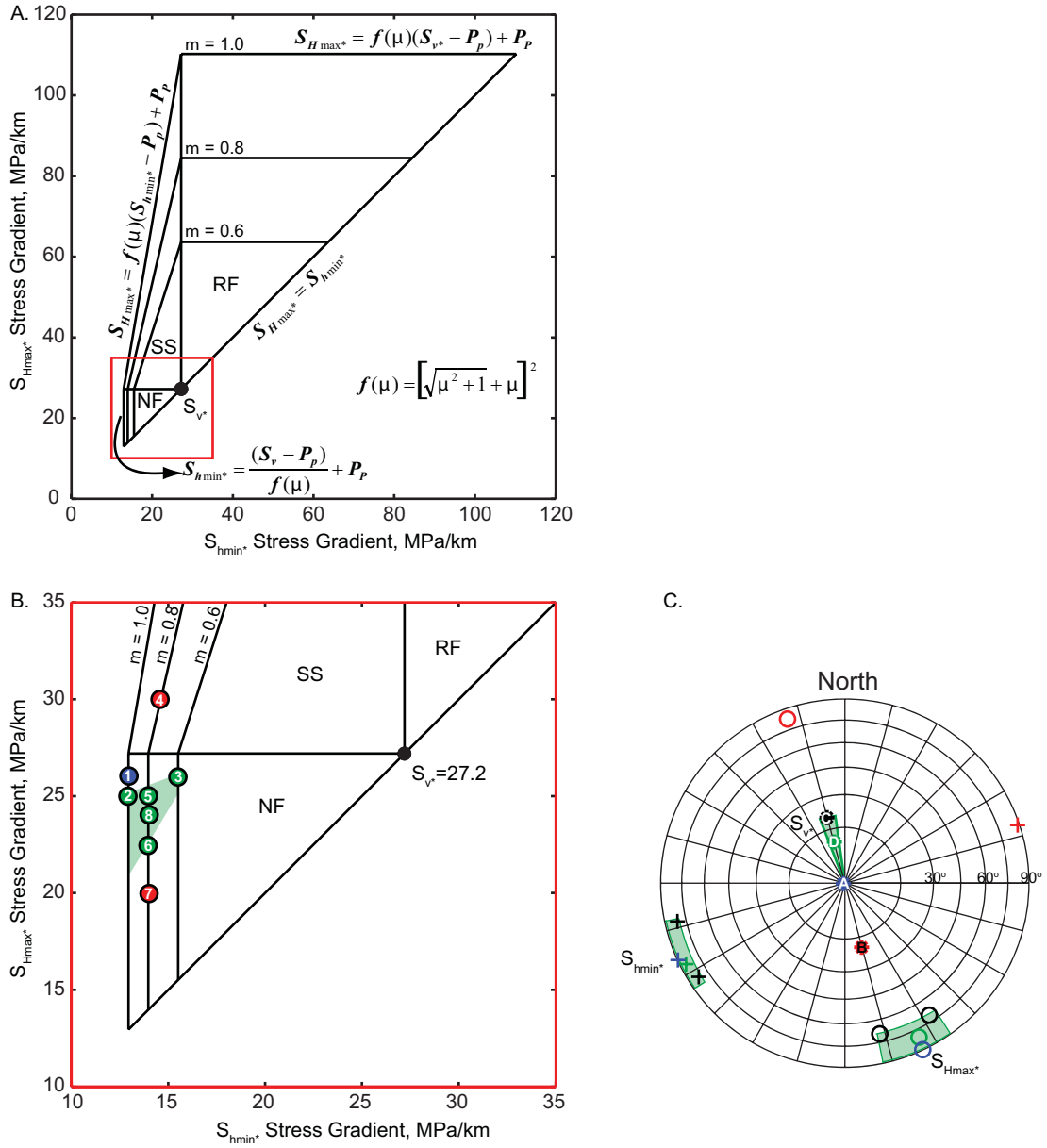

Figure 4-8: Constraining the far-field stress state. A.) The "constrain stress" polygons defined by frictional faulting theory for μ=0.6, 0.8, and 1. The stress regimes are labeled as NF=normal faulting, SS=strike-slip faulting, and RF=reverse faulting. B.) Enlarged view of red box in (A.). Stress magnitude parameters for models 1 through 8 that were tested are shown by circles and the acceptable range of stress magnitudes for the far-field stress model is shown by the green shaded area. The blue circle is the initial stress model, the green circles fall within the acceptable magnitude range for the far-field stress model, and the red circles fall outside the acceptable range of stress magnitudes. C.) Lower hemisphere plot of stress orientations. The green shaded areas are the acceptable range in orientations for the principal stresses. The blue model (A) is the initial stress model, the red model (B) is not acceptable, the black models (C) were used to test the range in horizontal stress orientations, and the green model (D) is a model with an average acceptable orientation.

The first assumption we made to constrain the initial stress model was that one of the principal stresses is vertical and the other two are horizontal. To test this assumption, we used new stress models with the stress magnitude parameters of 2 (Fig. 4-8b) and with the vertical stress deviated 10°, 15°, and 20° from vertical. First, the vertical stress was deviated with an azimuth of 345°. This is the azimuth of S_1 from the overcoring measurements and is normal to the bedding. We fixed the S_2 azimuth at 155°, but allowed the S_2 inclination angle and S_3 orientation to adjust as S_1 was deviated to maintain the orthogonal nature of the principal stresses. As the deviation angle increased, the breakout positions modeled in the far-field of the LIC118 borehole rotated clockwise around the borehole wall (looking down the borehole). The initial stress model predicted breakouts centered at 97° and 277° from the bottom of the hole. When the stress state was deviated 20° to the NNW, the breakouts were predicted at 108° and 288° from the bottom. The observed data are centered at approximately 105° and 285°. Therefore, the deviation of S_1 from vertical resulted in a slightly better fit to the observed breakouts. The deviation of S_1 towards the NNW had little to no effect on the failure modeled in the shorter boreholes in the near-field of the mining.

We then tested the sensitivity of the modeling to the azimuth of S_1 by rotating the azimuth by ± 5° from 345°. This slight rotation did not have a significant effect on the modeled failures. However, when we rotated the S_1 and S_2 azimuths by 180° (stress model 2B in Fig. 4-8) such that S_1 was deviated 20° from vertical with an azimuth of 165° and S_2 was deviated 20° from horizontal with an azimuth of 335°, the modeling was not consistent with the observations. The modeled breakouts were positioned at 85° and 265° from the bottom of the hole rather than at 105° and 285°. Therefore, this stress model was not acceptable. The conclusion from these tests was that S_1 is likely deviated 10-20° from vertical towards the NNW (Fig. 4-8c). Because S_1 is nearly vertical, we refer to it as S_{v*}. This principal stress orientation, which is nearly normal to the bedding is evidence of zero shear traction on the bedding planes.

Next we tested the azimuth of S_2. In the initial model, the azimuth of S_{Hmax} (S_2) was 155°. Above, we showed that S_{v*} is likely slightly deviated from vertical towards the NNW. This deviation results in S_2 being inclined 10-20° from horizontal with an azimuth of 155°. We refer to this slightly deviated S_2 as S_{Hmax*}. We tested the effect on the borehole failure modeling of rotating the azimuth of S_{Hmax*} clockwise to 168° and

counter-clockwise to 148°, which is shown by the black open circles in model 2C in Figure 4-8. Rotating S_{Hmax*} also resulted in the rotation of S_{hmin*} (S_{hmin} slight inclined from horizontal) as shown by the black (+)s in Figure 4-8c. In this modeling, S_{v*} was deviated 20° with an azimuth of 345º. The rotation of the S_{Hmax*} azimuth had very little effect on the breakouts modeled along the LIC118 borehole. However, this orientation had a significant effect on the orientations of the failures observed in the near-field vertical boreholes. These results are summarized in Table 4-3. The S_{Hmax*} azimuth of 148° resulted in a better fit to the observed borehole failure positions at sites 10 and 13, while an azimuth of 168° resulted in a more consistent model of the site 7V failures. The model with an S_{Hmax*} azimuth of 148° (also consistent with S_2 orientation in the overcoring measurements) fit most of the data better. However, an S_{Hmax*} azimuth of up to 168° is likely the limit of the range of acceptable azimuths (Fig. 4-8c).

Table 4-3: Observed and modeled positions of drilling induced tensile fractures (DITF) and breakouts (BO) in degrees from north for 3 vertical boreholes

Borehole	***Image Log Observations***		**SHmax* Azimuth: 168**		**SHmax* Azimuth: 155**		**SHmax* Azimuth: 148**	
	DITF	***BO***	**DIT F**	**BO**	**DIT F**	**BO**	**DIT F**	**BO**
Site 7V	*170*		162		156		150	
Site 10		*60*		80		72		66
Site 13	*152*	*62*	167	77	160	70	154	66

The third assumption that we tested is that the S_3 magnitude is being limited by a coefficient of sliding friction of μ=1.0 in a critically stressed crust. This value is the upper limit of the generally assumed range of μ (0.6 to 1.0) for the brittle crust (Byerlee, 1978; Townend and Zoback, 2000). It was chosen to constrain the S_{hmin} magnitude in the initial stress model because observations indicated that $S_{hmin} << S_{Hmax} \leq S_v$. Rock mechanics experiments carried out by Vincent Heesakkers (personal communication), indicate a μ=0.82 for the quartzite and a μ=0.58 for the cataclasite that is found in the fault trace of many pre-existing faults. Equation 4-1 shows that under frictional faulting theory the effective stress ratio between the maximum and minimum principal stresses is limited by a function of μ. A higher value for μ maximizes that ratio. As shown in Figure 4-8a, the "constrain stress" polygon, which is defined by frictional faulting theory, increases in size with increasing values of μ (Fig. 4-8a) (Moos and Zoback,

1990). For P_p=10 MPa/km, S_{v*} =27.2 MPa/km (slightly greater than S_v), and μ=1, S_{hmin*} can be as small as 12.9 MPa/km. While if μ=0.6, S_{hmin*} is limited to 15.5 MPa/km. To test this assumption, we compared the BEM results of stress models that are similar, except that their S_{hmin*} magnitudes were limited by μ=1 and 0.6, shown in green as models 2D and 3D in Figure 4-8. Their S_{Hmax*} gradients were also slightly different (25 and 26 MPa/km respectively) to ensure the maximum possible difference between S_{hmin*} and S_{Hmax*} in the μ=0.6 case.

Both stress models predicted breakouts that were consistent with the far-field observations in the LIC118 borehole. Model 2D, which was limited by μ=1.0, did a better job fitting the near-field observations. Because S_{Hmax*} was lower in 2D, the breakouts predicted at sites 10 and 13 and at the top of LIC118 had smaller widths and were more consistent with the observations. The tensile fractures at site 10 and 7V were also better represented with stress model 2D. There was not a significant difference between the results of the two models in the other boreholes. Model 3D was less consistent with the observations, but could not be ruled out. For this reason, we used it as a constraint on the range of acceptable stress magnitudes, which are shaded green in Figure 4-8b.

The last assumption we tested was the magnitude of S_{Hmax*}. The overriding assumption in our initial stress model was that the stress regime is normal faulting, as indicated in McGarr and Gay (1978) such that S_v (S_{v*}) ≥ S_{Hmax} (S_{Hmax*}) ≥ S_{hmin} (S_{hmin*}). We tested this assumption using model 4D, a strike-slip stress model in which S_{Hmax*}=30 MPa/km > S_{v*}=27.2 MPa/km > S_{hmin*}=14 MPa/km (Fig. 4-8). The results from this model clearly indicated that the far-field breakout observations could not be modeled with a strike-slip stress regime model (Fig. 4-9). Because breakouts form normal to the direction of maximum compression along the borehole, the near-horizontal S_1 of model 4D acting on a near-horizontal borehole resulted in breakouts that were modeled closer to the top and bottom of the borehole than to the sides of the borehole, as observed. The larger magnitude of S_1 also resulted in larger breakout widths (up to 180°) than the observed widths of about 60°.

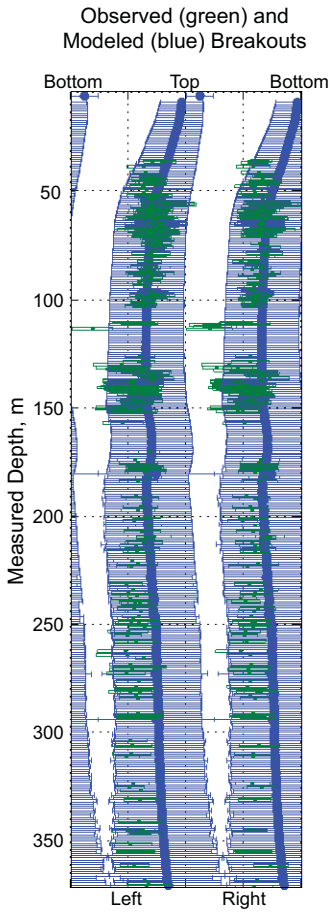

Figure 4-9: Observed (green) and modeled (blue) breakouts along the LIC118 borehole, based on a strike-slip stress model. This is shown as an "unwrapped" borehole wall, with the angle around the borehole plotted against measured depth. The data is plotted in a borehole reference frame looking down hole.

The third assumption not only constrained the magnitudes in the initial stress model to be in a normal faulting stress regime, but also assumed that the S_{Hmax} (S_2) gradient was much greater than the S_{hmin} gradient such that it was approaching the S_v gradient. To test this assumption, we compared the failure predictions from three stress models: 5D, 6D, and 7D, where the S_{Hmax*} gradients were 25 MPa/km, 22.5 MPa/km, and 20 MPa/km, respectively (Fig. 4-8).

All the models fit the far-field breakout observations in the LIC118 borehole. In general, the models with smaller S_{Hmax*} gradients better represented the absence of breakouts observed at the beginning of the LIC118, but were not as consistent with the other near-field observations. Stress model 5D predicted failures similarly to model 2D (Fig. 4-8). However, the drilling induced tensile fractures at sites 7V and 10 were only predicted at the beginning of the boreholes, not along the entire lengths. Stress model

6D predicted failures similarly to model 5D, except that it did a better job of predicting the absence of breakouts at the beginning of the LIC118 borehole and the smaller breakout widths at sites 10 and 13. Stress model 7D did the best job predicting the absence of failures at the top of the LIC118 borehole and width of breakouts at site 10, but did not predict any breakouts at site 13 or any tensile fractures at site 7V. Because of the lack of consistency with the near-field borehole observations, we excluded stress model 7D from the range of acceptable far-field stress states. We found that the S_{Hmax*} gradient should be at least 1.61 times the S_{hmin*} gradient, but less than S_{v*} by at least 1 MPa/km. As shown in the green shaded region of Figure 4-8b, we have limited the range of S_{Hmax*} gradients for an S_{hmin*} gradient of 14 MPa/km (μ=0.8) to be 22.5 to 25.5 MPa/km. The acceptable S_{Hmax*} range is smaller (25 to 26 MPa/km) for an S_{hmin*} of 15.5 MPa/km (μ=0.6) and larger (21 to 25) for an S_{hmin*} of 13 (μ=1.0).

Another interesting result of this work was that it provided a constraint on the rock strength of the quartzite. We found that changing the magnitudes of S_{hmin*} from 13 MPa/km to 15.5 MPa/km and S_{Hmax*} from 20 MPa/km to 26 MPa/km had little effect on the breakout observations in the far-field. This indicates that the breakout formation was primarily controlled by S_{v*}. The azimuth of S_{v*} affected the position of the breakouts modeled around the borehole wall, but did not greatly influence the widths of the breakouts. The magnitude of S_{v*} controlled the widths of the modeled breakouts and is very well constrain to be 27.0 ± 0.3 MPa/km. To model the breakouts, we used 200 MPa as the uniaxial compressive rock strength. This value was consistent with laboratory measurements (Heesakkers and Reches, personal communication) and resulted in a good fit to the breakout widths observed in the far field. However, if we modeled the breakouts with a rock strength of 190 or 210 MPa, the breakout widths begin to be over- or under-predicted, respectively. Therefore using the modeling results, we could constrain the rock strength as 200 ± 10 MPa.

4.6 DISCUSSION

4.6.1 Far-field Stress Model

We were able to constrain the range of far-field stress models that were consistent with the observed data in both the near- and far-field of the mining excavation. The far-

field stress model is summarized by the green shaded areas in Figure 4-8. The state of stress is a normal faulting regime ($S_{v*} > S_{Hmax*} > S_{hmin*}$) with principal stress orientations that are slightly deviated from vertical and horizontal and therefore denoted with a (*). The maximum principal stress, S_{v*}, is deviated 0-20º from vertical towards the NNW and has a magnitude gradient of 27.0 ± 0.3 MPa/km. The intermediate principal stress, S_{Hmax*}, is inclined 0-20º from horizontal with an azimuth of 145º to 168º and has a magnitude gradient of 21 to 26 MPa/km. The least principal stress, S_{hmin*}, is inclined 0-10º from horizontal with an azimuth of 235º to 258º and has a magnitude gradient of 13 to 15.5 MPa/km. Model 8D is a representative, best-fit far-field stress model (Fig. 4-8). The principal stress magnitude gradients are 27.2 MPa/km, 24 MPa/km, and 14 MPa/km; and principal stress orientations are an S_{v*} azimuth of 345º and plunge of 80º, an S_{Hmax*} azimuth of 157º and plunge of 10º, and a nearly horizontal S_{hmin*} with an azimuth of 247º.

4.6.2 Critically Stressed Crust

The virgin state of stress around TauTona is in a normal faulting regime and in frictional faulting equilibrium as predicted by Mohr-Coulomb failure criterion. This means that the crust is critically stressed, such that it is in a constant state of frictional failure along optimally oriented pre-existing faults. The rate of the brittle deformation in shield areas like the Kaapvaal Craton of South Africa is quite slow as compared to plate boundary regions (Zoback et al., 2002). This frictional failure results in stress drops that limit the stress magnitudes that can be sustained in the crust. A fault plane is optimally oriented when the shear stress (τ) resolved on the fault plane is equal to or greater than the product of the effective normal stress (S_n-P_p) resolved on the fault plane and the coefficient of sliding friction (μ) along the fault plane.

$$\tau \geq \mu(S_n - P_p) \qquad (4\text{-}2)$$

While the assumption of frictional failure equilibrium was used as an initial constraint on the far-field stress state, several different observations support this conclusion. One observation that supports the critically stressed crust is the localized breakout rotations observed along the LIC118 borehole (Figs. 4-6 and 4-7). Previous work has shown that localized rotations in the position of breakouts and interruptions in breakout formation is associated with stress perturbations from slip on nearby faults

(Barton and Zoback, 1994; Shamir and Zoback, 1992). In the next chapter, we examine the influence of critically stressed faults on the breakout formation in the LIC118 borehole.

In the far-field, faults that strike SSE and NNW and dip 50-85º are critically stressed. In a critically stressed crust, fractures in nearly optimal orientations with respect to the in situ stresses are near failure. Therefore, stress perturbations, such as those associated with the stope excavation, can "turn on" faults that were previously stable. This is important in the setting of deep underground mines, where large stress perturbations are occurring.

4.6.3 Recommendations for Implementation of Workflow

The workflow developed in this chapter is a new technique for constraining the far-field stresses near a deep underground mine. It combines elements of techniques that are used to constrain stresses in deep boreholes and oil and gas wells (Zoback et al., 2003) along with boundary element modeling. The implementation of this new technique in this study highlighted its strengths and indicated areas which could be improved upon with modifications in the data acquisition stage. However, it is important to recognize that there are a number of operational and financial constraints of working in an active mine.

The ability to incorporate the boundary element modeling of the mining induced stress perturbation was an essential step in this workflow. The BEM results were important for visualizing the extent of the stress perturbation associated with the excavation of the stope. The stress perturbation due to access tunnels could be seen to equilibrate about 2-3 tunnel radii away from the tunnel walls. However, the size of the stress perturbation signal from the stope, which is dipping, laterally extensive, and supported by pillars and backfill materials, could not be estimated with any simple rules of thumb. Using the BEM results, we confirmed that the state of stress at the end of the LIC118 borehole approached that of the far-field stress state, indicating that the failures observed at the end of the borehole were a result of the far-field stress state. Also, the BEM was necessary for modeling the borehole failure observations in the near-field perturbed stress state. Without the BEM, the data collected in the near-field boreholes could not be effectively interpreted.

In this study, we had data from one long, sub-horizontal borehole that reached into the far-field and eleven boreholes in the near-field of the mining excavation, six vertical and five deviated. Not all of these provided equally meaningful data. The long borehole was essential for providing data that could be analyzed with less dependence on the model of the mine used for the BEM. In the near-field, the vertical boreholes were easier to interpret and analyze than the deviated wells. This was primarily because the data acquisition in the vertical boreholes was easier and therefore the data quality was better, but it also results from the increasing complexity of the analysis when both the stress state and the borehole orientation are deviated from vertical. In this study, the deviated boreholes (particularly the ones at the DAF site) were very close to multiple access tunnels and the stope, which resulted in a much greater dependence on the accuracy of the geometry of the BEM for analyzing the modeling results.

In some of the boreholes, failures were not observed. While this information was important, if none of the near-field boreholes had failures it would have been difficult to constrain the stress model. Most of the boreholes that did not have failures were near enough to the floor of the stope and/or far enough away from the main stress concentration near the edge of the stope that they experience a significant stress relief. In the case of site 9, the region is under a double stope (where the gold stope region overlaps the green stope region (Fig 4-2)) and has significant stress relief. A BEM with an initial stress model can be used to model potential borehole locations so that they can be chosen in regions most likely to have borehole failures.

To optimize this methodology, we make several recommendations. First, one or more long boreholes that extend into the far-field stress state must be logged with a borehole camera to assess borehole failures in the virgin stress field. Increasing the number of boreholes that reach the far-field with different borehole trajectories will result in a more well-constrained stress model. In the near-field to the excavation, logging of vertical boreholes is preferable to deviated boreholes both for the ease of data acquisition and data analysis. These boreholes should be at least 10 m long (although longer boreholes are preferred) and located away from complicated tunnel intersections. If a borehole is located far from the edge of the stope, a greater distance is required between the borehole and the floor of the stope to ensure borehole failure occurrence. A borehole that is too close to the floor of the stope may show tensional

failure, but modeling those failures is difficult because of the strong dependence on the accuracy of the stope model, and therefore should be avoided. Our final recommendation is that the minimum principal stress magnitude should be measured in the boreholes that reach the far-field with minifrac tests, which are commonly used in oil and gas wells to measure S_3. Having a measurement of S_3 would decrease the number of assumptions that are need to constrain the stress state and would result in a more precisely constrained far-field stress state.

4.7 ACKNOWLEDGEMENTS

This chapter is based upon work supported by the National Science Foundation under Grant #0409605 (NELSAM). Any opinions, findings, and conclusions or recommendations expressed in this material are those of the author(s) and do not necessarily reflect the views of the National Science Foundation. Other sponsors of this work include Inter-Continental Drilling Program (ICDP), Anglogold, ISS International, and National Research Foundation (NRF). We would especially like to thank Ze'ev Reches and Vincent Heesakkers of the University of Oklahoma and Margaret Boettcher of the USGS in Menlo Park, CA, for their involvement in NELSAM. We also thank Shaun Murphy of Anglogold Ashanti and Gerrie van Asegen and Gerhard Hofmann of ISS International for their help with Map3D and acquiring the data for the modeling.

CHAPTER 5

EFFECTS OF MINING-INDUCED STRESS PERTURBATIONS ON PRE-EXISITNG FAULTS NEAR A DEEP SOUTH AFRICAN GOLD MINE[1]

5.1 ABSTRACT

Mining-induced earthquakes have been recorded in the deep underground mining region of Witwatersrand Basin in South Africa for over a century. The TauTona mine experiences an appreciable number of mining-induced earthquakes and is the site of the Natural Earthquake Laboratory in South African Mines (NELSAM) project. In the previous chapter, we constrained the virgin stress state around the TauTona mine and determined that it is a normal fault stress regime in frictional failure equilibrium. In this chapter, we investigate the likelihood of faulting to occur both on pre-existing fault planes that are optimally oriented to the virgin stress state and on faults affected by the mining-perturbed stress field, the latter of which is calculated with boundary element modeling. A fault is critically stressed when the shear stress resolved on the fault plane is equal to or greater than the product of the coefficient of sliding friction and the effective normal stress. With respect to the far-field stress state, the critically stressed faults are normal faults generally striking SSE and NNW. The mining-induced stress perturbations affect faults relatively closer to the mining excavation. We analyzed active faults observed in borehole image log data and mapped in the TauTona access tunnels. We also investigated the likelihood of fault reactivation on the Pretorius Fault Zone (PFZ), an ancient (Pre-Cambrian) fault system which intersects the NELSAM study area. As a result of this modeling, we were able to further constrain the far-field stress state. More importantly, by using this far-field stress state in a detailed boundary element model we were able to make several observations that lead to a better understanding of the mining-induced seismicity that is occurring around the NELSAM study area in TauTona. Finally, we make several recommendations that could potential increase safety in deep South African mines as development continues.

[1] This work is in preparation for submission to the Bulletin of the Seismological Society of America.

5.2 INTRODUCTION

Induced seismicity near deep underground mines has serious implications for mine safety. While many seismic events induced by mining are small with moment magnitudes (M_w) of less than 2, they are occasionally M_w 4 and greater. However, even the smaller events at depth inside a mine are very dangerous and can result in damage to the excavation, injuries or fatalities. Seismicity is induced in mining regions by the stress perturbations associated with the mining excavation. Increased understanding of which faults are likely to slip as the stress state is perturbed can lead to more informed decision making during the planning and execution of mine development and thus increased safety in the mines.

In the previous chapter, we constrained the far-field stress state around the TauTona gold mine of the Witwatersrand Basin of South Africa, one of the deepest underground mines in the world. We found that the stresses are in a normal faulting frictional failure equilibrium stress state. In this virgin stress field, the maximum principal stress is the weight of the overburden material and there is significant anisotropy in the horizontal stress magnitudes. In fact, we found that the state of stress is in frictional failure equilibrium, such that slip on well oriented faults is likely to occur at a very low rate.

For the past century, earthquakes have been reported in the Witwatersrand Basin. More than 60 years ago, these events were directly associated with the deep mining in the region (Gane et al., 1952). This deep underground mining region is located in the Archean Kaapvaal craton and is therefore considered to be tectonically stable. This does not mean that the stresses in the crust are relaxed, only that the rates of deformation are much lower than those observed near plate boundaries or more active intraplate regions. Many cratonic regions around the world have stress states that are in frictional failure equilibrium such that they are in a constant state of slow frictional failure along optimally oriented pre-existing faults (Townend and Zoback, 2000; Zoback et al., 2002). As summarized by Townend and Zoback (2000), evidence for failure equilibrium comes from several sources. These include (1) in situ stress measurements in deep boreholes (e.g., Brudy et al., 1997; Zoback and Healy, 1992), (2) earthquakes triggered by other earthquakes (e.g., Stein, 1999), and induced seismicity in intraplate regions (e.g., Raleigh et al., 1972; Zoback and Harjes, 1997). In the previous chapter, we used

borehole measurements to constrain the critically stressed far-field stress state. In this chapter, we are primarily interested in understanding the induced seismicity that has been observed in vicinity of the TauTona gold mine and its relationship to both the virgin and mining-perturbed stress fields.

In critically stressed intraplate regions, seismicity can be induced by even small perturbations in the stress field. Induced seismicity in intraplate regions is often thought of in terms of changes in fluid pressures due to fluid injection or reservoir impoundment (e.g., Raleigh et al., 1972) which result in increases in the fluid pressures acting on pre-existing faults. As discussed in previous chapters, a fault plane is optimally oriented for slip in the in situ stress field when the shear stress (τ) resolved on the fault plane is equal to or greater than the product of the effective normal stress (S_n-P_p) resolved on the fault plane and the coefficient of sliding friction (μ) along the fault plane.

$$\tau \geq \mu(S_n - P_p) \tag{5-1}$$

Therefore, by increasing the in situ pore pressure, P_p, with fluid injection or reservoir impoundment the effective normal stress is decreased and shear stress can more easily overcome $\mu(S_n$-$P_p)$ resulting in slip on faults.

However, in deep mining operations, P_p is rarely increased. In fact, the P_p is often decreased during the process of dewatering in which the pore fluids are pumped out. In some cases, this decrease in P_p can stabilize critically stressed faults by increasing the effective normal stress acting on them. In other cases, the decrease in P_p can induce faulting due to poroelastic stress changes. This induced faulting is typically controlled by two different mechanisms. With the first mechanism, faulting is induced in the crust outside the zone with reduced P_p by the interaction of the virgin stress state with the stresses caused by the P_p change and associated compaction (Segall, 1985, 1989). This is most often observed during the production of fluids in poorly consolidated sedimentary rocks that are susceptible to high rates of compaction and is therefore not applicable to the strong quartzite in the vicinity of TauTona.

With the second mechanism, the poroelastic coupling within the zone of decreased P_p results in a decrease in the total horizontal stress magnitude, S_h, which can induced normal faulting (Zoback and Zinke, 2002). Assuming no lateral strain, the relationship between the change in P_p (ΔP_p) and change in S_h (ΔS_h) can be determined by

$$\Delta S_h = \alpha \Delta P p \left(\frac{1-2\nu}{1-\nu} \right) \tag{5-2}$$

where ν is Poisson's ratio and α is Biot's coefficient ($\alpha = 1 - K_b/K_g$, where K_b is the bulk modulus of the dry rock and K_g is the bulk modulus of the rock forming mineral) (Brown et al., 1994). In the vicinity of TauTona, where the quartzite has an extremely small Biot's coefficient ($\alpha \approx 0$), the effect of even a complete drop in P_p on the horizontal stress magnitudes is not significant. Since the change in P_p from dewatering the mine should not have significantly affected the horizontal stress magnitudes near TauTona, this mechanism was unlikely to have had an effect on the induced seismicity observed near the mine.

In a deep underground mine, the large scale excavation of the stope results in very large perturbations in both principal stress magnitudes and orientations. In this chapter, we examine the critically stressed crust in the virgin stress state and investigate how the stress perturbations from the mining excavation affect the likelihood of slip on pre-existing faults in the crust. We define the likelihood of slip on pre-existing faults in terms of the Coulomb Failure Function (CFF), which describes the relationship between the shear and normal stresses resolved on a fault plane.

$$CFF = \tau - \mu\sigma_n \tag{5-3}$$

If CFF is zero or greater, then $\tau \geq \mu\sigma_n$ and the fault is critically stressed. The CFF of a fault depends on μ of the fault plane as well as its orientation with respect to the in situ stress conditions. Over small time scales, the fault μ and orientation are unlikely to change significantly. However, in the vicinity of a deep gold mine, the stress conditions can be greatly altered. We used boundary element modeling (BEM) to calculate the perturbation of the virgin stress state due to the mine excavation. With a model of the mining-perturbed stress field, we could determine how the CFF on observed faults is affected by the mining and better understand the mining-induced seismicity in the area.

5.3 STUDY LOCATION AND DATA

5.3.1 TauTona Gold Mine

The TauTona gold mine is one of the deepest underground mines in the world, with active mining deeper than 3.6 km. This mine is one of the locations being studied as

part of the Natural Earthquake Laboratory in South African Mines (NELSAM) project. The NELSAM project involvles mapping faults, collecting borehole image log and core data, and installing instruments such as seismometers, accelerometers, and strain meters in one of the deepest parts of the mine (Reches et al., 2006). The goal of this work is to observe seismicity in the very near-field as to better understand the mechanics and physics controlling earthquakes.

The layout of the mine is shown in Figure 4-2. As noted in the previous chapter, the mining occurs along 1-1.5 m thick beds of gold-bearing conglomerates, referred to as "reefs." The Carbon Leader Reef in the TauTona mine and the shallower Vertersdorp Contact Reef in the Mponeng mine dip about 20° to the SSE. The area of the reefs that have been excavated are referred to as the stope and the areas that are left behind for support are called pillars. The NELSAM study area is in southeastern portion of the mine and is located in the 118 and 120 mining levels, at approximately 3600 m depth. This is an area of active mining, which is primarily occurring on the southeastern side of the Pretorius Fault Zone (PFZ) and shown in yellow on Figure 4-2. The PFZ, which is a nearly vertical, normal-to-strike slip fault zone striking approximately 230°, cuts across the NELSAM study area (Fig 4-2). Although the PFZ is an ancient fault zone that was originally active more than 2 billion years ago, it is the largest fault zone in mine and is therefore the possibility of inducing slip on the fault is of some concern, particularly as mining continues on both sides of the fault.

5.3.2 Induced Seismicity Recorded in the NELSAM Study Area

An appreciable amount of seismicity has been recorded throughout the mine and near the NELSAM study area. The largest event experienced in the mine since 2005 was a M_w 3.2 and the largest event near the NELSAM project area was a M_w 2.5. Figure 5-1 shows the locations of 1625 earthquakes recorded from January 2005 through October 15, 2005 (Margaret Boettcher, personal communication). The spheres representing the events are scaled and color coded by M_w, which ranges from -1.6 to 2.3. Seven of these events have $M_w \geq 2.0$. The seismicity is shown in plan view and in a perspective view that is parallel to the PFZ. Most of the earthquakes are occurring above and below the stope, with few events occurring in the region in front of the stope edge. The greatest numbers of events are located below the stope. The daily peak in

seismic activity correlates with the blasting schedule and occurs between 18:00 and 19:00 (Margaret Boettcher, personal communication). During this time, the trigger level of the instruments is increased such that the smaller events that occur during this time are not recorded.

All the earthquakes shown in Figure5-1 were recorded by the seismic array deployed by the mining company. This array has ~25 1 and 3 component geophones that are spaced throughout the mine. These instruments range in frequency between 200 and 3000 Hz. Currently, the polarities of these instruments are unknown such that the moment tensors could not be determined. The locations of the earthquakes from this data have up to 50 m of uncertainty. As part of the NELSAM project, a new and more closely spaced array of seismometers is currently being deployed in the study area. As of August 2007, the NELSAM array has 7 working sites with a total of 14, 3 component instruments recording data up to 12 kHz. Two more sites (4 instruments) may be installed in the future. These sites contain a mix of a strong motion and a weak motion accelerometer or a weak motion accelerometer and a geophone. This array will provide better coverage in the NELSAM study area so that more of the smaller events can be recorded and the larger events can be more accurately located.

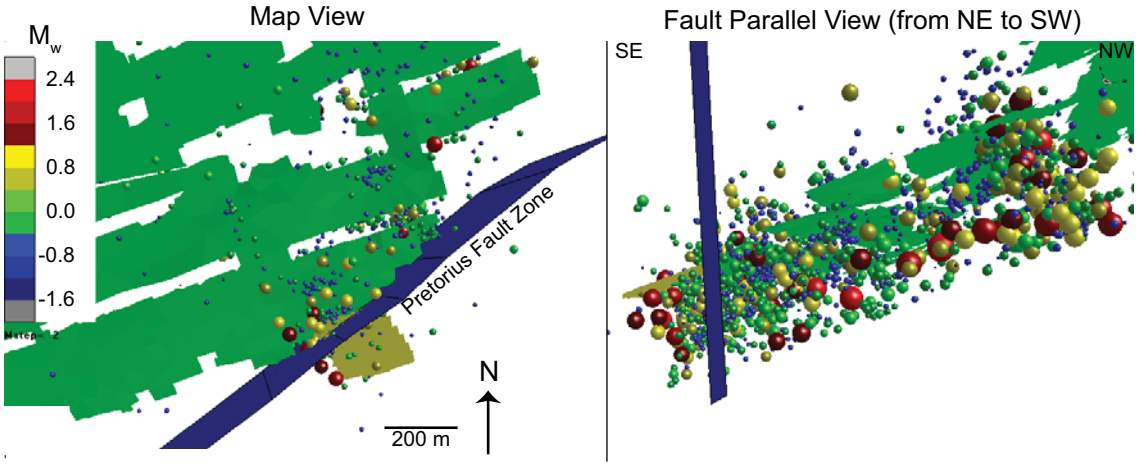

Figure 5-1: Seismicity in the NELSAM study area of TauTona recorded from January through October of 2005. The mining stope on the downthrown (NW) side of the PFZ (blue) is shown in green and the stope on the upthrown (SE) side of the PFZ is shown in yellow. The spheres represent earthquake hypocenters and are scaled and color coded by moment magnitude.

5.3.3 Borehole Image Log Data and Breakout Analysis Methodology

Image log data was collected in several boreholes with a borehole camera tool (Fig. 4-3; Table 4-2). In the image logs, we observed drilling induced failures such as tensile fractures and borehole breakouts as well as natural fractures that intersect the borehole. In this work, we focused on the 418 m of image log data collected in a sub-horizontal borehole referred to as LIC118, which extends towards the east into the far-field from the southeastern portion of the 118 level of the mine (Fig. 4-3). The breakouts observed in this borehole were used in the previous chapter to constrain the far-field stress state. In that work, we noted the localized rotations in the breakout positions and gaps in the occurrence of breakouts as evidence for the frictional faulting equilibrium stress state. In this chapter, we use forward modeling to show that these breakout rotations and gaps are not only consistent with the constrained stress state, but provide further support for the stress state.

We picked the positions and widths of the breakouts and the orientations of the natural fractures observed in LIC118 from the borehole image log (Fig. 4- 6). To analyze the breakout rotations and gaps with respect to the observed natural fractures, we followed the methodology proposed by Barton and Zoback (1994). When an observed natural fracture corresponded with a local breakout rotation or gap in the occurrence of breakouts, we determined whether the fracture orientation is critically stressed in either the virgin or mining-perturbed stress state. If the fracture was determined to be critically stressed in either the virgin or mining-perturbed stress state, we predicted the breakout response expected given the orientation of the borehole relative to the stress field perturbed by both the mining and slip on the fault. To do this, we needed to determine the slip vector on the fault. The slip direction is the direction of maximum shear stress (τ) resolved on the fault plane, which is a function of the fault orientation and the mining induced stress state at the fault location as described by Keilis-Borok (1959) for a fault patch of dimensions 2L X 2L in equation 5-4.

$$\boldsymbol{d} = \Delta\boldsymbol{\tau}_s \frac{16}{7\boldsymbol{\pi G}} \frac{2\boldsymbol{L}}{\sqrt{\boldsymbol{\pi}}} \tag{5-4}$$

The magnitude of the slip vector, d, depends on the fault patch size, the shear modulus of the faulted material, G, and the stress drop, $\Delta\tau_s$. Shamir and Zoback (1992) determined that the size of the slip patch is on the order of the size of the anomaly of the

breakout formation. The magnitude of $\Delta\tau_s$ is a percentage of the available shear stress in the slip direction and controls the magnitude of the anomaly. A stress drop of 100% results in a stress drop equal to the maximum shear stress resolved on the fault plane. Once the slip vector was determined, the breakout formation could be modeled based on the combined effects of the fault-perturbed stress field, mining-perturbed stress field, borehole trajectory, drilling conditions, and rock properties including rock strength and Young's modulus following the technique described by Peska and Zoback (1995). We then compared the predicted response with the observed breakouts for consistency. Consistency between the observed and modeled breakouts supported both the conclusion of frictional failure equilibrium and the state of stress that was constrained in the previous chapter.

5.3.4 Boundary Element Modeling of Mining-Induced Stress Perturbation

To investigate the likelihood of observed faults to slip and to model the breakout response to critically stressed faults, we needed to quantify the stress state at various locations around the mining excavation. In the previous chapter, we introduced the boundary element method for modeling the stress response to the mining excavation using the Map3D program (Wiles, 2005a). We used boundary element modeling (BEM) to determine the mining-perturbed stress state in regions of interest around the NELSAM study area. In particular, we were interested in quantifying the stress field along the LIC118 borehole, around the stope edge, and along mapped faults.

In the previous chapter, we modeled the stress response to the mining at 3 mining steps. In this work, we examined it at 6 mining steps (Fig. 5-2). In Figure 5-2, the stope is shown with colors that represent the mining steps, the white space is the intact rock and the PFZ is shown in black. Mining step one (green) is the extent of the excavation prior to any mining of the stope on the upthrown, southeastern side of the PFZ. Mining step two (magenta) represents the extent of mining in December 2004. Mining steps three through five are the same as mining steps one through three in the previous chapter and correspond to June 2005 (orange), January 2006 (blue), and June 2006 (red). The final mining step (purple) represents the mine development that is planned through 2012.

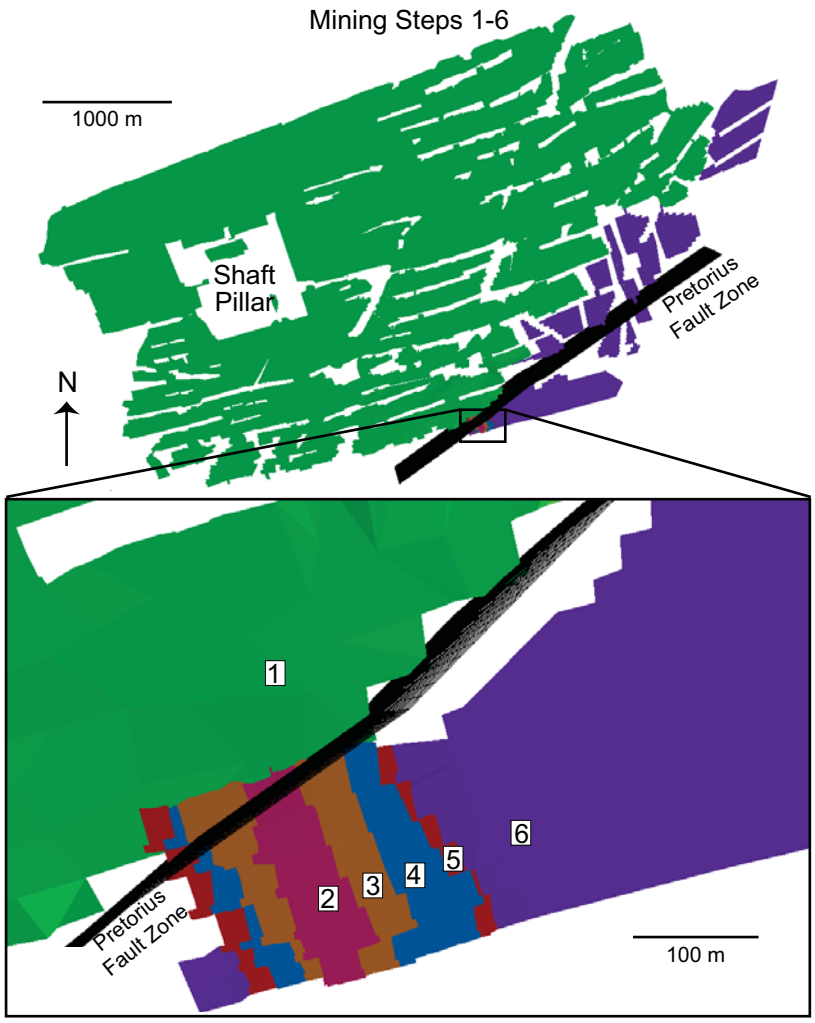

Figure 5-2: Extent of mining at the six mining steps modeled in the analysis. Mining step five represents the extent of the mining at the end of the borehole data collection and mining step six is the mining planned until 2012. The Pretorius fault zone is shown in black.

We defined the initial stress condition for the BEM as a representative stress state from the range of acceptable far-field stresses that was determined in the previous chapter. This is discussed in detail in the next section. During the modeling, we calculated the stress response for the six mining steps along several grids. We modeled the stresses along grids that are parallel and perpendicular to the edge of the mining stope to investigate the general trends of the mining-induced stress perturbations. We also modeled the stresses along the LIC118 borehole. The analysis of the breakouts observed in the LIC118 image log was carried out with the results of mining step three, which corresponds to the time when the borehole was drilled and logged with the borehole camera.

Finally, we modeled the stresses along four observed faults. Figure 5-3 shows the relative orientation of these faults along with the far-field stress model determined in the previous chapter and summarized in the next section. As will be quantitatively shown in the next section, the faults are not well-oriented for slip in the far-field stress state since the S_2 orientation and magnitude results in high normal stresses acting on them. Three faults (F1, F2, and F3) with evidence of recent slip were observed to intersect the tunnels that connect the 120 and 118 level tunnels in the NELSAM study area. The F1 has a strike of 55° and dips 81° to the southeast. The F1 fault orientation is similar to that of the general PFZ, but it dips to the southeast rather than the northwest. It is likely a segment of the fault zone. The F2 is bedding parallel with a strike of 85° and a dip of 20°. The third fault, F3, has a strike direction of 63° and dips 43°. The analysis of these fault planes focused on the change in the stress field between mining steps one and two. Another fault plane of interest was the general trend of the PFZ, which extends for several kilometers and was modeled by a series of grids with slightly variable orientations as shown in black in Figure 5-2. The analysis along this fault focused on the changes in the stress field at all the mining steps, with a particular focus on the planned mining development modeled in mining step six.

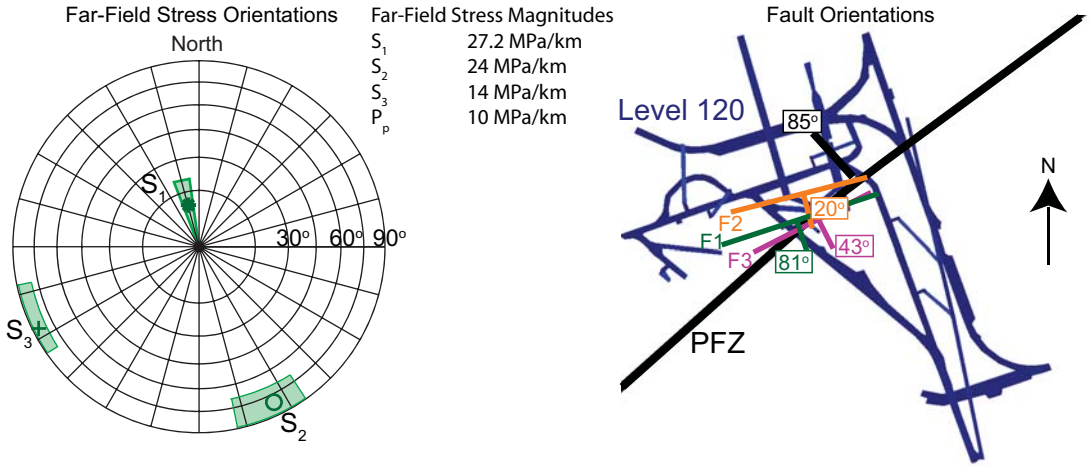

Figure 5-3: Summary of far-field stress state and fault locations. The range in stress orientations are shown by the green shaded regions in the stereonet plot, with an average orientation shown by the symbols. Average stress magnitudes are listed. F1 (green), F2 (orange), F3 (magenta), and PFZ (black) orientations are shown relative to each other. The numbers indicate the dip angle for each fault. The 120 level tunnels are shown for reference.

5.4 CRITICALLY STRESSED FAULTS IN THE VIRGIN STRESS STATE

5.4.1 Far-field Stress Model

In the previous chapter, we described the methodology that was used to determine the virgin stress state near TauTona gold mine. We found that the state of stress is a normal faulting regime ($S_{v*} > S_{Hmax*} > S_{hmin*}$) with principal stresses that are slightly deviated from vertical (S_{v*}) and horizontal (S_{Hmax*} and S_{hmin*}) and therefore denoted with a (*). As shown in Figure 5-3, the maximum principal stress, S_{v*}, is deviated 0-20º from vertical towards the NNW and has a magnitude gradient of 27.0 ± 0.3 MPa/km. The intermediate principal stress, S_{Hmax*}, is inclined 0-20º from horizontal with an azimuth of 145º to 168º and has a magnitude gradient of 21 to 26 MPa/km (Fig 4-8). The least principal stress, S_{hmin*}, is inclined 0-10º from horizontal with an azimuth of 235º to 258º and has a magnitude gradient of 13 to 15.5 MPa/km. For the analysis presented in this chapter, we used a far-field stress model that is representative of this range of acceptable stress models. In this model, the principal stress magnitude gradients are 27.2 MPa/km, 24 MPa/km, and 14 MPa/km; and principal stress orientations are an S_{v*} azimuth of 345º and plunge of 80º, an S_{Hmax*} azimuth of 157º and plunge of 10º, and a nearly horizontal S_{hmin*} with an azimuth of 247º. We assumed that the P_p is hydrostatic prior to mining, with a gradient of 10 MPa/km. The range of acceptable stress states also suggests that the coefficient of sliding friction (μ) on pre-existing faults ranges from 0.6 to 1. Rock mechanics experiments carried out by Vincent Heesakkers (personal communication), indicate a μ=0.82 for the quartzite and a μ=0.58 for the cataclasite that is found in the fault trace of many pre-existing faults. In this analysis, we assumed that μ=0.6 on the faults.

5.4.2 Critically Stressed Fault Orientations

In the virgin stress field, a normal faulting stress regime controls which pre-existing faults are critically stressed. The critically stressed faults in the far-field from the mining excavation generally strike SSE and NNW and have a steep dip angle (Fig. 5-4). The faults that are most optimally oriented for slip in the representative far-field stress model used in this analysis strike 153° and 343° with dip angles of 62° and 60°, respectively (red outlined Os in Fig. 5-3). The PFZ, which intersects the NELSAM

study area, is nearly vertical and strikes approximately 230° (black outlined O in Fig. 5-4). The PFZ is not critically stressed in the virgin stress field because it is nearly orthogonal to the S_{Hmax*} orientation such that a high normal stress is resolved on the fault plane (Figs. 5-3 and 5-4). Faults F1, F2, and F3 are also stable in the far-field stress state.

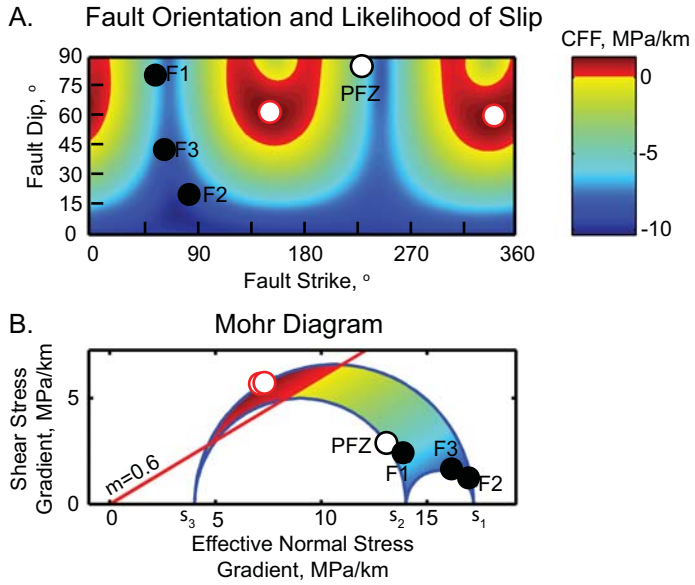

Figure 5-4: Critically stressed fault orientations in the virgin stress state. A.) Fault orientations defined by strike and dip and color coded by CFF. The red areas have positive CFF. The black outlined white O indicates the orientation of the PFZ, the black Os are the F1, F2, and F3 faults that are analyzed below, and the red outlined Os indicate the most optimally oriented faults in the virgin stress state. B.) Mohr diagram illustrating the relationship between the shear and effective normal stress gradients and the resulting CFF. The CFF is calculated assuming a μ=0.6.

5.4.3 Breakout Analysis and Critically Stressed Faults

Key evidence that supported the conclusion that the crust near TauTona is critically stressed was the observations of gaps in the breakout formation and localized rotations in the breakout positions near the end of the LIC118 borehole (Fig. 4-6). Previous studies have shown that these breakout characteristics result from localized stress perturbations that are associated with recently active faults (Barton and Zoback, 1994; Shamir and Zoback, 1992). As described above, we can forward model the breakout signature based on the in situ stress state, the borehole trajectory, the drilling conditions, the rock properties and the localized stress perturbation from slip on an optimally oriented fault (Barton and Zoback, 1994).

Because the borehole image log data are oriented, they could be used to determine the orientations of faults that intersect the borehole. Several natural fractures of varying orientations were observed to intersect LIC118 down to 190 m (measured depth). Unfortunately, the image log data in the deeper part of the LIC118 borehole that extends into the far-field stress state was of poor quality and any natural fractures that present could not be observed. Nevertheless, we did observe faults in the shallower section of the borehole that have orientations that are favorable for slip in the virgin stress field, which indicates that a population of critically stressed faults is present in the crust around TauTona.

Following the methodology of Barton and Zoback (1994), we found that recent slip on an optimally oriented fault intersecting the LIC118 borehole would result in a gap in the breakout record that is consistent with the observations in the image log. The stress drop associated with the fault slip reduced the stress concentration at the borehole wall to less than the compressive strength of the rock such that the breakouts no longer formed in the vicinity of the recently active fault. We illustrate this by modeling the breakout response in the LIC118 borehole to slip on a fault with the optimal orientation for the virgin stress field in Figure 5-5. In this example, we assumed 100% stress drop on a fault that is 11 m by 11 m (centered on the LIC118 borehole at a measured depth of 335 m), strikes 343°, and dips 60°. The 7.6 mm of slip modeled on this fault had a rake of 104.5° and resulted in a $\Delta\tau_s$ of 20.58 MPa. The size of the modeled gap in the breakout occurrence depends on the size of the patch that is assumed to slip, the stress drop that is assumed to occur and the strength of the rock (which is well constrained to be ~200 MPa). The gap was predicted reasonably well with the same size fault patch and a stress drop of 50% (i.e., 3.8 mm of slip with a $\Delta\tau_s$ of 10.29 MPa) or with a patch that was 6 m X 6 m with 100% stress drop (i.e., 4.2 mm of slip with a $\Delta\tau_s$ of 20.58 MPa).

This model suggests that a near complete stress drop is necessary to match the observed gaps in breakout occurrence. This agrees with the results of the modeling of Barton and Zoback (1994). In their paper, they noted that this large stress drop seems inconsistent with the small average stress drops (0.1 to 10 MPa) typically determined from the analysis of earthquake data (e.g., Brune, 1970; Hanks, 1977; McGarr and Gay, 1978). However, these results are consistent with analyses of peak acceleration that

predicted large stress drops over localized areas of fault patches (Hanks and Johnson, 1976; McGarr, 1981). Therefore, we concluded that the breakout observations in the LIC118 were not only consistent with far-field state of stress constrained in the previous chapter but also provide further support for a critically stressed crust.

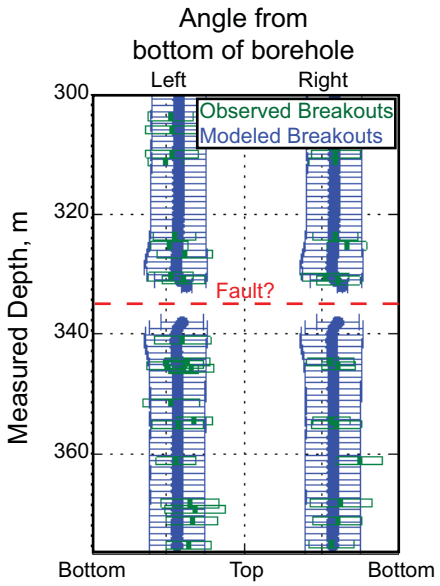

Figure 5-5: LIC118 borehole breakout observations (green) and modeled breakouts (blue) assuming slip a 11 m X 11 m fault patch striking 343° and dipping 60° that intersects the borehole at 335 m MD. A gap in the breakouts is predicted around the fault.

5.5 CRITICALLY STRESSED FAULTS IN THE MINING-PERTURBED STRESS STATE

5.5.1 General trends of the Mining-Induced Stress Perturbations

To examine the general trends in the mining-induced stress perturbations, we looked at the stress response along grids that are parallel and perpendicular to the mining stope. We investigated the trends in the stress perturbations that occur above and below the stope and in front of the stope edge. In Figure 5-6, the maximum principal stress (S_1) and minimum principal stress (S_3) after mining step five are plotted for three different cross sections: A-A', B-B' and C-C'.

Cross-section A-A' runs parallel to the strike of the stope in the NELSAM study area (Fig. 5-6). In this cross-section, we observed the mining-perturbed principal stress

magnitudes and orientations due to the influence of the "double stope" where the stopes that are offset by the PFZ overlap. Several observations were made from this cross-section. First, the stress orientations and magnitudes are affected for several hundred meters surrounding the stope. The S_3 orientation is less affected by the mining than the S_1 and S_2 orientations. The stresses are concentrated at the stope edges and reduced above and below the stope. The presence of the double stope has a strong effect on both the S_1 and S_3 magnitudes. The S_1 magnitude above and below the region of the double stope is lower than in the surrounding area that is only influenced by a single stope. This effect is observed for the entire 470 m height of the A-A' grid. In the region between the two stopes, the S_3 magnitude is greatly decreased such that it is modeled as going into tension (dark gray) over part of the region.

Cross-sections B-B' and C-C' run parallel to the dip direction of the stope (Fig. 5-6). In B-B', only the main stope is intersected. The S_1 and S_3 grids show the stress concentrations at the edge of the stope and the rotation of the stress orientations around the mining. In particular, S_1 rotates from being nearly vertical in the far-field to being nearly horizontal in the near-field to the mining. The stress state is perturbed for several hundred meters away. The major stress perturbation is within approximately 100 m of the stope, but more subtle effects are predicted over several hundred meters. In the C-C' cross-section, we again see the effects of the double stope. The stress concentrations at the edge of the stope are greatly diminished in the double stoped areas as compared the stope edge closest to C for both S_1 and S_3. In the S_3 grid, a zone of tension is again observed between the two stopes.

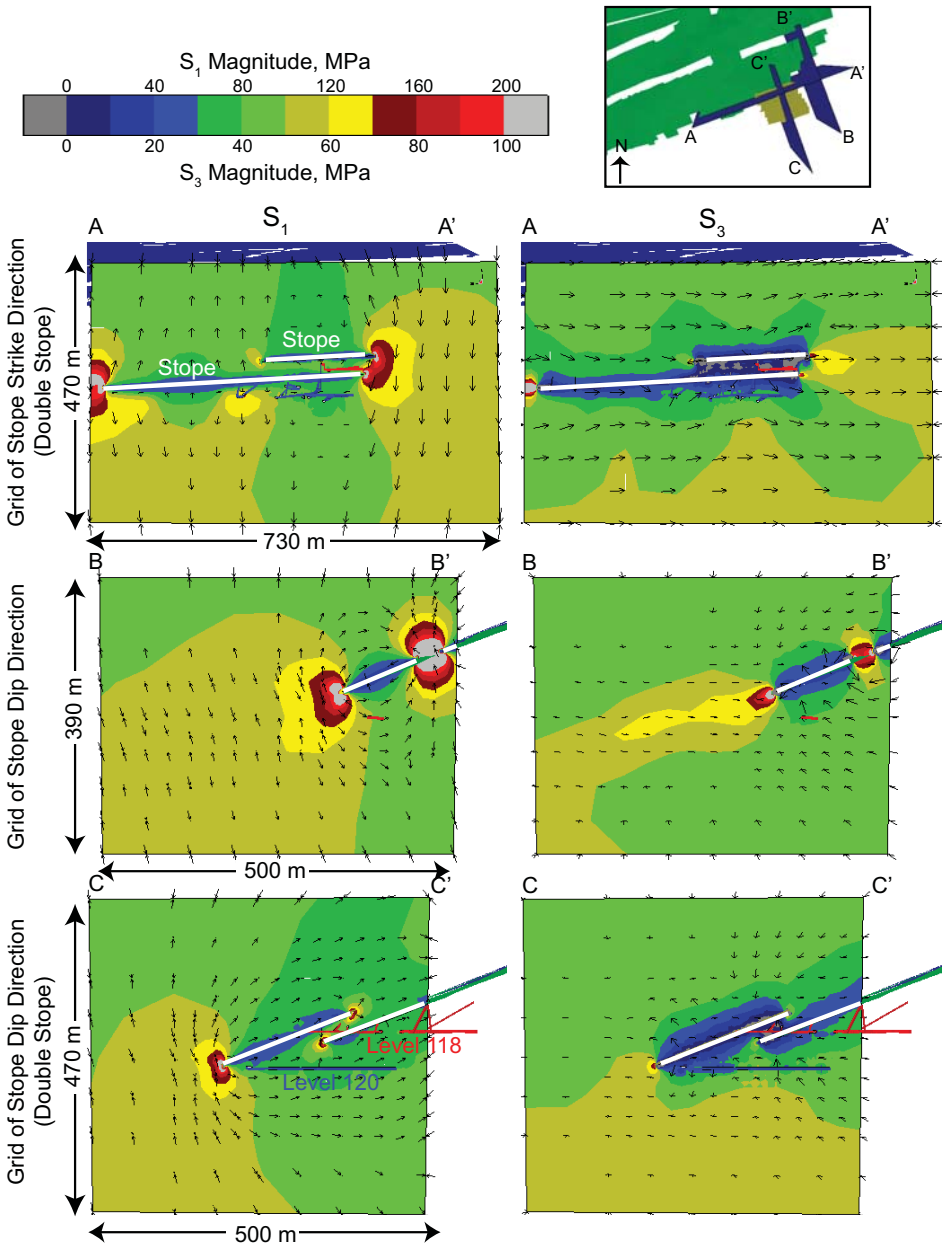

Figure 5-6: General trends in mining-induced perturbations in S_1 and S_3. Grid A-A' is parallel to the strike of the stope and grids B-B' and C-C' are parallel to the dip direction of the stope (see top right). Grids A-A' and C-C' show the effect of a "double stope". The intersections of the grids and the stopes are shown by the white lines. The panels on the left show S_1 and the panels on the right show S_3. The colors indicate stress magnitude (see top left) and the black arrows are 3D stress orientations.

5.5.2 Change in Critically Stressed Fault orientations

In Figure 5-6, we show that the principal stress orientations and magnitudes are greatly perturbed by the mining excavation for several hundred meters away from the stope. These changes in the principal stresses affect which fault orientations are

critically stressed. In some cases, faults that were critically stressed in the virgin stress state are stabilized by the stress perturbations. In other cases, faults that were stable in the far-field stress state become critically stressed as the stress field changes with the mining excavation. To investigate these changes, we examined two profiles along the B-B' cross-section that was introduced in Figure 5-6. These profiles are shown in Figure 5-7a. One profile (X-X') extends from the far-field towards the stope along the plane of the stope such that is passes through the main stress concentration at the stope edge. The second profile (Y-Y') extends vertically from the far-field below the stope up to the floor of the stope.

In Figure 5-7b, we illustrate that critically stressed fault orientations in the far-field stress state at X become more stable as the stresses become concentrated near the stope edge at X' because the magnitude of S_3 increases more rapidly than S_1. In the far-field stress state, faults that strike SSE and NNW and dip 45-90° have positive CFF values and are critically stressed. As the stope edge is approached along the plane of the stope, all of the principal stress magnitudes increase. This corresponds to an increase in the effective normal stress and a decrease in the CFF resolved on all the faults, moving them further away from failure. Within 90 m of the stope edge, no fault orientations are critically stressed, suggesting that the region of high stress concentration in front of the stope edge is the least likely region for induced slip on pre-existing faults to occur. This is supported by the earthquake locations in Figure 5-2, which show very few events occurring in that region. This analysis assumed hydrostatic P_p at all distances from the stope. While the hydrostatic P_p assumption is expected to be correct in the far-field, it is likely that there is some decrease in P_p within about 30 m of the stope due to the dewatering of the mine and the diffusion rate of the rock. A decrease in P_p would serve to stabilize the faults even more by further increasing the effective normal stress on pre-existing faults.

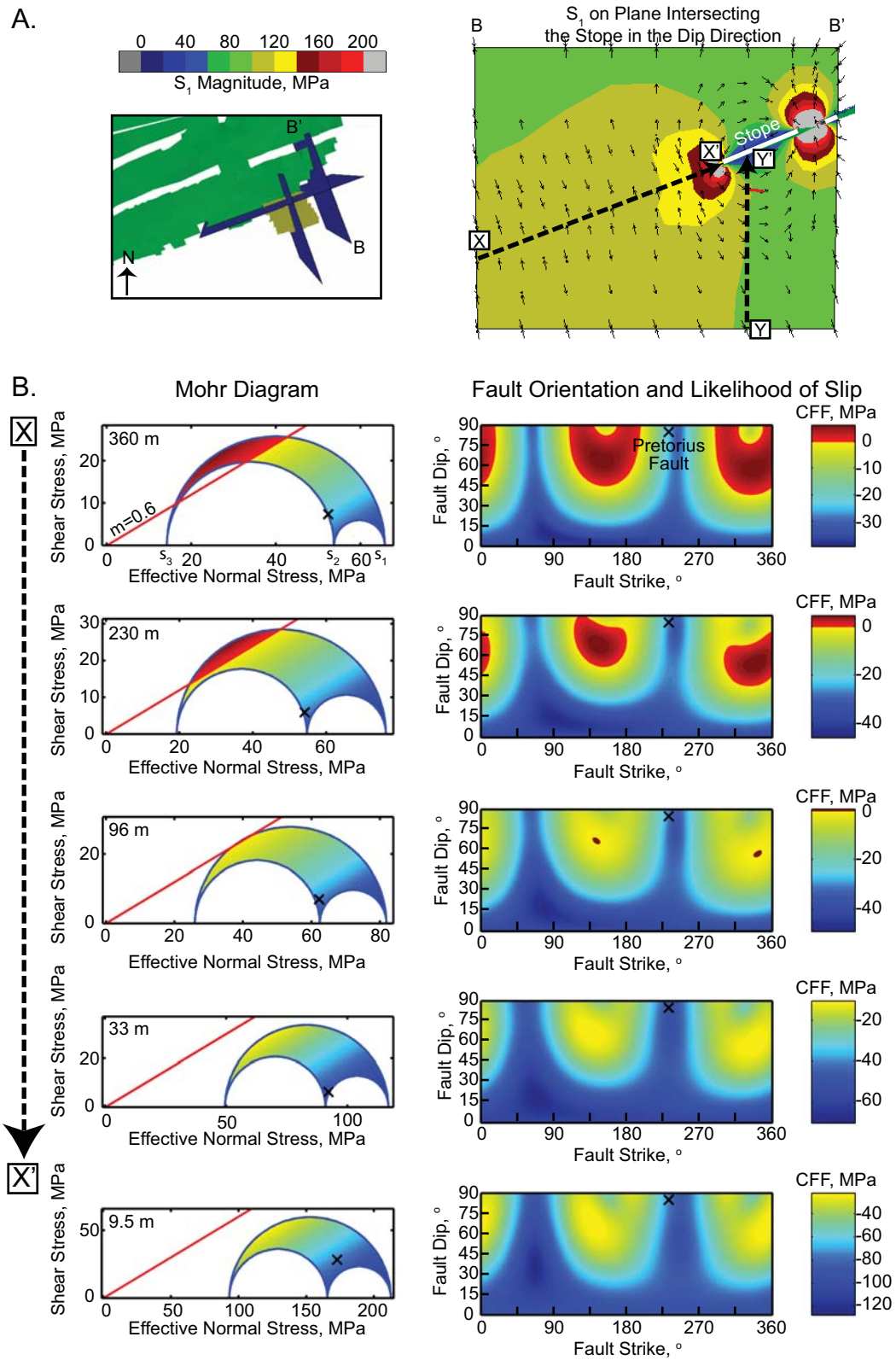
A.
0 40 80 120 160 200
S1 Magnitude, MPa
B'
B
N
S1 on Plane Intersecting
the Stope in the Dip Direction
B
B'
Stope
X'
Y'
X
Y
B.
Mohr Diagram
Fault Orientation and Likelihood of Slip
X
X'
360 m
230 m
96 m
33 m
9.5 m
m=0.6
Shear Stress, MPa
Effective Normal Stress, MPa
Pretorius
Fault
Fault Dip, °
Fault Strike, °
CFF, MPa

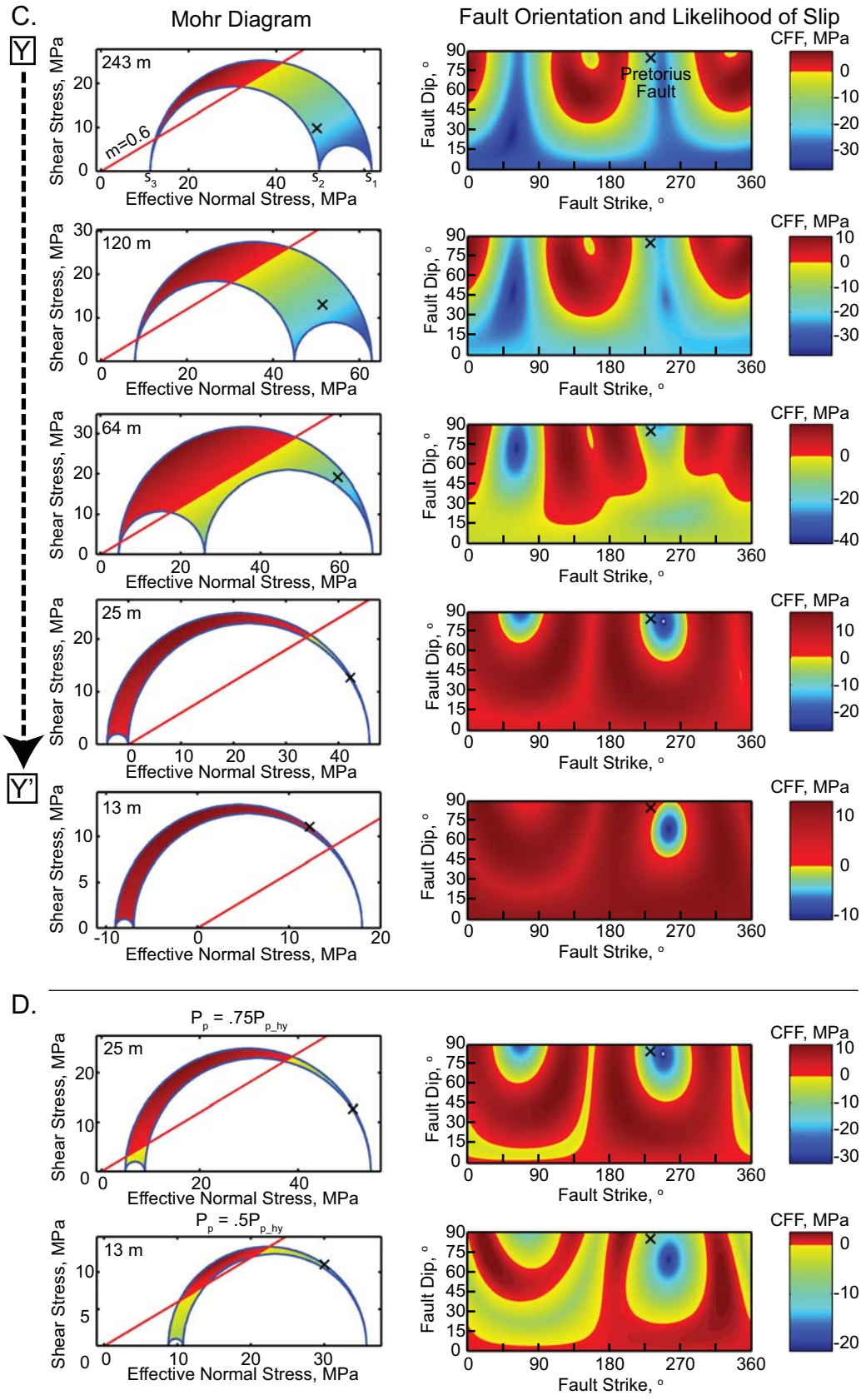
C.
Mohr Diagram
Fault Orientation and Likelihood of Slip
Y
Y'
243 m
120 m
64 m
25 m
13 m
m=0.6
Shear Stress, MPa
Effective Normal Stress, MPa
Fault Dip, °
Fault Strike, °
CFF, MPa
Pretorius Fault
D.
P_p = .75P_p_hy
P_p = .5P_p_hy

Figure 5-7: Changes in critically stressed fault orientations due to mining-induced stress perturbations. A.) Locations of B-B' cross-section and X-X' and Y-Y' profiles. B.) Changes in critically stressed fault orientations along the X-X' profile. Panels on the left are the Mohr diagrams for the stresses at different distances from the stope edge. Panels on the right plot the fault orientations in terms of strike and dip and their associated CFF values. Positive CFF values are red and indicate critically stressed fault orientations. The PFZ orientation is shown by the black X for reference. Analysis assumes P_p is hydrostatic and μ=0.6. C.) Changes in critically stress fault orientations along the Y-Y' profile. For further explanation see (B.) above. D.) Changes in critically stress fault orientations along the Y-Y' profile with reduced P_p near the floor of the stope.

Figure 5-7c shows the changes in critically stressed fault orientations along the Y-Y' profile. Again, in the far-field stress state at Y, normal faults that strike SSE and NNW are critically stressed. In contrast to the X-X' profile, as the stope is approached along this profile, more fault orientations become critically stressed. This is primarily due to the greater decrease in the S_3 magnitudes than S_1 magnitudes below the stope, which results in a decrease in the effective normal stress acting on the different fault planes. Almost all fault orientations become critically stressed within 13 m of the stope. The PFZ, shown by the X for reference, is far from failure in the virgin stress field but becomes critically stressed within 25 m from the floor of the stope (Y'). However, this analysis again assumed hydrostatic P_p. Because the mine is dewatered, there is some decrease in P_p within 10s of meters the stope. In Figure 5-7d, the critically stressed fault analysis for 25 m and 13 m from the stope is repeated with P_p values that are 75% and 50% of hydrostatic, respectively. With a lower P_p, fewer fault orientations became critically stressed. Therefore, the dewatering process is used not only to improve the working conditions in the mine, but also to stabilize some of the fault orientations near the stope.

5.5.3 Breakout Analysis and Critically Stressed Faults

In the previous sections, we looked at general trends in mining-induced stress perturbations and how they affect the critically stressed nature of hypothetical fault orientations. In this section, we focus on critically stressed faults observed in the LIC118 borehole and their influence on the formation of the breakouts observed in the image log. The observations in LIC118 show local rotations in the breakout position and gaps in the occurrence of breakouts which are indicative of stress perturbations from recent slip on critically stressed faults (Fig. 4-6). The borehole image logs from LIC118 also provided us with direct observations of natural fractures occurring in the

crust around the NELSAM study area. Therefore, we could test the far-field stresses estimated in the previous chapter by modeling the breakout variability around the natural fractures using the BEM results that predict the mining-induced stress perturbations along the length of the LIC118 borehole.

In order for a fault that is observed in LIC118 to have slipped recently, it must have been critically stressed in the virgin stress field or have become critically stressed as the mining excavation altered the in situ stress state at the location of the fault. Several faults observed along in the image log of the LIC118 borehole are critically stressed in the virgin stress state. In most cases, these remain critically stressed in the mining-perturbed stress state, but some become stabilized in the mining-perturbed stress field. Other faults are near the critically stressed threshold in the virgin stress state, but become critically stressed in the mining-perturbed stress field.

For 17 critically stressed faults observed in the LIC118 borehole, we modeled the response of the breakout formation to slip on the faults in the mining-perturbed stress field. The results of the breakout modeling associated with slip on these critically stressed faults are summarized in Table 5-1. The breakout response to the localized stress perturbation was variable and depended on the orientation of the fault, the trajectory of the borehole, the stress state along the borehole, and the rock strength (assumed to be 200 MPa in all cases). In some cases, the breakout positions were not significantly affected by slip on the fault. In other cases, the breakout position was modeled to have substantial rotation or there was a complete absence in breakouts. In most cases, the modeled results were consistent with the observed breakouts. The only cases in which there were significant discrepancies between the modeled and observed breakouts were when the faults were already critically stressed in the virgin stress field. This may suggest that those particular faults slipped in the past, but the local stress perturbations associated with the past slip have had time to equilibrate with the far-field stresses and therefore did not affect the breakout formation at the time of drilling.

Table 5-1: Summary of breakout modeling near critically stressed faults that intersect the LIC118 borehole

Fault Measured Depth along LIC118, m	Orientation, Strike/Dip	Critically Stressed, Virgin Stress State	Critically Stressed, Perturbed Stress State	Breakout Modeling Results
57.1	218/53	No	Yes	Consistent with observations, small amount of BO rotation
59.6	102/69	No	Yes	Consistent with observations, substantial amount of BO rotation
76.5	320/75	Yes	Yes	Fits rotation, over predicts BO widths
77	314/70	Yes	Yes	Similar but slightly better results than previous fault
87.8	110/85	No (close)	Yes	Consistent with observations, substantial amount of BO rotation
88.2	300/76	Yes	No	Consistent with observations, small amount of BO rotation
90.4	302/86	Yes	Yes	Consistent with observations, localized BO rotation
106.4	126/53	No (close)	Yes	Consistent with observations, predicts gap in breakout occurrence
112.4	342/75	Yes	Yes	Consistent with observations of rotation above fault, not below
112.5	346/51	Yes	Yes	Consistent with observations of rotation above fault, not below
112.6	344/56	Yes	Yes	Consistent with observations of rotation above fault, not below
119.5	330/53	Yes	Yes	Not consistent with observations
123.6	1/81	Yes	Yes	Little effect on BO rotation or width
130.7	117/79	Yes (close)	Yes	Consistent with observations, substantial amount of BO rotation
130.7	113/78	No (close)	Yes	Consistent with observations, substantial amount of BO rotation
159.5	123/89	Yes	Yes	Consistent with BO position, does not predict gap in BO occurrence
166.2	302/71	Yes	Yes	Consistent with BO position, does not predict gap in BO occurrence

In Figure 5-8, we show two examples of the breakout modeling analysis for faults that become more critically stressed due to the mining-induced stress changes. In the first example, we examined two faults that are similarly oriented (Fig. 5-8a). They were

both near frictional failure equilibrium in the virgin stress state and became critically stressed in the mining-perturbed stress state. These faults, which strike 113° and 117° and dip 78° and 79°, respectively, were observed near a localized rotation in breakout position at about 131 m measured depth in the LIC118 borehole. Since these faults became more critically stressed in the mining-perturbed stress state, they are likely to have experienced recent slip. Recent slip on these faults could have resulted in a local perturbation of the stress field that could have influenced the formation of breakouts along the LIC118 borehole. To evaluate the likelihood that slip on these faults affected the formation of the breakouts observed in the borehole, we modeled the slip that would occur on these faults in the mining perturbed stress field and predicted how the stress perturbation associated with this slip would affect the breakout formation in the borehole. Slip on a square fault patch of 64 m^2 centered on the borehole with one of these fault orientations in the mining-perturbed stress field would have a rake of 43.3° and 6.3 mm of dislocation. Assuming a stress drop of 75% to 100%, the stress relief would be 17.5 to 23.4 MPa. Based on this model, the predicted breakout formation in the LIC118 borehole closely matched the observed local breakout rotation. This result supports the far-field stress state constrained in the previous chapter

In Figure 5-8b, we illustrate that critically stressed natural fractures observed in the LIC118 borehole image log can also be responsible for the gaps in breakout occurrence that are observed in the mining-perturbed stress field. A fault striking 126° and dipping 53° was observed at 106.4 m measured depth. This fault orientation became critically stressed in the mining-perturbed stress state. The local stress perturbation associated with slip on a 100 m^2 square fault patch of that orientation (i.e., 11.4 mm of slip with a rake of 58.9°) centered on the borehole with 75-100% stress drop (25.2 to 33.6 MPa) would result in a gap in the formation of breakouts around it. This is consistent with the breakout observations at that depth.

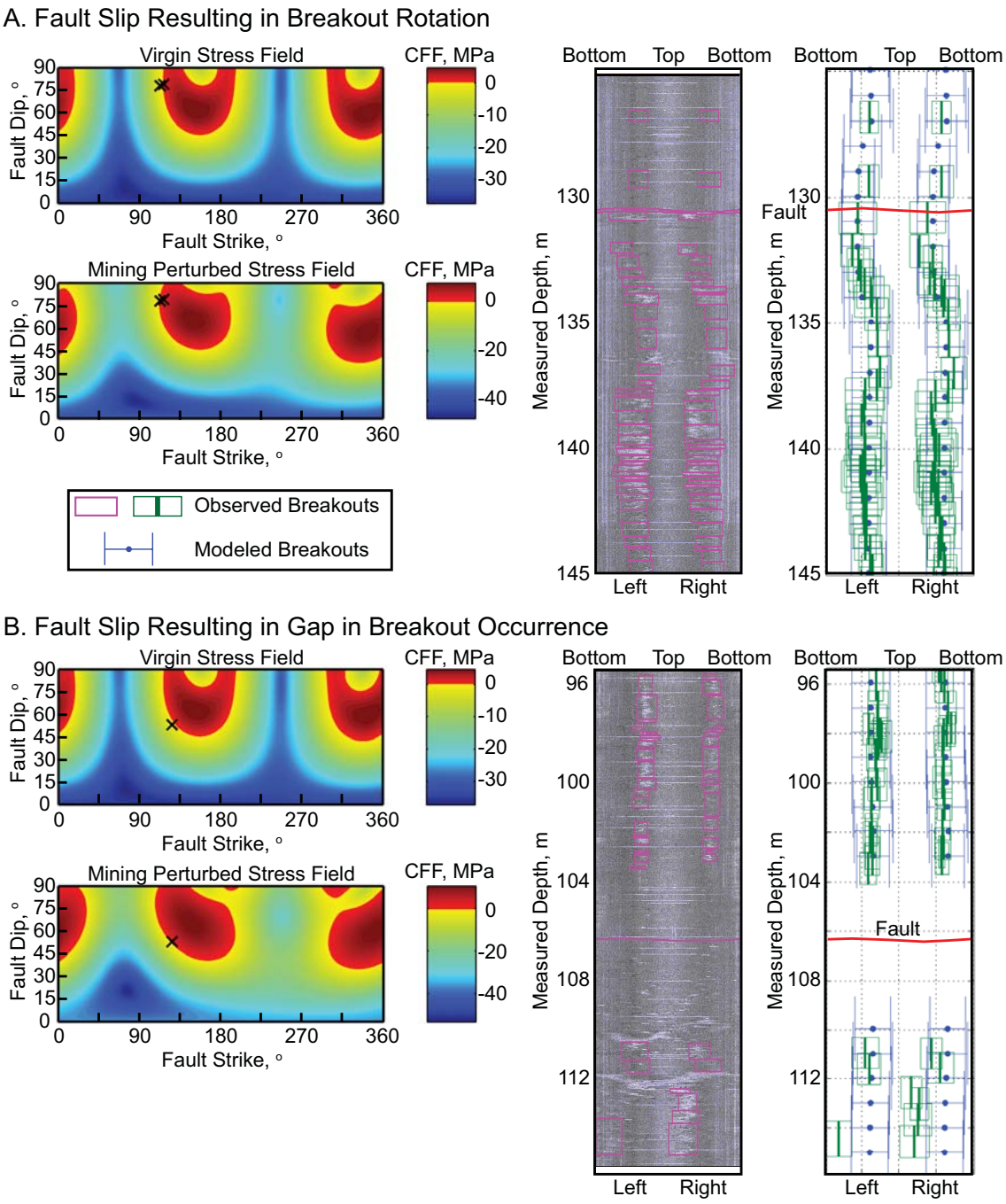

Figure 5-8: Two examples of modeling breakouts near critically stressed faults. A.) Modeling fault slip that results in a rotation in the breakout position. On the left the two fault orientations are plotted with the CFF for the virgin and mining-perturbed stress field. The center panel shows the borehole image log data and interpretation of the faults and breakouts. The data is shown as an unwrapped borehole in a reference frame of looking down the borehole. The panel on the right compares the observed breakouts (green) with the modeled breakouts (blue). The two faults are approximated by a single fault (red). B.) Modeling slip on a fault that results in a gap in breakout occurrence. The panels are the same as described for A.

5.6 OBSERVED MINING-INDUCED FAULT SLIP

5.6.1 Recorded Earthquake Locations and Focal Mechanisms

Once the NELSAM seismic instrumentation has been fully deployed, the earthquakes induced near the NELSAM study area will be more accurately recorded. With a more densely spaced array of seismometers, the events will be better located and their focal mechanisms will be better constrained. The locations and moment tensors can be used as another way to investigate the mining-perturbed stress state. The data necessary to analyze the mining-induced events that are recorded near the NELSAM study area were not available, but we established a workflow for this analysis. Therefore, when the earthquake locations and moment tensors become available they can be evaluated (Fig. 5-9).

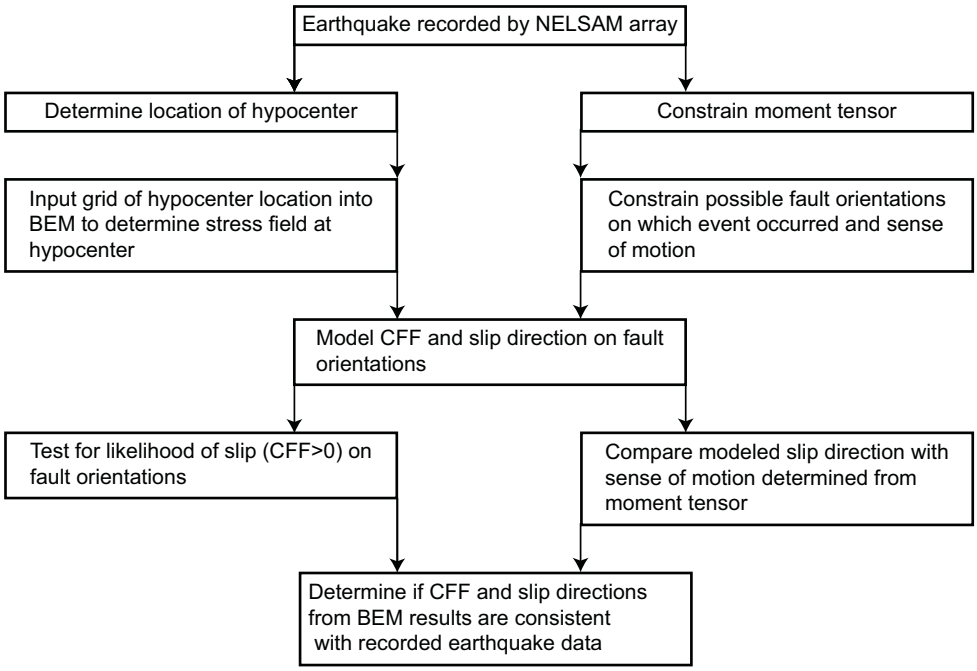

Figure 5-9: Workflow for analyzing earthquakes near the NELSAM study area in terms of the mining-induced stress state.

In Figure 5-9, we outline the steps of the workflow for evaluating the earthquakes that occur near the NELSAM study area in relation to the mining-perturbed stress state. When a mining induced earthquake is recorded by the NELSAM seismic array, the next step is to determine its location and constrain its moment tensor. Once an earthquake location is determined, we can input a grid at the hypocenter location into the BEM to

calculate the mining-perturbed stress state at that location. The moment tensor can be used to constrain the orientation of the fault that slipped and give the sense of motion. Once the stress field at the earthquake location is determined and the fault orientation along which the event occurred is constrained, the CFF and the slip direction (the direction of the maximum shear stress) can be modeled under the stress conditions at the hypocenter location. These modeled results can then be compared to the recorded observations to test for consistency in the likelihood of the fault to slip (positive CFF in the mining-perturbed stress state) and sense of motion. This technique is a way to determine whether the earthquakes that are occurring in the region around NELSAM support the constrained state of stress. If the earthquake observations are consistent with the modeling results, we will have another tool for investigating the mechanics controlling the induced earthquakes.

5.6.2 F1, F2, and F3 Fault Analyses

One aspect of the NELSAM project is mapping faults that intersect the access tunnels in the study area (Vincent Heesakkers and Ze'ev Reches, personal communication). During this mapping, evidence of recent slip was observed on some of these faults. The primary evidence of faulting was the observation of fresh rock powder along the fault traces. In one case, a rock bolt installed across a fault was offset, showing a displacement of about 1 cm. Three faults with fresh rock powder were mapped in the access tunnels that connect the 118 and 120 levels near the area where a large (M_w 2.2) event occurred on December 12, 2004. This time coincides with the early mining on the upthrown reef to the southeast of the PFZ. The three faults are located within a few meters of each other (Fig. 5-3). The seismic signal from the December 12, 2004 event contained evidence for at least three sub-events, which suggests that slip on one of the faults may have triggered slip on the other two (Margaret Boettcher, personal communication). The fault we refer to as F1 has a strike direction of 55° and dips 81° to the southeast. The F1 fault orientation is similar to that of the general PFZ, but it dips to the southeast rather than the northwest. It is likely a segment of the fault zone. One of other faults, F2, is bedding parallel with a strike of 85° and a dip of 20°. The third fault, F3, has a strike direction of 63° and dips 43°. All three of the fault orientations are stable in the virgin stress state (Fig. 5-4).

From the BEM results of the mining-induced stress state, we calculated the CFF values resolved on the fault planes for the extent of mining at different mining steps. To calculate CFF we assumed hydrostatic P_p (about 36 MPa at the fault depths) and μ=0.6. If in situ P_p magnitudes are sub-hydrostatic or the μ of the faults are greater than 0.6, the likelihood of slip on the faults decreases. We examined the change in CFF on the fault planes between mining step one and mining step two. Mining step one does not include any excavation on the up thrown section of the reef, while mining step two represents the beginning of the mining of the upthrown stope. Mining step two represents the extent of mining as of December 15, 2004, just a few days after the event occurred. When we used the representative far-field stress state described above as the initial stress condition in the BEM, there were zones within all of the fault planes that had positive CFF values indicating that slip could occur on these faults. However, no significant change in CFF was predicted between the two mining steps on any of the faults. This lack of change in CFF predicted between the two mining steps may indicate that the progression of mining from mining step one to mining step two was not directly responsible for triggering these events.

Nevertheless, because the timing of the event corresponded with active mining near the faults, it seemed likely that the progression of the mining might have played a role in inducing the event. Therefore, we decided to examine the change in CFF on the faults based on other far-field stress states within the range constrained in Chapter 4 to see if a change in CFF between the two mining steps could be modeled. In Figure 5-10, we show the analysis on the F1 fault using the BEM results calculated with a slightly modified far-field stress state. The far-field stress state in the new analysis was similar to the previously used far-field stress model except it had an S_2 magnitude gradient of 25.2 MPa/km rather than 24 MPa/km, an S_3 magnitude gradient of 13 MPa/km rather than 14 MPa/km, S_1 was deviated 15° from vertical rather than 10°, and S_2 was deviated 15° from horizontal rather than 10°.

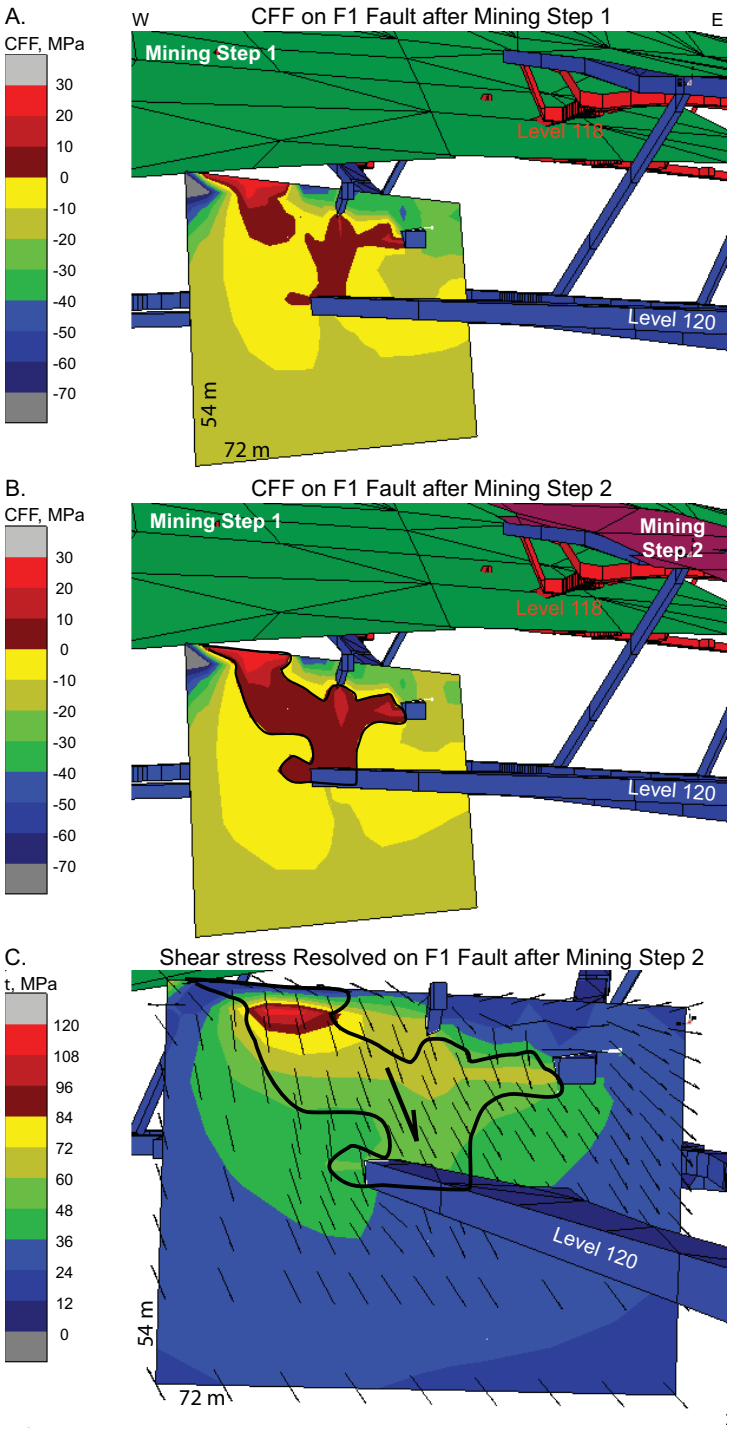

Figure 5-10: Modeling the potential for mining-induced seismicity on the F1 fault. A.) CFF resolved on F1 after mining step one (green), red colors indicates positive CFF. B.) CFF resolved on F1 after mining step two (magenta). The area of positive CFF (red colors) is increased relative to that in mining step one. The area with slip potential is outlined in black. C.) Shear stress resolved on F1 at mining step two. The black outline indicates the area of potential slip from B. The arrows indicate slip direction, with the bold arrow illustrating the average slip direction in the zone of positive CFF.

In Figure 5-10, we show that seismicity may have been directly induced by the mining as it progressed along the upthrown reef southeast of the PFZ. The CFF on the F1 fault at mining step one is plotted in Figure 5-10a such that red colors indicate positive CFF and a likelihood for slip. The areas of the fault with the greatest likelihood for slip were those closest to the stope (shown in green) and near the access tunnels that intersect the fault plane. The addition of the mining from mining step two, resulted in a stress perturbation that increased the area of the fault plane with positive CFF values (outlined in black in Figure 5-10b). The slip direction on F1 predicted from the shear stress resolved on the fault plane is oblique normal to left lateral strike slip faulting. No moment tensor for the M_w 2.2 event was available for comparison. However, if it becomes available it could be used to test for consistency between the observed sense of motion and the predicted slip direction.

Figure 5-11 shows the CFF resolved on the F2 and F3 faults at mining steps one and two. A significant area of each fault was modeled to have positive CFF values for both mining steps. The areas of the faults with positive CFF were those closest to the floor of the stope from mining step one. However, there was not a noticeable difference in the area of positive CFF between mining steps one and two. It is possible that the changes in mining-induced stress field between mining steps one and two reactivated F1. The slip on F1, which intersects F2 and F3, may have caused the critically stressed zones of these faults to reactivate. At this point, we can conclude that it is possible for pre-existing faults with very stable (CFF<<0) orientations to be "turned on" due to the stress perturbations induced by mining development. Increasing the complexity of the mine with large numbers of tunnels and overlapping stopes may increase this risk. The analysis presented here assumed hydrostatic P_p acting on the faults. It is possible that the P_p in the faults is less than hydrostatic and therefore the CFF values may be overestimated, especially close to the excavations.

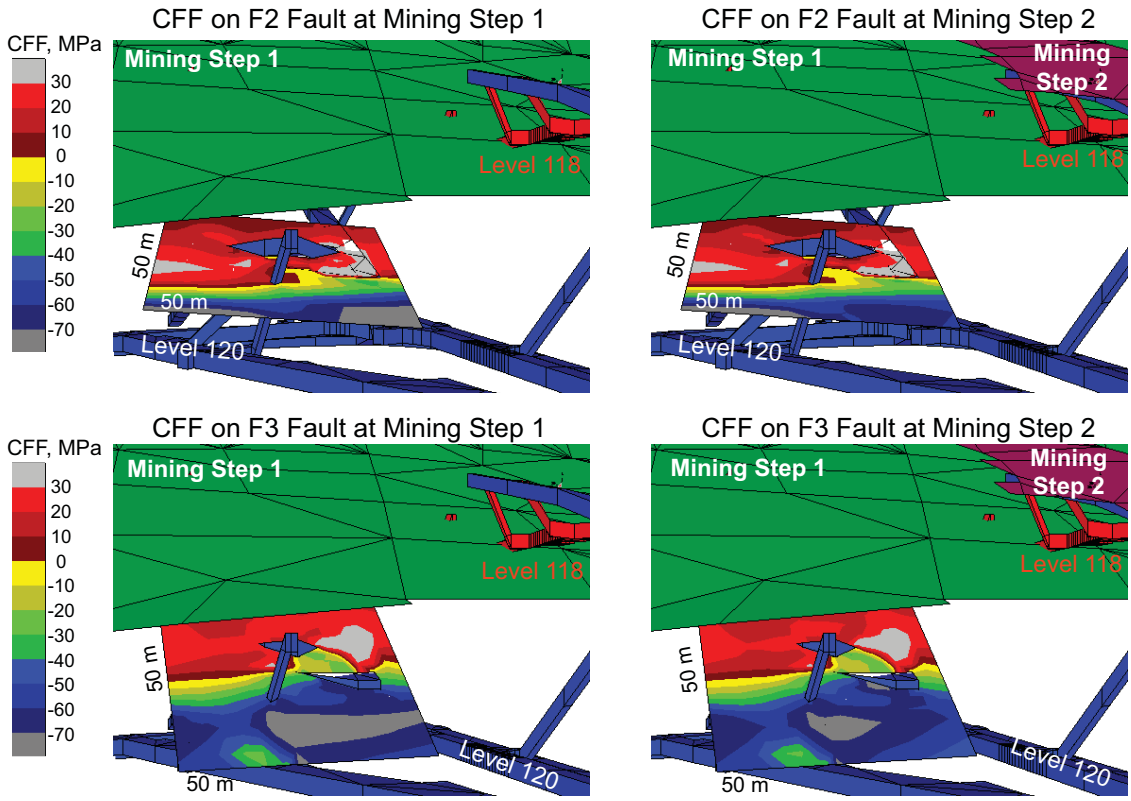

Figure 5-11: CFF resolved on F2 and F3 at mining steps one (left) and two (right). The red colors and light gray indicate the critically stressed areas of the faults.

5.6.3 Pretorius Fault Zone Analysis and Future Mining

The PFZ is the largest fault zone in TauTona. We determined that in the far-field, virgin stress state the orientation of the PFZ is stable (Fig. 5-4). However, we have shown that the stress perturbations related to the mining greatly alter the orientations and magnitudes of the principal stresses. We have also shown that the progression of mining likely led to slip on the F1 fault. This fault is probably a segment of the PFZ. As mining proceeds on both sides of the PFZ, concern about inducing a large earthquake increases. We wanted to examine how the recent mining had affected the stresses resolved on the plane of the PFZ and how the mining that is planned for the future will affect the likelihood of slip along the fault. Using the BEM results, we could evaluate the CFF on the PFZ as a result of the past and future mining development. A better understanding of the seismic hazards associated with the PFZ is necessary for increasing safety within the mine.

In Figure 5-12, we illustrate the CFF resolved on a 600 m X 3500 m section of the PFZ that intersects the NELSAM study area for three different mining steps. The areas

in red colors or light gray have positive CFF, assuming hydrostatic P_p and μ=0.6. The value of CFF may be overestimated on portions of the fault plane if P_p is sub-hydrostatic or μ>0.6. The fault zone was modeled with a series of grids, with slightly varying orientations. The nature of this modeling resulted in the discontinuities in CFF values from grid to grid. Figure 5-12a shows the CFF on the PFZ at mining step one. The extent of the development at mining step one is shown in the box in the lower right corner and in Figure 5-2. The fault is intersected by the stope in three places (shown by white lines) and the LIC118 borehole in the NELSAM study area. The results of this modeling suggest that prior to the mining on the upthrown stope, some regions of the PFZ near the intersection of downthrown stope were critically stressed. This is similar to the observations from the F1 fault analysis. Some smaller magnitude earthquakes may have occurred along the fault zone at this time, but no significant concentrations of events or large magnitude earthquakes were attributed to the PFZ.

As mining progressed on the upthrown reef to the southeast of the PFZ during 2005 though June 2006 (mining steps 2-5), the newly mined stope intersected the PFZ resulting in a double stoped area within the fault zone (Fig. 5-12b). At mining step five, the region of highest CFF and therefore most likely to slip was between the two stope intersections. The total area that wa critically stressed at this point was not significantly different than that after mining step one, but the CFF values in the double stoped region were higher. Again, no significant concentrations of events or large magnitude earthquakes were attributed to the PFZ at this time. Some events with M_w>2 did occur near the fault during this time that have not been directly linked to the PFZ (Fig. 5-1). However, as we observed in the analysis of the F1 fault, the change in CFF between mining steps one and two may have induced slip on the fault resulting in a M_w 2.2 event.

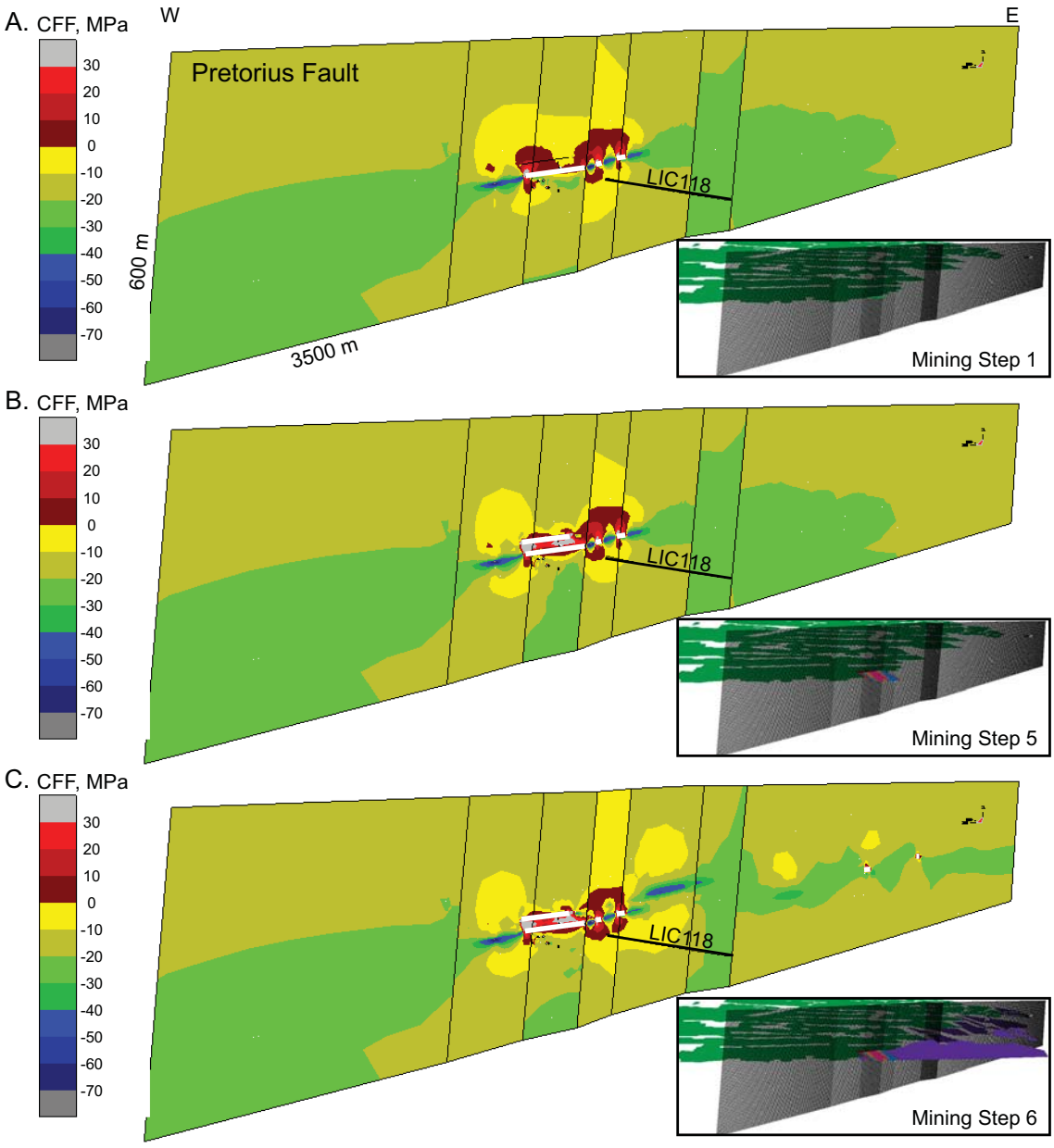

Figure 5-12: CFF resolved on the PFZ at mining steps one, five, and six. Positive CFF values are shown in red colors and light gray. The intersections of the stope and fault are indicated by white lines. The extent of mining for each mining step is shown on the lower right for each plot. A.) CFF at mining step one. B.) CFF at mining step five. C.) CFF after future development in mining step six.

Finally, in Figure 5-12c we investigate the change in CFF expected on the PFZ as mining progresses on both sides of the fault zone along the planned development through 2012 (mining step six from Fig. 5-2). The CFF values on the PFZ to the southwest of the double stoped region remained basically the same during this

excavation because most of the mining occurred to the east and northeast. Near the LIC118 intersection with the PFZ, the future mining altered the critically stressed area of the fault resulting in a decrease in CFF in the zone between the two small nearby stope intersections and an increase in CFF to the northeast of the LIC118 intersection. Further towards the northeast on the fault, the stope intersected the fault in two small areas. While the CFF near those intersections was altered from the previous mining step, only small regions directly around these intersections have positive CFF values. This modeling indicates that it is unlikely that the planned future mining will induce seismicity in the PFZ with magnitudes larger than any of the events that have been previously recorded in the area.

5.7 DISCUSSION AND CONCLUSIONS

We investigated the likelihood of faulting to occur on pre-existing fault planes that are optimally oriented both to the virgin stress state and to the mining-perturbed stress field calculated with BEM. Based on this work, there are three important issues that require further discussion. First, as a result of this investigation, we found further evidence to support our constrained stress state. Second, using this constrained stress state, we made important observations that lead to a better understanding of the mining-induced seismicity that is occurring around TauTona and the NELSAM study area. Finally, based on these results, we can make some recommendations for future mining development.

5.7.1 Evidence Supporting the Far-Field Stress State

In the previous chapter, we constrained the far-field stress state based primarily on observations of drilling induced failures observed in borehole image logs. We noted that the localized breakout rotations and gaps observed in the LIC118 borehole image log supported the assumption of a critically stressed crust. In this chapter, we confirmed that the local termination of breakouts was consistent with the predicted breakout formation response in the LIC118. By forward modeling the breakout formation, we showed that the stress perturbation associated with slip on a critically stressed fault in the far-field stress state would result in gaps in the breakout occurrence around the fault similar to the observed gaps in the image log data. This analysis supports the

assumption that the far-field stress state is in frictional failure equilibrium such that slow frictional failure is occurring on faults with optimal orientations to the far-field stress state. This analysis also supports the stress magnitudes and orientations in our far-field stress estimate because the slip on the faults with orientations that are critically stressed in this stress field result in a breakout formation consistent with the breakouts observations (i.e., breakout termination).

By using BEM, we modeled the mining-perturbed stress state that results from the superposition of the far-field stresses and the mining excavation. This tool provided us with the necessary stress information to allow us to model the signature of the breakouts along the LIC118 borehole as the stress field changes from the far-field towards the mining stope. We found that critically stressed natural fractures observed in the LIC118 borehole image data corresponded with localized breakout rotations and interruptions. Using the forward modeling approach, we showed that the modeled breakout formation around these faults was generally consistent with the observations. This again supports the validity of the constrained far-field stress model.

5.7.2 Discussion of Mining-Induced Seismicity

The region around the NELSAM study area experiences an appreciable amount of mining-induced seismicity. These events occur primarily below the mining stope, sometimes above the stope, and only occasionally out in front of the stope (Fig. 5-1). The locations of the events are consistent with the general trends we observed for the mining-perturbed stress field. Despite the high stress concentrations that occur in front of the stope edge, faults in this region tend to become more stable because of the high normal stresses resolved on the fault planes (Fig. 5-7b). However, in Figure 5-7c, we showed that the general decrease in the principal stress magnitudes directly below the stope reduces the effective normal stress acting on the faults resulting in higher CFF values and more critically stressed fault orientations.

While the generalized analysis of the mining-perturbed stress trends involved hypothetical faults in the crust, the breakout modeling and the analysis of the F1, F2, and F3 faults focused on faults observed to have been recently active. Both provided further evidence that previously stable fault orientations are indeed becoming critically stressed in the mining perturbed stress state. In the image log along the LIC118

borehole, we found several examples of pre-existing fault orientations that had a negative CFF in the virgin stress state and positive CFF in the mining-perturbed stress field. Assuming that recent slip on these faults had occurred, we were able to model the localized rotations in the breakout positions and gaps in the breakout formation around these faults (Fig. 5-8). This indicates that the faults have likely been recently reactivated and is evidence of mining-induced seismicity.

Initially, it seemed reasonable to focus the concern for fault reactivation on the PFZ since it is the largest fault zone in the mine. The orientation of this fault zone is not favorable for fault reactivation in the far-field, yet when the fault is near to or intersected by the stope it experiences a significantly altered stress state. While the potential for localized slip on the PFZ exists, particularly in areas near stope intersections with the fault, it is unlikely that a large scale earthquake on the order of M_w 3 to 5 will be induced on this fault (Fig. 5-12).

As in the past, mining-induced seismicity ranging in magnitude up to M_w 3 will continue as mining progresses. The deeper the mining progresses, the higher the stresses become, which increase the potential for more larger events (i.e., M_w 2-3) to occur. The PFZ has one of the most stable orientations in the far-field stress state, but become critically stressed under some of the mining-induced stress conditions. The mapping of faults in the TauTona mine as part of the NELSAM project and faults observed in the borehole image data suggest that faults of many different orientations are present through out the crust. As outlined in Table 5-1, we observed 17 faults in the LIC118 borehole image log data that were critically stressed or nearly critically stressed in the far-field stress state. Five of these faults became critically stressed as the mining progressed. These faults have a high potential for reactivation as the stress state is perturbed by the mining. However, these faults are more likely to slip before the mining reaches them. The fault orientations that become critically stressed only very near to the excavation are of particular interest because they have the potential to be extremely dangerous. In the next section, we discuss a potential method for targeting existing faults that have high likelihoods of slip as the mining progresses for induced seismicity prior to the excavation reaching them. This would serve as a means of preventing dangerous events from occurring near the stope face.

5.7.3 Recommendations for Future Mining

The future development of the mine is obviously constrained by many factors. The development is controlled by the structure of the reef along which the mining is occurring. It is further constrained by the need to maintain the structural integrity of the stope for both economic and safety considerations. As underground mines continue to get larger and deeper, the concern for maintaining and improving the safety also grows. In fact, the safety of the mining conditions must remain at the forefront of all decisions made on the future development of the mine. While the analysis in this chapter only addresses the seismic hazards associated with slip on pre-existing faults that are optimally oriented to the in situ stress field, we make a few recommendations that can guide at least part of the decision making process for planning future mining development.

Other than the principal stress orientations and magnitudes, P_p is a necessary parameter for characterizing the likelihood of a fault to slip. We were able to use BEM to predict the change in the principal stresses due to the mining, but we were unable to model the change in P_p around the mine. One limitation to the analysis presented in this work was the assumption that hydrostatic P_p existed not only in the far-field but also in the near-field to the mining. While the permeability of the quartzite is very low, and correspondingly the diffusion rate is low, the mine has experienced dewatering and is generally considered to be dry. It is undetermined how the P_p gradient varies from the far-field to the stope. Therefore, we recommend measuring P_p at varying distances from the mine activity. This could be done by setting packers at various depths along exploration boreholes drilled by the mine, such as the LIC118 borehole. Measurements should be taken in areas near active mining and in areas where mining occurred in the past. Because the diffusion rates are slow, these tests may require some time to reach equilibrium, but the measurements are important for understanding the seismic risks around the mine. As illustrated in Figure 5-7d, there is a significant difference in the likelihood of faults to slip when P_p is hydrostatic versus when it is sub-hydrostatic.

Because of the stress relief provided by the presence of the stope, the access tunnels are built beneath the stope. The addition of a second, overlying stope may occur where the reef is offset by a fault, as is the case in the NELSAM study area. This double stope provides more stress relief, which further decreases the stress concentration around the

tunnels. However, the drastic stress decreases in the area between the stopes increases the likelihood of shear slip on pre-existing faults and may also result in opening mode fractures. Before a double stope is planned, we recommend that these added risks are evaluated against the benefits of the stress relief on the tunnels.

Another recommendation is to minimize the intersection of the stope with major fault zones, as appears to be the case for the development planned at TauTona. In TauTona, previous mining that has intersected the fault zone has not induced any large scale event on the fault. However, this mining has increased the CFF and therefore likelihood that events, although primarily of small magnitude, could occur on the fault zone. The future mining planned for the region only indicates two small zones of the stope intersecting the fault zone. Because of this, the likelihood of slip on the fault in the future is not drastically higher than the existing slip potential.

Finally, as mentioned in the previous section, we feel that future investigations should examine the potential for using induced seismicity as a means of relieving stresses ahead of the mining. The BEM provides a predictive tool for quantifying the stress concentrations that occur as the mining progresses. The image logs from boreholes extending into areas predicted to have stress concentrations that are likely to result in change in the critically stressed fault orientations due to the future mining development (i.e., above and below the reef where the future mining will occur) provide a tool for observing the orientations of pre-existing faults likely to be reactivated as mining continues. This information can be used to develop more effective induced seismicity projects. By targeting faults with a high potential for reactivation very near to the excavation and causing them to slip before the excavation reaches them could reduce the seismic hazards associated with them. This could decrease the amount of damage caused in the excavation and increase safety for the mine workers.

5.8 ACKNOWLEDGEMENTS

This chapter is based upon work supported by the National Science Foundation under Grant #0409605 (NELSAM). Any opinions, findings, and conclusions or recommendations expressed in this material are those of the author(s) and do not necessarily reflect the views of the National Science Foundation. Other sponsors of this work include Inter-Continental Drilling Program (ICDP), Anglogold, ISS International,

and National Research Foundation (NRF). We would especially like to thank Ze'ev Reches and Vincent Heesakkers of the University of Oklahoma and Margaret Boettcher of the USGS in Menlo Park, CA, for their involvement in NELSAM. We also thank Shaun Murphy of Anglogold Ashanti and Gerrie van Asegen and Gerhard Hofmann of ISS International for their help with Map3D and acquiring the necessary data for the modeling.

CHAPTER 6

CHARACTERIZING MECHANISMS OF SHEAR WAVE VELOCITY ANISTOTROPY NEAR A SALT STRUCTURE IN DEEP WATER GULF OF MEXICO

6.1 ABSTRACT

The number of wells drilled through and near salt structures continues to increase. These wells are among the most expensive wells to drill and are prone to numerous drilling problems that can drastically increase their associated costs. Better understanding of the geomechanical setting in proximity to salt results in more successful drilling and completion of these wells. One promising area of study for investigating the perturbation of the stress field in and around salt bodies is numerical modeling. However, in order to apply the results of the simulated stress field from a numerical model to a well drilled near a real salt body with confidence, it is necessary to compare the modeled results to data observations. Therefore, it is important to have independent observations of the stress state near the salt body. One technique for determining principal stress directions uses cross-dipole shear wave velocity anisotropy data. However, shear wave velocity anisotropy can be induced by structural mechanisms as well as stress-related mechanisms. In this study, we investigated a technique proposed by Boness and Zoback (2006) to identify structure-induced velocity anisotropy and isolate possible stress-induced velocity anisotropy. The investigation used cross-dipole sonic data from three deep water sub-salt wells in the Gulf of Mexico. First, we determined the parameters necessary to ensure the quality of the fast azimuth data used in our analysis. We then characterized the quality controlled measured fast directions as either structure-induced or stress-induced based on the results of the Boness and Zoback (2006) technique. We found that this technique supplements the use of dispersion curve analysis for characterizing anisotropy mechanisms. We also found that this technique has the potential to provide information on the stresses that can be used to validate numerical models of salt-related stress perturbations.

6.2 INTRODUCTION

As oil and gas exploration moves into more complex environments, such as deep water, sub-salt reservoirs in areas like the Gulf of Mexico, drilling costs increase dramatically. With drilling costs reaching 10's to 100's of millions of dollars per well, the costs associated with drilling and wellbore stability problems are quite significant. Willson and Fredrich (2005) outline 15 different drilling hazards related to drilling through, near and under salt diapers. These include, but are not limited to, tectonic instability, rubble zones from perturbed tectonic stresses, salt gouge at low effective stress (due to near lithostatic pore pressure conditions), and highly fractured sediments leading to mud loss. Better understanding of the geomechanics in, near, and under the salt diapers can result in more successful drilling and completion of wells in these regions. It can also lead to better reservoir management through the understanding of hydraulic fracturing potential, fracture conductivity, and fluid flow directions.

The complexity of the stress fields found around salt structures is a function of the constitutive behavior of salt. Salt cannot support anisotropic stresses. However, the formations adjacent to salt bodies are typically subjected to anisotropic tectonic forces. Therefore, the stresses in the formations directly adjacent to the salt are perturbed from the far-field stress state in order to ensure equilibrium in the salt body and continuity in the stress field at the interface between the salt and the formation. This perturbed stress state is complex and difficult to quantify.

One promising area of study for investigating the perturbation of the stress field in and around salt bodies is numerical modeling. In Fredrich et al. (2003), they use finite element modeling to simulate the stress perturbations within and adjacent to salt bodies with spherical and circular horizontal sheet (i.e., pancake) geometries. This modeling incorporates a Multimechanism Deformation constitutive model (Munson, 1999) of the salt along with failure criteria (i.e., Drucker-Prager, Mohr-Coulomb, end-cap) for the deformation of the reservoir rocks (Fredrich and Fossum, 2002). However, as with any numerical model, in order to apply the results of a finite element simulation to the environment adjacent to a real salt body with confidence, it is necessary to compare the modeled results to data observations. Therefore, it is important to have independent observations of the stress state near the salt body. A complete model of the stress field requires quantifying the orientations and magnitudes of the three principal stresses and

the pore pressure magnitude. In this work, we tested a technique for determining the principal stress directions. While this is only part of what we want to know, it could give us a tool with which to constrain and test numerical models of salt structures.

One method for determining in situ principal stress orientations in oil and gas fields is to use the presence of drilling induced wellbore failures, such as breakouts and tensile fractures (reviewed in (Zoback et al., 2003)). These can be observed in electrical and sonic image logs of the wellbore walls. Breakouts can also be observed with 4- or 6-arm caliper data (Plumb and Hickman, 1985). Breakouts form at the wellbore wall if the stress concentration around the well exceeds the compressive strength of the rock (Zoback et al., 1985). Drilling induced tensile fractures form if the stress concentration around the well goes into tension. Assuming one of the principal stresses is vertical, in a vertical borehole, breakouts form at the wellbore walls in the direction of the minimum horizontal stress (S_{hmin}) where the stress concentration in greatest and drilling induced tensile fractures form in the direction of the maximum horizontal stress (S_{Hmax}). If the well and/or the stress field deviate from vertical, modeling can be used to determine the stress orientations based on the observations of the drilling induced failures (Brudy and Zoback, 1993; Peska and Zoback, 1995).

However, in the Gulf of Mexico oil and gas field setting this method is often ineffectual. Because of the soft sediments in the Gulf of Mexico, borehole elongations observed in the image log data or caliper data of wells that are even slightly deviated from vertical often result from the mechanical wear of the drill pipe, called keyseats, rather than from breakouts. Keyseats form at the top and bottom of the deviated wellbore so that they are parallel to the wellbore azimuth. Drilling induced tensile fractures primarily occur when the in situ stresses are in a strike-slip regime (the vertical stress (S_v) is the intermediate principal stress (S_2) such that $S_{hmin} \leq S_v \leq S_{Hmax}$) and $S_{hmin} << S_{Hmax}$ (Moos and Zoback, 1990). However, the state of stress in the Gulf of Mexico away from salt structures is typically normal faulting ($S_{hmin} \leq S_{Hmax} \leq S_v$). The state of stress in the formations adjacent to salt is highly variable, ranging from normal to thrust faulting depending on the spatial relationship to the deformation associated with the salt migration; and the principal stress orientations are often deviated from the typically assumed vertical and horizontal trajectories. Without clear observations of

these stress indicators and lack of constraint on the stress trajectories, it is difficult to constrain the principal stress directions.

Another technique employed to determine principal stress directions uses cross-dipole shear wave velocity anisotropy data. Shear wave velocity anisotropy can be induced by both structural- and stress-related mechanisms. In both of these mechanisms, a transverse isotropic (TI) model is assumed. In a TI model, the shear waves are polarized parallel and perpendicular to the planes normal to the formation symmetry (Thomsen, 1986). Structure-induced shear wave anisotropy results from the alignment of parallel planar features, such that the vertically propagating shear wave has a fast polarization direction along the strike of the planar features. These planar features result from lithologic alignment of minerals and grains (e.g., Hornby, 1998; Johnston and Christensen, 1995; Sayers, 1994), aligned macroscopic fractures (e.g., Liu et al., 1993; Mueller, 1991), and sedimentary bedding (e.g., Alford, 1986; Lynn and Thomsen, 1990). Stress-induced shear wave velocity anisotropy results from an anisotropic tectonic stress state, such that the vertically propagating shear wave is polarized with a fast direction parallel to S_{Hmax} (assuming that the principal stresses are aligned vertically and horizontally). The shear wave propagates faster in the direction parallel to open fractures and slower in the direction normal to the open fractures (Fig. 6-1). This polarization along the direction of S_{Hmax} can result from the presence of aligned microcracks, which open in the direction of S_{hmin} (e.g., Crampin, 1986, 1991; Crampin and Chastin, 2003), or preferential closure of pre-existing, randomly distributed fractures in the direction of S_{Hmax} (Boness and Zoback, 2004).

One method for determining the mechanism that is controlling the observed shear wave velocity anisotropy uses dipole shear sonic data, which requires advanced frequency-domain processing techniques (e.g., Plona et al., 2002). A dispersion curve plots the velocity) in the fast and slow directions against fr he waveform penetrate deepest into the formatio borehole. The slowness measured at the low frequ slowness and is used to define the slow direction. T to the wellbore wall and reflect the dispersive nature

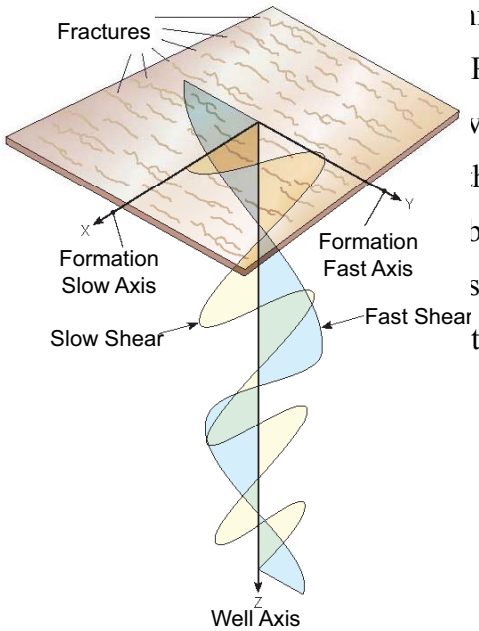

Figure 6-1: Schematic of fast and slow shear wave propagation in a stress-induced anisotropic medium (modified from (Brie et al., 1998)).

Depending on the anisotropy mechanism, the dispersion curves have characteristic signals. In some cases, the shape of the borehole influences the measured anisotropy, such that the borehole azimuth controls the fast direction and an isotropic formation may appear anisotropic in a certain frequency range (Leslie and Randall, 1990; Sinha and Kostek, 1996). When this occurs, the dispersion curve shows similar slowness values at the high and low frequencies and a separation in the mid-range frequencies, where the slow direction corresponds to the elongation direction (Fig. 6-2a). When the formation is anisotropic either due to a structure or stress related mechanism, the dispersion curves show other characteristic responses. For shear wave anisotropy that is induced by the structure (e.g., sedimentary bedding), the difference in the slowness between the slow and fast directions is independent of frequency (Winkler et al., 1998) (Fig. 6-2b). If the anisotropy is stress related, there is a characteristic crossover observed in the dispersion curve (Winkler et al., 1998). The fast direction is defined by the slowness at low frequencies. For stress-induced anisotropy, this is parallel to S_{Hmax} (assuming the principal stresses are aligned vertically and horizontally). At the higher frequencies, the slowness in the slow direction crosses over the slowness in the fast direction. This occurs because the stresses concentrate in the S_{hmin} direction near the wellbore wall (Fig. 6-2c).

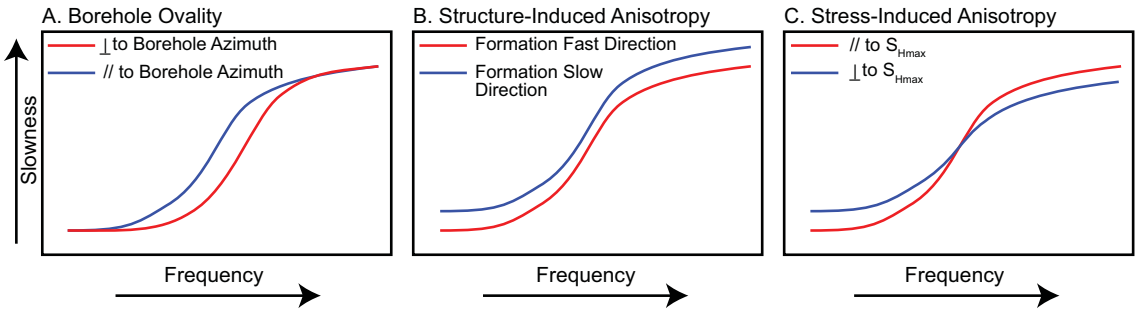

Figure 6-2: Schematic dispersion curves representative of different mechanisms: A.) borehole ovality, B.) structure, and C.) stress. The slowness is plotted in red and blue for the perpendicular polarization directions.

The frequency-domain processing required to plot dispersion curves is not part of the traditional processing of DSI data, which occurs in the time-domain. In this work,

we test a technique for characterizing the mechanisms controlling the anisotropy using the time-domain processed DSI data. The technique we tested was developed by Boness and Zoback (2006) to identify the structural-induced components of the cross-dipole sonic anisotropy data. They previously applied this technique near the San Andreas Fault in Parkfield, CA. By applying this technique near a salt diaper, we tested its effectiveness in another environment with complex structure and stress. In theory, if we can identify the structural-induced shear wave velocity anisotropy, we can isolate the stress-induced components and draw conclusions about the stress orientations.

For this investigation, we analyzed cross-dipole sonic shear wave well log data from three wells drilled near a salt diaper in the deep water Gulf of Mexico. The data used in this study was provided by BP. We examined (1) if stress-induced anisotropy is observed in the wells, (2) if this technique replaces or supplements dispersion curve analysis as a means for classifying the mechanisms of anisotropy, and (3) if this technique provides information that can be used to validate a potential numerical model of the salt-related stress perturbations.

6.3 MEASURING SHEAR WAVE ANISOTROPY: TRUE VERSUS APPARENT FAST DIRECTIONS

To measure the azimuthal shear wave velocity anisotropy of a formation, a borehole logging tool with dipole sonic acquisition capabilities was required. The tool used to measure shear wave velocity anisotropy in this work was the Dipole Sonic Shear Imager (DSI) (Schlumberger, 1995). In order to excite a shear wave, the DSI has two electrodynamic dipole transmitters, which are oriented perpendicular to each other and offset along the tool by 0.15 m. These excite a flexural wave that travels along the borehole. The transmitters operate in a frequency range of 0.8 to 5 kHz. The flexural wave excites shear waves that probe approximately 1.5 m into the formation, depending on the velocity. The receiver array, which starts 3.35 meters above the upper dipole transmitter, has eight receiver stations spaced 15.24 cm apart, each consisting of two pairs of piezoelectric hydrophones aligned with the dipole transmitters. Both the inline and crossline (90° out of line from the transmitted wave) waveforms of the waves excited by the two orthogonally mounted transmitters are recorded for a total of four waveforms. Using the Alford rotation processing technique, the fast and slow directions

and velocities of the shear wave are determined (Alford, 1986). The dispersive nature of the flexural wave is used to filter out the high frequency data and isolate the low frequencies that penetrate deeper into the formation (Sinha et al., 1994).

As discussed in Boness and Zoback (2006), the shear wave velocities are recorded along a plane that is normal to the wellbore orientation (Fig. 6-3). For this reason in TI formations, the shear wave velocity anisotropy is best observed by the tool if the borehole is perpendicular to the axis of symmetry. For example if the anisotropy is structurally controlled by the bedding, the optimal borehole orientation for recording dipole sonic data would be perpendicular to the bedding. Or, if the anisotropy is stress-induced as a result of anisotropic horizontal principal stresses, a vertical well is optimal. However, in practice, orthogonal alignment of the well and the formation axis of symmetry is frequently not the case. When the formation fast direction is at an angle to the acquisition plane, the recorded maximum and minimum shear wave velocities may not be the same as the absolute maximum and minimum velocities in the formation. Furthermore, the measured fast direction may not be the true formation fast direction. Because of the discrepancy between the acquisition plane and the fast direction of the formation, we needed to consider both true and apparent fast directions following Bonness and Zoback (2006). The true fast direction is the direction of absolute maximum shear wave velocity in the formation. The fast direction measured with the DSI in the acquisition plane normal to the wellbore is referred to as the apparent fast direction.

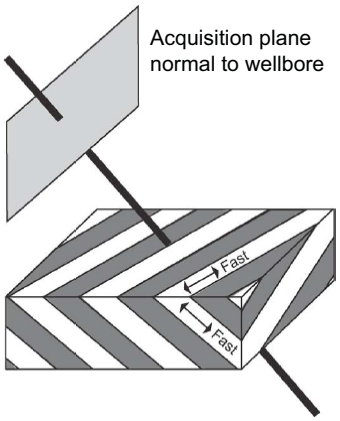

Figure 6-3: Example of the DSI acquisition plane geometry in relation to a formation with an arbitrarily aligned symmetry axis (used with permission from (Boness and Zoback, 2006)).

Boness and Zoback (2006) developed a formalism that can be used to determine the relationship between the true and apparent fast directions for an arbitrarily oriented borehole. Their 3D model can be used to compute the apparent fast direction that is expected to be measured by a dipole sonic tool for a known borehole trajectory and known fast direction orientation (e.g., from measured bedding orientations as in Figure 6-3). The theoretical apparent fast azimuth is described by the dip direction of the line of intersection between the plane normal to the borehole and the plane of the true fast direction. Using this model, the theoretical apparent fast azimuth for known bedding orientations can be determined, and the structure-induced measured apparent fast azimuths can be characterized. Measured fast directions that do not align with the theoretical structure-induced apparent fast directions are likely due to stress-induced velocity anisotropy.

6.4 DEEP WATER, SUB-SALT GULF OF MEXICO WELL LOG DATA

The data used in this study was acquired from three deep water (>1500 m) Gulf of Mexico wells (W, C, E) drilled near a large regional salt body (Fig. 6-4). The wells were drilled through the salt structure (approximately 2400-4000 m TVD), but the DSI data was acquired below that interval for each of the wells (outlined in orange for each well in Fig. 6-4b-d). For the depths that the data was collected, well W (the most westerly well) is about 830 m south of the salt structure (Fig. 6-4b) and well E (the most easterly well) is about 680 m south of the salt (Fig. 6-4d). Well C (the central well) was drilled down dip and deviated away from the salt structure such that the bottom of the well is about 2240 m south of the salt structure (Fig. 6-4c).

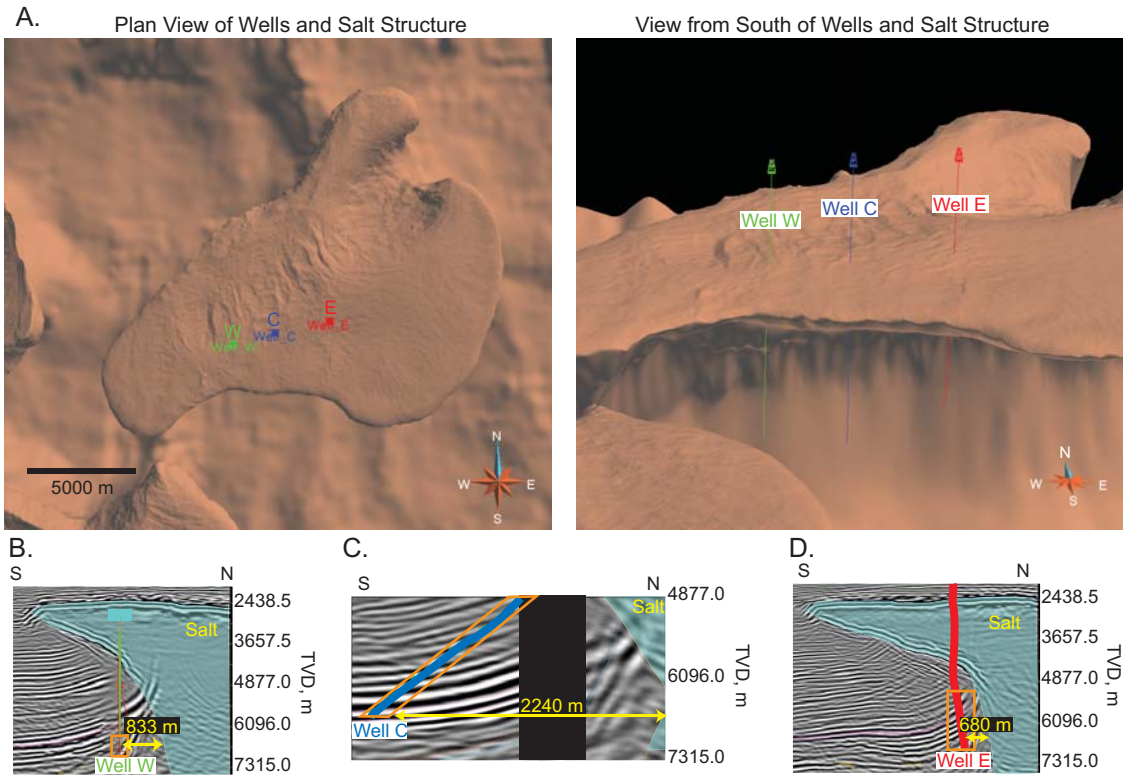

Figure 6-4: Locations of three deep water Gulf of Mexico wells in relation to the salt diaper. A.) Plan view and perspective view looking north of the wells and salt body. B.) South to north seismic cross section showing location of well W. The orange box indicates section of well with DSI data. C.) South to north seismic cross section showing location of well W. The orange box indicates section of well with DSI data. D.) South to north seismic cross section showing location of well E. The orange box indicates section of well with DSI data.

In addition to shear wave velocity anisotropy data collected by the DSI tool, several other types of borehole data were used in this study. We used 4-arm caliper data to examine the shape of the boreholes. Gamma ray logs were used so that we could compare the anisotropy in different rock types (i.e., sandstone versus shales). We also used dipmeter logs from the oil-based mud image logs (OBMI) to determine the orientations of the bedding that intersects the boreholes (Fig. 6-5). In all the wells, the bedding dips primarily to the south. The bedding in well W is not as consistent as it is in the other two wells, particularly in the depth range over which DSI data was collected. At these depths, the dip is generally less than 20°, but can be as great as 60°. The dip direction of the bedding in this zone is highly variable. Well C has the most consistent bedding orientations. The bedding dips towards the south and dips 18 to 30°. In Well E, the dip direction is towards the southeast in the upper portion of the well and

towards the south in the lower portion. The dip angle is the steepest of the three wells and ranges from 30 to 55°.

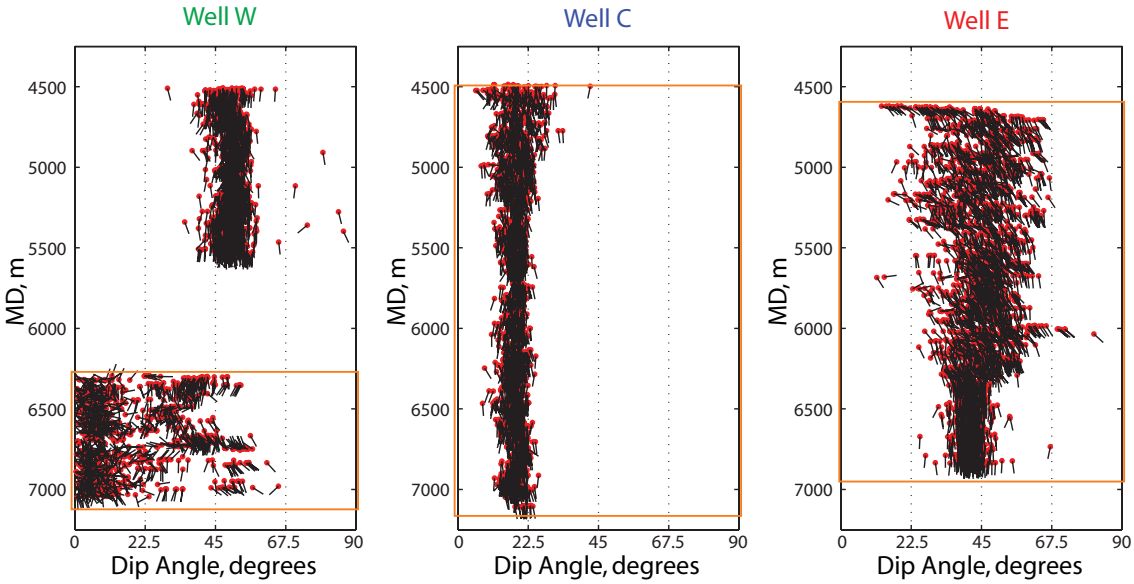

Figure 6-5: Tadpole plots of dipmeter data of the bedding for the three wells. The location along the x-axis direction indicates dip angle and the orientation of the "tail" indicates dip azimuth where up is north and right is east. The orange box indicates the measured depths along which DSI data was obtained.

6.5 QUALITY CONTROL OF LOG DATA

The plots on the left of Figure 6-6(a-c) show the raw apparent shear wave fast direction calculated from the DSI data for the three wells. The fast direction was determined at every measurement depth by Alford rotation (Alford, 1986) even if the data was not meaningful. Therefore, we applied a series of quality controls to the data. To honor the quality control criteria, (1) the fast azimuth error should be small, (2) velocity difference between the fast and slow directions should be large, (3) the minimum energy should be low and (4) cross-dipole energy difference should be significant. In cases where the wellbore is elongated due to keyseating, the effects of the wellbore ovality on the measured fast direction should also be removed.

The quality control filters used data parameters that were calculated during the processing of the DSI. For each well, we show the data that passes through (blue and cyan) and that is filtered out (black and gray) for each of the quality control criterion in both the shales and the sands (Fig. 6-6a-c). First, the fast azimuth error, which was calculated during the Alford rotation, was used to filter out data in which the fast

directions are poorly constrained. In all cases analyzed in this work, the fast azimuth error cutoff was less than 10°.

The slowness anisotropy was calculated from the slowness values in the fast and slow directions. It is defined as

$$\text{Slowness anisotropy (\%)} = \Delta t_{ss}\text{-}\Delta t_{sf}/\Delta t_{sm} * 100 \qquad (6\text{-}1)$$

where Δt_{ss} is the shear wave slowness in the slow direction, Δt_{sf} is the shear wave slowness in the fast direction, and Δt_{sm} is the mean shear wave slowness. We required that the slowness anisotropy be greater than 3% in the shales and 2% in the sands. The slowness anisotropy in the sands had a different cutoff than the shales because the average slowness in the sands was much lower than in the shales (Fig. 6-6). We also looked at the magnitude of the measured slowness to ensure that the data were reasonable. The slowness values from 4500 – 5800 m (MD) in well C were significantly higher than the monopole shear wave slowness and correspond to velocities between 760 to 1400 m/s as compared to 1200 to 2200 m/s in the deeper section of the well. While it is common for monopole shear wave velocity measurements to be inaccurate in slow formations, we were uncertain whether the dipole measurements were meaningful. For this reason, we only analyzed the DSI data below 5800 m in well C. This discrepancy between the monopole and dipole shear wave velocities was not observed in the other two wells.

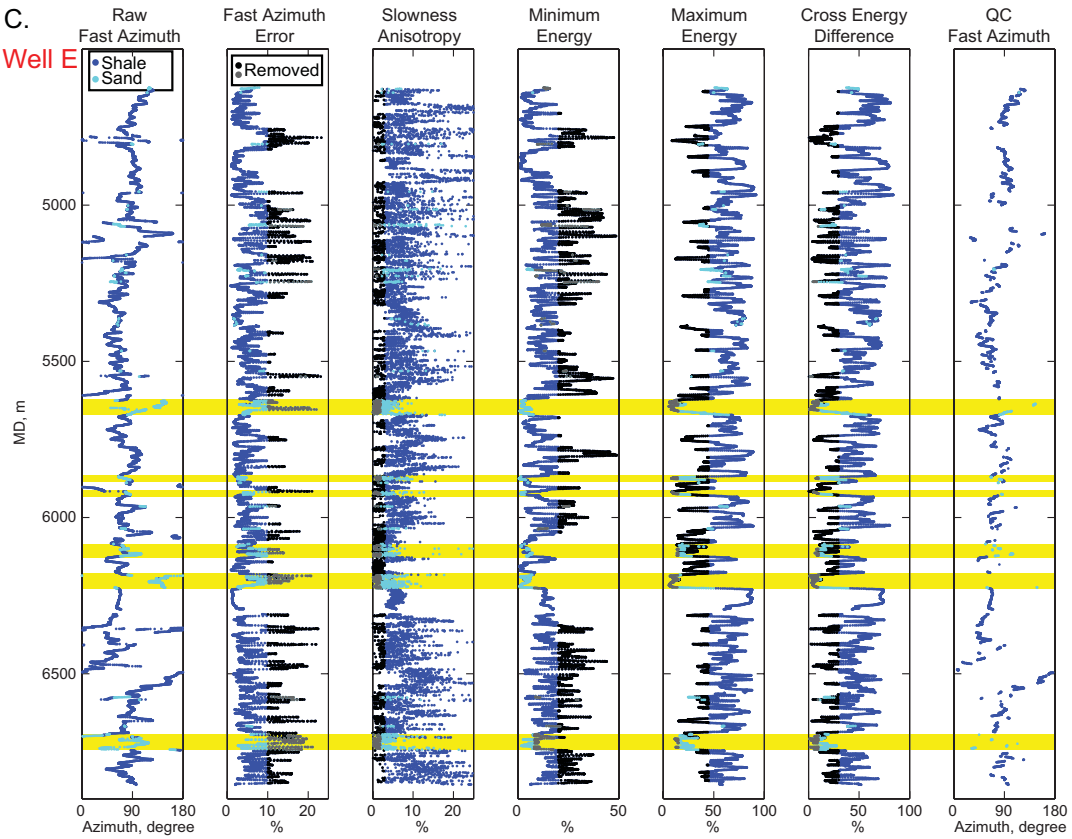
C.
Well E
Raw Fast Azimuth
Fast Azimuth Error
Slowness Anisotropy
Minimum Energy
Maximum Energy
Cross Energy Difference
QC Fast Azimuth
Shale
Sand
Removed
MD, m
5000
5500
6000
6500
0 90 180
Azimuth, degree
0 10 20
%
0 50
0 50 100
0 90 180

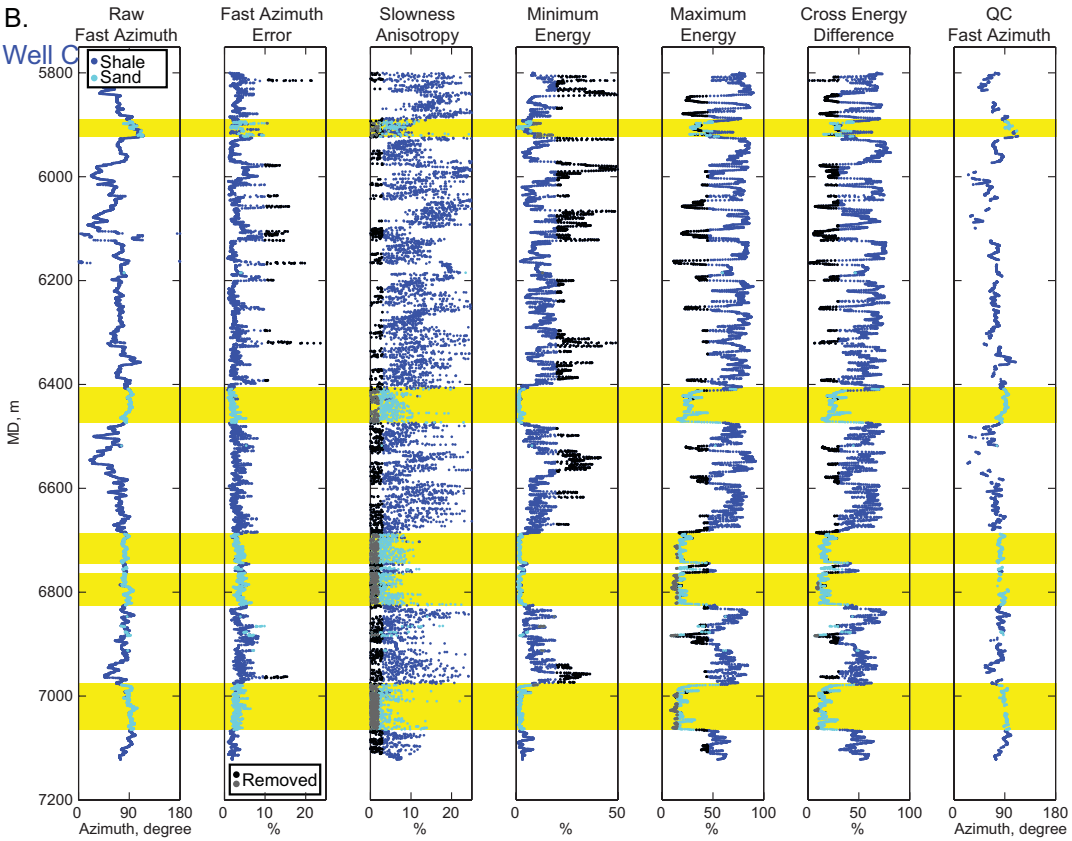
B.
Well C
Raw Fast Azimuth
Fast Azimuth Error
Slowness Anisotropy
Minimum Energy
Maximum Energy
Cross Energy Difference
QC Fast Azimuth
Shale
Sand
Removed
MD, m
5800
6000
6200
6400
6600
6800
7000
7200
0 90 180
Azimuth, degree
0 10 20
%
0 50
0 50 100
0 90 180

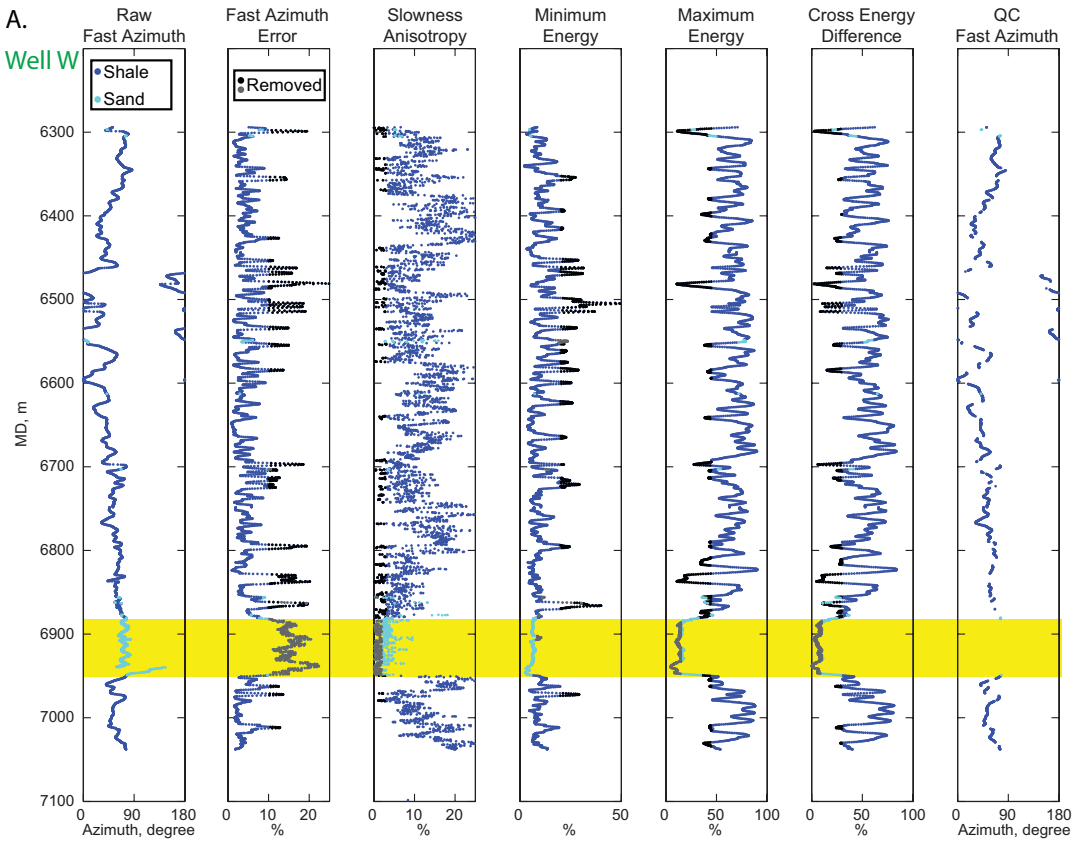

Figure 6-6: DSI data in the shales (blue) and sands (cyan) and the quality control filters applied to the data from the three wells: A.) well W, B.) well C, and C.) well E. Black (shale) and gray (sand) points indicate data that do not honor the quality control criterion for each filter. The significance of the cut-off values for each parameter is explained in the text. The yellow bars indicate major sand units.

Another way to ensure the quality of the fast directions was to examine the minimum and maximum energies in the cross-components as the waveforms are rotated (Sinha et al., 2000). The material is considered isotropic if both the minimum and maximum energies are small. If the data do not fit the assumed TI model (Thomsen, 1986), then the minimum energy will be large. Therefore, an anisotropic zone is one in which the minimum energy is small and there is a large difference between the minimum and maximum energies. To be included in our analysis, the data in the shales had to have a cross energy difference greater than 30%, with a minimum energy less than 20%, and maximum energy greater than 45% (Fig. 6-6). In the sands, the cross energy difference had to be greater than 10%, with a minimum energy less than 8%, and a maximum energy greater than 15% (Fig. 6-6). Lower energy values were used in the sands, because the high porosity sands were saturated with fluids and the waveform energy was greatly attenuated. Even with the revised quality control criteria, most of the

data in the sands of wells W and E did not meet the data standards. This was primarily due to high attenuation such that the values of the maximum energy and the cross-energy difference in the sands of these wells were very low. Well C sands exhibited significant anisotropy both in the velocity and energy measured in the slow and fast directions. The fast directions of the sands in well C were consistent, ranging from 75° to 100° rotating counter-clockwise with depth.

We also required that the fast azimuth rotation was limited to less than 5° over 1.52 m. This criterion ensured that the tool was operating correctly and the fast directions represent a physical mechanism. It primarily eliminated fast directions that were tracking the rotation of the tool in the wellbore rather than measuring shear wave velocity anisotropy in the formation. Another quality control that could be employed for the same reason removes fast directions that are parallel and perpendicular to the azimuth of the tool. Unfortunately, the tool azimuth was not available for these wells so we could not include this filter in the quality controls. The plots on the right side of Figure 6-6 (a-c) show the quality controlled fast azimuths that honor all of the criteria described above.

As mentioned above, another possible source of error in the shear wave anisotropy data results from the shape of the borehole. Keyseating, which enlarges the top and bottom of a deviated borehole due to mechanical wear, is common in wells drilled through soft sediments like those found in the Gulf of Mexico. Shear waves have a slower velocity in the direction of elongation (which is the same as the wellbore azimuth), so the fast azimuth may be biased normal to this direction. In theory, the borehole ovality results in apparent anisotropy in the mid-range frequencies that sample the damaged area and there should be little to no separation between fast and slow velocities at the high and low frequencies (Fig. 6-2a). Since the lower frequency shear wave data was used in this study, the effects of borehole enlargement should have been removed with the quality controls described above. However, as an extra precaution, we implemented a final quality control when the borehole was deviated from vertical and the caliper data indicated significant wellbore elongation along the top and bottom of well. When this was the case, we compared the quality controlled fast azimuths and the theoretical wellbore fast azimuth. If they were within 15° of each other, the fast

directions were attributed to the ovality of the wellbore and removed from the final analysis.

For the three wells, we examined the necessity for filtering the fast directions that were potentially biased due to the elongation of the wellbore (Fig. 6-7). Figure 6-7 shows the 4-arm caliper data for each of the wells. Separation between the caliper 1 (caliper arms 1 and 3) and the caliper 2 (caliper arms 2 and 4) diameters indicate that the wellbore is elongated. When caliper 1 is equal to caliper 2, the wellbore is in gauge and not elongated. The caliper data for both well W (Fig. 6-7a) and well E (Fig. 6-7c) showed that the wells were in gauge over their entire length. For this reason, we did not need to use a borehole ovality filter on the anisotropy data from these wells. These wells are nearly vertical so they were less susceptible to keyseating during drilling. Well C is deviated about 30° from vertical and keyseating is present along much of the length of the well. This is evident in the difference between the caliper 1 and caliper 2 diameters in the shales (Fig. 6-7b). However, the wellbore is in gauge through the sands. Based on this analysis, we only implemented the borehole ovality filter in the shales.

To filter out the fast directions in well C that likely resulted from the borehole ovality associated with keyseating, we used the borehole azimuth to determine the wellbore elongation fast direction (Figure 6-8). The wellbore elongation fast direction is normal to the borehole azimuth. Since well C was drilled towards the south, the fast direction due to elongation is towards the east. The quality controlled fast directions for well C that are within 15° of the wellbore elongation fast direction are shown in black in the second panel of Figure 6-8. In the shales, when the measured fast directions corresponded to the theoretical wellbore elongation fast direction, the data were filtered out. The last panel in Figure 6-8 shows the final quality controlled fast directions.

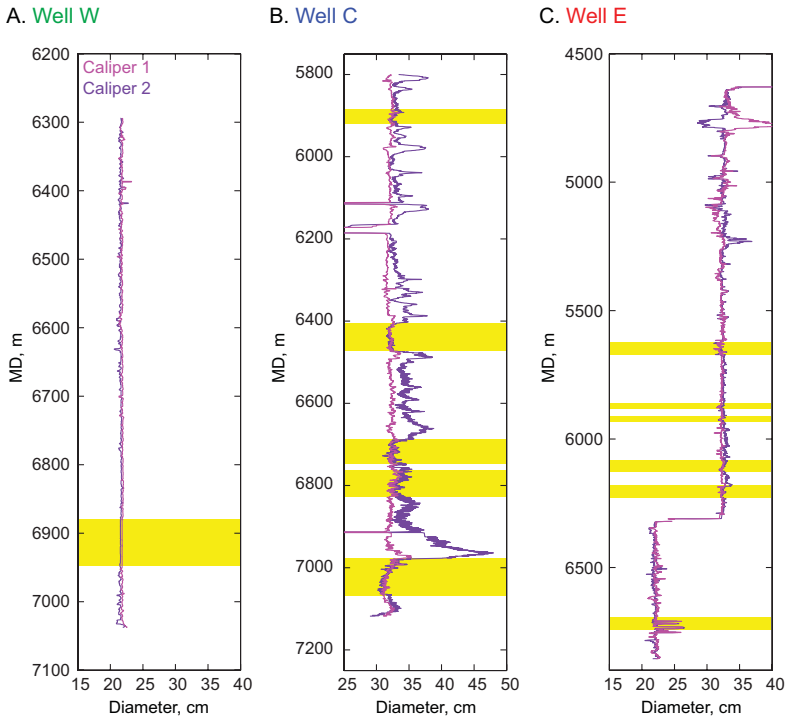

Figure 6-7: Borehole ovality from caliper data for (A.) well W, (B.) well C, (C.) and well E. Caliper 1 (magenta) and caliper 2 (purple) diameters are plotted.

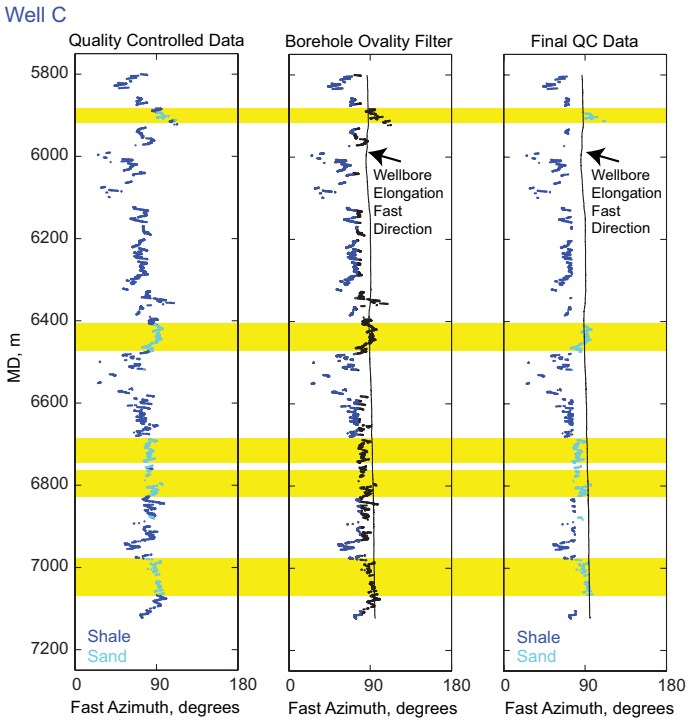

Figure 6-8: Filtering the quality controlled fast azimuths for borehole ovality for well C. The first panel shows the quality controlled fast directions characterized as either shale (blue) or sand (cyan). The second panel shows the wellbore elongation fast direction. The quality controlled fast directions that are within 15° of the wellbore fast direction are shown in black. The last panel shows the final quality controlled fast directions. Sand units are highlighted in yellow.

6.6 CHARARACTERIZING THE MECHANISMS OF ANISOTROPY

Once the DSI data was quality controlled, we could characterize it based on the mechanism (structure or stress) controlling the shear wave anisotropy using the technique developed by Boness and Zoback (2006) that was described above. First, we calculated the theoretical structural apparent fast direction that the DSI tool should measure based on the known bedding geometry from the dipmeter logs (Fig. 6-5) and the borehole trajectories. In this way, we accounted for the known TI anisotropy rather than assuming a horizontal or vertical TI anisotropy. We then compared the theoretical structure-induced fast directions with the measured quality controlled fast directions. Measured fast directions that were within 15° of the theoretical apparent fast directions were considered to be structure-induced. We then assumed that the remaining fast directions stress-induced.

The results of this analysis are summarized in Figure 6-9 for the three wells. The first panel shows the bedding strike, which is the structural true fast direction, in green. The second panel plots the theoretical structural apparent fast directions in magenta along with the quality controlled measured fast directions. The shales are shown in blue and the sands are in cyan. The third panel characterizes the measured data into structure-induced (black) or stress-induced (red). The wellbore elongation fast direction (black line) for well C is also shown for comparison (Fig. 6-9b). The fast directions that are within 15° of the theoretical apparent fast directions were characterized as structure-induced. Based on the process of elimination, the remaining fast directions were assumed to be stress-induced. An averaged stress-induced fast direction is indicated by the red dashed line.

In well W, the theoretical apparent fast azimuths reflect the incoherent bedding orientations observed in the dipmeter log, but a coherent fast azimuth signal was measured (Fig. 6-9a). The orientation of this fast azimuth is primarily about 60°, except for the zone of rotation at about 6500 m (MD) where the azimuth is about 20°. No quality controlled fast azimuths were measured in the major sand unit. We characterized the majority of the fast azimuths in the shales as stress-induced.

The DSI data from well C is analyzed in Figure 6-9b. We have two main observations. First, there is a clear separation of the two mechanisms. The structure-induced fast directions range from 80 to 100°. The stress-induced fast azimuths range

from primarily from 55 to 75°. The second observation is that the fast directions observed in the sands appear to be structure-induced, while much of the observed data in the shale appears to be stress induced.

In well E, the bedding orientations are less consistent above 6300 m (MD) than below that depth (Fig. 6-9c). There are zones with significant separation in the fast azimuths associated with the two mechanisms of anisotropy (above 5200 m and between 6300 and 6500 m), but the separation is less obvious than in well C. As in well W, most of the data in the sands was filtered out by the quality control criteria. Therefore, we do not see the relationship between the fast direction in the sands and the structure that was observed in well C. The assumed stress-induced fast azimuth rotates counter-clockwise from approximately 105° at the top of the well to 50°. However, there is significant overlap in the structure-induced and assumed stress-induced fast directions, particularly in the depth range of 5200 to 6200 m.

In Figure 6-10, we summarize the change in stress-induced apparent fast azimuths with respect to the geometry of the salt structure. The stress-induced fast azimuths are described as "apparent" fast directions because they were measured in a plane perpendicular to the wells. If the principal stresses are not align with that plane, then the measured fast azimuths do not reflect the absolute true stress-induced fast directions. Data from each well showed rotations in the fast azimuths with depth. At the bottom of the depth range for each well, the fast azimuths (black lines) are approximately parallel to the salt stem. In well W, the data indicate very consistent stress-induced apparent fast azimuths at the top and bottom of the depth interval, but show a significant rotation to the north in the middle. In well C, which is deviated towards the south, the fast azimuths rotate clockwise with depth until they are nearly parallel to the salt stem. Well E has the longest depth interval of DSI data and the data closest to the salt structure. The shallowest data are nearly perpendicular to the salt stem. The majority of the data indicate fast azimuths that are approximately parallel to the salt stem. However, near the deepest part of the well (dark gray) the fast azimuth rotates to nearly north-south but quickly rotates back to an azimuth of about 70°. This rotation may indicate the presence of an active fault.

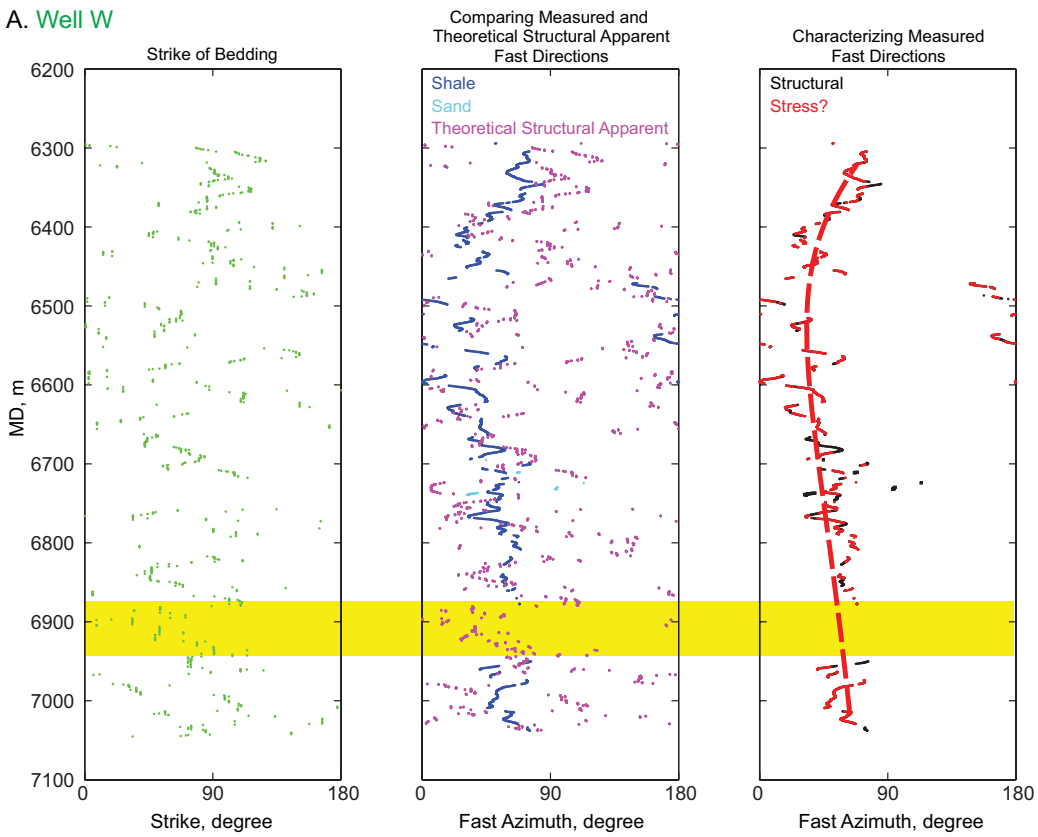
A. Well W
Strike of Bedding
Comparing Measured and Theoretical Structural Apparent Fast Directions
Characterizing Measured Fast Directions
Shale
Sand
Theoretical Structural Apparent
Structural
Stress?
MD, m
6200
6300
6400
6500
6600
6700
6800
6900
7000
7100
0
90
180
Strike, degree
Fast Azimuth, degree
Fast Azimuth, degree

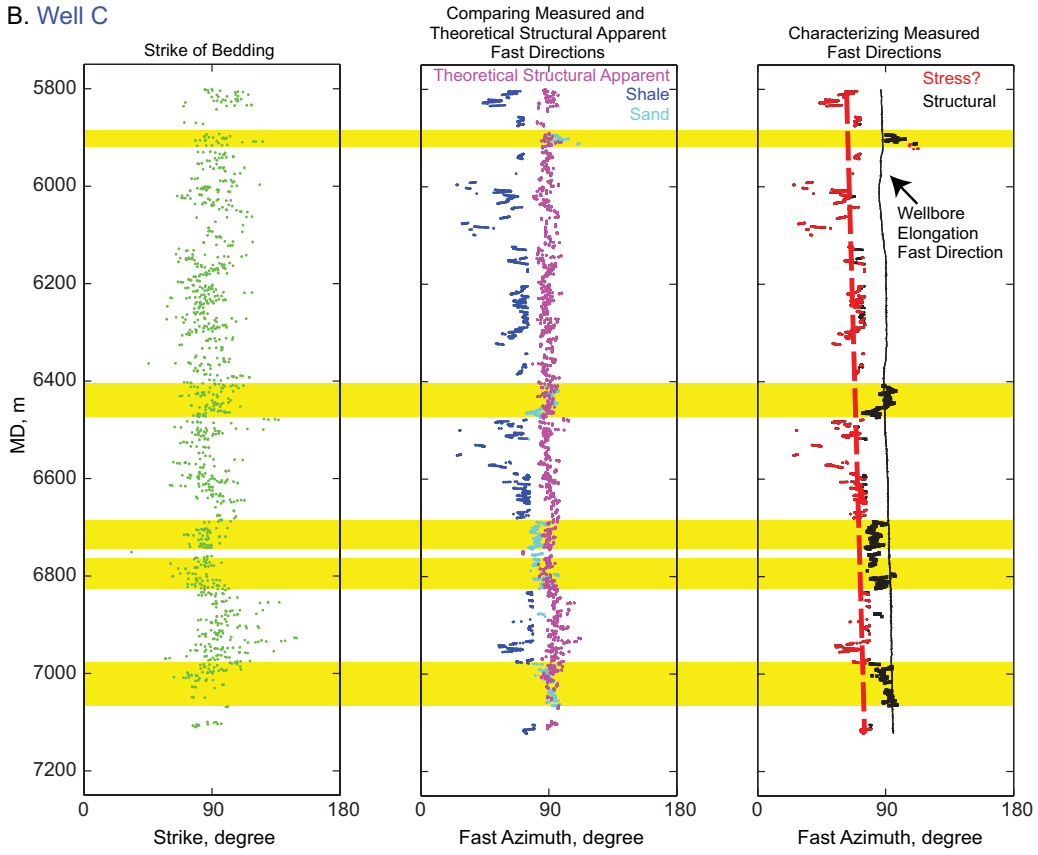
B. Well C
Strike of Bedding
Comparing Measured and Theoretical Structural Apparent Fast Directions
Characterizing Measured Fast Directions
Theoretical Structural Apparent
Shale
Sand
Stress?
Structural
Wellbore Elongation Fast Direction
MD, m
5800
6000
6200
6400
6600
6800
7000
7200
0
90
180
Strike, degree
Fast Azimuth, degree
Fast Azimuth, degree

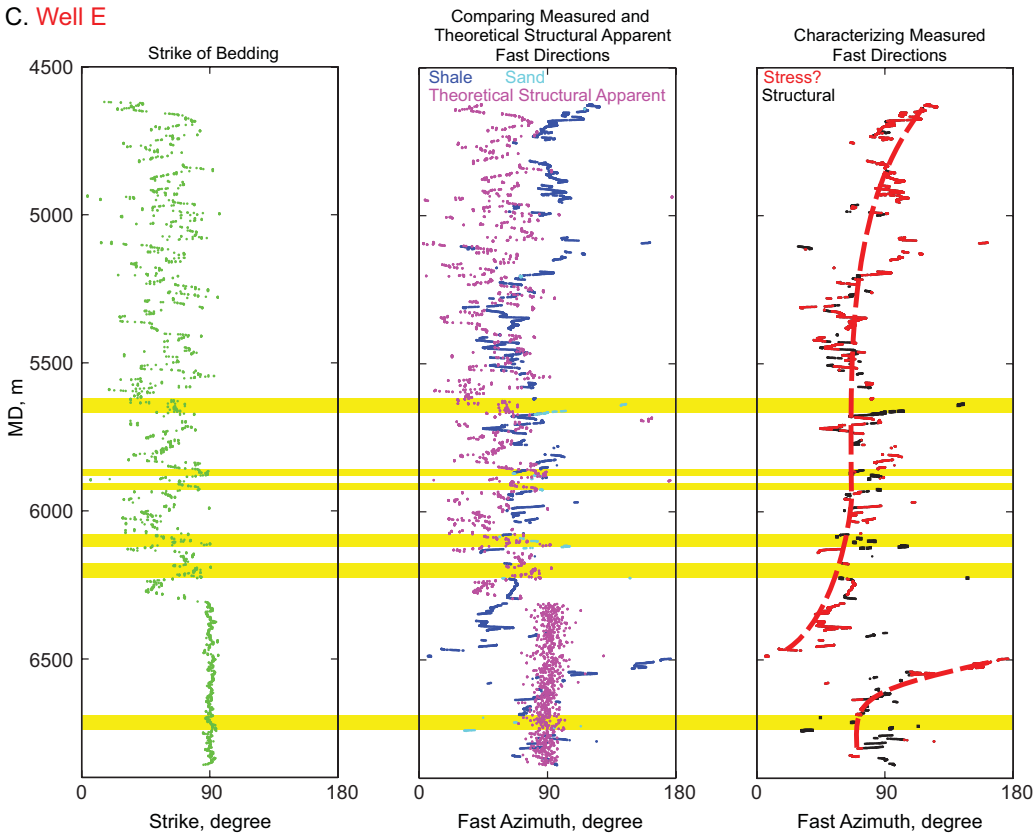

Figure 6-9: Characterizing the mechanisms controlling the shear wave velocity anisotropy in (A.) well W, (B.) well C, and (C.) well E. The first panel shows the strike of bedding (green). The second panel plots the theoretical structural apparent fast azimuths (magenta) determined from the bedding data and well trajectories along with the quality controlled fast directions characterized by lithology (shales in blue and sands in cyan). The third panel characterizes the measured data into structure-induced (black) or stress-induced (red). An averaged stress-induced fast direction is indicated by the red dashed line in the third panel. Sand units are highlighted in yellow.

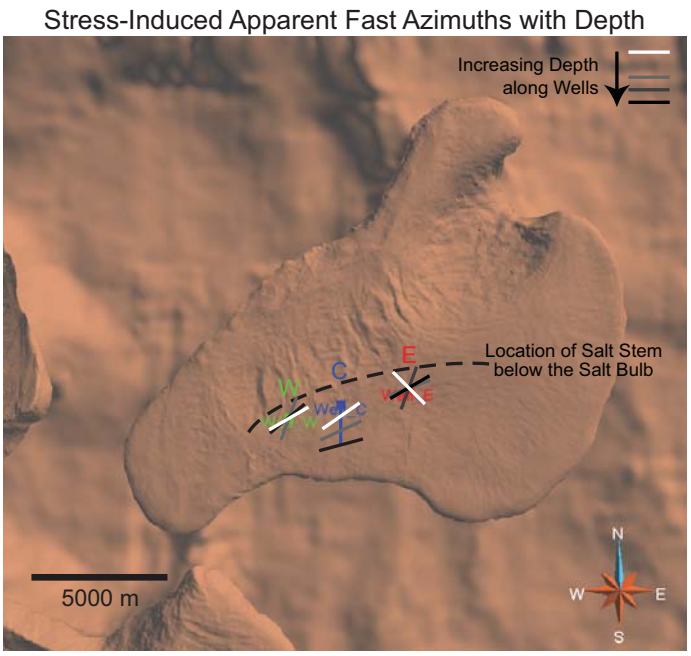

Figure 6-10: Summary of stress-induced apparent fast azimuths. The lines indicate the averaged fast directions at the top (white), middle (gray), and bottom (black) of the depth ranges for which DSI data was analyzed in the wells. The black dashed line approximates the location of the stem of the salt below the salt bulb.

6.7 DISCUSSION

The shear wave anisotropy observed in dipole sonic data is influenced by several factors, making it difficult to analyze. In this particular dataset, we encountered certain challenges due to the borehole trajectories and limitations in the available data. Because the azimuth of the well C is similar to the dip direction of the bedding, the theoretical structural apparent fast direction is similar to the theoretical wellbore fast direction. This makes it more difficult to distinguish if the observed fast directions were associated with the damage zone of the wellbore or intrinsic to the structure of the formation. Also, the dataset lacked information that would have made the analysis more complete. For example, without the azimuth of the DSI tool during data acquisition, we were limited in the quality controls that could be applied to the data. If the measured fast azimuths were tracking the azimuth of the tool, it would indicate that the data do not reflect the anisotropy of the formation. We also did not have access to dispersion curves. As discussed below, these could have been used to confirm the mechanisms controlling the observed anisotropy.

One of the goals of this investigation was to determine if stress-induced anisotropy was measured in the wells. While we did observe quality controlled fast directions in all

three wells that were not attributed to the known structural fast directions, uncertainty remains as to whether they can be definitively characterized as stress-induced. In all the wells, the assumed stress-induced anisotropy was occurring in the shales rather than the sands, despite the fact that shales are typically considered to be highly susceptible to structure-induced anisotropy (Hornby, 1998; Johnston and Christensen, 1995). Well C was the only well in which the shear waves recorded in the sands indicated anisotropy. The anisotropy in these sands appears to be structure-induced. This is consistent with the thinly bedded turbidite sands found in the region.

One factor that could influence the fast azimuths recorded in the sands versus the shales is the depth of penetration of the shear waves. This is controlled by the frequency of the wave and the velocity of the formation. In theory, the stress concentration around the borehole should equilibrate with the far-field stress state at a distance of 3 borehole radii away, which is approximately 0.35 to 0.5 m for these wells. We indicated above that the dipole sonic shear waves sampled the formation at a depth of penetration of about 1.5 m from the borehole wall; however this is just an average value. In the shales, the shear wave velocities range from 1200 to 1900 m/s such that for a frequency of 800 Hz the wavelength is 1.5 to 2.37 m. In the sands, with velocities ranging from 1500 to 2300 m/s, the wavelength is 1.87 to 2.87 m. Therefore, the low frequencies of the shear waves should be penetrating outside the influence of the borehole stress concentration for both lithologies, and the depth of penetration of the waves should not be a factor..

A limitation of this technique is that once we identified the stress-induced apparent fast directions, we could not determine the true maximum compressive stress direction from the measured apparent stress-induced fast direction. As in the case of the bedding, if the stresses are not aligned with the borehole then the DSI tool is measuring an apparent fast direction rather than a true fast direction. If the wellbore is deviated from vertical, but the principal stresses are aligned vertically and horizontally, then the azimuth of the true and apparent fast directions are the same, but the apparent dip of the fast direction differs from the true dip (which is 0°). However, in the complex stress environment near a large salt structure, it is likely that the principal stresses are deviated from the typically assumed orientations of a vertical stress and two horizontal stresses. In this case, the apparent fast direction measured by the tool is a line (with an azimuth and dip) projected onto a plane normal to the wellbore trajectory. This line marks the

intersection of the plane normal to the wellbore and the plane defined by the two principal stress orientations controlling the fast and slow directions of the formation. Without more information about the plane containing the principal stresses, we could not determine the absolute true stress fast directions.

Therefore, independent confirmation that the data is stress-induced is necessary to fully characterize the data. One possible source of this confirmation is dispersion curve analysis. If the data is indeed stress-induced, the dispersion curves should show the characteristic crossover illustrated in Figure 6-2c. If the anisotropy is related to a borehole damage zone, the dispersion curve will look more like the schematic in Figure 6-2a. Unfortunately, because the frequency-domain processing required for the creation of dispersion curves is not part of the traditional processing of the DSI data, we did not have the dispersion curves available for this investigation.

This touches on the second goal of this investigation, which was to determine if this technique replaces or supplements dispersion curve analysis as a means for classifying the mechanisms of anisotropy. Based on the analysis of this dataset, it is apparent that this technique cannot replace dispersion curve analysis. However, this technique does supplement it. First, the quality controls implemented in this work remove anisotropy data that are not meaningful. This limits the data for which dispersion curve analysis should be completed. This technique also identifies the fast directions most likely controlled by either structural- or stress-related mechanisms. This initial classification can be useful for indicating the range of data to be examined in the dispersion curve analysis.

The final goal of this work was to determine if this technique provides information that can be used to validate a potential numerical model of the salt-related stress perturbations. Despite the fact that we cannot determine the absolute true stress-induced fast direction, we believe that this technique does have applications for validating numerical modeling results. If the numerical model simulates the principal stress orientations around the salt body along the borehole trajectories, we can determine the true stress-induced fast directions predicted by the model. Those true fast directions can be used as input into the Boness and Zoback (2006) formalism in the same way that the bedding structure was used in this investigation. Based on the true fast directions from the numerical model, we can calculate the theoretical apparent stress-induced fast

directions that would be measured in the well by the DSI tool. We can then test for consistency by comparing these theoretical apparent stress-induced fast directions to the measured apparent stress-induced fast directions. If the modeled fast azimuths are consistent with the measured fast azimuths, then it provides supporting evidence for the numerical modeling results.

6.8 ACKNOWLEDGEMENTS

This work was completed with support from the Stanford Rock Physics and Borehole (SRB) consortium. We would like to thank Wayne Wendt of BP for providing us with the data for this project. A special thanks to Naomi Boness and Dan Moos for their expertise in analyzing shear wave data.

REFERENCES

Alford, R. M., 1986, Shear data in the presence of azimuthal anisotropy: Annual International Meeting, Society of Exploration Geophysics, Expanded Abstracts, v. 56, p. 476-479.

Anderson, R. A., D. S. Ingram, and A. M. Zanier, 1973, Determining Fracture Pressure-Gradients from Well Logs: Journal of Petroleum Technology, v. 25, p. 1259-1268.

Baranoski, M. T., R. A. Riley, and M. E. Wolfe, eds., 1996, Cambrian-Ordovician Know Group unconformity play: The atlas of major Appalachian gas plays, v. 25, West Virginia Geological and Economic Survey Publication, 181-187 p.

Barton, C. A., and M. D. Zoback, 1994, Stress perturbations associated with active faults penetrated by boreholes - Possible evidence for near-complete stress drop and a new technique for stress magnitude measurement: Journal of Geophysical Research-Solid Earth, v. 99, p. 9373-9390.

Barton, C. A., M. D. Zoback, and D. Moos, 1995, Fluid-flow along potentially active faults in crystalline rock: Geology, v. 23, p. 683-686.

Blanton, T. L., and J. E. Olson, 1999, Stress magnitudes from logs: effects of tectonic strains and temperature: SPE Reservoir Evaluation and Engineering, v. 2, p. 62-68.

Boness, N. L., and M. D. Zoback, 2004, Stress-induced seismic velocity anisotropy and physical properties in the SAFOD Pilot Hole in Parkfield, CA: Geophysical Research Letters, v. 31.

Boness, N. L., and M. D. Zoback, 2006, A multiscale study of the mechanisms controlling shear velocity anisotropy in the San Andreas Fault Observatory at Depth: Geophysics, v. 71, p. F131-F146.

Brie, A., T. Endo, D. Hoyle, D. Codazzi, C. Esmersoy, K. Hsu, S. Denoo, M. C. Mueller, T. Plona, R. Shenoy, and B. Sinha, 1998, New Directions in Sonic Logging: Oilfield Review, v. Spring.

Brown, K. M., B. Bekins, B. Clennell, D. Dewhurst, and G. K. Westbrook, 1994, Heterogeneous hydrofracture development and accretionary fault dynamics: *Geology*, v. *22*, p. 259-262.

Brudy, M., and M. D. Zoback, 1993, Compressive and tensile failure of boreholes arbitrarily-inclined to principal stress axes - Application to the KTB boreholes, Germany: International Journal of Rock Mechanics and Mining Sciences & Geomechanics Abstracts, v. 30, p. 1035-1038.

Brudy, M., and M. D. Zoback, 1999, Drilling-induced tensile wall-fractures: implications for determination of in-situ stress orientation and magnitude: International Journal of Rock Mechanics and Mining Sciences, v. 36, p. 191-215.

Brudy, M., M. D. Zoback, K. Fuchs, F. Rummel, and J. Baumgartner, 1997, Estimation of the complete stress tensor to 8 km depth in the KTB scientific drill holes: Implications for crustal strength: Journal of Geophysical Research-Solid Earth, v. 102, p. 18453-18475.

Brune, J. N., 1970, Tectonic stress and the spectra of seismic shear waves from earthquakes: Journal of Geophysical Research, v. 75, p. 4997-5009.

Byerlee, J., 1978, Friction of rocks: Pure and Applied Geophysics, v. 116, p. 615-626.

Carr, T. R., D. F. Merriam, and J. D. Bartley, 2005, Use of relational databases to evaluate regional petroleum accumulation groundwater flow, and CO_2 sequestration in Kansas: AAPG Bulletin, v. 89, p. 1607-1627.

Cartwright, P., and G. Walker, 2000, In-situ stress measurement, 83 level shaft pillar area, TauTona mine, AngloGold, *in* R. M. T. Ltd., ed.

Chang, C., M. D. Zoback, and A. Khaksar, 2006, Empirical relations between rock strength and physical properties in sedimentary rocks: Journal of Petroleum Science and Engineering, v. 51, p. 223-237.

Coyle, B. J., and M. D. Zoback, 1988, In situ permeability and fluid pressure measurements at approximately 2-km depth in the Cajon Pass research well: Geophysical Research Letters, v. 15, p. 1029-1032.

Crampin, S., 1986, Anisotropy and Transverse Isotropy: Geophysical Prospecting, v. 34, p. 94-99.

Crampin, S., 1991, Wave-Propagation through Fluid-filled Inclusions of Various Shapes- Interpretation of Extensive-Dilatancy Anisotropy: Geophysical Journal International, v. 104, p. 611-623.

Crampin, S., and S. Chastin, 2003, A review of shear wave splitting in the crack-critical crust: Geophysical Journal International, v. 155, p. 221-240.

Deutsch, C. V., 2002, Geostatistical reservoir modeling: Applied Geostatistics: New York, Oxford University Press, 376 p.

Durrheim, R. J., A. Haile, M. K. C. Roberts, J. K. Schweitzer, S. M. Spottiswoode, and J. W. Klokow, 1998, Violent failure of a remnant in a deep South African gold mine: Tectonophysics, v. 289, p. 105-116.

EIA, 2007, Short-term Energy Outlook - June 2007, Energy Information Administration (EIA).

EPA, 2002, eGRID2002: Emissions and Generation Resource Integrated Database, <http://www.epa.gov/cleanenergy/egrid/download.htm>, Nov. 15, 2004.

EPA, 2006, eGRID2006: Emissions and Generation Resource Integrated Database, Environmental Protection Agency, Environmental Protection Agency

Fairchild Jr., N. R., and J. R. Williamson, 1998, Application of advanced stimulation technologies in the Appalachian Basin: Field case study of well performance several years later: 1998 Society of Petroleum Engineers Eastern Regional Meeting, SPE 51047, p. 95-108.

Fredrich, J. T., D. Coblentz, A. F. Fossum, and B. J. Thorne, 2003, Stress Perturbations Adjacent to Salt Bodies in the Deepwater Gulf of Mexico: SPE Annual Technical Conference and Exhibition, p. #84554.

Fredrich, J. T., and A. F. Fossum, 2002, Large-scale Three-Dimensional Geomechanical Modeling of Reservoirs: Examples from California and Deepwater gulf of Mexico: Oil and Gas Science and Technology-Revue de L'IFP, v. 57, p. 423.

Gaarenstroom, L. R., A. J. Tromp, M. C. Jong, and A. M. Brandenburg, 1993, Overpressures in the Central North Sea: implications for trap integrity and drilling safety: Petroleum Geology of Northwest Europe: 4th Conference.

Gane, P. G., A. L. Hales, and H. A. Oliver, 1946, A seismic investigation of the Witwatersrand earth tremors: Bulletin of the Seismological Society of America, v. 36, p. 49-80.

Gane, P. G., P. Seligman, and J. H. Stephen, 1952, Focal depths of Witwatersrand tremors: Bulletin of the Seismological Society of America, v. 42, p. 239-250.

Gay, N. C., 1972, Virgin rock stresses at Doornfontein gold mine, Carletonville, South Africa: Journal of Geology, v. 80, p. 61-79.

Gay, N. C., 1975, In-situ stress measurements in southern Africa: Tectonophysics, v. 29, p. 447-459.

Gay, N. C., 1977, Principal horizontal stresses in southern Africa: Pure and Applied Geophysics, v. 115, p. 3-10.

Gibowicz, S. J., and A. Kijko, 1994, An Introduction to Mining Seismology: New York, Academic Press, 399 p.

Gupta, N., P. Jagucki, J. R. Sminchak, D. Meggyesy, F. Spane, T. S. Ramakrishnan, and A. Boyd, eds., 2005, Determining carbon sequestration reservoir potential at a site-specific location within the Ohio River Valley Region: Proceedings of the 7th International Greenhouse Gas Control Technologies (GHGT-7), v. 1: Vancouver, Canada, Elsevier, 9 p.

Gupta, N., P. Wang, B. Sass, P. Bergman, and C. Byrer, 2001, Regional and site-specific hydrogeologic constraints on CO_2 sequestration in the Midwestern United States saline formations: GHGT-5.

Haimson, B., and C. Fairhurst, 1970, In situ stress determination at great depth by means of hydraulic fracturing: 11th Symposium on Rock Mechanics, p. 559-584.

Hanks, T. C., 1977, Earthquake stress drops, ambient tectonic stresses and stresses that drive plate motions: Pure and Applied Geophysics, v. 115, p. 441-458.

Hanks, T. C., and D. A. Johnson, 1976, Geophysical assessment of peak accelerations: Bulletin of the Seismological Society of America, v. 66, p. 959-968.

Hareland, G., and R. Harikrishnan, 1996, Comparison and verification of electric-log-derived rock stresses and rock stresses determined from the mohr failure envelope: SPE Formation Evaluation, v. 11, p. 219-222.

Hofmann, G. F., and S. K. Murphy, 2007, Coulomb stress triggering in the underground mining environment: 1st Canada-U.S. Rock Mechanics Symposium.

Hornby, B. E., 1998, Experimental laboratory determination of the dynamic elastic properties of wet, drained shales: Journal of Geophysical Research-Solid Earth, v. 103, p. 29945-29964.

Huenges, E., J. Erzinger, and J. Kuck, 1997, The permeable crust: Geohydraulic properties down to 9101 m depth: Journal of Geophysical Research, v. 102, p. 18255-18265.

IPCC, ed., 2007, Climate Change 2007: The Physical Science Basis: Forth Assessment Report of the IPCC: Cambridge, Cambridge University Press, 1009 p.

Isaaks, E. H., 1990, The application of Monte Carlo methods to the analysis of spatially correlated data: Ph.D. thesis, Stanford University, Stanford, CA, 213 p.

Jaeger, J. C., and N. G. W. Cook, 1979, Fundamentals of rock mechanics: London, Chapman and Hall, 593 p.

Jagucki, P. E., N. Gupta, F. Spane, and J. R. Sminchak, 2005, Evaluation of CO_2 sequestration opportunities in the Cambro-Ordovician carbonates of the Ohio River Valley region, American Geophysical Union Fall Meeting 2005, San Francisco, CA.

Johnston, J. E., and N. I. Christensen, 1995, Seismic Anisotropy of Shales: Journal of Geophysical Research-Solid Earth, v. 100, p. 5991-6003.

Keilis-Borok, V. I., 1959, On estimation of the displacement in an earthquake source and of source dimension: Ann. Geofis., v. 12, p. 205-214.

Kirsch, G., 1898, Die Theorie der Elastizitat und die Bedurfnisse der Festigkeitslehre: VDI Z, v. 42, p. 707.

Leslie, H. D., and C. J. Randall, 1990, Eccentric Dipole Sources in Fluid-Filled Boreholes - Numerical and Experiemental Results: Journal of the Acoustical Society of America, v. 87, p. 2405-2421.

Liu, E. R., S. Crampin, J. H. Queen, and W. D. Rizer, 1993, Behavior of Shear-Waves in Rocks with 2 Sets of Parallel Cracks: Geophysical Journal International, v. 113, p. 509-517.

Lucier, A., M. D. Zoback, N. Gupta, and T. S. Ramakrishnan, 2006, Geomechanical aspects of CO_2 sequestration in a deep saline reservoir in the Ohio River Valley region: Environmental Geosciences, v. 13, p. 1-19.

Lynn, H. B., and L. A. Thomsen, 1990, Reflection Shear-Wave Data Collected near the Principal Axes of Azimuthal Anisotropy: Geophysics, v. 55, p. 147-156.

McGarr, A., 1971, Violent deformation of rock near deep-level, tabular excavations- seismic events: Bulletin of the Seismological Society of America, v. 61, p. 1458-66.

McGarr, A., 1981, Analysis of peak ground motion in terms of a model of inhomogeneous faulting: Journal of Geophysical Research, v. 86, p. 3901-3912.

McGarr, A., J. Bicknell, E. Sembera, and R. W. E. Green, 1989, Analysis of exceptionally large tremors in two gold mining districts of South Africa: Pure and Applied Geophysics, v. 129, p. 295-307.

McGarr, A., and N. C. Gay, 1978, State of stress in the earth's crust: Annual Reviews of Earth and Planetary Science, v. 4, p. 405-436.

McGarr, A., R. W. E. Green, and S. M. Spottiswoode, 1981, Strong ground motion of mine tremors: some implications for near-source ground motion parameters: Bulletin of the Seismological Society of America, v. 71, p. 295-319.

McGarr, A., S. M. Spottiswoode, and N. C. Gay, 1975, Relationship of mine tremors to induced stresses and to rock properties in the focal region: Bulletin of the Seismological Society of America, v. 65, p. 981-93.

McGarr, A., and G. A. Wiebols, 1977, Influence of mine geometry and closure volume on seismicity in a deep-level mine: International Journal of Rock Mechanics and Mining Sciences & Geomechanics Abstracts, v. 14, p. 139-45.

Moos, D., and M. D. Zoback, 1990, Utilization of Observations of Well Bore Failure to Constrain the Orientation and Magnitude of Crustal Stresses - Application to Continental, Deep-Sea Drilling Project, and Ocean Drilling Program Boreholes: Journal of Geophysical Research-Solid Earth and Planets, v. 95, p. 9305-9325.

MRCSP, 2005, Midwest Regional Carbon Partnership: Phase 1 Final Report, Batelle Memorial Institute, U.S. Department of Energy, p. 262.

Mueller, M. C., 1991, Prediction of Lateral Variability in Fracture Intensity Using Multicomponent Shear-Wave Surface Seismic as a Precursor to Horizontal Drilling in the Austin Chalk: Geophysical Journal International, v. 107, p. 409-415.

Munson, D. E., 1999, Multimechanism-Deformation Parameters of Domal Salts Using Transient Creep Analysis, Report SAND99-2104, Albuquerque, NM, Sandia National Laboratories.

NETL, 2007, Carbon Sequestration Technology Roadmap and Program Plan, *in* D. o. Energy, ed., National Energy Technology Laboratory, p. 48.

Palmer, I., Z. Moschovidis, and J. Cameron, 2007, Modeling shear failure and stimulation of the Barnett Shale after hydraulic fracturing, SPE106113: 2007 Society of Petroleum Engineers Hydraulic Fracturing Technology Conference.

Peska, P., and M. D. Zoback, 1995, Compressive and Tensile Failure of Inclined Well Bores and Determination of in-Situ Stress and Rock Strength: Journal of Geophysical Research-Solid Earth, v. 100, p. 12791-12811.

Pine, R. J., P. Ledingham, and C. M. Merrifield, 1983, Insitu Stress Measurement in the Carnmenellis Granite .2. Hydrofracture Tests at Rosemanowes Quarry to Depths of 2000-M: International Journal of Rock Mechanics and Mining Sciences, v. 20, p. 63-72.

Plona, T. J., M. R. Kane, B. K. Sinha, and J. Walsh, 2002, Evaluating Stress-Induced Anisotropy and Mechanical Damage from Cross-Dipole Sonic Data Using Dispersion Analysis: SPE/ISRM Rock Mechanics Conference, p. #78233.

Plumb, R. A., and S. H. Hickman, 1985, Stress-Induced Borehole Elongation - a Comparison between the 4-Arm Dipmeter and the Borehole Televiewer in the Auburn Geothermal Well: Journal of Geophysical Research-Solid Earth and Planets, v. 90, p. 5513-5521.

Pruess, K., J. Garcia, T. Kovscek, C. Oldenburg, J. Rutqvust, C. Steefel, and T. Xu, 2002, Intercomparison of numerical simulation codes for geological disposal of CO_2, LBNL-51813, p. 86.

Rahman, M. K., M. M. Hossain, and S. S. Rahman, 2002, A shear-dilation-based model for evaluation of hydraulically stimulated natrually fractured reservoirs: International Journal for Numerical and Analytical Methods in Geomechanics, v. 26, p. 469-497.

Raleigh, C. B., J. H. Healy, and J. D. Bredehoeft, 1972, Faulting and crustal stress at Rangely, Colorado, *in* J. C. Heard, ed., ,Flow and Fracture of Rocks: Washington, D.C., American Geophysical Union, p. 275-284.

Raleigh, C. B., J. H. Healy, and J. D. Bredehoeft, 1976, Experiment in Earthquake Control at Rangely, Colorado: Science, v. 191, p. 1230-1237.

Reches, Z., 2006, Building a natural earthquake laboratory at focal depth, IODP-ICDP Fault Zone Drilling Workshop, Miyazaki, Japan, Scientific Drilling.

Reches, Z., and H. Ito, 2007, Scientific Drilling of Active Faults: Past and Future, *in* U. Harms, C. Koeberl, and M. D. Zoback, eds., Scientific Drillings Continental Scientific Drilling a Decade of Progress, and Challenges for the Future, Springer, p. 235-258.

Reches, Z., T. Jordan, M. Johnston, M. Zoback, V. Heesakkers, M. Zechmeister, S. Murphy, and G. van Aswegen, 2006, Study of near-field earthquake process; progress of the NELSAM Project in Tautona Mine, South Africa, 2006 Annual Meeting, Seismological Society of America San Francisco, CA, USA, Seismological Research Letters.

Reches, Z., T. H. Jordan, M. J. Johnston, and M. Zoback, 2005, Drilling across active faults in deep mines in South Africa for monitoring earthquake processes in the near-field: Eos Trans. AGU Fall Meeting Supplement, v. 86, p. Abstract T43D-01.

Reinecker, J., O. Heidbach, M. Tingay, B. Sperner, and B. Muller, 2005, The 2005 release of the World Stress Map.

Riley, R. A., M. T. Baranoski, J. B. Hickman, and D. M. Powers, 2003, Rose Run structure and isopach map of Ohio and Kentucky, AAPG Eastern Section Meeting, Pittsburg, PA.

Riley, R. A., J. A. Harper, M. T. Baranoski, C. D. Laughrey, and R. W. Carlton, 1993, Measuring and Predicting Reservoir Heterogeneity in Complex Deposystems: The Late Cambrian Rose Run Sandstone of Eastern Ohio and Western Pennsylvania, prepared for the U.S. Department of Energy, p. 257.

Sayers, C. M., 1994, The Elastic-Anisotropy of Shales: Journal of Geophysical Research-Solid Earth, v. 99, p. 767-774.

Schlumberger, 1995, DSI* Dipole Shear Sonic Imager: Oilfield Marketing Services, Houston, TX, p. 36.

Segall, P., 1985, Stress and Subsidence from Subsurface Fluid Withdrawal in the Epicentral Region of the 1983 Coalinga Earthquake: Journal of Geophysical Research, v. 90.

Segall, P., 1989, Earthquakes Triggered by Fluid Extraction: Geology, v. 17, p. 942-946.

Shafeen, A., E. Croiset, P. L. Douglas, and I. Chatzis, 2004, CO_2 sequestration in Ontario, Canada. Part I: Storage evaluation of potential reservoirs: Energy Conversion and Management, v. 45, p. 2645-2659.

Shamir, G., and M. D. Zoback, 1992, Stress Orientation Profile to 3.5 Km Depth near the San-Andreas Fault at Cajon Pass, California: Journal of Geophysical Research-Solid Earth, v. 97, p. 5059-5080.
Sinha, B. K., M. R. Kane, and B. Frignet, 2000, Dipole dispersion crossover and sonic logs in a limestone reservoir: Geophysics, v. 65, p. 390-407.
Sinha, B. K., and S. Kostek, 1996, Stress-induced azimuthal anisotropy in borehole flexural waves: Geophysics, v. 61, p. 1899-1907.
Sinha, B. K., A. N. Norris, and S. K. Chang, 1994, Borehole Flexural Modes in Anisotropic Formations: Geophysics, v. 59, p. 1037-1052.
Sminchak, J. R., and N. Gupta, 2003, Aspects of induced seismic activity and deep-well sequestration of carbon dioxide: Environmental Geosciences, v. 10, p. 81-89.
Span, R., and W. Wagner, 1996, A new equation of state for carbon dioxide covering the fluid region from the triple-point temperature to 1100 K at pressures up to 800 MPa: Journal of Physical and Chemical Reference Data, v. 25, p. 1509-1596.
Spottiswoode, S. M., and A. McGarr, 1975, Source parameters of tremors in a deep-level gold mine: Bulletin of the Seismological Society of America, v. 65, p. 93-112.
Stein, R., 1999, The role of stress transfer in earthquake occurrence: Nature, v. 402, p. 605-609.
Tezuka, K., 2006, Hydraulic injection and microseismic monitoring in the basement gas reservoir in Japan, 2006 SPE Forum Series in Asia Pacific - Hydraulic Fracturing Beyond 2010: Society of Petroleum Engineers, Macau, China, Society of Petroleum Engineers.
Thomsen, L., 1986, Weak Elastic-Anisotropy: Geophysics, v. 51, p. 1954-1966.
Townend, J., and M. D. Zoback, 2000, How faulting keeps the crust strong: Geology, v. 28, p. 399-402.
van Genuchten, M. T., 1980, A closed-form equation for predicting the hydraulic conductivity of unsaturated soils: Soil Science Society of America Journal, v. 44, p. 892-898.
White, M. D., N. Gupta, M. E. Kelley, and J. R. Sminchak, eds., 2005, Assessment of CO_2 injection and monitoring strategies at the Mountaineer Power Plant site using scalable numerical simulation: Proceedings of the 7th International Greenhouse Gas Control Technologies (GHGT-7) Conference, v. IIb: Vancouver, Canada, Elsevier, 4 p.
Wickstrom, L. H., E. R. Venteris, and J. A. Harper, 2005, Characterization of Geologic Sequestration Opportunities in the MRCSP Region: Phase 1 Task Report, Ohio Division of Geological Survey, Battelle Memorial Institute, U.S. Department of Energy, p. 152.
Wiles, T. D., 2005a, Map3D user's manual, Mine modelling (Pty).
Wiles, T. D., 2005b, Rockburst prediction using numerical modelling-realistic limits for failure prediction accuracy: Sixth International Symposium on Rockburst and Seismicity in Mines, p. 57-63.
Wiles, T. D., 2006, Reliability of numerical modelling predictions: International Journal of Rock Mechanics and Mining Sciences, v. 43, p. 454-472.
Wiles, T. D., R. Lachenicht, and G. van Aswegen, 2000, Integration of deterministic modelling with seismic monitoring for the assessment of rockmass response to mining: Part I Theory: Fifth International Symposium on Rockburst and Seismicity in Mines, p. 379-387.
Willson, S. M., and J. T. Fredrich, 2005, Geomechanics Considerations for Through- and Near-Salt Well Design: SPE Annual Technical Conference and Exhibition, p. # 95621.
Winkler, K. W., B. K. Sinha, and T. J. Plona, 1998, Effects of borehole stress concentrations on dipole anisotropy measurements: Geophysics, v. 63, p. 11-17.
Wiprut, D., and M. D. Zoback, eds., 2002, Fault reactivation, leakage potential, and hydrocarbon column heights in the northern North Sea: Hydrocarbon Seal Quantification, v. NPF Special Publication 11: Amsterdam, Elsevier Science B.V., 203-219 p.
Xu, T. F., E. Sonnenthal, N. Spycher, and K. Pruess, 2006, TOUGHREACT - A simulation program for non-isothermal multiphase reactive geochemical transport in variably saturated geologic media: Applications to geothermal injectivity and CO2 geological sequestration: Computers & Geosciences, v. 32, p. 145-165.
Zoback, M. D., 2007, Reservoir Geomechanics: Cambridge, Cambridge University Press, 449 p.
Zoback, M. D., C. A. Barton, M. Brudy, D. A. Castillo, T. Finkbeiner, B. R. Grollimund, D. B. Moos, P. Peska, C. D. Ward, and D. J. Wiprut, 2003, Determination of stress orientation and magnitude in deep wells: International Journal of Rock Mechanics and Mining Sciences, v. 40, p. 1049-1076.

Zoback, M. D., and H. P. Harjes, 1997, Injection-induced earthquakes and crustal stress at 9 km depth at the KTB deep drilling site, Germany: Journal of Geophysical Research-Solid Earth, v. 102, p. 18477-18491.

Zoback, M. D., and J. H. Healy, 1992, Insitu Stress Measurements to 3.5 Km Depth in the Cajon Pass Scientific-Research Borehole - Implications for the Mechanics of Crustal Faulting: Journal of Geophysical Research-Solid Earth, v. 97, p. 5039-5057.

Zoback, M. D., D. Moos, L. Mastin, and R. N. Anderson, 1985, Well Bore Breakouts and Insitu Stress: Journal of Geophysical Research-Solid Earth and Planets, v. 90, p. 5523-5530.

Zoback, M. D., J. Townend, and B. R. Grollimund, 2002, Steady-state failure equilibrium and deformation of intraplate lithosphere: International Geology Review, v. 44, p. 383-401.

Zoback, M. D., and J. C. Zinke, 2002, Production-induced normal faulting in the Valhall and Ekofisk oil fields: Pure and Applied Geophysics, v. 159, p. 403-420.

Zoback, M. D., and M. L. Zoback, 1989, Tectonic stress field of the conterminous United States: Geological Society of America Memoirs, v. 172, p. 523-539.

Zoback, M. L., M. D. Zoback, J. Adams, M. Assumpcao, S. Bell, E. A. Bergman, P. Blumling, N. R. Brereton, D. Denham, J. Ding, K. Fuchs, N. Gay, S. Gregersen, H. K. Gupta, A. Gvishiani, K. Jacob, R. Klein, P. Knoll, M. Magee, J. L. Mercier, B. C. Muller, C. Paquin, K. Rajendran, O. Stephansson, G. Suarez, M. Suter, A. Udias, Z. H. Xu, and M. Zhizhin, 1989, Global Patterns of Tectonic Stress: Nature, v. 341, p. 291-298.